

General Disclaimer

One or more of the Following Statements may affect this Document

- This document has been reproduced from the best copy furnished by the organizational source. It is being released in the interest of making available as much information as possible.
- This document may contain data, which exceeds the sheet parameters. It was furnished in this condition by the organizational source and is the best copy available.
- This document may contain tone-on-tone or color graphs, charts and/or pictures, which have been reproduced in black and white.
- This document is paginated as submitted by the original source.
- Portions of this document are not fully legible due to the historical nature of some of the material. However, it is the best reproduction available from the original submission.

LIBRARY

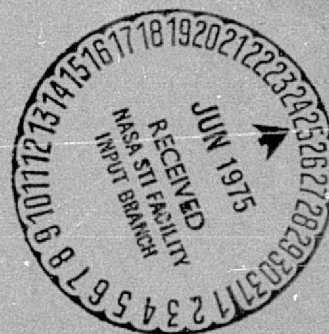
NATIONAL AERONAUTICS AND SPACE ADMINISTRATION

*The Deep Space Network
Progress Report 42-27*

March and April 1975

(NASA-CR-142944) THE DEEP SPACE NETWORK N75-25020
Progress Report, Mar. - Apr. 1975 (Jet
Propulsion Lab.) 210 p HC \$7.25 CSDL 17B

63
6/32 Unclas
25500



JET PROPULSION LABORATORY
CALIFORNIA INSTITUTE OF TECHNOLOGY
PASADENA, CALIFORNIA

June 15, 1975

Preface

Beginning with Volume XX, the Deep Space Network Progress Report changed from the Technical Report 32- series to the Progress Report 42- series. The volume number continues the sequence of the preceding issues. Thus, Progress Report 42-20 is the twentieth volume of the Deep Space Network series, and is an uninterrupted follow-on to Technical Report 32-1526, Volume XIX

This report presents DSN progress in flight project support, tracking and data acquisition (TDA) research and technology, network engineering, hardware and software implementation, and operations. Each issue presents material in some, but not all, of the following categories in the order indicated:

Description of the DSN

Mission Support

- Ongoing Planetary/Interplanetary Flight Projects
- Advanced Flight Projects

Radio Science

- Radio Science Support
- Special Projects

Supporting Research and Technology

- Tracking and Ground-Based Navigation
- Communications—Spacecraft/Ground
- Station Control and Operations Technology
- Network Control and Data Processing

Network Engineering and Implementation

- Network Control System
- Ground Communications
- Deep Space Stations

Operations

- Network Operations
- Network Control System Operations
- Ground Communications
- Deep Space Stations

Planning and Facilities

- TDA Planning
- Facility Engineering

In each issue, the part entitled "Description of the DSN" describes the functions and facilities of the DSN and may report the current configuration of one of the five DSN systems (Tracking, Telemetry, Command, Monitor and Control, and Test and Training).

The work described in this report series is either performed or managed by the Tracking and Data Acquisition organization of JPL for NASA.

Errata

In the article, "A Multiple-Rate Digital Command Detection System With Range Cleanup Capability," by J. R. Lesh, which appeared in *The Deep Space Network Progress Report 42-26*, pp. 91-101, the following corrections should be made:

On page 92, second column, third paragraph, line 5 should read, "For example, if $\overline{f_{sc}}$ denotes a square wave."

On page 93, first column, paragraph three, line 10 " \overline{c}_i by a transmission c_i ," should read " c_i by a transmission \overline{c}_i ."

On page 95, first column, second paragraph, line 3, the expression " c_K " should read " \overline{c}_K ."

CONTENTS

DESCRIPTION OF THE DSN

DSN Functions and Facilities	1
N.A. Renzetti	

MISSION SUPPORT

Ongoing Planetary/Interplanetary Flight Projects

Mariner 10 Mission Support	5
E. K. Davis	
NASA Code 311-03-21-60	
Viking Mission Support	10
D. J. Mudgway, A. I. Bryan, H. C. Thorman, and D. W. Johnston	
NASA Code 311-03-21-70	
Pioneer Venus 1978 Mission Support	28
R. B. Miller	
NASA Code 311-03-21-90	
Helios Mission Support	36
P. S. Goodwin, W. G. Meeks, and S. E. Reed	
NASA Code 311-03-21-50	

SPECIAL

A Dynamic Model for Analysis of Solar Energy Systems	41
C. L. Hamilton	
NASA Code 311-03-31-30	

SUPPORTING RESEARCH AND TECHNOLOGY

Tracking and Ground-Based Navigation

The QVLBI Doppler Demonstration Conducted With Mariner 10	52
C. C. Chao and V. J. Ondrasik	
NASA Code 310-10-60-50	
Distribution Amplifiers for Hydrogen Maser Frequency Standard	64
G. Lutes	
NASA Code 310-10-61-07	

Communications-Spacecraft/Ground

Galois Switching Functions and Their Applications	68
B. Benjauthrit and I. S. Reed	
NASA Code 310-20-67-08	

The Superior Conjunction of Mariner 10 81
R. M. Goldstein and C. T. Stelzried
NASA Code 310-20-66-07

**S/X Band Experiment: Effect of Discontinuities on the
Group Delay of a Microwave Transmission Line 87**
R. W. Beatty and T. Y. Otoshi
NASA Code 310-20-66-06

Graphs With Multiple Nodes for Printed Circuitry 97
H. Taylor
NASA Code 310-20-67-08

Station Control and Operations Technology

DSN Research and Technology Support 107
E. B. Jackson and A. I. Price
NASA Code 310-30-69-02

**Instrumental Polarization of the Goldstone 64-m Antenna
System at 2388 MHz 112**
G. S. Downs and P. E. Reichley
NASA Code 310-30-69-08

Network Control and Data Processing

An NCS Standard Interface for the XDS 900 Series Computers 117
W. Lushbaugh
NASA Code 310-40-72-02

NETWORK AND FACILITY ENGINEERING AND IMPLEMENTATION

Deep Space Stations

High-Reliability Microcircuit Procurement Program in the DSN 124
E. F. Zundel
NASA Code 311-03-42-94

**Simulation Time Switch Assembly: A New Conjoint Station
Time Switching Capability 126**
M. J. Galitzen
NASA Code 311-03-42-48

Automatic Space Noise Recorder 133
R. W. Livermore
NASA Code 311-03-114

An Evaluation of the Use of a Cathode Ray Tube Light Pen Option Within the Deep Space Station Monitor and Control Subsystem	136
J. Thomson NASA Code 311-03-42-53	
Computation of Gravity RMS for HA-DEC Antennas	139
M. S. Katow and R. Levy NASA Code 311-03-14-31	
Structural Data Checks With Computer Graphics	148
M. S. Katow and R. H. Patton NASA Code 311-03-14-31	
Magnetic-Tape Module Copy and Verification System	154
R. Billings and M. Martin NASA Code 311-03-14-42	
Deep Space Network Sequence of Events	159
M. Puchalski NASA Code 311-03-13-11	

OPERATIONS

Network Operations

X-Band Tracking Operations During the Viking Orbital Phase	165
A. L. Berman NASA Code 311-03-13-20	
Tracking Operations During the Pioneer 11 Jupiter Encounter	172
A. L. Berman and R. S. Schlaifer NASA Code 311-03-13-20	

PLANNING

TDA Planning

TDA Data Management Planning: Construction of Maximal Daily Tracking Schedules	187
C. A. Greenhall NASA Code 311-03-31-30	
Quality Assurance Training and Certification Program	192
R. L. Sirpilla and L. H. Fisler NASA Code 311-03-32-20	

Quality Assurance

Hydrogen Gas-Fueled Diesel Engine Feasibility Demonstration	199
R. Reynolds NASA Code 311-03-41-08	

DSN Functions and Facilities

N. A. Renzetti

Office of Tracking and Data Acquisition

The objectives, functions, and organization of the Deep Space Network are summarized. Deep space station, ground communication, and network operations control capabilities are described.

The Deep Space Network (DSN), established by the National Aeronautics and Space Administration (NASA) Office of Tracking and Data Acquisition (OTDA) under the system management and technical direction of the Jet Propulsion Laboratory (JPL), is designed for two-way communications with unmanned spacecraft traveling approximately 16,000 km (10,000 mi) from Earth to the farthest planets of our solar system. It has provided tracking and data acquisition support for the following NASA deep space exploration projects, for which JPL has been responsible for the project management, development of the spacecraft, and conduct of mission operations:

- (1) Ranger.
- (2) Surveyor.
- (3) Mariner Venus 1962.

- (4) Mariner Mars 1964.
- (5) Mariner Venus 1967.
- (6) Mariner Mars 1969.
- (7) Mariner Mars 1971.
- (8) Mariner Venus/Mercury 1973.

The DSN has also provided tracking and data acquisition support for the following projects:

- (1) Lunar Orbiter, for which the Langley Research Center carried out the project management, spacecraft development, and mission operations functions.

- (2) Pioneer, for which the Ames Research Center carried out the project management, spacecraft development, and mission operations functions.
- (3) Apollo, for which the Lyndon B. Johnson Space Center was the project center and the Deep Space Network supplemented the Spaceflight Tracking and Data Network (STDN), which is managed by the Goddard Space Flight Center (GSFC).
- (4) Helios, a joint United States/West Germany project.
- (5) Viking, for which the Langley Research Center provides the project management and Lander spacecraft, and conducts mission operations, and for which JPL provides the Orbiter spacecraft.

The Deep Space Network is one of two NASA networks. The other, the Spaceflight Tracking and Data Network, is under the system management and technical direction of the Goddard Space Flight Center. Its function is to support manned and unmanned Earth-orbiting and lunar scientific and advanced technology satellites. Although the DSN was concerned with unmanned lunar spacecraft in its early years, its primary objective now and into the future is to continue its support of planetary and interplanetary flight projects.

A development objective has been to keep the network capability at the state of the art of telecommunications and data handling and to support as many flight projects as possible with a minimum of mission-dependent hardware and software. The DSN provides direct support to each flight project through that project's tracking and data systems. This management element is responsible for the design and operation of the hardware and software in the DSN which are required for the conduct of flight operations.

As of July 1972, NASA undertook a change in the interface between the network and the flight projects. Since January 1, 1964, the network, in addition to consisting of the Deep Space Stations and the Ground Communications Facility, had also included the Mission Control and Computing Facility and had provided the equipment in the mission support areas for the conduct of mission operations. The latter facilities were housed in a building at JPL known as the Space Flight Operations Facility (SFOF). The interface change was to accommodate a hardware interface between the network operations control functions and the mission control and computing functions. This resulted in the flight project's picking up

the cognizance of the large general-purpose digital computers, which were used for network processing as well as mission data processing. It also assumed cognizance of all of the equipment in the flight operations facility for display and communications necessary for the conduct of mission operations. The network has already undertaken the development of hardware and computer software necessary to do its network operations control and monitor functions in separate computers. This activity became known as the Network Control System implementation. A characteristic of the new interface is that the network provides direct data flow to and from the stations via appropriate ground communications equipment to Mission Operations Centers, wherever they may be; namely, metric data, science and engineering telemetry, and such network monitor data as are useful to the flight project. It accepts command data from the flight project directly into the ground communications equipment for transmission to the station and thence to the spacecraft in a standardized format.

In carrying out its functions, the network activities can be divided into two general areas. The first includes those functions which are associated with the in-flight support and in tracking the spacecraft; its configuration can be characterized as follows:

- (1) *DSN Tracking System.* Generates radio metric data; i.e., angles, one- and two-way doppler and range, and transmits raw data to mission control.
- (2) *DSN Telemetry System.* Receives, decodes, records, and retransmits engineering and scientific data generated in the spacecraft to Mission Control.
- (3) *DSN Command System.* Accepts coded signals from Mission Control via the Ground Communications Facility (GCF) and transmits them to the spacecraft in order to initiate spacecraft functions in flight.

The second category of activity supports testing, training, and network operations control functions and is configured as follows:

- (1) *DSN Monitor and Control System.* Instruments, transmits, records, and displays those parameters of the DSN necessary to verify configuration and validate the network. Provides operational direction and configuration control of the network and primary interface with flight project mission control personnel.

- (2) *DSN Test and Training System.* Generates and controls simulated data to support development, test, training, and fault isolation within the DSN. Participates in mission simulation with flight projects.

The capabilities needed to carry out the above functions have evolved in three technical areas:

- (1) The Deep Space Stations that are distributed around Earth and which, prior to 1964, formed part of the Deep Space Instrumentation Facility. The technology involved in equipping these stations is strongly related to the state of the art of telecommunications and flight/ground design considerations and is almost completely multimission in character. Table 1 gives a description of the Deep Space Stations and the Deep Space Communications Complexes (DSCCs) they comprise.
- (2) Ground communications. This technology supports the Earth-based point-to-point voice and data communications from the stations to the Network Operations Control Area at JPL, Pasadena, and to the Mission Operations Centers, wherever they may be. It is based largely on the capabilities of the common carriers throughout the world which are engineered into an integrated system by the Goddard Space Flight Center for support of all NASA programs. The term "Ground Communications Facility" is used for the sets of hardware and software needed to carry out the functions.

The Network Operations Control Center is the functional entity for centralized operational control of the network and interfaces with the users. It has two separable functional elements; namely, Network Operations Control and Network Data Processing.

The functions of the Network Operations Control Center are:

- (1) Control and coordination of network support to meet commitments to network users.
- (2) Utilization of the network data processing computing capability to generate all standards and limits required for network operations.
- (3) Utilization of network data processing computing capability to analyze and validate the performance of all network systems.

The personnel who carry out the above functions are on the first floor of Building 230, wherein mission operations functions are carried out by certain flight projects. Network personnel are directed by an Operations Control Chief. The functions of the Network Data Processing are:

- (1) Processing of data used by Network Operations Control for the control and analysis of the network.
- (2) Display in Network Operations Control Area of data processed in Network Data Processing Area.
- (3) Interface with communications circuits for input to and output from Network Data Processing Area.
- (4) Data logging and production of the intermediate data records.

The personnel who carry out these functions are located in Building 202, which is approximately 200 m from Building 230. The equipment consists of minicomputers for real-time data system monitoring, two XDS Sigma 5's, display, magnetic tape recorders, and appropriate interface equipment with the ground data communications.

Table 1. Tracking and data acquisition stations of the DSN

DSCC	Location	DSS	DSS serial designation	Antenna		Year of initial operation
				Diameter, m (ft)	Type of mounting	
Goldstone	California	Pioneer	11	26(85)	Polar	1958
		Echo	12	26(85)	Polar	1962
		(Venus) ^a	13	26(85)	Az-El	1962
		Mars	14	64(210)	Az-El	1966
Tidbinbilla	Australia	Weemala	42	26(85)	Polar	1965
		Ballina	43	64(210)	Az-El	1973
—	Australia	Honeysuckle Creek	44	26(85)	X-Y	1973
Madrid	Spain	Robledo	61	26(85)	Polar	1965
		Cebreros	62	26(85)	Polar	1967
		Robledo	63	64(210)	Az-El	1973

^aA maintenance facility. Besides the 26-m (85-ft) diam Az-El mounted antenna, DSS 13 has a 9-m (30-ft) diam Az-El mounted antenna that is used for interstation time correlation using lunar reflection techniques, for testing the design of new equipment, and for support of ground-based radio science.

Mariner 10 Mission Support

E. K. Davis

DSN Systems Engineering Office

This is the last in a series of DSN mission support articles on the Mariner Venus/Mercury 1973-Mariner 10 Project. This report covers the period from February 15 through April 15, 1975. The primary objective during this time was, of course, a successful third encounter of the planet Mercury on March 16, 1975. Other special support activities included trajectory correction maneuver number 8 conducted on March 7, 1975, and restabilization of the spacecraft via acquisition of the reference star Canopus. This period also saw the DSN involved in (1) assisting the Project in obtaining adequate tracking coverage, (2) monitoring DSN implementation for Viking to assure maintenance of capabilities required for Mariner 10, and (3) conducting pre-encounter data flow tests to verify Network support readiness. As planned, the extended mission was terminated during this period, marking the end of the highly successful Mariner Venus/Mercury 1973-Mariner 10 Project.

I. Trajectory Correction Maneuver Number 8

As reported in the previous article, trajectory correction maneuver number 7, conducted on February 13, 1975, was not of the required accuracy. The DSN interface organization assisted the Project in negotiating additional Deep Space Station (DSS) tracking time in order to rapidly and accurately determine the post-burn orbit. Readers are reminded that Mariner 10, at this time, had the lowest priority among the projects supported by the DSN (Pioneers 10 and 11, Helios A, and Viking). However, a minimum but adequate number of additional tracking passes were made available. By late February 1975, orbit solutions indicated that about 50% of the 3-sigma target

error ellipse was within the planetary impact-capture zone. An eighth trajectory correction maneuver was, therefore, required to give the spacecraft the required 90% probability of no impact.

Trajectory correction maneuver number 8 was planned and supported on March 7, 1975. The maneuver was of a sun-line type with the spacecraft placed in the all-axis-inertial mode during the engine burn. Following the burn, the spacecraft was, however, returned to the roll-drift, solar-sailing mode to assure preservation of attitude control gas for Mercury encounter operations. A slow, 24-hour-period roll rate was planned to help accommodate later acquisition of Canopus and to provide suitable

telecommunications link conditions for loading the encounter sequence in the spacecraft computer. In keeping with coverage conflict resolution agreements described in the previous article, trajectory correction maneuver number 8 was timed to be supported by DSS 63. This minimized impacts on other flight project support, particularly Helios A, which obtained zero-longitude support from the German tracking station. Deep Space Network support of the maneuver, as well as special post-burn radio metric data generation activities, was very satisfactory, leading to rapid verification that the required aim point had been achieved.

II. Canopus Acquisition

Canopus acquisition, the next critical event prior to encounter, proved to be a delicate and difficult operation. Uncertainty in the spacecraft roll rate and less than continuous 64-meter subnet coverage contributed to the acquisition problem. Again, for coverage conflict resolution purposes, it was planned that Canopus acquisition would be conducted during the DSS 63 view period. Assuming accurate knowledge of the spacecraft roll rate, the planned procedure was to send a command sequence which would turn on the roll axis attitude control when Canopus entered the tracker's field of view. With the slow spacecraft roll rate, Canopus would then still be acquired following the 18-minute round trip light time. The spacecraft would then be placed in the roll-axis-inertial control mode to preclude the possibility of a bright particle incident causing loss of roll reference prior to or during encounter. Consequently, the acquisition could be accomplished without risking the possibility of attitude control gas depletion due to oscillations induced by a roll sea:ch.

Obviously, accurate knowledge of the spacecraft's roll position and roll rate was essential to achieving Canopus acquisition using the described procedure. The reader is reminded that communications with the spacecraft while in the roll-drift mode was via the spacecraft's low-gain, omnidirectional antenna. The resulting antenna pattern provided only a few peaks and deep nulls in a relatively flat signal level for determining spacecraft roll. However, through comparison of 64-meter deep space station received signal level with the known antenna pattern, the Project expected to be able to clock the spacecraft roll with sufficient precision to initiate the acquisition sequence.

Scheduled DSS 63 passes on March 10, 11, and 12, 1975, were devoted to spacecraft roll timing, and the Project's calculations indicated that the best time for an acquisition

attempt fell at a time when no 64-meter DSS coverage could be made available. Therefore, Project took action to slow the spacecraft roll such that the Canopus crossing would be delayed to occur over DSS 43, where partial-pass coverage could be scheduled. However, the ensuing acquisition attempt on March 12, 1975, was not successful.

The next acquisition attempt on March 13, 1975, was also unsuccessful since the spacecraft roll rate was apparently higher than expected, resulting in the spacecraft being stopped about 7 degrees beyond Canopus. Project then executed a series of spacecraft roll direction changes in an attempt to find Canopus but without success. Concern grew and a spacecraft emergency was declared. The DSN negotiated with the Helios Project JPL representative for release of DSSs 14 and 43 from Helios A to support two Mariner passes. Although Helios agreed in this one case, there was strong opposition to any further reduction in 64-meter subnet coverage; to do so would seriously impact Helios prime mission objectives at perihelion on March 15, 1975. At one point, in the absence of 64-meter DSS support, DSS 12 employed an experimental tracking loop of 3-Hz bandwidth in the Block III receiver to improve signal detection capabilities. This effort was successful in providing the Project with critical signal level information which indicated that the spacecraft was, in fact, rolling toward a position of improved signal rather than toward a deep null. It was rapidly becoming clear that the low-gain antenna mapping technique was not an adequate tool for Canopus acquisition.

It was decided that the spacecraft high-gain antenna, with its narrow beam and precisely calibrated pattern, offered the best means of determining the spacecraft's position and, consequently, Canopus acquisition. This required stopping the spacecraft roll and pointing the high-gain antenna at Earth. The plan was put into effect, and DSS 42 was employed to first get a precise calibration on the roll position. Then, using the received signal level and the pattern to confirm roll position, the spacecraft was allowed to roll-drift toward Canopus. This process took place in carefully controlled steps to assure success. The spacecraft was stopped 40 degrees short of Canopus and again at 7 degrees short to confirm the roll position. At this point, signal level readouts from DSS 63 were provided every 5 seconds as the spacecraft rolled the last 7 degrees. The reported signal levels tracked very precisely along the predicted plot. At the proper time, allowing for one-way communications, the roll-drift stop commands were sent to be received at the spacecraft while Canopus was still acquired by the spacecraft tracker. The technique worked and Canopus was acquired.

The spacecraft was stabilized to celestial reference, and the encounter sequence was initiated shortly thereafter.

III. DSN Encounter Readiness Tests

As described in the previous article, a brief but adequate test plan was designed to revalidate DSN 64-meter subnet encounter support configurations and data flow capabilities. As planned, this test plan was executed in early March 1975 but not without some difficulties. Very limited DSS time was available for tests due to the higher priority activities of other projects as well as Mariner 10's critical events described above. By March 6, 1975, the situation had become critical, and special steps were taken to gain additional test time for a concentrated effort on March 7 and 8, 1975. Stations were instructed to give priority to completion of internal system performance tests. Negotiations with the Viking Project resulted in cancellation of one Viking systems integration test in order to provide DSS 14 test time for Mariner 10.

All test objectives were met by March 10, 1975, and the DSN held a brief encounter readiness review on March 13, 1975. Although the review verified that DSN preparations for encounter were adequate and complete, concern continued to be expressed regarding the limited number of test and training exercises and regarding use of the newly implemented Block IV receiver-exciter configuration at DSS 14.

In addition, it was also planned that end-to-end data flow tests would be conducted with the spacecraft following Canopus acquisition on March 12, 1975. The availability of actual spacecraft data rather than simulated data would have provided a precise demonstration. Unfortunately, these tests were cancelled due to Canopus acquisition difficulties. Consequently, the DSN-supported third encounter had the benefit of only one successful test with each supporting 64-meter station.

IV. Mercury Third Encounter

The encounter sequence was initiated on March 15, 1975, with turn-on of the TV cameras at about 1000 GMT over DSS 63. An incoming TV mosaic was performed as planned; however, the planned color mosaic was delayed 2 hours due to a spacecraft inertial reference update being required. Ground commanding was required to accomplish the color TV mosaic over DSS 14. Problems at the DSS 14 Block IV exciter-transmitter interface caused command aborts during the second command of this sequence. Action was taken to re-establish DSS 14 command capability via the Block III exciter. Although this was

subsequently accomplished, the color mosaic sequence was too far behind the time line and had to be aborted.

Before further discussing DSN support for encounter and another problem associated with that support, it is important to first understand the objectives and situation. The primary objective of third Mercury encounter was the investigation of Mercury's magnetic field and particles. The aim point was optimized to provide acquisition and return of these non-imaging data. Also, as reported in the previous article, third encounter offered excellent geometry for the celestial mechanics experiment through the continuous acquisition of two-way doppler data and ranging points. As a secondary objective, TV data were to be acquired at the full resolution, 117-kbps rate. The non-imaging 2450-bps science was the prime data type having priority over data for accomplishment of other objectives. Consequently, the DSN configuration was such to assure the acquisition, recording, and real-time handling of 2450-bps data rather than video data as on previous encounters. This meant that redundant DSN equipment and data paths were assigned to the non-imaging science rather than to video. Attention was, however, also given to the generation of radio metric data for celestial mechanics purposes and to the acquisition of TV data, but not at the expense of the prime data type.

As with previous Mercury encounters, acquisition of full resolution video data at 117 kbps depended upon proper operation of an experimental, R&D super-cooled maser-ultra cone at DSS 43. This R&D ultra cone was installed at DSS 43 prior to Mercury first encounter to provide for mission enhancement well beyond that which could be gained via the standard 22-kbps mission. Successful use of the ultra cone on the first two Mercury encounters resulted in TV science returns well beyond expectations. R&D devices are only occasionally used in the DSN for operational support with the understanding that they are for mission enhancement purposes, for experimental tests in parallel with operations, and are provided on a best-efforts basis with spares, documentation, testing, and training much less than that normally associated with operational commitments. Use of such equipment carries a higher risk of failure which must be weighed against the potential increase in returns. On Mariner Venus/Mercury 1973, the returns were well worth the gamble. The foregoing is offered to point out that failures in R&D equipment should not be unexpected and that such failures should not be considered as having a serious effect on primary objectives. Some other post-encounter reports offered comments to the contrary.

As the reader might suspect, the DSN had problems with the R&D ultra cone super-cooled maser at DSS 43 during third encounter. On March 14, 1975, word was received that the maser was not cooling down as expected. DSN maser cognizant design engineers were assigned to work with DSS 43 via voice circuit in an all-out effort to effect repairs. The maser was removed, equipped with new cross head and cleaned. JPL engineers continued coordination with DSS 43 throughout March 14-16, 1975, and provided special recommendations regarding cool-down procedures. This effort was not successful and the maser remained warm.

The failure was reported to the Project and frequent progress reports were provided in order that the Project could be ready to make a decision as encounter approached. Even with the standard cone and maser at DSS 43, two options were still open: (1) acquire 117-kbps video containing a high bit error rate (6-10 bits in error per 100) while gaining area coverage or (2) change the data rate to 22 kbps to acquire very high quality but quarter-frame pictures. The Project opted in favor of quality rather than quantity and chose the 22-kbps rate.

The DSN provided continuous, high-quality acquisition and real-time handling of the 2450-bps non-imaging data throughout the third encounter. Also, continuous two-way S-band doppler data were generated, and periodic ranging points were acquired as required for celestial mechanics. DSS 43 performed in an excellent manner for acquisition and transmission of all 22-kbps video data in real time to JPL. Therefore, overall DSN support for this encounter was very satisfactory.

Following encounter, the DSN supported a number of science calibration and spacecraft engineering tests through March 24, 1975. On March 24, data received reflected that the spacecraft had depleted its attitude gas supply. Shortly thereafter, at 1200 GMT, the command was sent to turn off the spacecraft transmitter. DSS 63 observed loss of signal one round-trip light time later indicating that the mission indeed had ended.

Table 1 summarizes some of the significant Project and DSN accomplishments and firsts which were associated with the very productive Mariner Venus/Mercury 1973 mission.

Table 1. Significant Project/DSN mission achievements

First multi-planet gravity assist mission
First spacecraft to photograph Venus
First spacecraft to approach and photograph Mercury
First spacecraft to have multiple encounters with target planet
First spacecraft to effectively conserve attitude control gas by the "solar sailing" technique
First spacecraft to successfully complete eight trajectory correction maneuvers
First JPL spacecraft to transmit full resolution pictures in real time from planetary distances
First mission to use dual-frequency radio transmission
First mission to use arrayed ground station antennas to improve signal-to-noise ratio

Viking Mission Support

D. J. Mudgway, A. I. Bryan, and H. C. Thorman
DSN Systems Engineering Office

D. W. Johnston
Network Operations Office

This article reports the results of RF compatibility tests with the first Viking Flight Orbiter, Lander, and Spacecraft at the Spacecraft Compatibility/Monitor Station, Merritt Island, Florida (STDN(MIL 71)) in January and February 1975.

It also includes the status of the continuing series of mission configuration tests and operational training tests being conducted throughout the DSN, as well as a report on a series of data system compatibility tests involving the flight spacecraft on the launch pad at the Cape, STDN (MIL 71), and the Viking Mission Control and Computing Center at JPL, Pasadena.

I. Background

Previous articles in this series described progress in Viking RF compatibility testing at the Compatibility Test Area, JPL, Pasadena (CTA 21), the start of mission configuration testing at the Pioneer and Mars Deep Space Stations (DSSs 11 and 14), and some of the early work in operational testing at the stations. Activity in all these areas has continued, and in some cases, has now been completed. This article reports completed or continuing work in each of these areas.

II. Viking Lander No. 1 Radio Frequency Compatibility Tests

This assessment and status is derived from test results obtained between STDN (MIL 71) and the Viking Lander Capsule No. 1. These compatibility tests were conducted

at the Kennedy Space Center (KSC), Florida for 55 h from 30 January through 7 February 1975, and the test results verify telecommunications design compatibility between Capsule No. 1 and the DSN.

A. Test Objectives

The objective of the tests was to verify telecommunications design compatibility between the DSN and the Viking Lander Capsule No. 1. The test criteria and parameters simulated direct communications between a Lander flight article on Mars and a 64-m antenna station. Design compatibility had been previously established between the DSN and the Spacecraft Test Lander at CTA-21.

A selected set of standard tests was performed for verifying transponder, RF, command, telemetry and radio metric compatibility. In addition, special tests to

verify synchronization under varying data patterns were performed.

B. Test Conditions

An S-band radio frequency air link of approximately three miles was used between the capsule and the ground station. Radio frequency link amplitude variations were a maximum of 1.0 dB peak-to-peak as established from link stability tests conducted prior to the initialization of the compatibility test program. The test configuration used is shown in Fig. 1.

The ground station software used in these tests was the Telemetry and Command Data and the Planetary Ranging Assembly Data, both of which are officially released for Viking Project support.

C. Test Results

Significant events and other items of the test results, are described below.

- (1) The following radio frequency acquisition tests were performed:

- (a) Carrier acquisition and threshold: (1) downlink one-way, (2) uplink one-way, and (3) downlink two-way.
- (b) Spacecraft receiver acquisition, pull-in range, tracking range and rate.
- (c) Downlink phase jitter: (1) residual carrier phase jitter, and (2) residual subcarrier phase jitter.
- (d) Radio frequency downlink spectrum analysis.
- (e) Transponder rest frequency (voltage controlled oscillator).
- (f) Auxiliary oscillator frequency.

The criteria that were established for these tests were met. For those tests without criteria, the data were obtained for information. No significant problems were encountered or identified.

- (2) Tests of command performance with doppler were conducted. The criteria that were established for these tests were exceeded. Symbol period alarms/aborts were experienced when the subcarrier oscil-

lator frequency was offset. An improper pulse polarity on the 1-k pulse per second signal to the millisecond clocks in the Telemetry and Command Processors was found to be the problem. This was corrected by inverting the pulse polarity of the 1-k pps at the Frequency and Timing Subsystem source. Proper corrective action was verified by retest with the spacecraft. DSN documentation will be revised to reflect proper polarity of all timing signals.

- (3) The following metric data tests were performed:

- (a) Ranging polarity verification.
- (b) Ranging acquisition threshold.
- (c) Ranging delay verification.

The polarity of the transmitted ranging signal was verified at strong uplink and downlink signal levels. The criteria for the ranging delay measurement were met. The Block IV exciter was found to invert the ranging code, whereas the Block III exciter did not show this anomaly. Corrective action requires only type-in changes to the Planetary Ranging Assembly software during operations. The software provides this capability.

- (4) Tests were made for telemetry performance with and without doppler. The criteria that were established for these tests were met. Problems encountered were as follows: the station kept losing downlink signal while attempting to perform a low-signal telemetry performance test in a two-way mode with the spacecraft. A faulty switch module in the Block IV exciter was found to be operating intermittently, which switched the spacecraft between two-way and one-way. The faulty switch was bypassed and the test was successfully completed. The 9-track original data records gave excessive write errors during telemetry performance testing. A 1-h maintenance period was used to restore proper operation of the units; reseating of data decoder assembly-original data record interface cables resolved the problem.
- (5) Viking Lander Capsule No. 1-STDN (MIL 71)-Network Operations Control Center telemetry verification tests were conducted. Figure 1 shows the configuration used during the telemetry performance tests to verify the capsule telemetry. The NOCC received and verified as good the 8.33-bps engineering data and the 250-bps block coded data.

III. Viking Orbiter No. 1 Radio Frequency Compatibility Tests

This assessment and status is derived from test results obtained between STDN (MIL 71) and the Viking Orbiter No. 1. These compatibility tests were conducted at the Kennedy Space Center, Florida, from 27 February to 1 March 1975 for 24 h. Although all tests specified were not completed and the air link signal variations during many of the tests exceeded the expected variations, sufficient tests were completed to verify that no incompatibility exists.

A. Test Objectives

The objective of the tests was to verify telecommunications compatibility between the DSN and the Viking Orbiter No. 1. The test criteria and parameters simulated direct communications between an Orbiter flight article in Martian orbit and a 64-m antenna station. Design compatibility had been previously established between the DSN and the Viking Orbiter No. 1 at JPL (CTA 21) as reported in Ref. 1.

A selected set of standard tests, as specified in Ref. 3 was performed for verifying transponder, RF, command, telemetry and radio metric compatibility.

B. Test Conditions

An S-band, two-way RF air link, and an X-band, one-way RF air down-link were used between the flight article and the ground station. Each RF air link was approximately seven miles long. The test configuration is shown in Fig. 1.

S-band RF link variations were observed to be 0.5 dB peak-to-peak during the first few hours of the test, but later degraded to 6.0 dB peak-to-peak. These conditions existed during daylight hours on 27 February 1975 and also during nighttime hours on 28 February through 1 March 1975. X-band RF link variations were observed to be as low as 2.0 dB peak-to-peak and as high as 8.0 dB peak-to-peak. These conditions existed during nighttime hours on 28 February through 1 March 1975 and appeared to be a function of wind velocity. With approximately 3 h of scheduled test time remaining on 1 March 1975, the STDN (MIL 71) S-Band antenna was found to be off boresight by approximately 4 deg (attributed to wind perturbations). The antenna was realigned and signal level increases of 12.0 dB uplink and 15.0 dB downlink

resulted. The realignment also resulted in reduction of S-band RF link variation from 5.0 dB peak-to-peak to 0.2 dB peak-to-peak.

The ground station software utilized in performing these tests was supplied by the DSN and was a subset of software officially released to the station for Viking Project support. The programs consisted of:

- (1) Telemetry and Command Program, which provides independent control of the commanding and telemetry handling functions. Commands may be controlled manually from the station or automatically from the Mission Control and Computing Center. Telemetry may be decoded, formatted and transmitted to the Mission Control and Computing Center for decommutation and display.
- (2) Planetary Ranging Assembly Program, which provides either continuous spectrum or discrete spectrum operation for determining very accurate range estimates of a spacecraft at planetary distances.

C. Test Results

Significant events and/or other items in the areas of radio frequency acquisition and tracking performance, telemetry, command and metric data generation are described below.

- (1) The following radio frequency acquisition and tracking tests were performed:
 - (a) Downlink threshold one-way.
 - (b) Uplink threshold.
 - (c) Downlink threshold two-way.
 - (d) Spacecraft receiver pull-in range and rate.
 - (e) Carrier residual phase jitter.
 - (f) Transponder rest frequency.
 - (g) Auxiliary oscillator frequency.
- (2) Problems encountered:
 - (a) The spacecraft Radio Frequency Subsystem (RFS) operator at the Spacecraft Checkout Facility (Building AO) had the test transmitter on, and the spacecraft was acquired during downlink threshold (one-way) test 1B. Test was performed in three-way instead of one-way.

- (b) Two-way carrier phase jitter was performed with an uplink signal level of -121 dBm instead of -70 dBm. STDN (MIL 71) uplink power level during this test was adjusted for maximum spacecraft signal level. Test criteria were not met.
 - (i) Tests 4A and 4B specify the 700-Hz offset acquisition to be performed with the Block III exciter configured for ramping. However, the ramp generator does not provide a "clean" RF spectrum as does the voltage-controlled oscillator when not configured for ramping. During offset acquisition, one or more undesirable spectral components pushed the voltage controlled oscillator away from its "captive range" and prevented acquisition. With the ramp capability removed and the exciter driven by the voltage controlled oscillator, acquisition was accomplished on both RFS receivers.
 - (ii) Uplink ramp function stopped at $+28$ -kHz carrier offset on two attempts during test 4A; switched to Block IV exciter and performed the test successfully.
- (3) A test of command capability under doppler conditions was conducted.
- (4) Problems encountered: during the command performance test 9A, with the Command Modulator Assembly in the Idle 1 mode (command subcarrier only), the Viking Orbiter Test Capsule reported "Ready for commanding." The station then sent the commands without first advancing to Idle 2 to acquire bit sync. Since the Orbiter cannot detect command data without having bit sync lock, the block of 5 commands was rejected. Subsequently, using the correct idle sequence, all commands were successfully completed.
- (5) A ranging channel delay threshold and polarity verification test was performed.
- (6) Problems encountered: during first run of test 10C, the S-band antenna at STDN (MIL 71) was found to be 4 deg off boresight as a result of high winds. The pointing error was corrected and the test was rerun successfully.
- (7) a. The following telemetry tests were performed:
 - (a) Downlink Spectrum Analysis
 - (b) Modulation Index and Spectrum Analysis
 - (c) Telemetry Performance Test
- (8) Problems encountered:
 - (a) Due to an insufficient downlink signal level over the Building AO/STDN (MIL 71) air link, the telemetry spectrum test 13B was not run. Some photos were taken and original data records were taped. However, the high noise level rendered both media unacceptable for spectrum analysis. The required photos will be taken of the spacecraft Radio Frequency Subsystem (RFS) support equipment when the Orbiter returns to Building AO for continued system testing.
 - (b) During the telemetry performance tests, 14A and 14B, the link variations were too large (signal varied from ± 1 to ± 3) to permit Y-factor settings. The tests were therefore run at higher signal levels with estimated signal-to-noise ratios based on downlink carrier settings. Under these conditions, telemetry demod losses could not be verified. However, the DSN capability to track and process telemetry data under doppler conditions was verified. Test results indicated no incompatibility.

D. Radio Frequency Air Link Performance

A posttest calibration of the RF link (S-band and X-band) was performed on 3 March 1975. A three-hour S-Band differenced range vs integrated doppler (DRVID) stability run was performed using the Planetary Ranging Assembly software to establish initial ranging acquisition and estimate drift changes over 5-min sample periods. A histogram of deviation vs number of samples is shown in Fig. 2. During the same time period, an S-band amplitude stability run was performed. Each printout shows the mean automatic gain control voltage, the one sigma standard deviation and the number of samples averaged over a 10-min. period. In similar fashion, a 2 h and 10 min. X-band DRVID stability run was performed. The data associated with this test are shown in Fig. 3.

E. Concerns

The fact that active command data can be sent without sending the "Idle 2" signal (subcarrier + bit sync) for a minimum of 6.25 s should draw special attention for mission operations. If the command software does not have a built-in constraint, special attention must be given to operating procedures (both at the Mission Control and Computing Center and the DSS) to ensure that the required command acquisition sequence is transmitted prior to command data.

The Block IV uplink ramp generator was the source of two problems as noted in subparagraph III-C. It should be noted that this ramp generator is not used during flight operations.

IV. Viking Spacecraft No. 1 Radio Frequency Compatibility Tests

This assessment and status is derived from test results obtained between STDN (MIL 71) and the Viking Spacecraft No. 1. This 6-h compatibility test was conducted at the Kennedy Space Center, Florida, on 22 March 1975.

A. Test Objectives

The objectives of the compatibility test were as follows:

- (1) Verify in the spacecraft configuration the capability of the Viking Orbiter No. 1 to receive Viking Orbiter commands and reject Viking Lander Capsule commands.
- (2) Verify in the spacecraft configuration the capability of the Viking Lander Capsule No. 1 to receive Viking Lander Capsule commands and reject Viking Orbiter commands.

B. Test Conditions

An S-band RF air link of approximately three miles was used between the flight article and the ground station. The test configuration is shown in Fig. 1.

The ground station software used in performing these tests was supplied by the DSN and was a subset of software officially released to the station for Viking Project support. The software consisted of the Telemetry and Command Program, which provides independent control of the commanding and telemetry functions. Commands may be controlled manually from the station or auto-

matically from the Mission Control and Computing Center. Telemetry may be decoded, formatted and transmitted to the Mission Control and Computing Center for decommutation and display.

C. Test Results

Significant events and other items of the test results are described below.

- (1) The following command tests were performed:

- (a) Orbiter/lander command discrimination test 3A (Side 1).
- (b) Orbiter/lander command discrimination test 3B (Side 2).

- (2) Problems encountered: during the initial attempt to transmit commands to the Orbiter on Side 1 (test 3A, Step 9), it was noted that Lander Command Detector 1 toggled in and out of lock. The test conditions under which this anomaly occurred were (1) uplink Signal Level (total power) set at -99.85 dBm, (2) orbiter subcarrier frequency of 512.0 Hz, and (3) bit sync acquisition sequence (Idle 2)

Upon detection of this discrepancy, on-line trouble shooting was initiated in real time. The Command Modulator Assembly was returned to Idle 1 (subcarrier only) and the lock status of Lander Command Detector 1 was monitored. Under this condition, a stable out-of-lock condition was detected. The Command Modulator Assembly was reconfigured to offset the orbiter subcarrier to a frequency of 512.1 Hz. Monitoring of the lock status of the Lander Command Detector 1 while Idle 1 and Idle 2 were transmitted showed that the detector toggled in and out of lock only with Idle 2 present. Photographs of the signal on the interface wires were taken during this on-line investigation with negative results. With these data for off-line investigation and analysis, it was decided to continue with the test in accordance with the procedure and to document test discrepancies.

During the conduct of test 3A, Lander Command Detector 1 lock status at no time indicated an in-lock condition when the command waveform to the Orbiter was Subcarrier \oplus Bit Sync \oplus Data. Further, the false in-lock condition of Lander Command Detector 1 with Idle 2 present occurred at strong uplink signal as evidenced by the test results at -143 dBm.

The anomolous in-lock conditions identified above were not noted on Lander Command Detector 2 during the accomplishment of test 3B.

V. Viking Lander No. 2 Compatibility Tests

These tests were performed from 7 April through 9 April 1975 for 24 h.

A. Test Objectives

The objectives of the tests were to verify telecommunications design compatibility between the DSN and the Viking Lander Capsule No. 2. The test criteria and parameters simulated direct communications between a Lander flight article on Mars and a 64-m antenna Deep Space Station.

A selected set of standard tests, was performed for verifying transponder, RF, command, telemetry and radio metric compatibility.

B. Test Conditions

An S-band RF air link of approximately three miles was utilized between the flight article and the ground station. RF link amplitude variations were a maximum of 1.0 dB peak-to-peak during the tests as established from link stability tests conducted prior to the initialization of the compatibility test program. The test configuration is shown in Fig. 1.

The ground station software utilized in performing these tests was supplied by the DSN and was a subset of software officially released to the station for Viking Project support. The software consisted of the Telemetry and Command Program, which provides independent control of the commanding and telemetry functions. Commands may be controlled manually from the station or automatically from the Mission Control and Computing Center. Telemetry may be decoded, formatted and transmitted to the Mission Control and Computing Center for decommutation and display.

C. Test Results

Significant events and/or other items in the areas of radio frequency acquisition and tracking performance, telemetry, command, and metric data generation are described below.

- (1) The following radio frequency tests were performed:

- (a) Carrier acquisition and threshold: downlink one-way, uplink one-way, and downlink two-way.
- (b) Spacecraft receiver acquisition, pull-in range, tracking range and rate.
- (c) Downlink phase jitter: residual carrier phase jitter and residual subcarrier phase jitter.
- (d) RF downlink spectrum analysis.
- (e) Transponder rest frequency (VCO).
- (f) Auxiliary oscillator frequency.

The criteria that were established for these tests were met. For those tests without criteria, the data were obtained for information. No significant problems were encountered or identified.

- (2) The following command test was performed: command performance with doppler. The criteria that were established for this test were met. No significant problems were encountered or identified.
- (3) The following metric data tests were performed:
 - (a) Ranging polarity verification.
 - (b) Ranging acquisition threshold.
 - (c) Ranging delay verification.

The polarity of the transmitted ranging signal was verified at strong uplink and downlink signal levels. The criteria for the ranging delay measurement was met. No significant problems were encountered or identified.

- (4) The following telemetry test was performed: telemetry performance with/without doppler. The criteria that were established for this test were met. No significant problems were encountered or identified.

VI. Mission Configuration Tests

The previous article covered the percentage of strong-signal Mission Configuration Tests (MCTs) completed at the time of writing, with details of the testing at the Mars Station at Goldstone, California. Figures 4 and 5 herein represent the current test status of the 64-m and primary Viking 26-m subnets, showing the planned vs actual status as of mid-April. The initial blocks of time, as previously stated, represent the strong signal tests preparatory to

start of Operational Verification Tests (OVTs). System Integration Tests (SITs) and Ground Data System (GDS) Test.

The second time blocks represent the low signal telemetry bit error and doppler jitter tests, which do not affect the station configuration and are carried out on a non-interference basis for completion prior to launch.

Summarizing the test status, all the stations are on or ahead of schedule and there is a high degree of confidence that all remaining tests will be completed prior to launch as scheduled.

VII. Operational Verification Testing and Training

Personnel training is a multifaceted item and many different activities contribute to the preparation of the DSS staff for support of the Viking Flight Operations System tests and flight support. Examples are the mission independent training to familiarize the crews with the calibration, operation, and maintenance of equipment in a stand-alone mode, and reading of the Viking Network Operations Plan to apply the Viking procedures to the operation of the equipment. These are in conjunction with becoming familiar with the spacecraft and the Viking mission, with on-site exercises simulating Viking operations. The most significant training vehicle, however, is participation in the Operational Verification Tests, and these are designed expressly to exercise the Network functions and procedures to the greatest degree possible. Provided that the on-site training prerequisites have been met, these tests are instrumental in raising the level of training from approximately 15% to approximately 80% in a relatively short time.

This rapid increase in training proficiency, however, is dependent upon having each of the tests scheduled on a particular day and time of day to enable each DSS crew to participate equally. In practice, this is proving to be extremely difficult as the only time available is that between Pioneer and Helios tracks at the same time of day every day. Rescheduling crews is extremely difficult and costly, therefore the total block time is being stretched to complete the training for Viking.

Following is a brief synopsis of each of the tests carried out with DSSs 11, 14, 42, 43, 61, and 63 to date.

A. DSS 11

1. OVT — 1 (2-5-75). The first test with DSS 11 was a partial success but contained many Simulation Conversion Assembly (SCA) problems due to minor procedural errors and operator unfamiliarity. All telemetry and command procedures that were attempted were well executed, and the SCA procedures were modified subsequent to the test.

2. OVT — 2 (2-11-75). This test was considered 90% complete. Again, SCA problems were encountered, along with personnel interface problems with the Network Data Processing Area for SCA support. Interface procedures were modified to prevent a recurrence.

3. OVT — 3 (2-18-75). This test was attempted with little success. Due to data transfer delays compounded by SCA and Data Decoder Assembly hardware problems, the test was only 10% successful. However, valuable training was obtained isolating and rectifying the failures.

4. OVT — 4 (2-19-75). This test was 75% successful. The test was delayed by SCA hardware problems, specifically video conditioners.

5. OVT — 5 (2-23-75). This test was considered 100% successful and all items were covered. Only minor procedural errors, which were corrected readily, hindered the test slightly, if at all.

6. OVT — 6 (2-25-75). This test was another completely successful effort.

7. OVT — 7 (2-26-75). This test was only 95% successful because the analog playback portion of the sequence of events had not been completed. A Symbol Synchronizer Assembly problem on the prime Telemetry and Command Subsystem string forced a change-over to the backup; the transition plus the repair of the Symbol Synchronizer Assembly during the test was excellent.

As a result of these seven OVTs, DSS 11 was considered capable of supporting Viking operations with no foreseen difficulty.

B. DSS 14

1. OVT — 1 (2-12-75). Test No. 1 was conducted with DSS 14 in a planetary configuration. Fifty percent of the sequence of events was accomplished and valuable training obtained. Familiarity with the 6-channel Simulation Conversion Assembly was gained along with Viking planetary configurations and procedures.

2. OVT — 2 (2-15-75). This test was 35% completed. Two Data Decoder Assembly failures coupled with Simulation Conversion Assembly procedural problems used up 3½ h of test time. A lot was learned to aid future tests, and the pretest calibration procedures for the 6-channel Simulation Conversion Assembly were generally overhauled in the light of experience gained from the test.

3. OVT — 3 (2-16-75). Test No. 3 was considered 90% successful. Only the playback portions were not met. Data-transfer/Simulation Conversion Assembly delayed the test start and this was the main reason for not being 100% complete.

4. OVT — 4 (2-20-75). This test was very successful (90%) considering only 4 of 6 data channels were available. Block decoder Assembly 2 and Data Decoder Assembly 4 were red allowing only 4 telemetry channels to be used. However, the test ran very smoothly and other than Original Data Record recall, all major objectives were met.

5. OVT — 5 (2-27-75). Two Data Decoder Assemblies were down plus a bad copy of the Simulation Conversion Assembly drop F was discovered. All objectives, except recalls, were met.

6. OVT — 6 (3-19-75). This test was considered 90% successful. Test time was lost due to real-time operations priority.

7. OVT — 7 (3-30-75). This test was considered 100% successful. All objectives accomplished.

C. DSS 42

1. OVT — 1 (3-8-75). This test was considered 70% successful; not all telemetry rates were processed due to loss of time because of unfamiliarity with the Simulation Conversion Assembly.

2. OVT — 2 (3-27-75). Outside of an initially bad attempt at Analog Original Data Record playback, all objectives were met and the test was a complete success.

3. OVT — 3 (3-29-75). This test was 90% successful. No Digital Original Data Record replay was attempted because of a delay caused by a Simulation Conversion Assembly to Subcarrier Demodulation Assembly data routing problem.

4. OVT — 4 (4-4-75). This test was 100% successful from an operational standpoint. A discrepancy report referred to the inability to locate frame synchronization of 8.333 bps.

5. OVT — 6 (4-16-75). Because the prime processor string was down, the shared processor was used for half of the test. The test proved 100% successful.

6. OVT — 7 (4-17-75). This test was 100% successful. At this point DSS 42 appears to be well qualified to support the Viking Mission.

D. DSS 43

OVT — 1 (4-14-75) was 60% successful. Problems with the Simulation Conversion Assembly's channels 5 and 6 caused considerable delays.

E. DSS 61

1. OVT — 1 (4-8-75). This test was considered 85% successful. Encountered some minor procedural errors and failed in an attempt at Digital Original Data Record recall.

2. OVT — 2 (4-13-75). This test was 100% successful. All test objectives were met.

3. OVT — 3 (4-16-75). This test was 100% successful. All objectives achieved.

F. DSS 63

1. OVT — 1 (4-5-75). This test was considered 100% successful. A slight core allocation problem in the Simulation Conversion Assembly core buffer, but it was corrected and did not impact test result.

2. OVT — 2 (4-9-75). This test was 100% successful with all objectives met.

3. OVT — 3 (4-14-75). This test was 100% successful, meeting all test objectives. Also, mated-Lander commanding was successfully performed, as an additional sequence of events item.

G. Conclusion

The planned schedule was to support System Integration Tests after each Station shift had participated in at least one Operational Verification Test; the OVTs were to be completed with all shifts prior to support of the first Ground Data System test at that station. These criteria

could not be met at DSS 14. While Fig. 6 reflects this problem, it also shows that the testing and training will be completed before the Planetary Verification Tests commence.

VIII. Viking Data System Compatibility Tests

From January through April 1975, STDN (MIL 71) participated in a series of Viking command and telemetry tests with communications support by NASA Communications/Ground Communications Facility (NASCOM/GCF) and operations support by the Network Operations Control Center. The test series began with a DSN-Viking Mission Control and Computing Center Systems Integration Test and proceeded to a Ground Data System Test. Both of these tests involved simulated command operations and simulated telemetry data. These tests were followed by a set of Mission Precursor tests with the Viking Orbiter and Viking Lander mated flight spacecraft mounted on the launch vehicle at Kennedy Space Center. After completion of the precursor tests, a set of flight article compatibility tests was conducted with the Orbiter and Lander located at their respective Eastern Test Range system test buildings.

The precursor tests and the flight article compatibility tests were supervised by the Viking Project Compatibility Test Manager with participation by the Viking Flight Team in the mission support area at JPL.

A. STDN (MIL 71) Equipment Configuration and Performance

The DSS Command Subsystem configuration used for these tests is shown in Fig. 7.

The DSS Telemetry Subsystem configuration for mated-spacecraft tests, in which the telemetry was received on the orbiter downlink, is shown in Fig. 8.

The DSS Telemetry Subsystem configuration for the Viking Lander flight compatibility test, FCT-1, in which the telemetry was received on the Lander direct downlink, is shown in Fig. 9.

The Simulation Conversion Assembly of the DSS Test and Training Subsystem was operated in the computer-remote ("long-loop") mode to support telemetry simulation for the system integration test and the ground data system test, and was operated in the computer-local ("stand-alone") mode for pretest telemetry data transfer verification in each of the remaining tests. During these

tests, there were no failures in the Simulation Conversion Assembly. A couple of malfunctions occurred in the Command Subsystem, and several failures were encountered in the Telemetry Subsystem.

B. System Integration Test

The STDN (MIL 71) system integration test was conducted on 9 January and 18 February. The purpose of the test was to verify the integrity of the STDN (MIL 71)/Viking Mission Control and Computing Center interfaces. The sequence of events provided for simulated Viking Orbiter, Viking Orbiter-Lander, and Viking Lander command operations and processing of dual-subcarrier simulated telemetry data at all the rates shown in Figs. 8 and 9.

Approximately half of the test objectives were completed on 9 January and the remainder on 18 February. Discrepancies encountered during the 9 January portion of the test were:

- (1) A timing problem in the Data Decoder Assembly-A1 introduced frequent errors in the Viking Lander 500-bps and 1000-bps block coded telemetry data.
- (2) The Block Decoder Assembly on channel 3 of the TCP-A caused errors in the Viking Orbiter 16-kbps block coded telemetry data.

Subsequent to the 9 January test, intensive troubleshooting and testing were done at STDN (MIL 71) to prepare the station for the Lander telecommunications RF compatibility testing of 30 January through 7 February and for the remaining system integration test. Prior to 18 February, two engineering verification tests were conducted with Network Operations Control Center support. The system integration test was successfully completed on 18 February and no discrepancies were encountered on that date.

C. Ground Data System Test 7.0

This test was conducted on 11 March and 18 March. From the DSN viewpoint, the test sequence was equivalent to the system integration test sequence. In the Mission Control and Computing Center, however, the ground data system test involved more output and display processing. STDN (MIL 71) encountered the following equipment malfunctions on 11 March, but the backup capability available permitted the test to proceed so that over half of the test objectives were completed on that date.

- (1) The first problem encountered was that the Original Data Record tape unit on Telemetry and Command Processor (TCP)-A did not operate properly. The low- and medium-rate telemetry data were therefore paralleled through TCP-B to obtain a good Original Data Record.
- (2) The second problem encountered was that Subcarrier Demodulator Assembly-1 would not lock up on data from the receiver. Subcarrier Demodulator Assembly-2 was used and the test continued in that configuration until the end of the test.
- (3) The third problem encountered was that Data Decoder Assembly-A1, which was assigned to TCP channel 3 for this test, was putting the wrong time in the wideband data blocks. This did not impact the real-time processing of the high-rate telemetry data but did cause impact on the 9-track Original Data Record playback.
- (4) The fourth problem encountered was that Command Modulator Assembly-2 started giving alarms that would not clear when a reinitialization was performed. Command Modulation Assembly-2 was to be used for Lander-direct commanding. The Lander-direct command operation was transferred to TCP-A and Command Modulator Assembly-1.

Ground Data System Test 7.0 was successfully completed on 18 March. The only DSN anomaly encountered on that date was a 10-min. data outage that occurred when Symbol Synchronizer Assembly-A2 and the Block Decoder Assembly were unable to acquire lock when the data rate was changed from 16 kbps to 2 kbps. A reinitialization of TCP channel 3 cleared the problem.

The results of the System Integration Test and Ground Data System Test 7.0 indicated that the Ground Data System was ready for the Mission Precursor Tests and the Flight Article Compatibility tests.

D. Mission Precursor Tests

The precursor tests were conducted with the mated spacecraft mounted on the launch vehicle with S-band telecommunications from the Orbiter.

1. **Flight Events Demonstration.** The Flight Events Demonstration was conducted on 1 April. The STDN (MIL 71) received low- and high-rate telemetry on the

Orbiter link and also processed low-rate telemetry received from nearby near-Earth stations. There was no commanding required. No problems were experienced at STDN (MIL 71) during this test.

2. **Viking Orbiter Precount Test.** The Viking Orbiter Precount Test was conducted on 2 April. This test involved remote commanding as well as telemetry processing over the full range of data rates. Again, no problems were experienced at STDN (MIL 71).

3. **Viking Lander Prelaunch Checkout.** The prelaunch checkout precursor was conducted on 3 April. The test sequence included Orbiter commanding and also Lander-capsule commanding through the Orbiter. Telemetry included both Orbiter and Lander data on the Orbiter subcarriers.

At the start of the test, the Command Modulator Assembly on TCP-B(CMA-2) was not ready to be turned over to the Project. The Command System Cognizant Operations Engineer at JPL was called in and he isolated the problem and instituted a temporary fix that permitted Command Modulator Assembly-2 to provide its scheduled support of the test.

During this test, the Data Decoder Assembly-A1 started putting the wrong time in the wideband data blocks output on TCP channel 3. A front panel reload was tried, to no avail. Then the Frequency and Timing Subsystem drawer was replaced without correcting the problem. Finally, TCP-A was reloaded and Data Decoder Assembly-A2 was assigned to channel 3. TCP-A was checked out by command and telemetry data flow tests and returned to Project use. After the test, STDN (MIL 71) found and replaced a bad power supply that appeared to be causing the time error problem in Data Decoder Assembly-A1. However, the same symptoms have occurred on this Data Decoder Assembly in subsequent tests, and the cause of this malfunction was not finally determined until April 29.

4. **Terminal Countdown Demonstration.** The Terminal Countdown Demonstration was conducted on 5 April. The test sequence was essentially the same as for the Flight Events Demonstration. The STDN (MIL 71) function was to receive and process telemetry received from the spacecraft and from nearby near-Earth stations.

The test was successfully completed, but during the first half of this test the Demodulator Decoder Assembly-A1 timing problem showed up again in the 2-kbps output of

TCP-A, channel 2. Also, an unusually large number of data block error bursts occurred in the NASCOM line during this test.

E. Flight-Article Compatibility Tests (FCT)

Tests FCT 3, 4, and 1 were conducted after the Viking Orbiter and Lander had been returned from the pad to their respective system test facilities. Test FCT-2 had been conducted earlier at JPL, and is reported here for completeness.

- (1) FCT-3 was conducted on 10 April. The test sequence represented the command and telemetry activities related to the preseparation checkout portion of the mission. Telecommunications to STDN (MIL 71) were via the Orbiter link. Telecommunication from the Lander to the Orbiter were via cable between the two spacecraft. The start and end of the test sequence were delayed about 3½ h due to spacecraft trouble. STDN (MIL 71) encountered some equipment faults but was able to switch to backup equipment. The command activities and the telemetry stream processing were not impaired, except that the telemetry time tags were in error during a short portion of the test.

During the pretest data transfers, the Block Decoder Assembly (on TCP-A, channel 3) was turned back to the station for troubleshooting and repair. It was repaired and brought back into service in time for processing of high-rate telemetry. TCP-B was used for low-rate telemetry while the Block Decoder Assembly was being repaired.

Timing errors in Data Decoder Assembly-A1 were observed when that equipment was configured for processing of high-rate telemetry on TCP-A, channel 3. Therefore, TCP-A was reconfigured to use Data Decoder Assembly-A2 on channel 3.

The Data Decoder Assembly on channel 2 of TCP-B (DDA-B1) also exhibited some time-tag errors during this test. That equipment has subsequently been repaired and retested with no recurrence of the problem. Recall of Original Data Records was not required at end of test. However, if a recall had been needed, it would have been necessary to recall the entire Original Data Record because the occasional erroneous time tags might have precluded a time-selective recall. Also, due to

the exchange of equipment, it would have been difficult to know which recorder contained data for a given time period.

- (2) FCT-4 was conducted on 15 April. The test sequence represented the command and telemetry activities related to the Lander capsule separation, descent, entry, and Mars landing events of the mission. The VHF link from the Lander capsule to the Orbiter was by cable. Spacecraft anomalies encountered during the test extended the time required to complete the test. There were no equipment malfunctions and only one procedural problem.
- (3) FCT-1 was conducted on 17 April. The test sequence represented a set of Lander activities on the Martian surface with direct S-band telecommunications to STDN (MIL 71).

Upon completion of pretest telemetry and command data transfer verifications, an operational system was available to the Project prior to start of the test. Due to two problems in TCP-A, STDN (MIL 71) was configured to use TCP-B as the prime string at FCT-1A "test start" time. During the pretest data transfer, an input/output control problem was encountered on TCP-A. After this unit was reloaded and verified, TCP-A was declared prime and used throughout the remainder of the test without any impact on telemetry data or command activity. During this test, the TCP-B string was kept in a hot backup mode. It was found in the pretest checkout that Data Decoder Assembly-A1 still had a timing error problem, therefore Data Decoder Assembly-A1 was not used during the test.

In the final hour of the FCT-1B test, when the downlink was acquired, it was observed in the Network Control Center that the high-rate telemetry from TCP-A was good. However, the low-rate telemetry (8½ bps) output from TCP-A was poor due to fluctuations of signal-to-noise ratio. Therefore, the low-rate telemetry from TCP-B was added to the high-speed data line and validated in the Network Operations Control Center. The test conductor was then given the choice to process the good 8½ bps stream from TCP-B instead of the poor stream from TCP-A. After completion of the test, a test of the TCP-A low-rate channel was conducted in which it was determined that a simple, two-type-in, reinitialization of the channel eliminated the signal-to-noise ratio fluctuations. The

only other problem encountered by the DSN was a 5-min outage of one of the eight NASCOM voice circuits. Support of command activity was satisfactory throughout the test as it was in most of the previous tests.

- (4) FCT-2 was conducted at CTA 21 on 20 January while Orbiter-2 was still in the Spacecraft Assembly Facility prior to shipment to KSC. This test and also a special Orbiter Performance Analysis Group (OPAG) "end-to-end test" and a special VHF relay test, were supported by CTA 21, GCF, and NOCC. As with subsequent FCTs, these tests were supervised by the Viking Compatibility Test Manager, and the Viking Flight Team participated.

The DSN elements supporting FCT-2 and the associated special tests performed very satisfactorily and with no malfunctions.

F. NASCOM/GCF Support

The satisfactory operation of voice, high-speed data, and wideband data circuits provided by NASCOM and GCF was vital to the success of these tests.

G. Network Operations Control Center (NOCC) Support

The network data processing area function implemented by the Network Control System Block II provided real-time displays of telemetry data and command system data received via high-speed data line.

The Block II Network Control System (NCS) implementation does not provide any real-time displays of telemetry data received via wideband data line; therefore, the only visibility of wideband telemetry was by Block I line printer dumps of data blocks, which is an awkward and time-consuming method to validate telemetry system status. (Block III NCS implementation will provide real-time wideband telemetry displays.)

There was no station monitor data available in the Network Operations Control Center nor at the station because STDN (MIL 71) does not have a monitor subsystem. Within the implementation constraints described, the Network Operations Control Center performed admirably throughout this series of tests.

H. Conclusions

Results of the tests described above lead to the following conclusions:

- (1) STDN (MIL 71), NASCOM/GCF, and NOCC were effectively utilized as elements of the ground data system for premission engineering tests and flight team preliminary training.
- (2) The successful support of these tests depended heavily on the availability of redundant equipments, particularly in the telemetry subsystem.
- (3) The most persistent problems encountered were related to low reliability of Data Decoder Assemblies A-1 and B-1, and the Block Decoder Assembly hardware. In contrast, Data Decoder Assembly-A2 exhibited surprisingly high reliability.
- (4) Command Subsystem performance and Simulation Conversion Assembly performance at STDN (MIL 71) were very satisfactory.
- (5) NASCOM/GCF performance was also quite satisfactory.
- (6) The Network Data Processing functions provided useful, independent DSN validation of command and telemetry status, within the constraints of the present implementation.
- (7) There were no software problems in the STDN (MIL 71) subsystems nor in the Network Data Processing Area during these tests.

Acknowledgment

The work described above was carried out under the cognizance of the following members of the DSN Engineering Staff: Viking Orbiter and Lander RF Compatibility Tests, A. I. Bryan and R. P. Kemp; STDN (MIL 71)/VMCCC Data System Compatibility Tests, H. C. Thorman and H. G. Lemasters. The MCT and OVT testing were carried out under the supervision of the Network Operations Project Engineer, D. W. Johnston.

Reference

1. *The Deep Space Network Progress Report 42-24, September and October 1974.*
Jet Propulsion Laboratory, Pasadena, California, Dec. 15, 1974.

ORIGINAL PAGE IS
OF POOR QUALITY

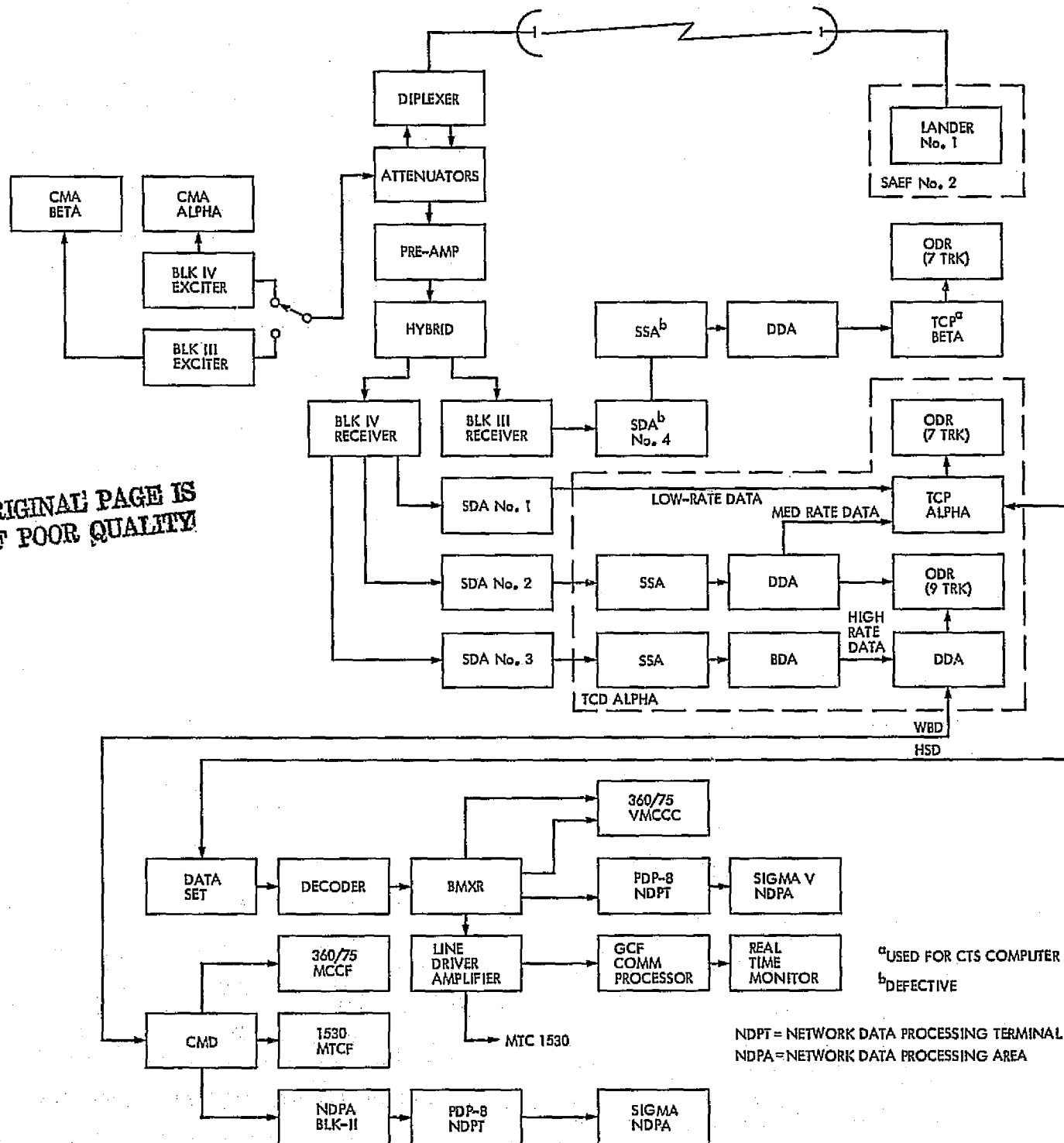


Fig. 1. DSN/Viking lander capsule No. 1/NOCC/VMCCC telecommunications test configuration, Jan. 30, 1975

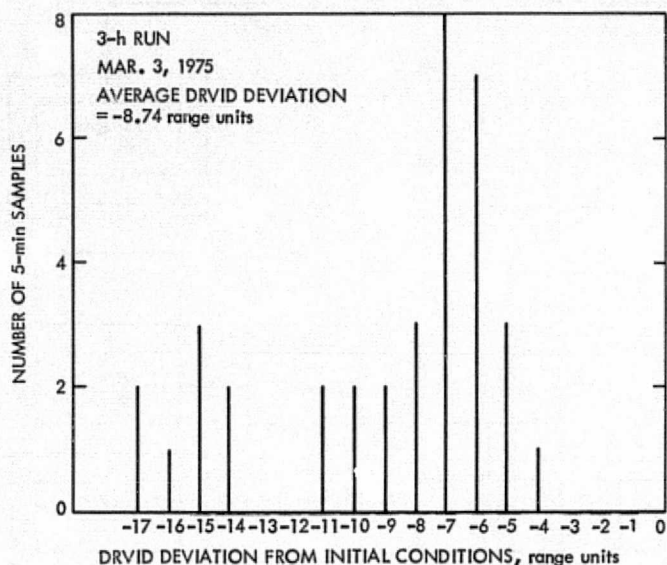


Fig. 2. Building AO/STDN (MIL 71) S-band DRVID stability

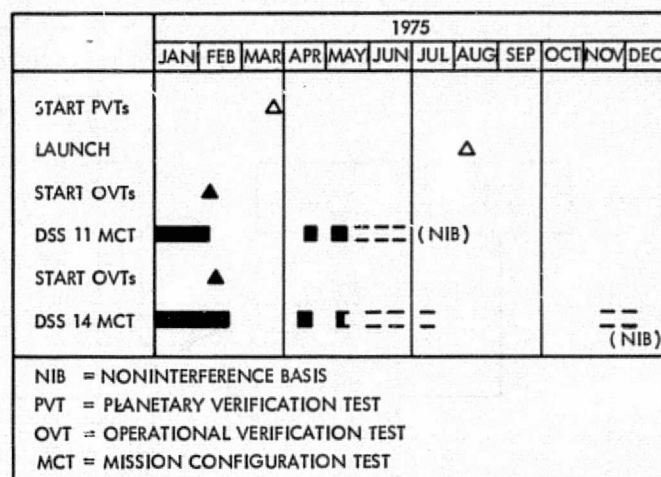


Fig. 4. MCT status for DSSs 11 and 14

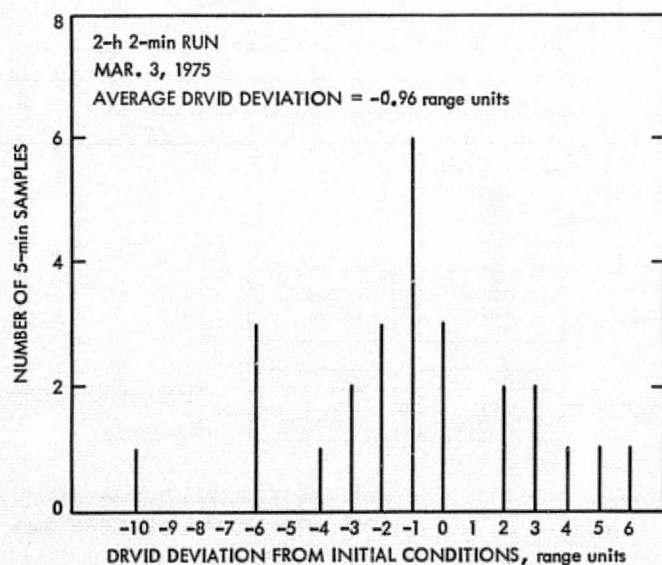


Fig. 3. Building AO/STDN (MIL 71) X-band DRVID stability

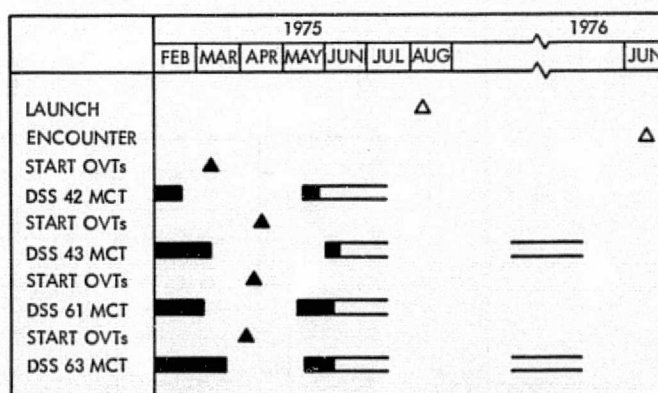


Fig. 5. MCT status for DSSs 42, 43, 61, and 63

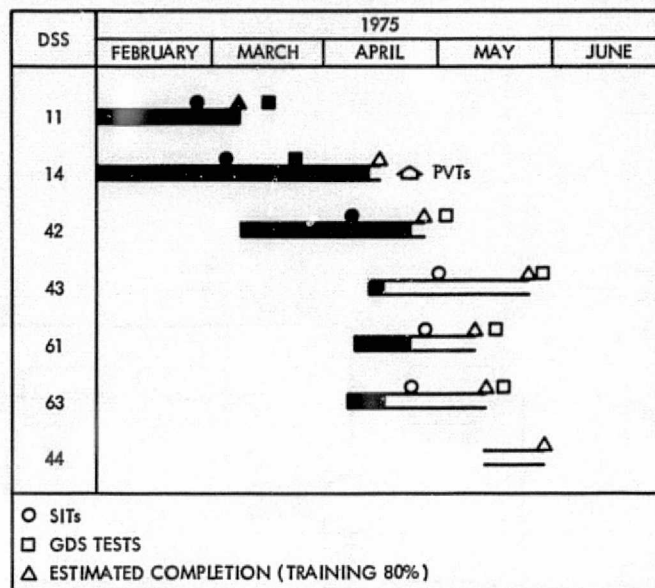


Fig. 6. OVT/training status summary

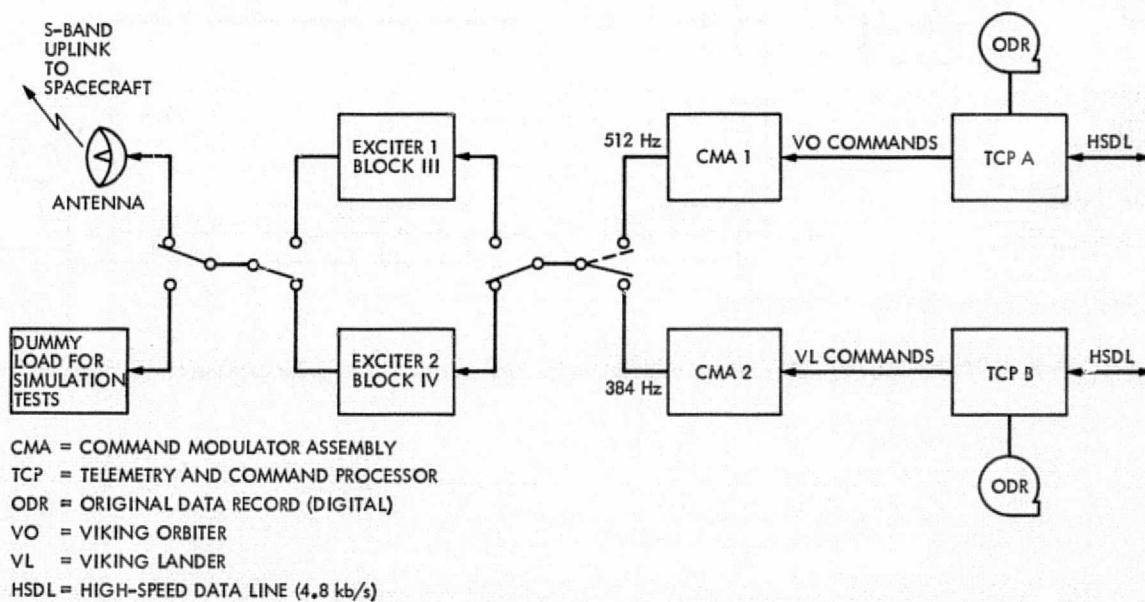


Fig. 7. STDN (MIL 71) DSS command subsystem configuration for Viking orbiter and lander tests

SCA SIMULATION CONVERSION ASSEMBLY
 SDA SUBCARRIER DEMODULATOR ASSEMBLY
 SSA SYMBOL SYNCHRONIZER ASSEMBLY
 DDA DATA DECODER ASSEMBLY*
 BDA BLOCK DECODER ASSEMBLY
 WBDL WIDEBAND DATA LINE (28.5 kbits/s)

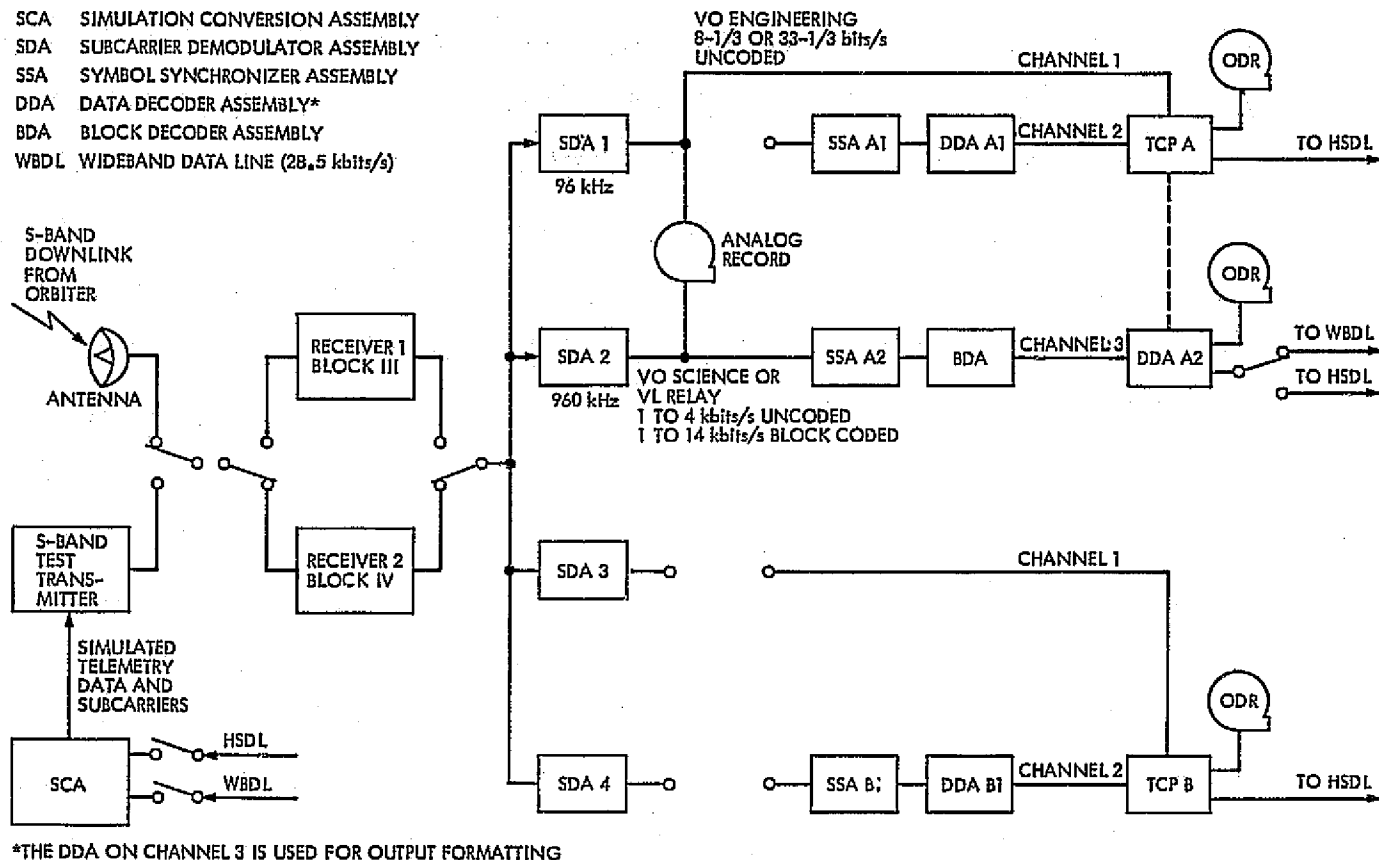


Fig. 8. STDN (MIL 71) DSS telemetry subsystem configuration for Viking orbiter and lander capsule mated spacecraft tests

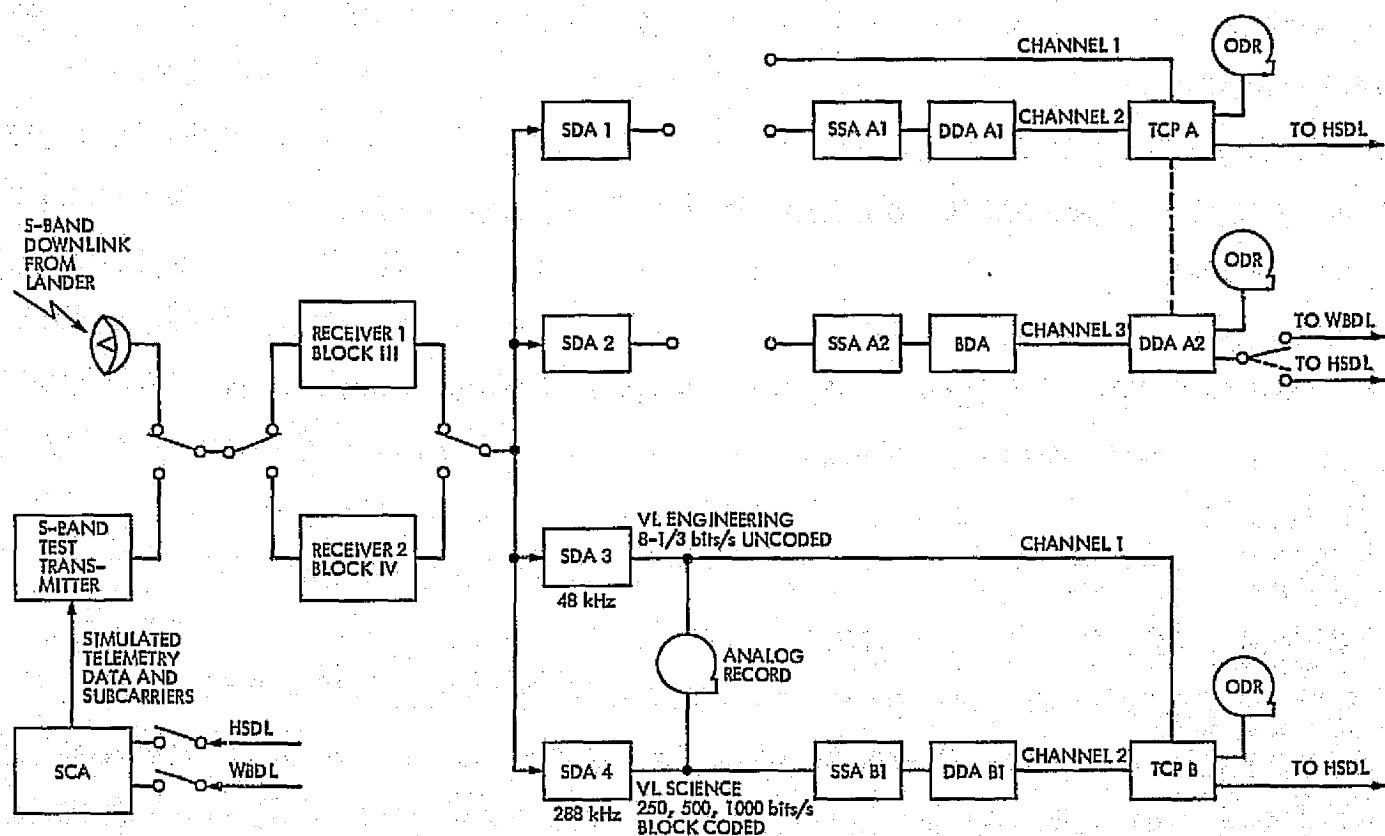


Fig. 9. STDN (MIL 71) DSS telemetry subsystem configuration for Viking lander (direct) tests

Pioneer Venus 1978 Mission Support

R. B. Miller

DSN Systems Engineering Office

The current status of the Pioneer Venus 1978 Mission is described. The frequency allocation and latest version of the Deep Space Station configuration for the Multiprobe Mission are also presented.

I. Introduction

The Pioneer Venus 1978 Project will consist of two missions: an Orbiter Mission and a Multiprobe Mission. The spacecraft will be constructed by Hughes Aircraft Company, under contract to Ames Research Center, which has Project Management responsibility. The Orbiter Mission will be launched in May 1978 and the Multiprobe Mission in August 1978; both missions will arrive at the planet Venus in early December 1978. The Multiprobe Mission will last on the order of two hours, and the Orbiter Mission will last 243 Earth days, which is one Venusian day.

Reference 1 describes the Multiprobe Mission spacecraft, the science payload of the Multiprobe Mission, and the entry sequence and associated telecommunications aspects of the Multiprobe Mission. Reference 2 describes the preliminary plans of the DSN for the configuration of the Deep Space Stations (DSSs) in support of the multiprobe entry sequence. The majority of this article will concentrate on the frequency allocation, which has been approved for the Pioneer Venus 1978 Mission, the frequency profile of the multiprobe entry and its effect on bandwidth requirements, and an update to the planned

DSN configuration at DSSs 14 and 43, which will be supporting the multiprobe entry.

II. Significant Recent Milestones

The Project Approval Document was signed by NASA Headquarters in October 1974. With the passing of that milestone, the key working groups, as far as Project interaction with the DSN is concerned, were able to form in order to start some of the detail work on the Ground Data System and the telecommunications aspect of the mission. There will be four working groups of concern to the DSN established for the Pioneer Venus Project. The first is a Telecommunications Working Group, whose primary purpose is to ensure that the spacecraft is compatible with the Deep Space Network of the Tracking and Data Acquisition System. The first meeting of the Pioneer Venus spacecraft/DSN Telecommunications Working Group was held on January 29, 1975, at the Jet Propulsion Laboratory. A first meeting of the Pioneer Venus Spacecraft/DSN Compatibility Testing Subgroup of the Telecommunications Working Group was held at the Ames Research Center on April 22, 1975. Key characteristics of the Compatibility Test Plan, as they are

developing, will be reported in subsequent Progress Report articles.

The second working group is the Pioneer Venus Ground Data System Working Group. The purpose of this group is to determine the requirements of, and to establish the design criteria for, the Pioneer Ground Data System, and to ensure that the Ground Data System Plan is compatible with and within the capabilities of the Deep Space Network portion of the Ground Data System. The first meeting of the Ground Data System Working Group was held on April 16, 1975. This working group has been scoped to consider all aspects of the Pioneer Ground Data System, including Pioneers 6 through 11 and, therefore, will concern itself with existing Ground Data System problems as well as Ground Data System plans between now and the establishment of the Pioneer Venus Ground Data System.

The third working group will be the Mission Operations Working Group, whose purpose will be to develop the Operations Plan, operational sequences, and test and training plans for the Pioneer Venus Mission. It was decided to incorporate the Mission Operations activities into the Ground Data System Working Group for the time being, until the Mission Operations activities increase to the point to warrant a separate working group. It is estimated that the Mission Operations Working Group will be established in early 1976.

The fourth working group will be the Near-Earth Working Group for Pioneer Venus, which will be a Tracking and Data Acquisition responsibility and will be established by the Tracking and Data System Manager for the Pioneer Venus Mission. The purpose of the Near-Earth Working Group will be to coordinate the Near-Earth Network Support for the Pioneer Venus launches.

III. Pioneer Venus Frequency Allocation

The Pioneer Venus 1978 frequency allocation was completed on February 19, 1975. The Project was under considerable time constraints at the time that the frequency allocation was requested; therefore, in order to minimize the time necessary to accomplish the allocation, the allocation was made in regions of the deep space channels where there was clearly no conflict or potential conflict with other missions. Any channel that might have potential interference with another project was rejected in order to save the time necessary to do a proper analysis of the potential interference. For this reason, the Multiprobe Mission was moved to the low end of the deep space channels to avoid a potential conflict with GEOSAT,

which is a European satellite that will be operating in the high end of the deep space channels. The GEOSAT problem looked workable because of basic agreements that had been reached between NASA and the European Space Agency; however, the Pioneer Project elected to go with the low end allocation in order to avoid the extensive negotiations that would be necessary with the European Space Agency. The resulting frequency allocations are shown in Table 1.

For the multiprobe, the frequencies were selected to be adjacent because of the Differential Very Long Baseline Interferometry (DVLBI) experiment's requirement to pack all the received frequencies from the multiprobe as close together as possible. Because of this requirement, the probe frequencies that were selected do not correspond to official deep space channels, but this violation of the usual philosophy of selecting specified deep space channels was considered acceptable, since these probes will be active for only two hours during the entire mission. The bus, however, will be active for the cruise phase of the mission; therefore its frequency was selected corresponding to a deep space channel. In the nominal mission, referring to Table 1, the frequencies that will be present during the multiprobe entry phase will be from small probe 1 through small probe 3. The spare small probe frequency will be the only spare transmitter available and would be used in any one of the three small probes in the event of a failure before launch. The bus has a prime frequency, which has been allocated Channel 6, and a flight redundant frequency, which has been allocated Channel 8. The redundant frequency can be switched to in the event of an in-flight failure of the prime transponder.

For the Orbiter Mission, the prime transponder was selected as Channel 12 and the flight redundant as Channel 11. In addition, there is a spare transponder, which was allocated Channel 17. That spare transponder could end up either in the orbiter, the bus, or the large probe in the event of a pre-flight failure. Because of the DVLBI requirement, it is most likely if the large probe transponder fails before launch that one of the bus channels would be put in the large probe and the spare transponder put as the redundant channel for the bus. In that way, it would take a double failure before one of the probe or bus frequencies fell outside of this contiguous set of frequencies, making it unusable for the DVLBI experiment.

Note that there is no uplink to the small probes and no X-band downlink, except from the orbiter and in the spare transponder. The X-band is for radio science purposes only; therefore there will be no X-band telemetry.

IV. Multiprobe Frequency Separation and Total Bandwidth Requirement

The typical doppler profile for the multiprobe entry is shown in Fig. 1. The large, over 80 kHz, doppler pulse at entry corresponds to the time of blackout; therefore this doppler pulse will not have to be tracked by the DSN receivers. However, the DSN will have to reacquire after blackout and the doppler pulse is completed. Notice that the RF signals from the four probes turn on only 22 minutes prior to entry. For the first 5 minutes after RF turn-on, however, there will be no modulation on the downlink, so that a stronger, unmodulated carrier will be available for the initial acquisition. Also note in this and subsequent figures that the probe entries are shown as simultaneous for simplicity; however, their actual time of entry and corresponding time of RF turn-on will be separated by 5 to 10 minutes from probe to probe.

Figure 2 shows the origin of the total bandwidths required for each of the spacecraft involved in the multiprobe entry. For the small and large probes, the large doppler pulse of Fig. 1 is included and results in shift "b"; the pre-entry doppler is shown as shift "a." The small and large probe doppler shifts are shown as the same even though the large probe is in two-way, because it is assumed that the DSN will have acquired the uplink and will be ramping to compensate for the doppler. If the uplink is not acquired, the large probe will be in one-way and the one-way shift would still be correct. Ten times the subcarrier frequency (out to the fifth harmonic) is added to the doppler shift for the small probes, large probe, and bus, shown as item "c." The subcarriers for the small probes are 4 kHz; for the large probe, 8 kHz; and for the bus, 32.7 kHz. Notice that no doppler shift is shown for the bus, because the bus will have been retarded in flight prior to the entry phase so that all probes will have completed their entry before the bus hits the atmosphere of Venus.

Frequency uncertainty, "d," is added to allow for uncertainty in the transmitted frequency from the probes. This uncertainty is 10 kHz for the small probes because of their very stable oscillators, while it is 30 kHz for the large probe because a conventional auxiliary oscillator is used.

The final amount added to the bandwidth is the doppler uncertainty, "e," for which 5 kHz has been allowed. The result is a total bandwidth of 156 kHz for the small probes and 237 kHz for the large probe, while the bus requires 338 kHz. These bandwidths determined the spacing in the frequency allocation shown in Table 1. These bandwidths

are shown together with the doppler profile with the proper frequency spacing in Fig. 3.

The DSN is also required to produce a reference tone on the top and bottom of the total bandwidth of the entry for the sake of calibration purposes for the DVLBI experiment. Therefore, the total bandwidth that has to be captured through a single open-loop receiver for the DVLBI experiment is 1.142 MHz. Recalling the sparing philosophy, described in Section III, Fig. 4 shows the worst-case total bandwidth that might have to be acquired in the event that the prime transponder on the bus failed, and one of the small probe's transmitters failed prior to launch, requiring the use of the spare small probe transmitter. This would expand the total bandwidth, including the DSN-generated tones, to 1.727 MHz.

V. Deep Space Station Configuration for the Multiprobe Entry

Figure 5 shows the currently planned configurations for Deep Space Stations 14 and 43 for the multiprobe entry. This is an update of the corresponding figure in Ref. 2. The configuration has been determined from the strategy of trying to capture the most data in real-time in digital form via closed-loop receivers, while providing a backup pre-carrier detection analog recording via individual open-loop receivers to recover data for those time periods when the closed-loop receivers are not in lock. During the multiprobe entry, a 26-meter antenna will receive telemetry from the bus, although the bus signal will be present through one port of open-loop receiver 4 for the purpose of the DVLBI experiment.

There are five closed-loop receivers, which is one more than the standard 64-meter configuration. The fifth receiver is necessary since the large probe may be in two-way or one-way. Since there are only four Symbol Synchronizer Assemblies (SSAs), the strategy is to switch one of the SSAs after the Subcarrier Demodulator Assembly (SDA) output to whichever receiver has locked up on the large probe (either in two-way or one-way). The configuration shown assumes that sequential decoding will be accomplished in the new Telemetry Processor Assemblies (TPAs), therefore enabling the elimination of the Data Decoder Assemblies. Because there will only be two TPAs at each station and therefore a capability to process only two sequentially decoded streams in real-time, it is planned to provide a recording of the soft decisions out of the SSAs. Determining which streams at each of the two stations are decoded in real-time and which are merely recorded after the SSA will be a Project decision based on the total mission design. This is the reason that the actual

connections between the SSAs and the SSA recordings and TPAs are left open. The result is that the DSN will be capable of outputting two different probe streams from each of the two stations in real-time all the way back to the control center at the Ames Research Center if the Project desires.

For the predetection recording, the actual bandwidths determined from the frequency allocation are 300 kHz for the large probe and 200 kHz for each of the three small probes. The actual bandwidth requirement for the DVLBI port of the open-loop receiver is in the range of 1.14 to 1.73 MHz, depending upon whether it is a nominal mission or not. The required rate of the digital recorder for the DVLBI experiment is 6.85 to 10.36 megabits per second. This comes from double sampling the bandwidth required plus 3-bit quantization, which makes the digitization rate six times the required bandwidth at S-band.

For the predetection recordings, the data from each probe are recorded on a separate track of an analog recorder. Recovery of the predetection data will be accomplished by playing back the data from one probe at a time through an up-converter back to S-band into a conventional closed-loop receiver and associated telemetry stream of SDA, SSA, and TPA. The DSN has committed to the Project that the loss in this playback will be only 1 dB plus or minus 0.5 dB compared to the closed-loop receiver's real-time performance.

The interface with the Project for the wind drift measurement using DVLBI is assumed to be the digital recording that is produced in real-time. This issue is still being negotiated with the Project and the experimenter. In addition, the experimenter requires that two or three non-DSN stations be equipped to support the DVLBI experiment. The relative responsibilities of the Project and the NASA Office of Tracking and Data Acquisition in providing the necessary equipment for the non-DSN stations are still being negotiated.

References

1. Miller, R. B., "Pioneer Venus 1978 Mission Support," in *The Deep Space Network Progress Report 42-23*, pp. 37-40, Jet Propulsion Laboratory, Pasadena, Calif., Oct. 15, 1974.
2. Miller, R. B., "Pioneer Venus 1978 Mission Support," in *The Deep Space Network Progress Report 42-20*, pp. 17-19, Jet Propulsion Laboratory, Pasadena, Calif., Apr. 15, 1974.

Table 1. Pioneer Venus 1978 Frequency Allocations

Spacecraft or radio unit	Deep space channel	Uplink S-band, MHz	Downlink S-band, MHz	Downlink X-band, MHz
Multiprobe				
Spare small probe	N/A	None	2291.394837	None
Small probe 1	N/A	None	2291.550797	None
Large probe	N/A	2110.317247	2291.747237	None
Bus prime	6a,b	2110.584105	2292.037037	None
Small probe 2	N/A	None	2292.281357	None
Small probe 3	N/A	None	2292.437317	None
Bus redundant	8a,b	2111.266204	2292.777778	None
Orbiter				
Redundant	11a,b,c	2112.289352	2293.888889	8410.925927
Prime	12a,b,c	2112.630401	2294.259259	8412.283950
Spare transponder	17a,b,c	2114.335648	2296.111111	8419.074073

ORIGINAL PAGE IS
OF POOR QUALITY

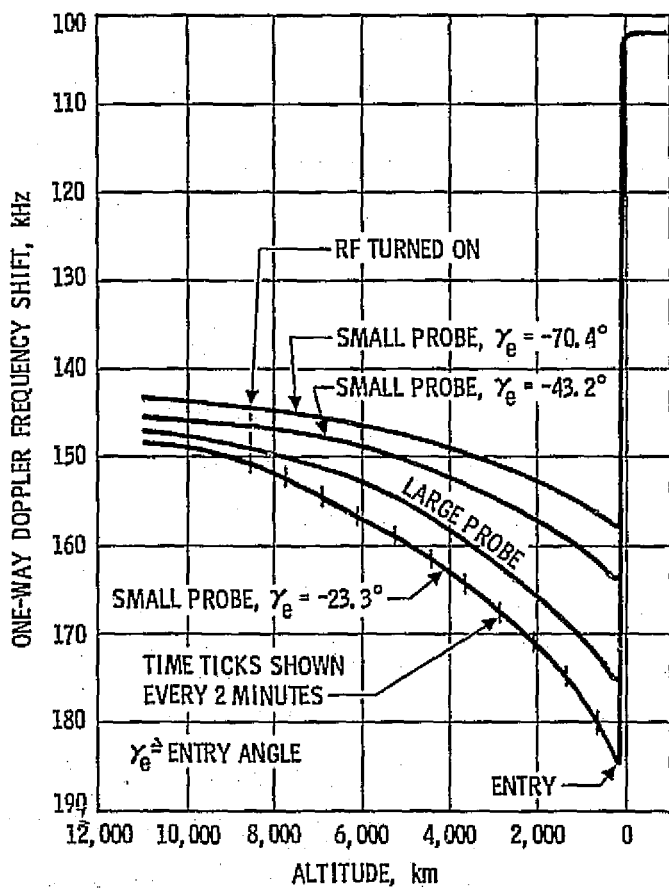


Fig. 1. Pioneer Venus 1978 representative doppler profiles for multiprobe entry

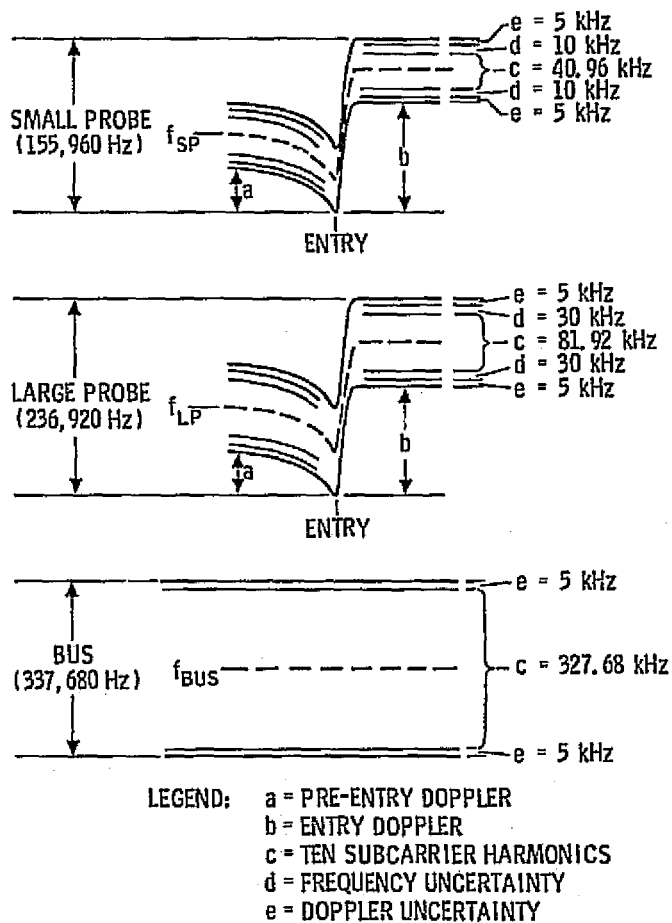


Fig. 2. Pioneer Venus 1978 multiprobe frequency bandwidths required

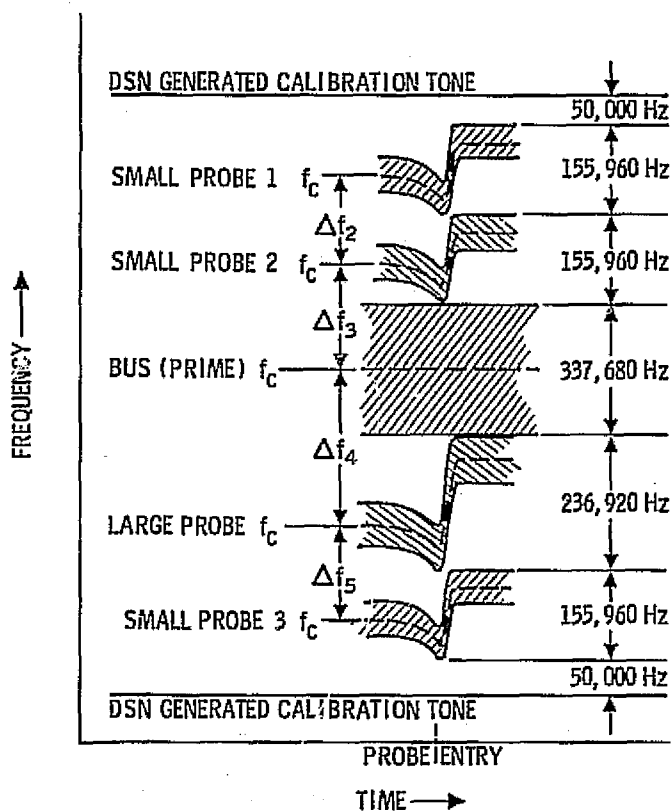


Fig. 3. Pioneer Venus 1978 nominal multiprobe frequency separation and doppler profile

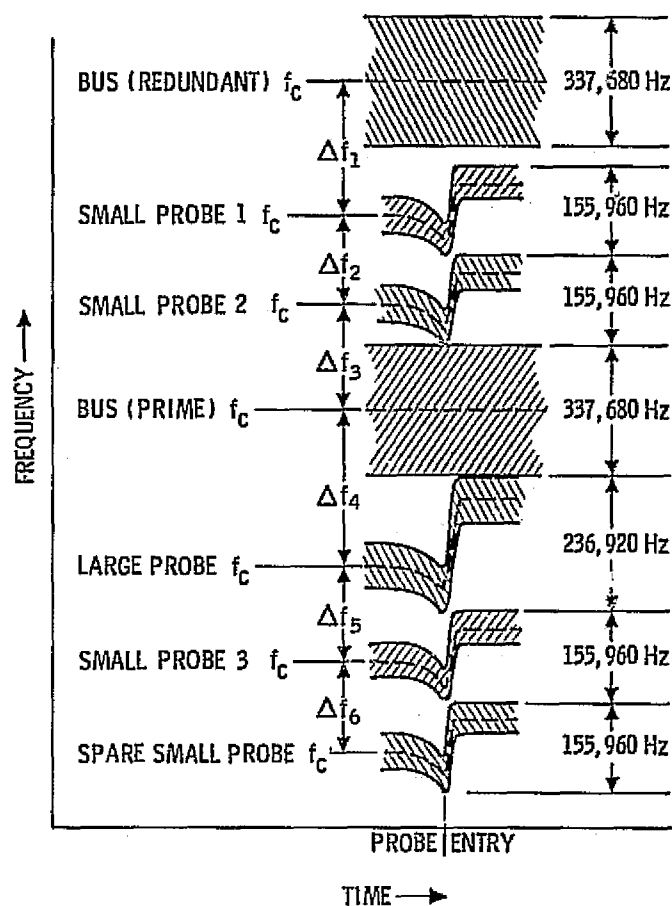


Fig. 4. Pioneer Venus 1978 maximum multiprobe frequency separation and doppler profile

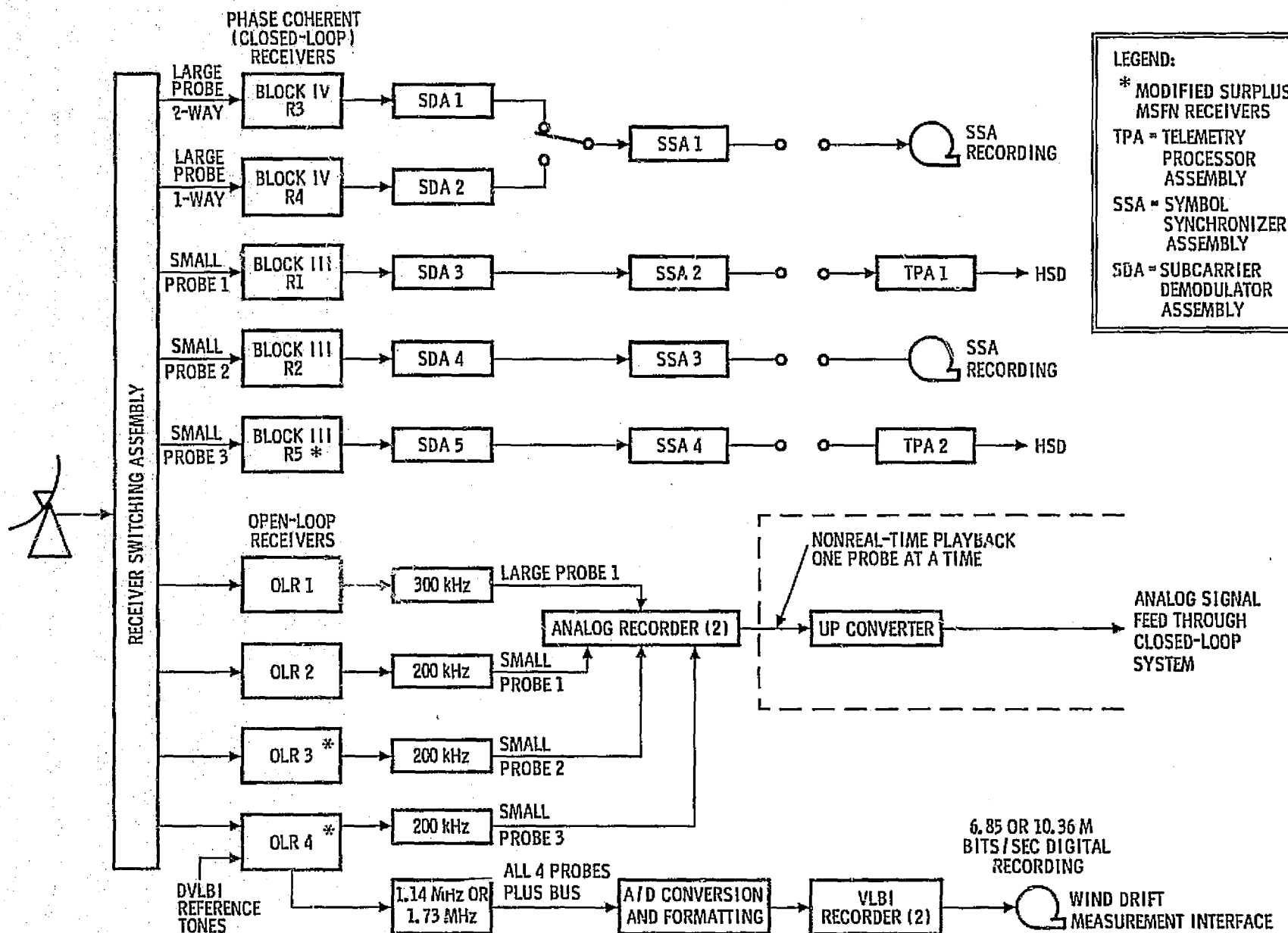


Fig. 5. Configuration for telemetry data recovery and interferometry experiment for Pioneer Venus 1978 multiprobe entry

Helios Mission Support

P. S. Goodwin

DSN Systems Engineering Office

W. G. Meeks and S. E. Reed

Network Operations Office

Helios-1 spacecraft has now completed its first perihelion passage of the Sun. This article covers the DSN support to Helios-1 from its passage in front of the Sun (inferior conjunction) through its first perihelion passage, with particular emphasis upon the quantity and quality of the DSN support.

I. Introduction

This is the third article in a recent series pertaining to the Helios-1 flight support that has been provided by the DSN. The previous article (Ref. 1) discussed the Helios Mission Phase I/II handover and the changes in operational interfaces between the DSN and German Flight Operations Teams after Project Operations Control returned to the German Space Operations Center (GSOC) from JPL. A spacecraft high-gain antenna signal variation anomaly, with its attendant impact upon the committed Helios-1 tracking schedule, was also described. The DSN System Performance and tracking coverage reported in that article closed as Helios-1 was completing its first inferior conjunction. This article continues from the latter event up through completion of the first Helios-1 perihelion passage.

II. Helios Mission Status and Operations

A. Helios-1 Inferior Conjunction

Helios inferior conjunction offered the DSN an extraordinary performance calibration point, prior to the first Helios-1 superior conjunction. Helios-1 inferior conjunction occurred from February 16 through 22, 1975. This time period is in respect to the time that the Sun-Earth-Probe (SEP) angle was five degrees or less. On February 18, 1975, Helios-1 crossed in front of the Sun's photosphere, at which time a total telemetry blackout occurred.

The inferior conjunction data collection objective was twofold. The first objective was to improve the data collection procedures and to verify that sufficient data would be available to perform the desired analysis during

superior conjunction. The second objective was to compile a reliable data base so as to generate predicts on the excessive system noise temperature (SNT) versus the SEP angle, and to also predict the SEP angle versus the system noise temperature ratio residuals.

Both objectives were met and subsequently applied to a Pioneer superior conjunction with predicted results, but the Pioneer SEP angle was 1.8 degrees, whereas Helios-1 will have an SEP angle of less than 0.5 degrees from May 2 to 13, 1975. The solar noise effects upon the telecommunications link are expected to increase dramatically during this period. These data will then be used to provide improved predictions of expected noise, improved data monitoring, and considerations for future mission planning.

B. Helios-1 Perihelion

On March 15, 1975, at 0912:14.7, Universal Time, Helios-1 reached its first perihelion at 0.3094343 AU. The performance of all spacecraft and DSN subsystems was excellent throughout the perihelion period.

The perihelion, which occurred 86 days after launch, was the focal point of scientific interest, but a 25-day period surrounding perihelion encompassed the expanded region of scientific interest. During this period of high scientific interest, the spacecraft traversed an unexplored region of inner solar system space. The results of Helios-1 perihelion objectives, which are to study the properties of the Sun's influence on Earth, are still being analyzed. The DSN objective to provide continuous coverage and achieve optimum performance in order to maximize the return of scientific data in both quantity and quality was met.

Optimizing the performance of the Deep Space Stations (DSSs 12, 14, 42, 43, 44, and 62) supporting Helios during this special coverage period was the major thrust of the planning and scheduling effort. Special pre-pass readiness tests for each prime and backup station were conducted throughout the perihelion period. Full redundancy of station coverage was not practical during this, the major phase of the Helios-1 mission, due to the significant requirements also placed on the DSN by the Mariner and Pioneer Projects during March 1975. The scheduling of backup stations to provide coverage was planned and did occur when the Mariner Project declared a spacecraft emergency on March 13, 1975. This required 64-meter antenna coverage to ensure that the Mariner 10 spacecraft was in a stable attitude prior to its third encounter of Mercury on March 16, 1975, which was one day after Helios-1 perihelion. All perihelion commitments were met by all elements of the DSN, and the perihelion phase activities were quickly supplemented by those activities relating to superior conjunction.

C. Helios-1 Superior Conjunction Plan

As Helios-1 sped through the perihelion region and successfully fulfilled its science criteria from that region of unexplored space, new scientific objectives came into focus as it approached superior conjunction. The primary emphasis during the first Helios superior conjunction is the accumulation of science data for the Faraday rotation and celestial mechanics experiments.

The Helios-1 superior conjunction has two periods of interest. The first period of interest is for the Radio Frequency Analytical Study by the DSN. The second is the Project period of interest. The dates of the defined period of DSN analytical and Project scientific studies, encompassing the first Helios-1 superior conjunction, are from April 7 to June 24, and April 13 to June 8, 1975, respectively. This conjunction will not result in a complete spacecraft occultation by the Sun, but the SEP angle will sweep across within 0.43 degrees of the Sun's photosphere.

The period of DSN analytical interest is when Helios-1 is within plus and minus 5 degrees of the SEP angle.

The highest period of scientific interest is when Helios-1 is within plus and minus 3 degrees of the SEP angle. The dates and degrees of SEP angle are as follows:

SEP, deg	Entry date	Exit date
5	4/7/75	6/24/75
4	4/10/75	6/16/75
3	4/13/75	6/8/75
2	4/18/75	5/29/75
1	4/24/75	5/20/75
0	5/2/75	5/13/75

1. Faraday rotation. As Helios-1 approaches the solar disk proximity, telecommunications with the spacecraft will be nearly impossible, if not totally blacked out by solar-generated noise. At this time, the Faraday rotation experiment will be within its region of critical interest. In conjunction with the Faraday rotation data accumulation, the DSN will also analyze spectral broadening of the spacecraft's radio frequency (RF) link and the observed quadrupod effects in conjunction with the increased system noise temperatures at DSS 14.

DSS 14 is the experimenter's prime station for retrieving the Faraday rotation data. Weather data and

system noise temperature data are gathered from around the Network. DSS 14 supports weather data, automatic polarimeter tracking data in both the correlation and phase lock modes, and open-loop receiver data during periods of non-coherent operations. The experimenter will provide his Helios-B requirements to the Project Office later this year. The Helios-B requirements will be derived from the knowledge obtained from the results of the analysis of Helios-1 data reduction.

2. Celestial mechanics. The celestial mechanics experiment employs the Helios-1 radio metric data obtained during real-time tracking of the spacecraft to derive information regarding the Sun and its planet's ephemeris. Further, as the spacecraft's radio signal passes close to the Sun while enroute to Earth, possible bending effects due to the Sun's gravity may be noted. Such effects, predicted by Einstein, would be most noticeable as an increased range measurement caused by the longer (i.e., bent) path taken. Such an effect would have a magnitude of approximately 200 *microseconds* out of a total round-trip time of 1/2 hour. The measurement of such a small quantity requires extreme care and precision by the DSN. Further, this measurement will be made in the presence of an extremely large noise level due to the effects of the solar corona. This is, therefore, the challenge to be met during the Helios-1 solar occultation (blackout) period.

D. Actual Versus Scheduled Tracking Coverage

This tracking coverage report, encompassing the time period between February 10 and April 14, 1975, spans two important periods of the Helios-1 scientific mission phase. The two major Helios-1 events that occurred during this time were inferior conjunction and perihelion. In addition to Helios perihelion, there were also increased Mariner 10 and Pioneer 10/11 activities that occurred simultaneously.

The DSN commitment to provide continuous tracking coverage throughout this phase of the Helios Mission was met. A total of 168 tracks had been scheduled at DSSs 12, 14, 42, 43, and 62. The number of actual tracks supported during this time frame was 172. This included demonstration passes at DSSs 43 and 44 and two extra tracks at DSS 12. One of the extra tracks at DSS 12 was to provide backup commanding when DSS 14 incurred Command System problems, which will be discussed later in this report. The second additional track at DSS 12 occurred when a Mariner 10 spacecraft emergency was declared. DSS 14, which was supporting Helios at the time of the emergency, was then required to support Mariner 10. DSS 12 was called up to support Helios in real-time, this resulting in Helios data outage of approximately 20 minutes.

The long-range schedule, which had not included plans for a third Mariner 10 encounter of Mercury, had projected 64-meter station coverage throughout the 25 days of perihelion coverage. The added requirement to support a third Mercury encounter would result in a loss of 64-meter station coverage to the Helios perihelion coverage. When it was ascertained that there would be a third encounter, four Helios 64-meter tracks were given over to Mariner, through negotiations, to ensure a successful finale to the Mariner Project. In total, only six 64-meter station tracks were lost to Mariner 10.

On March 24, 1975, Pioneer 11 had a superior conjunction, and Pioneers 10 and 11 were also in a spiral alignment at the same time. During this period, which was equally important to the Pioneer Project, several tracking passes at 64-meter stations were shared.

The sharing of resources during March to optimize tracking coverage resulted not only in the DSN meeting the Helios-1 commitments, but also successfully culminated in the highly active Helios, Mariner, and Pioneer Project events being met during March 1975.

III. DSN System Performance for Helios

A. Telemetry System

The Helios Telemetry System performance during the months of February and March 1975 continued to follow the predicted levels of performance, which had been the case since launch, with only minor variations. In the time span from launch through January 1975, the telecommunications link performance had exceeded the predicted performance levels. The performance trend in February averaged out to slightly below the predicted level. The March performance returned to the previous level, while the incongruities of February remain unexplained. It should be noted, however, that the above variations in performance basically lie within the pre-flight uncertainty tolerance and only infrequently exceed the predicted margin of tolerance.

While there was no single incident of significance reported as a telemetry failure, there were two categories of discrepancy reports (DRs) that contributed to almost 50% of the total reported failures within the Telemetry System. These two categories are Data Decoder Assembly (DDA) failures and Automatic Total Recall System (ATRS) failures.

The DDA failures have historically been the prime contributor to the total number of DRs, but in the past two months, ATRS discrepancy reports have attributed to

approximately 20% of all DRs. These two categories of DRs have received special attention from the DSN Operations Analysis Group.

During March 1975, the Block IV receiver at DSS 14 became operational. The analysis of the Helios link performance, based on the usage of the Block IV receivers, has not been satisfactorily validated due to insufficient evaluation time.

The DSN Operations Analysis Group continues to monitor the spacecraft's performance on medium-gain and high-gain antenna operations. The spacecraft's performance, compared to predictions, appears to be slightly better on the medium-gain antenna. This could be due to the signal level variations that have been observed on the high-gain antenna, as reported in the previous article. It has not been ascertained at this time that these variations occur only during high-gain antenna operations, but the magnitude and the effects on performance have not been detected during medium-gain antenna operations.

B. Tracking System

The DSN Tracking System performance for Helios through March 1975 has continued to be nominal. The spacecraft was tracked a total of 178 times during this reporting period. The trend analysis of doppler noise and two-way doppler residuals has not revealed any deviations away from the predicted performance. There were no significant Helios tracking discrepancy reports opened during this period.

C. Command System

The total Helios DSN-supported command activity, from launch through March 1975, has totaled 12,503 commands. The cumulative command aborts during this period of support were six. Four aborts were termed Project aborts, when a command is aborted remotely by Project, and two were system aborts. A system abort is the result of a Deep Space Station Command System failure.

The two system aborts both occurred at DSS 14 during March 1975. In addition to the two aborts, more than seven hours of station command capability were lost before the problem could be isolated. The seven hours of lost command capability are an accumulated total from nine different tracking periods.

The problem was, in fact, two problems within the Command Modulation Assembly (CMA). The combination of the two problems produced intermittent anomalous

conditions; this contributed to the lengthy delay of its isolation. Initially, what appeared to be software-oriented, and later proved to be hardware problems, also caused delays in isolation. With the hardware corrections, a new preventive maintenance procedure will also provide an increase in the level of command reliability.

DSS 43 also encountered hardware problems that resulted in a loss of command capability during periods of inclement weather. Heavy rainfall resulted in excessive levels of reflected transmitter power within the antenna microwave system, which caused the transmitter to automatically shut down. The excessive reflected power will be corrected by replacing a section of mismatched waveguide on the diplexer. Until the waveguide is replaced, the transmitter is operated at only 5 kW.

The only other significant Command System anomaly occurred at DSS 42. Project commanding was delayed 180 minutes when numerous subcarrier frequency alarms were received. A subsequent investigation revealed that installation of a new equipment rack next to the Frequency and Timing Subsystem (FTS), on a non-interference basis with Helios tracking, probably resulted in a spurious malfunction of the FTS Subsystem. The command activity was such that commanding could be delayed until DSS 62 had acquired and was in a green command posture.

IV. Conclusions

The Helios-1 spacecraft has now completed its first inferior conjunction and perihelion passages. Helios-1 has also met its prescribed initial scientific objectives, with all 10 of its experiments remaining active. As the spacecraft continues in its orbit around the Sun and its first superior conjunction occurs, the passive experiments (celestial mechanics and Faraday rotation) become the prime scientific experiments. During the reporting period of this article, the scheduling of DSN resources by all current flight projects was especially high. With the occurrence of superior conjunction, the Helios-1 spacecraft will have completed its Phase II mission milestones. The Helios-1 Mission Phase III support requirements will result in reduced level of Project support activities from the DSN.

The 11th Joint Working Group Meeting has been scheduled for the latter part of May 1975. This meeting will emphasize the Helios-B launch preparation activities. Helios-B activities will then be on an ever-increasing scale throughout the remaining portion of the year. Thus, the reduced Helios-1 support will be offset by increasing Helios-B activity. These and related topics will be treated in future issues of this report.

Reference

1. Goodwin, P. S., "Helios Mission Support," in *The Deep Space Network Progress Report 42-26*, pp. 22-26, Jet Propulsion Laboratory, Pasadena, Calif., Apr. 15, 1975.

A Dynamic Model for Analysis of Solar Energy Systems

C. L. Hamilton
TDA Planning Office

A dynamic analysis technique for evaluating the performance of solar energy systems is needed as part of the Goldstone Energy Conservation Project. This article reports progress in the construction of a model simulating prospective solar energy systems and of the computer programs in which it is embodied. The modeling approach is discussed as applied to a general baseline configuration for prospective systems, and the two programs that have been completed are described.

I. Introduction

Part of the Goldstone Energy Conservation Project involves development of an analysis technique for evaluating the performance of solar energy systems. Unlike conventional systems, which can be turned on and allowed to run at steady state as long as they are needed, solar-powered systems are largely dynamic in nature. This report describes progress in construction of a model designed to simulate prospective solar energy systems under consideration for the Goldstone Space Communications Complex (GSCC), taking into account the time dependencies inherent in their operation. The model is described together with the computer program in which it is embodied.

A primary requirement placed on the program that embodies the desired dynamic model is that it be convenient and easy to use. Since it is intended to analyze

the performance of many alternative solar energy systems, the program should be modular, allowing quick and simple substitution of components in the system under study. The program documentation and code are to be written so that the functioning of the model can be understood easily even by readers unfamiliar with its development. In particular the mathematical relationships should be readily traceable throughout.

II. The Approach

We begin by postulating a baseline system designed to meet the energy needs at GSCC, powered primarily by solar sources. For the purposes of the model, this system is characterized in terms of key parameters describing the operation and interaction of all the component subsystems. The parameters of interest fall into two categories. The first kind, primary levels, is accumulated quantities

(an example would be the amount of fuel in a storage tank) describing the state of a component at a particular instant in time. The second type of parameter comprises the instantaneous rates of change for the levels at the same time. Rates depend only on the magnitude of one or more levels, a set of constants characteristic of the properties of associated subsystems, and any exogenous inputs (driving forces) that affect those subsystems. In short, the rates provide a means for coupling system components with each other and with the surroundings. The time course of these parameters is determined by stepwise computation of all variables at small time intervals, starting from pre-specified initial values for each level involved (Ref. 1).

The necessary calculations are embodied in the program in the form of several computational modules, each of which contains all the relationships necessary to describe operation of a system component (or assembly of components) as well as its interfaces with other components. These computational modules are imbedded in a program structure that ultimately will allow extensive user manipulation of inputs, outputs, and the control variables that govern the time frame over which analysis is carried out. Modification of the program to incorporate the characteristics of an alternate system component involves substitution only in the appropriate computational module; it can be accomplished in a few minutes once the characterization of the alternate component is complete.

III. The Baseline System

Figure 1 is a block diagram of the baseline GSCC energy system, showing overall energy flow. It envisions parallel conversion of the solar sources, sunlight and wind, into dc electricity. The dc output can be converted for direct use to satisfy some of the complex's ac demand or it can go to generate hydrogen and oxygen by electrolysis of water. Both gases can then be stored for use in the existing engine-generators, which will retain capability for burning petroleum fuel as well. Waste heat from the engines will satisfy some of the heating and air-conditioning requirements. Provision is made for input of commercial electricity as needed, but it is intended that only a small part of the total energy be purchased. The contribution of commercial electricity is considered to be negligible for modeling purposes.

Translation of the physical system into linked computational modules is illustrated in Fig. 2. With the exception of the blocks depicting hydrogen and oxygen production and storage, each system component in Fig. 1 is represented by a corresponding module in Fig. 2. The

characterizations of electrolysis and of the storage of its products are combined into a single Hydrogen-Oxygen Module. One computational module does not appear explicitly in the physical block diagram. That is the Dispatch Module, which contains the strategy governing how the energy is routed through the various available pathways. Arrows in Fig. 2 represent the direction of information transfer occurring in the model; the corresponding labels identify the nature of the data involved.

Both the physical system and the system of computational modules divide themselves naturally into subsystems. The physical subsystems are delineated in Fig. 1 by double-lined blocks. There are two subsystems, solar and wind, that carry out initial processing of the input energy. They are separated from each other because the processes involved are physically different and because the time dependencies of the wind speed and solar radiation inputs differ markedly from each other. The central subsystem contains the components devoted to further energy conversion, storage, and distribution, while the remaining one is made up of the load to be satisfied.

Division of the system of computational modules into groups is analogous; these are surrounded by broken lines in Fig. 2. A key characteristic of the dissection is that the connections between groups are one-way. A group either delivers information to other groups or receives information from others, but does not do both. This means that the corresponding subsystems can be modeled separately, using separate computer programs. The advantages of this arrangement are illustrated in the following discussion.

IV. The Programs

The programs to be employed for dynamic analysis of solar energy systems are to be written in MBASIC and implemented on JPL's Univac 1108 A system, accessed through remote terminals such as Execuports. They are developed using top-down design and structured programming. The Level 1 flowchart in Fig. 3 illustrates the general structure of a representative dynamic model program. After initialization, which includes specification of starting values for all primary levels, and selection of input and output options, the program enters an integration loop. There, values for all necessary rates at time T are calculated, as well as any useful parameters that may be derived from them. Next, the values chosen for output are stored at desired intervals. Finally the primary level values are updated to correspond to time $T + DT$ and computation goes back to traverse the loop again. When integration is complete, the stored output is

printed or plotted, depending on the output medium chosen by the user.

As can be seen from Fig. 2, the model calculations depend on several exogenous inputs. These represent the influences exerted by the surroundings on the performance of various pieces of the system. Inputs are provided as data files consisting of day-hour tables containing values of the appropriate parameters for each hour in a year. These data files are themselves the result of models, and are subject to refining and upgrading as work on those models progresses. In general, however, their contents do not vary between runs of the system simulation model.

For computational stability, the integration interval DT must be small relative to the shortest time constant in the system being simulated. At a minimum, simulation of a year's system operation entails 8760 iterations of the program's calculation loop ($DT = 1$ h). It is to be expected that the system components will exhibit considerable variation in characteristic response time, and some will require integration at intervals much smaller than one hour. To increase economy of computer use, it is desirable to include as few calculations in the integration loop as possible, and to minimize the number of times the loop must be traversed. Using separate programs for computational groups helps to achieve these ends. For example, while using the dynamic model to perform analyses, it is not necessary to run the SUN or WIND groups each time the model is run if the analyses do not involve any variation in components of the solar or wind subsystems. The information output from the SUN and WIND groups is analogous to that contained in the data files for exogenous inputs, and can, in fact, be considered as pseudo-exogenous inputs to the group labeled SENS-MOD2 in Fig. 2. Therefore, the programs SUN and WIND are intended to generate data files consisting of hourly electrical output rates; they will be run once whenever alteration is made in appropriate system components or the input data files are upgraded, and the resulting sets of output files will in turn be used as input whenever the program SENSMOD2 is used.

Note that, while the computational modules representing the load components are here included in the group SENSMOD2 and the corresponding program, they can be separated as SUN and WIND were. If it should prove desirable, another one or two groups (and programs) can be created to represent load functions.

At this writing, the programs SUN and WIND have been designed, coded, and tested. Data files have been generated with WIND. Work on SENSMOD2 (Solar

ENERgy System MODEL, version 2¹) is in progress. The following sections provide more detailed description of how the programs are put together.

A. SUN

Level 1 design for SUN is shown in Fig. 4. That program is intended to compute the hourly average electrical output of a solar thermal generating subsystem consisting of collector, heat storage, and heat engine. Inputs to the program include hourly average values of solar radiation intensity, hourly values for the angle of incidence of that radiation on the collector surface, and hourly average readings of ambient temperature. Output, in units of kWh/h, is stored in data files standardized for input into SENSMOD2 and represents a year's operation, hour by hour, of the subsystem, starting at 0000 GMT January 1 and ending at 2400 GMT December 31.

A Level 1 design chart illustrates gross program structure only. Examination of lower levels is necessary to see the way in which the computational modules of Fig. 2 are imbedded in that structure. The key program modules here (not to be confused with computational modules) are those labeled CALC and UPDATE. Before discussing these, however, a digression into the response times characteristic of the solar subsystem components is in order.

It was discovered early that the solar collector exhibited unusual behavior as far as time constants were concerned. The collector can be characterized as a fluid-containing structure that absorbs energy in the form of solar radiation. Energy is removed from the structure by loss mechanisms (primarily conduction and radiation) and deliberate extraction through circulation of the fluid. The loss rate shows a nonlinear temperature dependence, as it represents contributions from two processes with different temperature dependences. Extraction rate is also nonlinear with temperature, owing to the way in which temperature-dependent flow control is specified. The net result is a thermal time "constant" that is not constant, but that varies by a factor of about six over the temperature range encountered in operation. While delivering heat to storage, the collector time constant is quite short, about 0.7 h as it is presently characterized.

In contrast, the heat storage and heat engine module computations can be carried out quite satisfactorily at integration intervals of one hour. The heat storage time constant is long, and the heat engine is essentially a

¹Version 1 was a preliminary one, covering all components of the system.

steady-state device—either on or off and delivering a nearly constant output when on.

To cope with these widely varying response time characteristics and their effect on computing time requirements, a further economizing step was taken. Advantage was taken of the fact that the only information the solar collector computational module requires from the rest of the subsystem is the temperature of the fluid returning from storage, which is relatively constant and can certainly be regarded as constant for an hour at a time. An initial value of that return temperature could also be provided as a function of initial values of primary levels within the heat storage computational module. Under these circumstances, it was possible to nest a variable-step-size integration loop for the solar collector module alone within an hour-by-hour loop performing the calculations for the other two modules. Figures 5 through 7 contain the flow charts describing insertion of the collector integration loop DT-VARY into the main one. The flow charts shown represent increasing levels of detail. For example, Chart 1.4 (Fig. 5) is an expansion of block 4 in Chart 1 (Fig. 4), Chart 1.4.2 (Fig. 6) is block 2 in Chart 1.4 expanded, etc.

Representation of the "normal" computational modules, those for heat storage and the heat engine, occurs in the UPSTREAM, COUPLE, and DOWNSTREAM blocks of CALC, and in UPDATE. Each of these program modules is represented by a subprogram that can be called from the computer and listed separately. Distribution of each computational module into the several program modules is necessitated by the two-way information flow between computational modules and by the need during execution of the program to stop and store desired information for output before primary levels are updated. For illustration, representation of the heat engine module is described below in detail.

A complete characterization of the heat engine computational module comprises the information contained in Figs. 8 and 9. Figure 8 is an indented list of the relationships defining the behavior of the heat engine under analysis and giving values to the characteristic constants incorporated therein. Figure 9 shows the relationships in the form of a calculation tree and allows visualization of the order in which computation is carried out and how information is transferred between computational modules.

A listing of the subprogram UPSTREAM will contain, in initialization statements, values for all the constants specified in Fig. 8. The heat engine module contains no

primary levels; for those computational modules that do, initial values would be supplied in those statements also. The initialization statements also contain tables describing any empirical relationships needed to characterize a component. The heat engine module has no tables. Separate, identified initialization statements are included in UPSTREAM for each computational module, to facilitate substitution. UPSTREAM also contains all equations below the solid dividing line in Fig. 9 (other computational modules have more than one equation; all equations for a module are grouped into one labeled set of statements). The UPSTREAM calculations represent all steps that can be carried out in one computational module without using a value calculated in another.

COUPLE is made up of a series of labeled statements, one for each computational module, that transfer variable values computed in that module to the modules requiring them. Its purpose is to simplify keeping track of the interfaces between components. In Fig. 9 variable transfers are denoted by a large X. Their operation is easier to conceptualize if the transfer is considered to occur into a computational module as implied in Fig. 9 rather than out of it as written in the SUN code. The reverse direction is imposed in the case of SUN by the nature of the interface between the solar collector integration loop and the main one.

In the case of the heat engine module, all the equations above the line in Fig. 9 are contained in a labeled group of statements in the subprogram DOWNSTREAM. For computational modules with primary levels, DOWNSTREAM has all remaining equations except the ones updating the primary levels to $T + DT$. Those appear, after output data for time T are stored, in subprogram UPDATE.

Revision of the program to analyze the performance of an alternate solar collector involves changing statements in the subprogram ALLSOL to reflect the characteristics of the new collector. Examination of alternate versions of any of the "normal" system components entails revising clearly identified statements in each of the four subprograms discussed above, a practice that is much simpler in execution than in appearance and that helps guard against making errors in defining the interfaces between components.

B. WIND

WIND is a less complex program than SUN, representing a less complex subunit in Fig. 2. It takes as input hourly average values of wind speed and computes from them the hourly average output during a year's operation

of a wind turbine generator. The result is a set of data files standardized for input into SENSMOD2 containing hourly values of electricity generated from wind, in MWh/h.

G. SENSMOD2

Current effort is directed toward completion of the model and program for SENSMOD2. This program will

be implemented first in an abbreviated version with limited capability for handling input and output options. Assembly of a complete set of operational programs and production of preliminary output data on operation of the whole energy system is a high priority goal. Concurrent and following activity will be devoted to refinement of component characterization packages and implementation of the program's full user option capability.

Reference

1. Forrester, J. W., *Principles of Systems*, Wright-Allen Press, Inc., Cambridge, Mass., 1968.

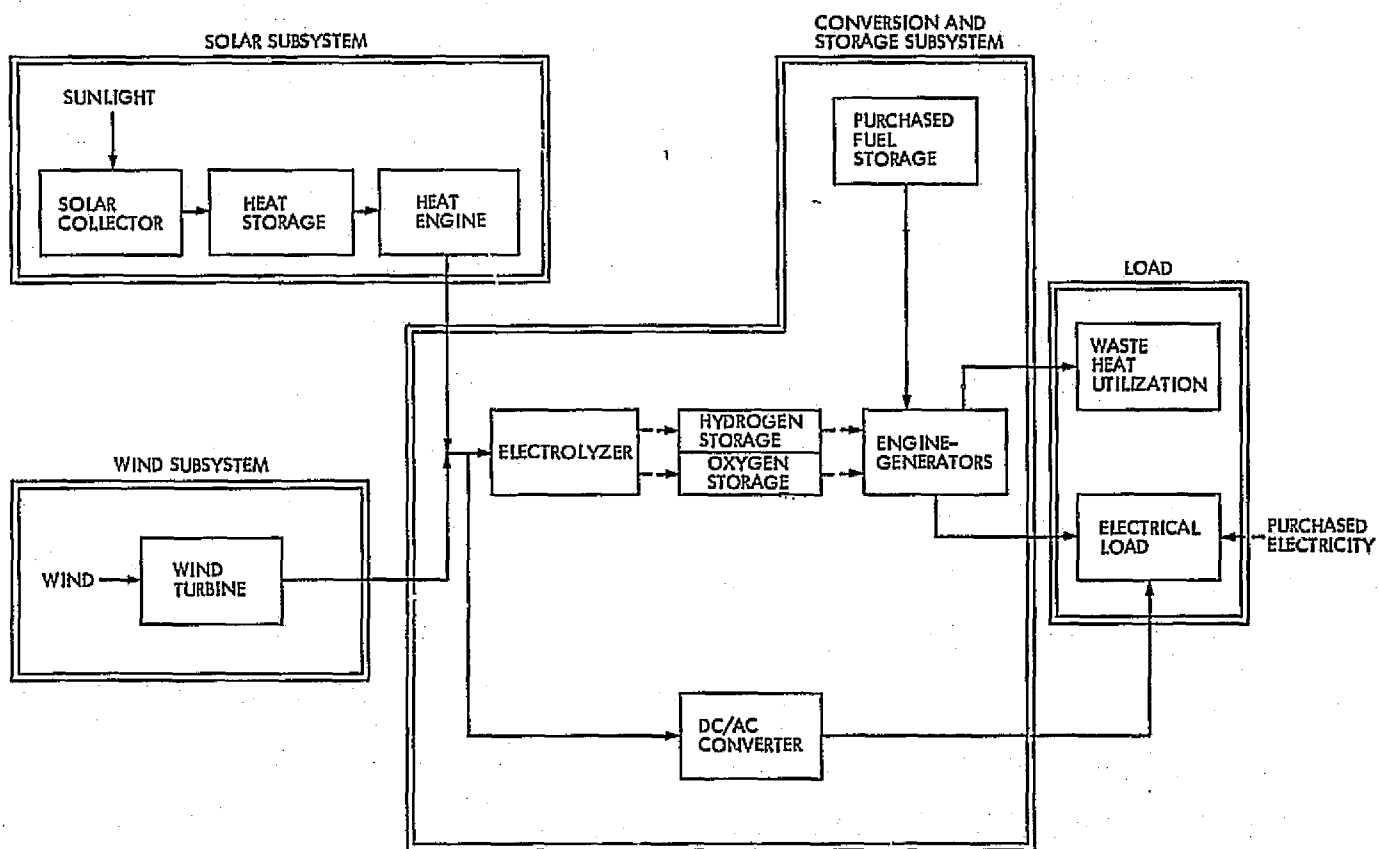


Fig. 1. Baseline solar energy system

ORIGINAL PAGE IS
OF POOR QUALITY

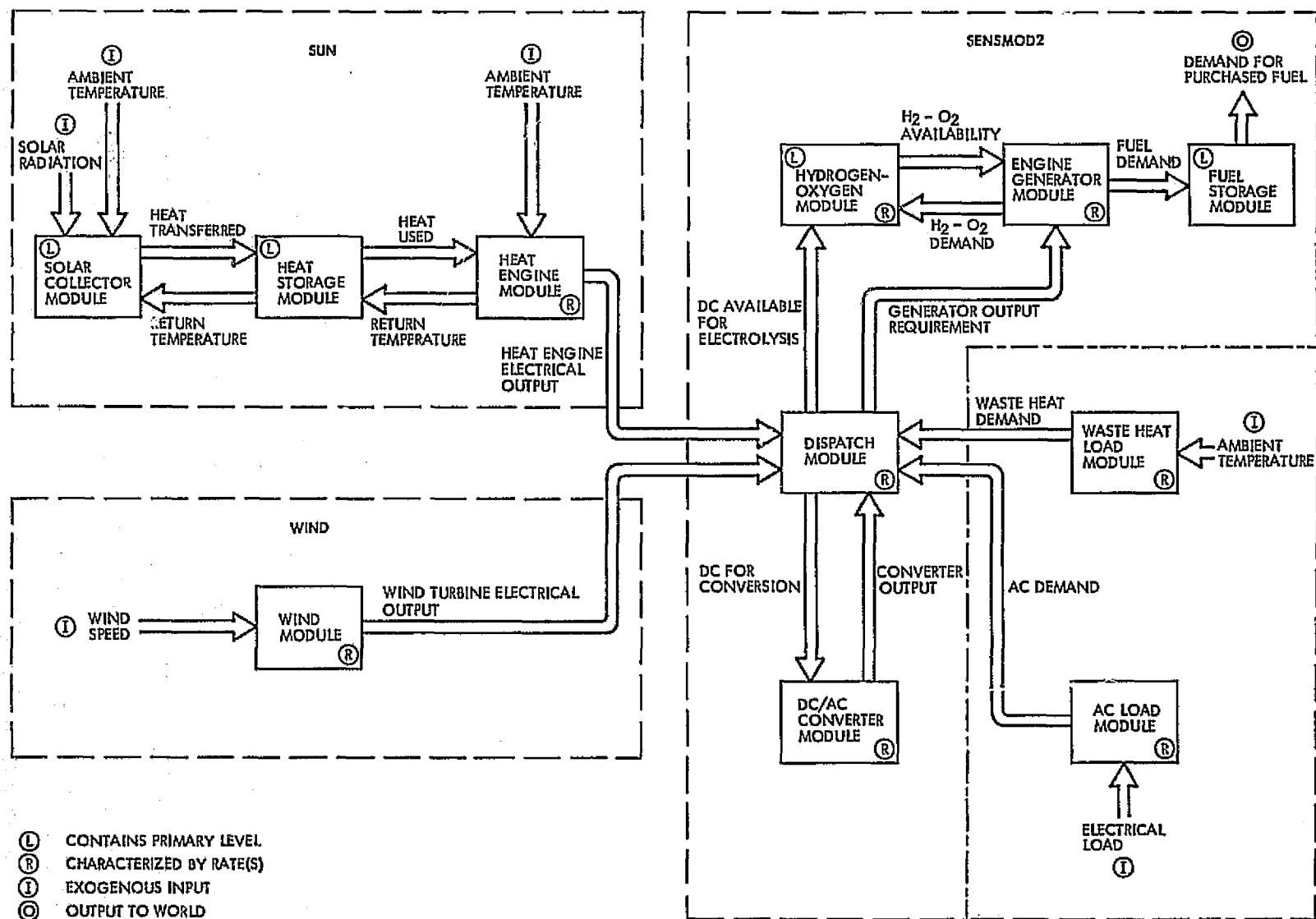
ORIGINAL PAGE IS
OF POOR QUALITY

Fig. 2. Computational modules and data flow

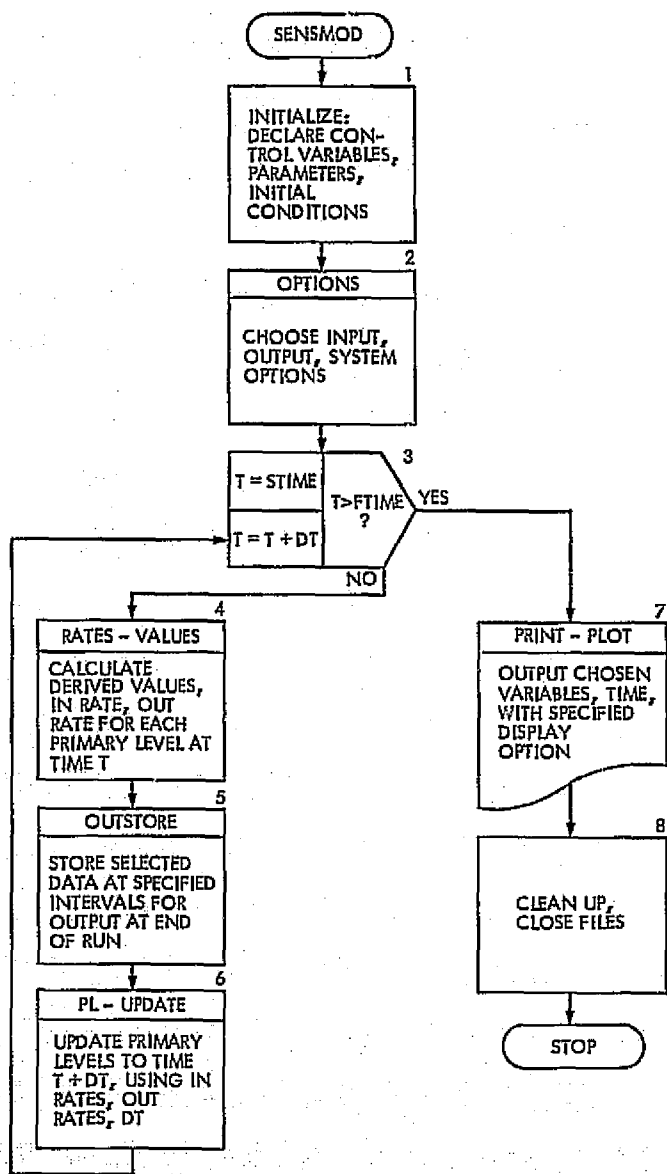


Fig. 3. Level 1 design, representative dynamic model program

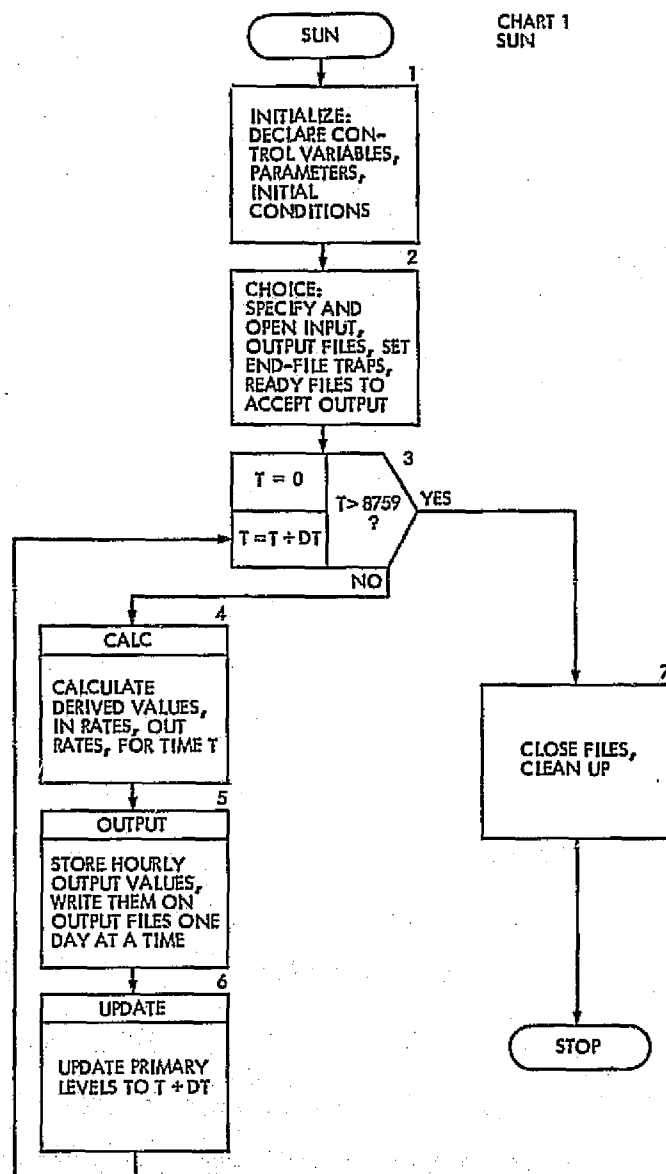


CHART 1
SUN

Fig. 4. Level 1 design, program SUN

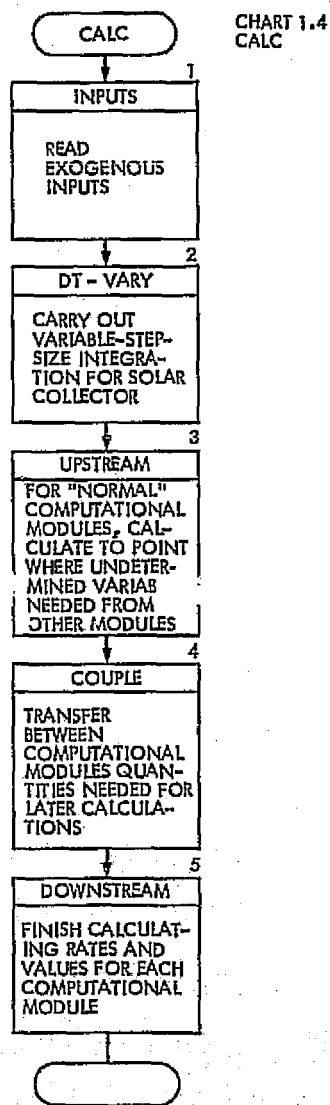


Fig. 5. Partial Level 2 design, program SUN

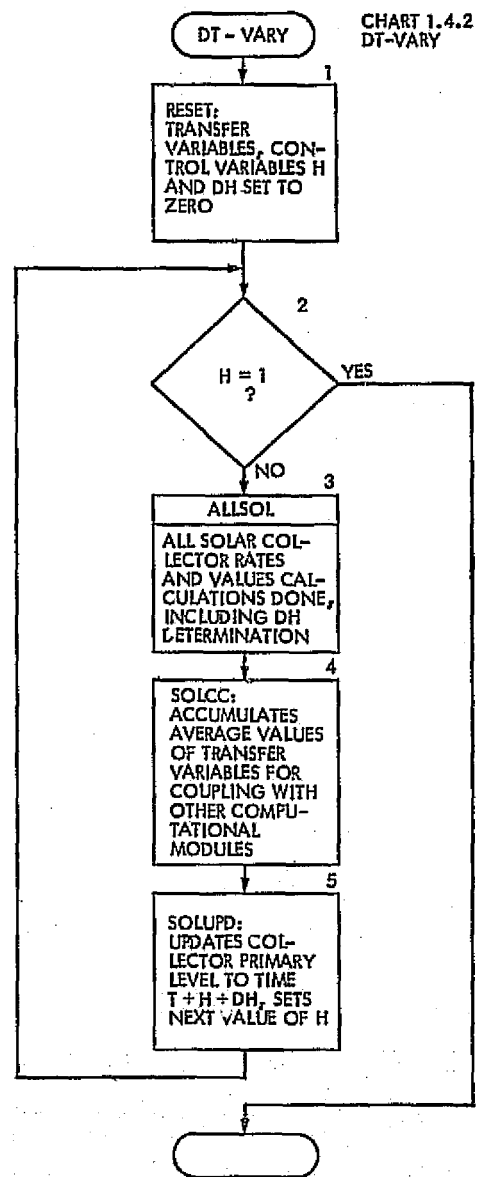


Fig. 6. Partial Level 3 design, program SUN

ORIGINAL PAGE IS
OF POOR QUALITY

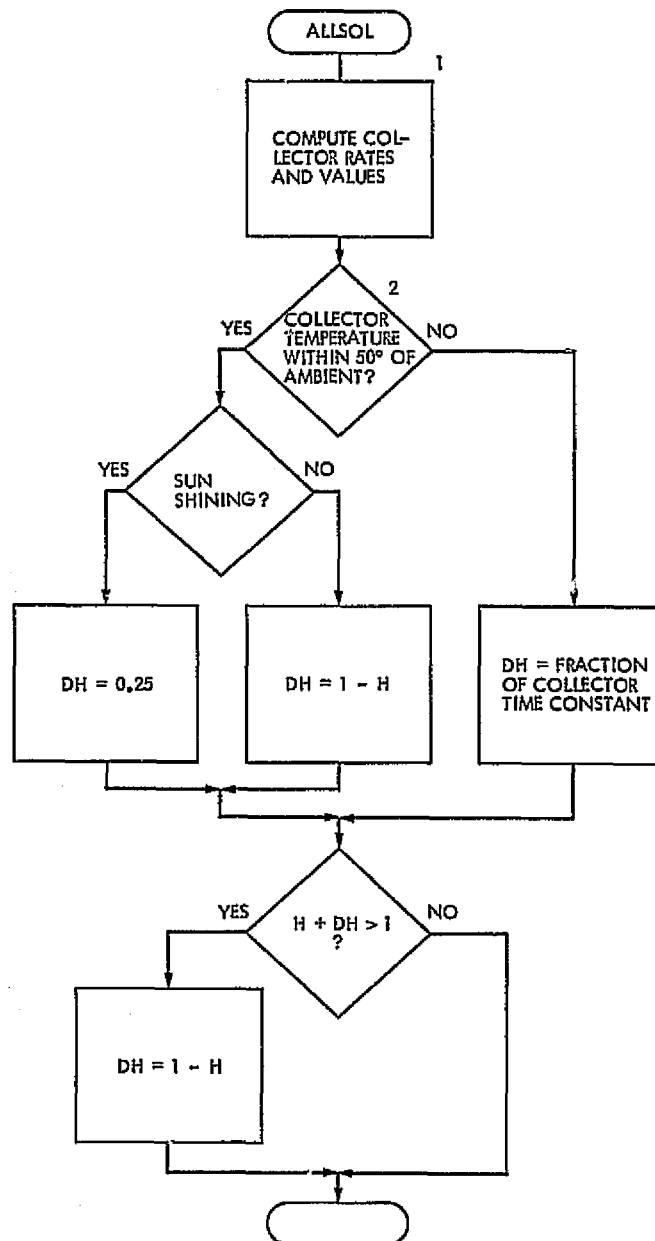


Fig. 7. Partial Level 4 design, program SUN

3.1	HEAT ENGINE OUTPUT RATE	$HEOR = HEIR * CYEFF * MEFF * GEFF$	kWh/h
3.1.1	HEAT ENGINE INPUT RATE	$HEIR = WFFR * [(REFT - SNKT) * WFSH + WFHV]$	kWh/h
3.1.1.1	WORKING FLUID FLOW RATE	$WFFR = EFR$ from 2A.2.1.1	kg/h
3.1.1.2	REFERENCE TEMPERATURE	$REFT = 38$	°C
3.1.1.3	SINK TEMPERATURE	$SNKT = AMBT + 10$	°C
3.1.1.3.1	AMBIENT TEMPERATURE	$AMBT$ - exogenous input	°C
3.1.1.4	WORKING FLUID SPECIFIC HEAT	$WFSH = 0.0007$	kWh/kg°C
3.1.1.5	WORKING FLUID HEAT OF VAPORIZATION	$WFHV = EFHV$ from 2A.2.1.5	kWh/h
3.1.2	CYCLE EFFICIENCY	$CYEFF = CEFF * RCCE$	n.d.
3.1.2.1	CARNOT EFFICIENCY	$CEFF = (WFD - SNKT) / (WFD + 273)$	n.d.
3.1.2.1.1	WORKING FLUID DELIVERY TEMPERATURE	$WFD = EFD$ from 2A.2.1.5.1	°C
3.1.2.1.2	SINK TEMPERATURE	$SNKT$ from 3.1.1.3	°C
3.1.2.2	RATIO OF CYCLE TO CARNOT EFFICIENCY	$RCCE = 0.9$	n.d.
3.1.3	MECHANICAL EFFICIENCY	$MEFF = 0.8$	n.d.
3.1.4	GENERATOR EFFICIENCY	$GEFF = 0.9$	n.d.

Fig. 8. Relationships within heat engine computational module

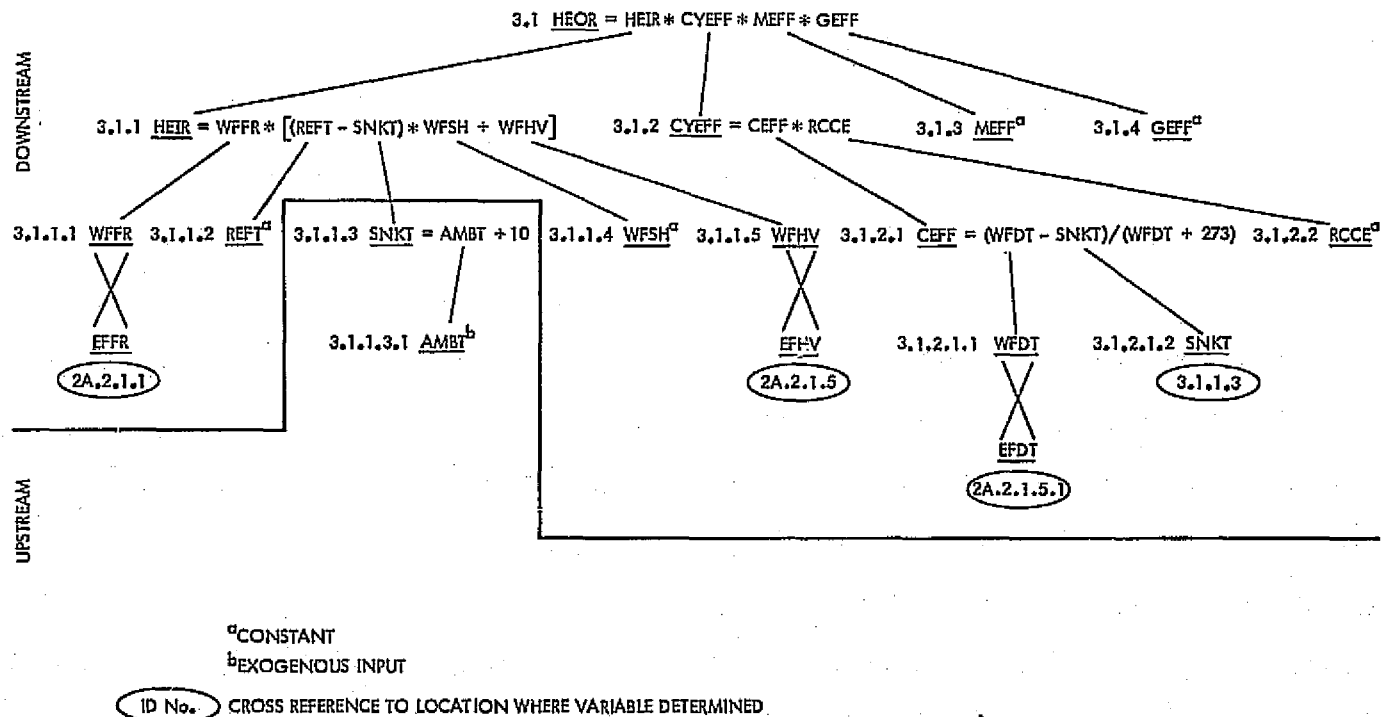


Fig. 9. Calculation tree for heat engine computational module

The QVLBI Doppler Demonstration Conducted With Mariner 10

C. C. Chao and V. J. Ondrasik
Tracking and Orbit Determination Section

The Mariner 10 differenced doppler (QVLBI) demonstration conclusively showed that this new data type can reduce the effects of moderate unmodeled spacecraft accelerations (10^{-10} km/s²) by an order of magnitude and reduce the effects of the solar corona by a factor of five. The differenced data solutions were also very useful in making real-time navigation decisions for use by the Mariner 10 project.

I. Introduction

Two of the primary error sources that limit interplanetary navigational capabilities are unmodeled spacecraft accelerations and charged particles in the solar corona and space plasma. Small unmodeled accelerations that may only perturb the trajectory by 10 km over a one-month time span can degrade the data sufficiently to produce a 1,000-km error in the estimate of the position of the spacecraft. The influence of the space plasma upon navigational accuracies is difficult to predict because of its random nature. However, space plasma events have been observed in the radio metric data that could cause 1,000-km navigational errors. The solar corona is often the dominant error source when the Sun-Earth-spacecraft angle is less than 10 deg and may produce navigational errors as large as several thousand kilometers.

Analysis and simulations (Refs. 1 and 2) have shown that the navigation of spacecraft subject to these error sources

can be greatly enhanced by simultaneously obtaining doppler data from two widely separated stations. However, before this new simultaneous doppler data type, sometimes called Doppler Quasi Very Long Baseline Interferometry (DOPPLER QVLBI), can be incorporated into a mission design, it is necessary to obtain flight data and demonstrate that the expected improvement in navigational capabilities can actually be achieved.

The first attempt at demonstrating the advantages of simultaneous doppler data was made in 1971 with Mariner 9 two-way and three-way data taken from Deep Space Stations (DSSs) 12 and 41 during the month and a half prior to Mars encounter. The results (Ref. 3) though promising, are not conclusive because there was only a limited amount of data and inadequate knowledge about the behavior of the frequency system.

In 1973 it was decided to conduct the general simultaneous doppler demonstrations in the five basic phases described in Table 1.

The short baseline experiments mentioned in Table 1 are necessary to determine the quantities that describe the characteristics of the frequency system. These numbers can then be incorporated into accuracy analysis studies to determine the quality of the simultaneous doppler data. The first short baseline experiment was conducted during the summer of 1973 using Pioneer 10 and 11 data. Results (Refs. 4 and 5) indicate that the frequency offsets between stations using Rb standards vary slowly and linearly with a long term (2×10^6 s) stability on the order of 2 parts in 10^{12} ($\Delta f/f$). Accuracy analysis studies (Ref. 6) predict that the corresponding simultaneous doppler data should be capable of reducing the effects of moderate ($10^{-10} \rightarrow 10^{-11}$ km/s²) unmodeled accelerations by an order of magnitude.

The purpose of phase 2 of the simultaneous doppler demonstration was to show that the underlying principles of the differencing technique are sound. This was accomplished during the Pioneer 10 encounter by showing that the orbit determination (OD) solution based upon differenced two-way and three-way doppler data was two or three orders of magnitude better than the corresponding solutions based upon only the conventional two-way data when the spacecraft was subject to large (10^{-8} km/s²) unmodeled accelerations produced by the Jovian satellites. The detailed results of this demonstration are described in Ref. 7.

Mariner 10 provided an excellent opportunity for showing that simultaneous doppler data based upon Rb oscillators are capable of reducing the sensitivity of the orbit determination solution to moderate unmodeled accelerations ($10^{-10} \rightarrow 10^{-11}$ km/s²) by an order of magnitude. The first nine-month period of the Mariner 10 simultaneous doppler demonstration is the primary subject of this article and is described in some detail in later sections. The demonstration was successful and generally gave the expected results although there were some surprises.

To provide simultaneous doppler data which, when differenced, are capable of substantially reducing problems produced by small (10^{-12} km/s²) unmodeled accelerations typical of Mariner-type spacecraft will probably require hydrogen masers and possibly dual frequency data. A short baseline experiment to determine the quality of H-maser doppler data may be able to be performed in 1975. It is anticipated that a definitive simultaneous doppler demonstration using H-masers and dual frequency

data will take place during Viking if the necessary data are taken.

II. Strategy

The best demonstration of the navigational advantages of a new data type is obtained from comparisons of orbit determination estimates of a spacecraft trajectory based upon the new data types, and based upon conventional data types with the actual trajectory. Currently, the only means of determining the actual (to within a few kilometers) trajectory of a spacecraft is to use both pre- and postplanetary encounter data. Unfortunately, for orbit determination, two weeks before both the Venus and the first Mercury encounters there were maneuvers. The uncertainty in these maneuvers is large enough so that even though the encounter data are extremely powerful, they are useless in determining the premaneuver trajectory with an accuracy better than approximately 100 km. Therefore, the desired precise comparison of trajectory estimates based upon the new data type and the conventional data type with the actual trajectory will be available only for two-week data arcs preceding Venus and Mercury encounters. Restricting the study to these short arcs immediately preceding encounter has two major deficiencies. First, since the data are so close to encounter, the orbit determination solution is primarily a spacecraft position determination. Errors in the velocity terms, because of the long mapping time, could be of primary importance. If the data were taken far away from encounter, errors would not be immediately visible in solutions based upon data taken just before encounter. This limitation is particularly important in a demonstration involving simultaneous doppler data from which the position of the spacecraft is relatively better determined than its velocity. The second deficiency resulting from restricting the study to data taken two weeks before Venus and Mercury would not permit analysis of long data arcs. Since the influence of error sources is often quite different if the solution is based upon long data arcs as opposed to short data arcs, an analysis of long data arcs is very valuable. Following sections will discuss the results of orbit determination solutions based upon five data arcs. The time and length of these two short and three long arcs are illustrated in Fig. 1. Also included in Fig. 1 are some of the events, which occurred during the Mariner 10 mission, that were particularly important to navigation. As discussed above, the short arcs of data are particularly important because a comparison can be made between the solutions based upon simultaneous doppler and solutions based upon conventional data with the actual trajectory, which is known to an accuracy of a few

kilometers. The actual trajectory of the spacecraft during the time period of the long arcs is uncertain to 50–500 km and therefore definitive demonstrations using long arc data cannot be accomplished. However, because of the importance of investigating the value of the data taken during these long arcs we will include the results of the analysis of these data.

In trying to determine the orbit of a spacecraft from a particular arc of radio metric data, the normal procedure is to make many solutions using different combinations of data types (e.g.; doppler-only, doppler plus range), different parameters in the estimate list [e.g., state (position and velocity of the spacecraft) only, state plus station locations], and different amounts of data. This procedure was followed in both the real-time and postencounter orbit determination portion of the simultaneous doppler demonstration. For the sake of brevity and clarity, only a small representative fraction of the many results will be shown in latter sections. Unless otherwise indicated, the orbit determination solutions that will be shown will be based upon doppler and range data where either the state only, or state and station locations were estimated. A frequency bias and drift for each station may also be estimated when three-way doppler data are used. The usual a priori information on the estimated parameters and data weights on the range, two-way doppler, and differenced doppler are shown in Table 2. The data weights are not primarily picked to represent the real quality of the various data types. Rather, they are chosen to establish a relative strength of the data types. In a solution employing differenced doppler data, the conventional data are deweighted so that they are used only to provide geocentric range and range-rate information, and will not influence the declination and right ascension estimates that are sensitive to unmodeled accelerations.

III. Quality of Three-Way Doppler Data

The simultaneous doppler data used in this demonstration were obtained by using conventional two-way and three-way doppler data. As mentioned earlier, the three-way data contain a temporal bias that may severely limit their effectiveness.¹ Because of the importance of establishing the quality of the three-way data, it will be worthwhile to pause and take a general look at this problem before proceeding into a discussion of the orbit determination solutions. The more information that can be obtained relating to the behavior of these biases will allow

the development of more effective techniques to reduce their degrading influence on navigational capabilities. For example, if the three-way biases were constant for each station, their effect on navigation could be almost entirely eliminated by simply estimating constant biases in the orbit determination process.

As mentioned earlier, the best means of determining the quality of the three-way data was by conducting short baseline experiments. This was first done in the summer of 1973 with the Pioneer 10 and 11 spacecraft and showed that the biases between DSSs 12 and 14 were typically about 10 mHz and fairly constant over a ten-day interval, but had a noticeable drift of about 1 mHz/week over a 60-day interval. Because of its importance this short baseline experiment was repeated a number of times during Mariner 10. Figure 2 shows the average difference of one minute two-way and three-way data on the indicated days between DSSs 12 and 14. The standard deviation about this average was less than 5 mHz. Since station location and transmission media errors will produce less than a 0.5-mHz error (Ref. 4) almost all of the 10–20 mHz difference can be attributed to differences in the frequency systems at DSSs 12 and 14. Also included in Fig. 2 is the 6-mHz difference in the two-way and three-way data taken from Pioneer on March 26, 1973. From Fig. 2 it is apparent that these differences between the two-way and three-way data on 80% of the passes may grossly be described by a combination of a constant bias and a linear drift with time. The remaining three passes on January 25 and 28 and March 18 deviated considerably from such a model for reasons that are currently unexplained.

Accuracy analysis studies based upon the results of the short baseline experiments indicate that for orbit determination solutions based upon differenced doppler data, a constant frequency bias should always be included in the list of estimated parameters and a linear drift term should also be estimated for data arcs longer than two weeks. Figure 3 contains the estimate of the biases and drift terms from data taken during four data arcs. This figure shows that the drift terms estimated in the long arc solutions tend to connect the frequency biases computed within each data arc. However, it is also readily apparent that the current bias and linear drift model does not represent reality as closely as one would like.

IV. Pretrajectory Correction Maneuver 2 (TCM 2) Solutions

The first differenced doppler solutions were made using data starting 30 days prior to the second trajectory correction maneuver (TCM 2) and continuing until a few

¹The three-way biases problem can probably be eliminated by obtaining Simultaneous Interference Tracking Technique (SITT) data. This extremely clever technique was developed by G. Wood of JPL.

days before the maneuver. Unfortunately, as shown in Fig. 4, the simultaneous doppler data were very sparse and consisted mainly of passes less than one hour in length. Representative aim plane solutions for both the conventional and the differenced data solutions are shown in Fig. 5. Also included in Fig. 5 is the current best estimate (CBE) of the actual trajectory based upon encounter data. The accompanying uncertainty is fairly large (100 km) because of uncertainties in the magnitude and direction of TCM 2.

During this time span the spacecraft was subjected only briefly to unmodeled accelerations that were larger than the 3×10^{-12} km/s² Mariner 10 specifications. Since the difference data solutions can be expected to be superior only when there are unmodeled spacecraft accelerations or some other common error source affecting the data, it is not surprising that the conventional solutions based upon almost continuous data will be generally better than the differenced data solutions. Indeed, it is surprising that the difference data solutions are so good since there was so little data.

One of the interesting features of Fig. 5 is that the conventional data solutions are highly correlated, all having nearly the same value for B•T, while the differenced data solutions are more independent. The position of the spacecraft in the ecliptic (i.e., the B•T direction) is generally much better determined than the direction out of the ecliptic (i.e., B•R) from conventional data, because most of the geocentric acceleration occurs in the ecliptic and this acceleration will be a strong source of B•T information. In the differencing process most of the acceleration information is removed so that the differenced doppler solutions will not in general determine B•T significantly better than B•R.

V. TCM 2 to Venus Encounter

On January 28, 1974, seven days before Venus encounter, Mariner 10 experienced a large gas leak of 80-min duration at the conclusion of a gyro test. This leak gave the spacecraft a 1.8×10^{-9} km/s² acceleration in the Earth direction, and it was speculated at the time that it could possibly move the encounter trajectory by over 100 km. Since a 100-km miss at Venus would have severely limited the science return at Mercury, all possible efforts were made to quickly reestablish the orbit of the spacecraft so that another pre-Venus maneuver could be made if necessary. Processing the conventional two-way doppler data and completely ignoring the gas leak gave errors in the estimate of the encounter trajectory of over 700 km. Much better results were obtained by treating the

gas leak as a motor burn that was included in the list of estimated parameters. Figure 6 shows that the solutions obtained in this way agreed with the current best estimate (using pre- and postencounter data) in the aim plane to within 50 km.

Fortunately, for a few days following TCM 2, a relatively large amount of three-way data was taken. Using these data along with the extensive three-way data coverage following the gas leak provided enough information to give viable simultaneous differenced doppler solutions. Since the differenced doppler solutions should be insensitive to unmodeled accelerations such as large gas leaks, it was not necessary to model the gas leaks as a solve-for instantaneous maneuver. As shown in Fig. 6, the real-time differenced doppler solutions agreed with the current best estimate of the aim plane parameters to within 30 km and were generally as accurate as the better conventional data batch and sequential filter solutions. Having a real-time differenced doppler solution during this most critical navigation period was extremely valuable and provided a great deal of confidence that an additional pre-Venus maneuver was not necessary. In principle, the differenced data should be superior to the batch solution where the leak is modeled as a maneuver, since estimating a maneuver essentially breaks the arc in two. The differenced data solution should also be better than the usual sequential filter solution since it requires no modeling of the accelerations.

As has just been shown, the simultaneous doppler data can be extremely useful in reducing the problem caused by large ($> 10^{-10}$ km/s²) unmodeled accelerations of short duration, such as the January 28 episode on Mariner 10 and the Encounter-7 day "happening" of Mariner 7. It is much more common for the unmodeled spacecraft accelerations to be smaller in magnitude and to continue for many days. As mentioned in the introduction, preflight accuracy analysis studies indicated that for systems based on a rubidium oscillator, the differenced doppler orbit determination solution will be superior to the conventional solution when the spacecraft is subject to continuous moderate unmodeled accelerations on the order of $10^{-10} \rightarrow 10^{-11}$ km/s². Although the Mariner did not experience any such unmodeled acceleration of this size except for very brief times, it was easy to generate a continuous unmodeled acceleration of 10^{-10} km/s² by simply not modeling the solar pressure. When the solar pressure model is turned off, the before-the-fit two-way doppler residuals gradually increase from a few millihertz at the epoch, 13 days before encounter (E-13), to 1.7 Hz one day before encounter. As shown in Fig. 7 the orbit determination solution based upon the conventional data

for the spacecraft experiencing such an unmodeled acceleration is in error by 400 km.

Turning off the solar pressure model should produce virtually no change in the before-the-fit residuals of the differenced doppler data, since this data type should be insensitive to unmodeled accelerations. The real data confirmed this expectation because the before-the-fit differenced doppler residuals based upon nominal trajectories with the solar pressure turned on and off both gave residuals of a few millihertz. The aim plane solutions using the differenced doppler data with the solar pressure model turned off are almost as good as the solutions with the solar pressure model turned on. As shown in Fig. 7, the difference between the predicted aim plane coordinates and the actual values are 45 km at E-5 days and 17 km at E-1 day. Thus, there is more than an order of magnitude improvement in the aim plane solution in using the differenced data rather than the conventional data. This is an extremely important result. Not only does it demonstrate the superiority of the differenced data in dealing with unmodeled accelerations, but it also indicates that our preflight accuracy analysis studies can accurately predict the advantages of new data types.

VI. Venus Encounter to TCM 3

During the period between Venus encounter and TCM 3 (13 days before Mercury) the spacecraft experienced several episodes of moderate unmodelable accelerations. As shown in Fig. 8, the solutions based upon conventional data and the batch filter separated into three groups depending on whether state or state and stations were estimated and whether near-Venus data were or were not included. The scatter between these conventional data solutions was 250 km, which was 2-1/2 times the accuracy required by the mission. The sequential solutions using the conventional data were much less scattered (~75 km). The solutions based upon the differenced doppler also were much less scattered (50 km) and showed very little dependence on what parameters were estimated.

Also included in Fig. 8 is the current best estimate (CBE) of the premaneuver trajectory. Because of the pre-Mercury maneuver this CBE has an associated uncertainty of 50 km. From Fig. 8, it is clear once again that, in the presence of moderate unmodeled accelerations, the batch filter solutions using the differenced doppler data are nearly an order of magnitude superior to batch filter solutions using conventional data.

VII. TCM 3 to Mercury Encounter

TCM 3 occurred 13 days before Mercury encounter. During those 13 days only 9 passes with good overlapping data were taken. The simultaneous data were seriously degraded by an apparent 20-mHz jump in the frequency system of station 43. These data have been processed, however, since there are only a small amount of data and they are corrupted by the frequency jump; the results will not be shown here. In passing we will just mention that the orbit determination results agree with the CBE to within 50-100 km.

VIII. TCM 4 to TCM 5 (Superior Conjunction)

Between TCM 4 (May 9, 1974) and TCM 5 (July 2, 1974), the Sun-Earth-probe (SEP) angle remained under 7 deg and reached a minimum of about 1.7 deg at superior conjunction. The effect of the solar corona on the doppler data was very significant and generated data noise as high as 0.2 Hz (at 300-s count time). Because the ray paths of the signals from the spacecraft to widely separated tracking stations are very similar, the effect of the solar corona on the down-link two-way and three-way data should be nearly common. Thus it was hoped that differencing the two-way and three-way data should remove much of the noise induced by the solar corona. Figure 9 shows the two-way, three-way, and differenced data residuals from a pass of data taken four weeks before superior conjunction. It is clear from this figure that the effects on the two-way and three-way data are nearly common and the noise on the differenced data is 5-10 times smaller than the noise on the conventional two-way data. Figure 10 contains the per-pass standard deviations of both the 5-min conventional and differenced doppler data. Generally the differencing process reduces the noise by a factor of 5.

Unfortunately, the Australian stations were usually unavailable for tracking between the fourth and fifth maneuvers. The differenced doppler data during this period consisted of 1- to 3-h Spain-Goldstone tracking passes. Even with this limited amount of data, the long arc for the second Mercury encounter solutions using the differenced data agreed with the conventional long arc solutions to within a few hundred kilometers. Because of the large noise contained in the data around superior conjunction, the short arc (10 to 20 days) conventional data solutions (both batch and sequential) were generally quite unstable, having a scatter of approximately 2,000 km. However, the short arc differenced data solutions were much better having a scatter of about 500 km. This factor-

of-four improvement in the orbit determination solutions brought about by the differencing process is very encouraging.

If the noise in the differenced doppler data can be attributed entirely to electrons in the solar corona, an estimate of the electron density gradient can be made. The ray paths that pass the Sun at 4.5 solar radii and continue to Goldstone and Madrid are separated by about 2,000 km when they pass the Sun. For this particular pass the average difference between the three-way and two-way doppler residuals was about 0.035 Hz. Therefore, the gradient of the electron density would be $0.035 \text{ Hz}/2000 \text{ km} = 0.017 \text{ Hz}/1000 \text{ km} = 1.1 \times 10^{14} \text{ (electrons/m}^2\text{)}/\text{s}/1000 \text{ km}$.

IX. Conclusions

The Mariner 10 differenced doppler (QVLBI) demonstration conclusively showed that this new data type can reduce the effects of moderate unmodeled spacecraft accelerations (10^{-10} km/s^2) by an order of magnitude and reduce the effects of the solar corona by a factor of five. The differenced data solutions were also very useful in making real-time navigation decisions for use by the Mariner 10 project. To demonstrate that the differenced data can be used to effectively remove the effects of small (10^{-12} km/s^2) unmodeled accelerations, it will probably be necessary to have full S-band—X-band (S/X) charged particle calibrations and either frequency systems based on hydrogen masers or SITT Data. Hopefully, such data will be available from the Viking spacecraft for the two months preceding the encounter with Mars.

Acknowledgment

The authors wish to thank S. J. Reinbold and R. E. Koch for their constant help in the data processing and making O. D. runs. Thanks are also due to K. W. Yip for his assistance during TCM 3 (Mercury delivery).

References

1. Ondrasik, V. J., and Rourke, K. H., "Applications of Quasi-VLBI Tracking Data Types to the Zero Declination and Process Noise Problems," paper presented at AAS/AIAA Astrodynamics Specialties Conference, AAS No. 71-339, August 17, 1971.
2. McDanell, J. P., "Earth- Based Orbit Determination for Solar Electric Spacecraft with Application to a Comet Encke Rendezvous," paper presented at AIAA 11th Aerospace Sciences Meeting, AIAA Paper No. 73-174, January 10, 1973.
3. Mulhall, B. D., Chao, C. C., Johnson, D. E., and Zielenbach, J. W., "Report of the Two-Station Doppler Demonstration Conducted with Mariner 9," *The Deep Space Network Progress Report 42-20*, January-February 1974. Jet Propulsion Laboratory, Pasadena, California.
4. Chao, C. C., Wong, S. K., and Lubeley, A., "Short Baseline QVLBI Demonstrations—Part I," Technical Report 32-1526, Vol. XVIII. Jet Propulsion Laboratory, Pasadena, California, September, 1973.
5. Chao, C. C., Preston, R. A., and Nance, H. E., "Short Baseline QVLBI Demonstration—Part II," *The Deep Space Network Progress Report 42-20*, January-February 1974. Jet Propulsion Laboratory, Pasadena, California.
6. Ondrasik, V. J., and Rourke, K. H., "An Analytical Study of the Advantages Which Differenced Tracking Data May Offer...", Technical Report 32-1526, Vol. IV. Jet Propulsion Laboratory, Pasadena, California.

7. O'Reilly, B. D., and Chao, C. C., "An Evaluation of QVLBI OD Analysis of Pioneer 10 Encounter Data in the Presence of Unmodeled Satellite Accelerations," *The Deep Space Network Progress Report 42-22*, May-June 1974. Jet Propulsion Laboratory, Pasadena, California.

Table 1. QVLBI doppler demonstrations

Phase	Spacecraft	Baseline	Frequency system	Purpose
1	Pioneers and Mariners	Short ^a	Rb ^c	Determine pertinent characteristics of Rb oscillator
2	Pioneer 10	Long ^b	Rb	Show that simultaneous doppler reduces effects of large unmodeled accelerations ($> 10^{-8}$ km/s ²) by two orders of magnitude
3	Mariner 10	Long	Rb	Show that simultaneous doppler reduces effects of moderate unmodeled accelerations ($10^{-10} \rightarrow 10^{-11}$ km/s ²) by an order of magnitude
4	Helios, Pioneer, Mariner, Viking	Short	H ^d	Determine pertinent characteristics of H-maser
5	Viking	Long	H	Show that simultaneous doppler reduces effects of small unmodeled accelerations (10^{-12} km/s ²) by order of magnitude

^aDistance between tracking stations less than ~ 100 km.

^bDistance between tracking stations greater than ~ 5000 km.

^cRb = rubidium.

^dH = hydrogen.

Table 2. Estimated and considered parameters and their a priori values

Parameter	Estimated a priori	Considered a priori
$\begin{Bmatrix} X \\ Y \\ Z \end{Bmatrix}$ S/C position	10^4 km	
$\begin{Bmatrix} \dot{X} \\ \dot{Y} \\ \dot{Z} \end{Bmatrix}$ S/C velocity	1 km/s	
A100 \dot{f} (frequency offset)	1.0×10^{-10} (0.229 Hz)	14.42×10^{-12} (0.03 Hz)
A200 \dot{f} (frequency drift)	1.0×10^{-10} (0.229 Hz/ 10^6 s)	0.3×10^{-17} (0.0069 Hz/ 10^6 s)
$\begin{Bmatrix} r_s \\ L_o \\ z \end{Bmatrix}$ station location in cylindrical coordinates	3 m 0.54772×10^{-4} deg 15 m	3 m 0.54772×10^{-4} deg 15 m
$\begin{Bmatrix} GR \\ GX \\ GY \end{Bmatrix}$ solar pressure coefficients		0.5 D-1
$\begin{Bmatrix} ATAR \\ ATAX \\ ATAY \end{Bmatrix}$ nongravita- tional accelerations		1. D-11
$\begin{Bmatrix} MUF \\ MUP \\ MUB \\ NUF \\ NUP \\ NUB \end{Bmatrix}$ solar pressure coefficients		1. D-2
Data weights		
Differenced doppler		0.007 Hz
Conventional 2-way doppler		0.7 Hz
Range		10 km

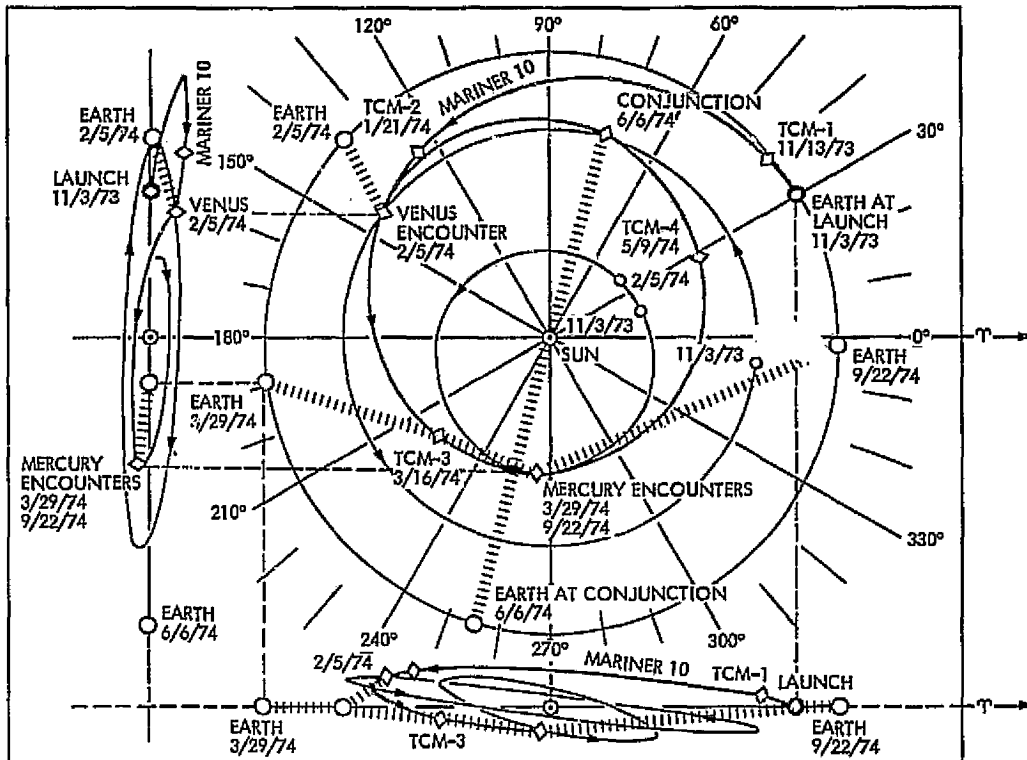


Fig. 1. Mariner 10 trajectory viewed from above and edge-on; relative inclinations are 3 deg for Venus and 7 deg for Mercury

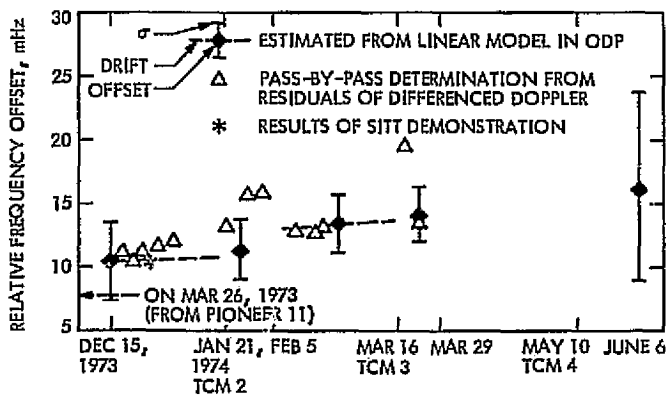


Fig. 2. Values of relative frequency offset of short baseline QVLBI demonstrations (DSSs 12 and 14)

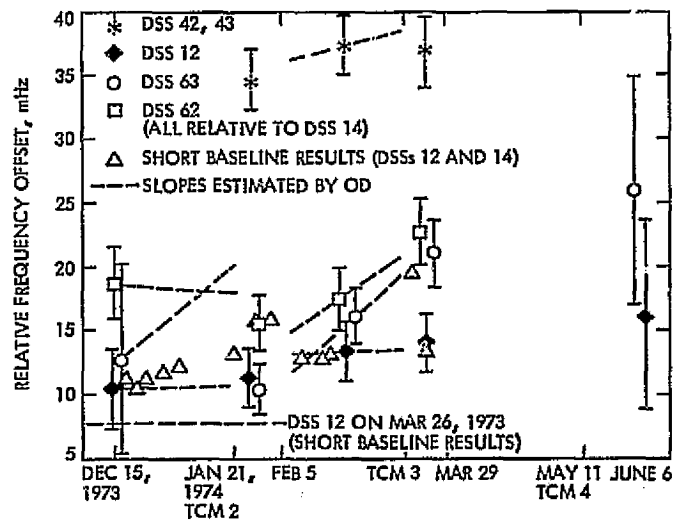


Fig. 3. Values of estimated frequency offset relative to DSS 14

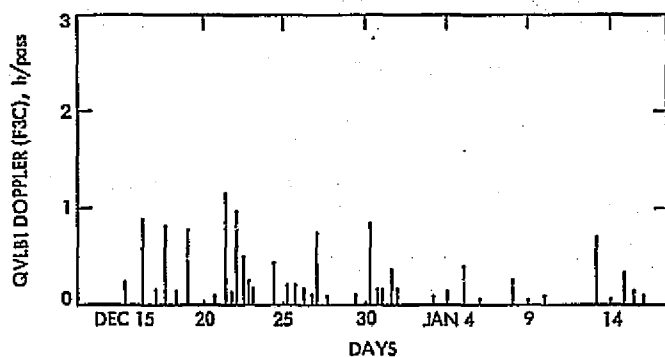


Fig. 4. Distribution of QVLBI doppler data (Dec 15 to TCM 2)

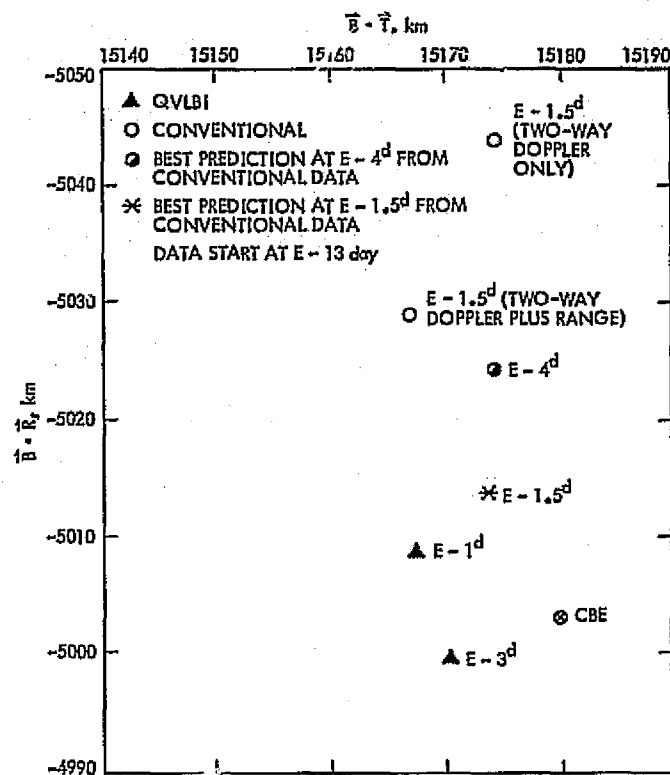


Fig. 6. B-plane predictions a few days before Venus encounter

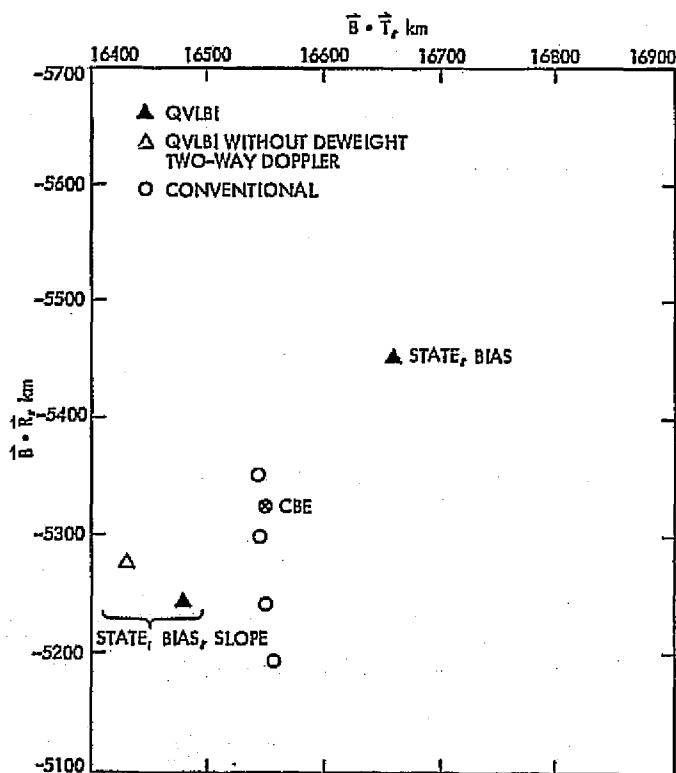


Fig. 5. Venus B-plane predictions pre-TCM 2

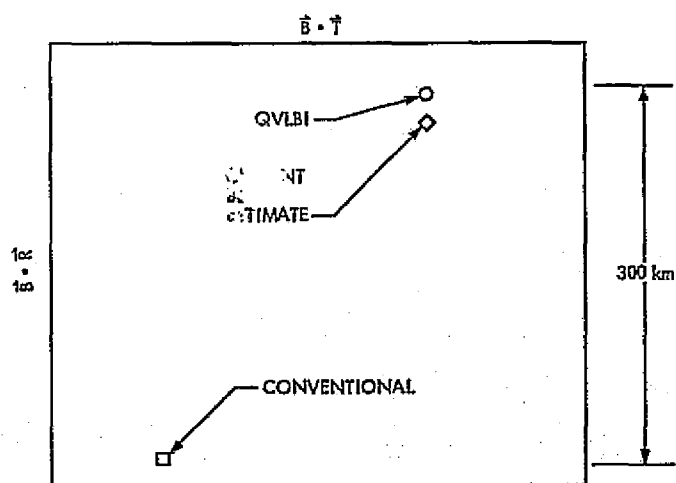


Fig. 7. Conventional and differenced data solutions using data from Venus -13 d to Venus -3 d with no solar pressure model

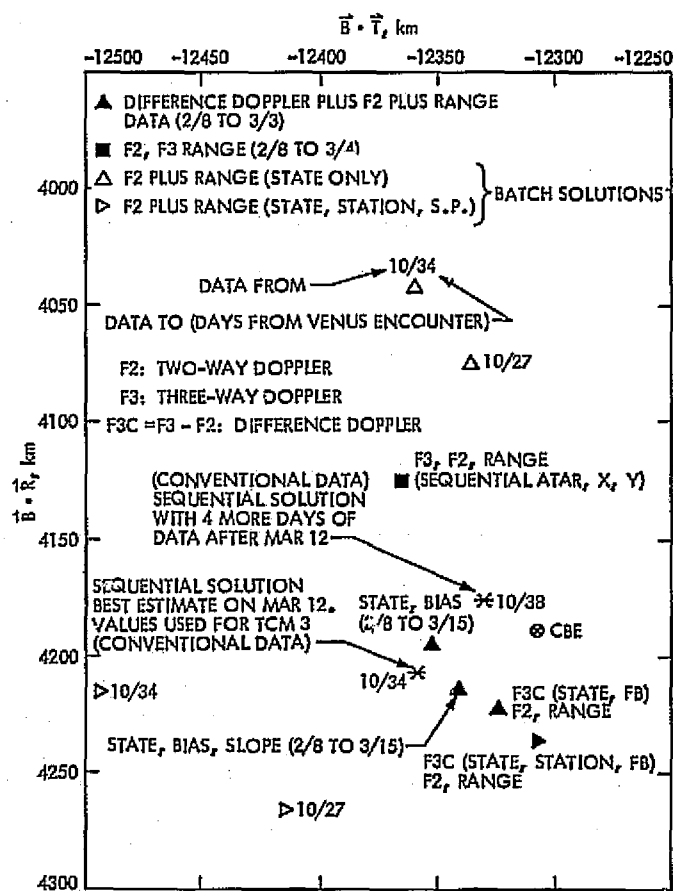


Fig. 8. Mercury B-plane predictions at TCM 3

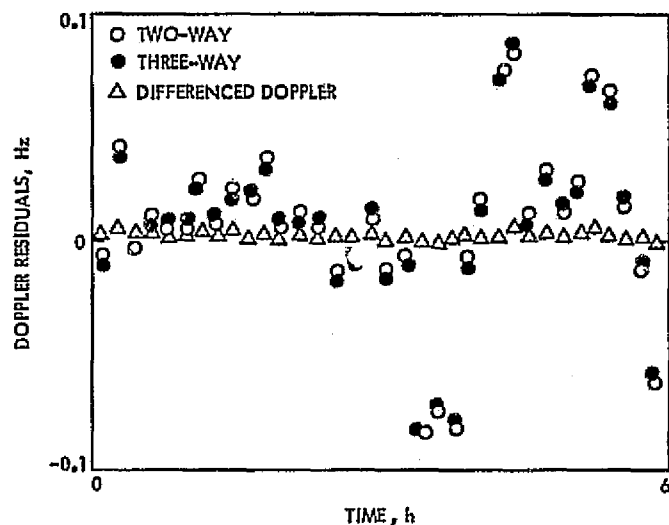


Fig. 9. Two-way, three-way, and differenced doppler four weeks before superior conjunction

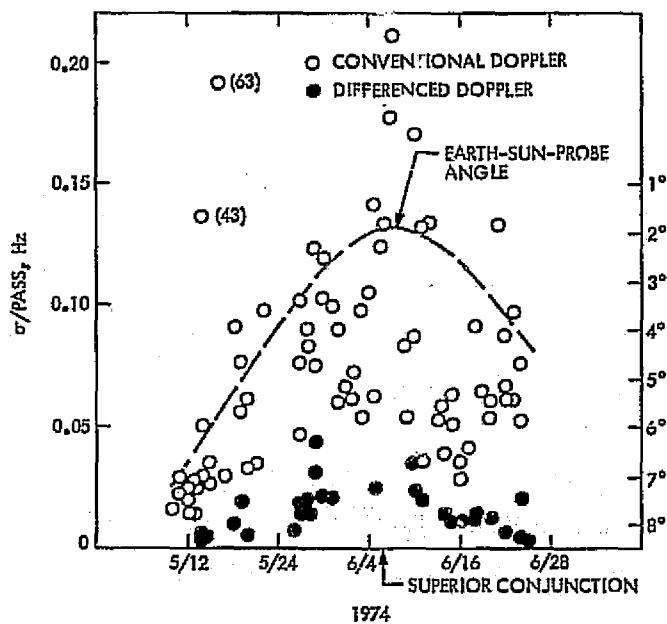


Fig. 10. Standard deviation per pass of two-way and differenced doppler residuals

Distribution Amplifiers for Hydrogen Maser Frequency Standard

G. Lutes

Communications System Research Section

Distribution amplifiers have been developed for the hydrogen maser frequency standard. These amplifiers are optimized for low phase noise, high isolation between outputs, and low phase drift with temperature in order to minimize degradation of the signals.

Distribution amplifiers have been developed to distribute the various frequencies provided by the hydrogen maser frequency standard. These amplifiers are optimized for low phase noise, high isolation between outputs, and low phase drift with temperature. Optimization of these parameters minimizes degradation of the hydrogen maser frequency standard output. When one output is shorted, unloaded, or has a signal inadvertently applied to it, the effect on other outputs is minimal due to the high isolation between outputs.

The circuit consists of a four-way hybrid power splitter and four isolation amplifiers on a single printed circuit board plus the required power supply decoupling that is contained within cavities in the chassis (Fig. 1).

The four-way hybrid power splitter has > 30 dB isolation between outputs when driven from a $50\text{-}\Omega$ source. This isolation contributes to the isolation between outputs of the distribution amplifier. Each of the four outputs from the power splitter drives one of the four isolation amplifiers.

The isolation amplifier is a two-stage unity gain amplifier consisting of a common emitter stage with collector to base feedback driving a complementary emitter follower. A complementary emitter follower is used because it is more efficient than a one-transistor emitter follower and has lower output impedance. The complementary emitter follower in itself has high inherent negative feedback, and at the same time provides a high-impedance load for the first stage, increasing its open loop voltage gain, thereby increasing the negative feedback in the first stage.

The large amount of negative feedback minimizes phase noise (which is an inverse function of negative feedback), reduces phase drift with temperature, lowers harmonic distortion, stabilizes the input and output impedance, and broadbands the amplifier.

Build-out resistors at the input and output of each amplifier provide the required impedance and low voltage standing wave ratio (VSWR).

Output-to-input isolation is maximized by this circuit configuration. A common emitter stage has the best voltage isolation and an emitter follower stage has the best current isolation. By combining a common emitter stage with an emitter follower stage, best output-to-input isolation is obtained for a two-stage amplifier.

The chassis which conforms to the standard DSN configuration contains an inner cover with cavities that match cavities in the chassis. The printed circuit board is sandwiched between the chassis and inner cover. Each amplifier section on the printed circuit board is enclosed within one pair of cavities in the chassis and inner cover. This minimizes RF leakage between isolation amplifiers.

The opposite side of the chassis contains four separate and isolated power supply decoupling lines. The power is

supplied to each amplifier through a separate set of chassis channels that contain three series RFI filters. This decoupling provides > 120 dB of isolation from one power supply line to any other.

Typical test results for the 1- to 30-MHz distribution amplifiers are shown in Table 1.

A 100-MHz version of this distribution amplifier was also developed. It is basically the same as the 1- to 30-MHz version, except the first stage is a complementary common emitter stage and faster transistors are used throughout. This version is optimized for use at 100 MHz. It has capacitors in the input and output circuits to cancel the inductive reactance.

Output to output isolation in this version is typically greater than 70 dB.

Table 1. Test results for the 1- to 30-MHz distribution amplifiers

Parameter	Result
Input impedance (50 Ω nominal)	< 1.1:1 VSWR from 1 to 30 MHz
Output impedance (50 Ω nominal)	< 1.2:1 VSWR from 1 to 30 MHz
Total harmonic distortion	< 5% at +18 dBm output power
Gain flatness	± 0.5 dB from 1 to 30 MHz
Drive level for full output (+18 dBm)	+19 dBm \approx 80 mW
Isolation, output to output	> 100 dB between any two outputs from 1 to 30 MHz
Phase noise	< -140 dB below a 5-MHz carrier in a 1-Hz bandwidth 5 Hz from the carrier
Phase drift with temperature	≈ 9 m deg/ $^{\circ}$ C at 5 MHz
Power supply requirements	-15 V at 134 mA

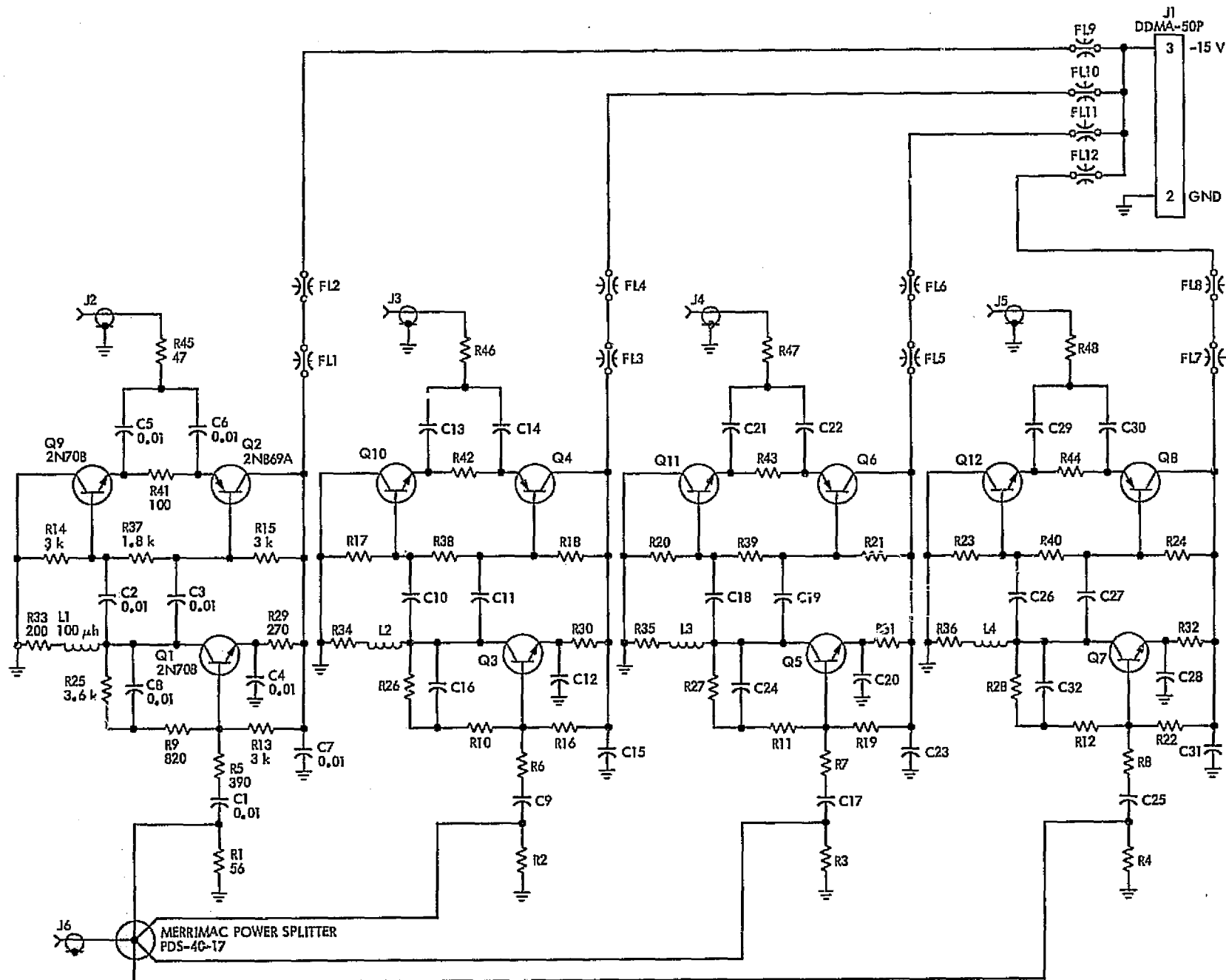


Fig. 1. Schematic, 1- to 30-MHz distribution amplifier

Galois Switching Functions and Their Applications

B. Benjauthrit and I. S. Reed
University of Southern California

The Boolean difference expansion of Boolean algebra is generalized to finite (Galois) fields. A systematic method is provided for calculating the coefficients of this type of multivariable polynomial expansion. It is applied then to the synthesis of switching functions. Applications include multivalued logics as well as binary-valued logics.

I. Introduction

As the computer technology continues to flourish, logic design grows ever more complex. This, combined with the rapid advance of the integrated circuit technology, indicates the need for alternative logic designs which are simple and systematic in nature. Towards this end, this article generalizes to finite fields an expansion of Boolean algebra (Ref. 1). This expansion over finite fields includes the transform recently provided by Menger in Ref. 2 for single variable functions. This result was previously described in Ref. 3 for finite fields having 2^n elements where n is any positive integer.

Since the circuit design methods introduced in this article utilize polynomial expansions of finite or Galois fields, it is appropriate to call the physical realizations of this new expansion Galois switching functions. Such functions can be implemented in the same manner as logic networks using AND and OR gates. Nonetheless, instead of using only single gates, they often employ complex modules. To keep pace with the technology of large-scale integrated (LSI) circuits, following Menger (Ref. 2), such modules will be referred to as Galois PLUS and Galois TIMES gates.¹

The present approach of mapping mathematical descriptions onto hardware differs from the Fourier-like transform technique discussed elsewhere (Ref. 4). The relationship of the mathematics to the circuit in the transform method is often lost and difficult to appreciate. Though the new method, presented here, still involves considerable mathematics, its complexity is compensated partly by the transparency of its mapping onto hardware.

¹Rigorous treatments of these gates may be found in Refs. 3, 5, and 9.

Since the mathematical background necessary for this presentation is ubiquitous (Refs. 6 and 12), it will not be provided here. Several points of attraction for this type of logic design are presented. A few suggestions for future research in this area are also made.

II. The Polynomial Expansions

The polynomial expansion for single-variable Galois switching functions will be given first; then the result is extended to multivariable Galois switching functions. From this, a formal definition of Galois switching functions is also described.

Theorem 1 below, though given by Menger (Ref. 2), is reexpressed without proof here in a form needed to develop the multivariable expansion to be described in Theorem 2.

THEOREM 1: For any function $F: GF(p^n) \rightarrow GF(p^n)$, there exists a unique function $f: \{0, 1, \dots, p^n - 1\} \rightarrow GF(p^n)$ such that

$$F(x) = \sum_{k=0}^{p^n-1} f(k)x^k \quad (1)$$

where the function f is given by

$$\begin{aligned} f(0) &= F(0) \\ f(k) &= \sum_{\gamma \in GF(p^n)} [F(0) - F(\gamma)]\gamma^{-k}, 0 < k < p^n \end{aligned} \quad (2)$$

so that $F(x)$ has the following "power series" expansion:

$$F(x) = F(0) + \sum_{k=1}^{p^n-1} \left[\sum_{\gamma \in GF(p^n)} [F(0) - F(\gamma)]\gamma^{-k} \right] x^k \quad (3)$$

The existence of Eq. (1) has long been known (Ref. 6). A more generalized version of it was first proven by Reed and Solomon (Ref. 7). Edwards (Ref. 8) later proved Eq. (1) in its present form when dealing with synthesis of switching networks. Menger provided Eq. (2) in his Theorem 2, a more generalized version of the Boolean difference described by Reed (Ref. 1). From Eq. (2), one can compute the coefficients $f(k)$ in Eq. (1).

With Theorem 1 and the recognition that Eq. (2) is a generalized Boolean difference, a method was found in Ref. 3 for deriving any multivariable polynomial expansion over Galois fields $GF(2^n)$. This method is now extended to the general Galois field $GF(p^n)$.

Let us first symbolize Eq. (2) differently by defining a generalized finite "difference" as follows:

$$f(k) = \Delta_{x^k} F(0) = \sum_{\gamma \in GF(p^n)} [F(0) - F(\gamma)]\gamma^{-k} \quad (4)$$

where $0 < k < p^n$. Equation (4) is a sum of weighted differences $[F(0) - F(\gamma)]$ over the field $GF(p^n)$. For $GF(2)$, it simply reduces to the usual Boolean difference (Ref. 1). This is the reason for calling the above sum a finite difference. Due to the linearity of Eq. (4) in the differences $[F(0) - F(\gamma)]$,

$$\begin{aligned} f(k_1, k_2) &= \Delta_{x_1^{k_1} x_2^{k_2}} F(0, 0) = \Delta_{x_1^{k_1}} \left[\Delta_{x_2^{k_2}} F(0, 0) \right] \\ &= \sum_{\gamma \in GF(p^n)} \left[\Delta_{x_2^{k_2}} F(0, 0) - \Delta_{x_2^{k_2}} F(\gamma_1, 0) \right] \gamma_1^{-k_1} \end{aligned}$$

But

$$\Delta_{x_2^{k_2}} F(0, 0) = \sum_{\gamma_2 \in GF(p^n)} [F(0, 0) - F(0, \gamma_2)] \gamma_2^{-k_2}$$

and

$$\Delta_{x_2^{k_2}} F(\gamma_1, 0) = \sum_{\gamma_2 \in GF(p^n)} [F(\gamma_1, 0) - F(\gamma_1, \gamma_2)] \gamma_2^{-k_2}$$

both also by Eq. (4). Hence, using the linear property of Σ ,

$$\begin{aligned} f(k_1, k_2) &= \sum_{\gamma_1 \in GF(p^n)} \left[\sum_{\gamma_2 \in GF(p^n)} [F(0, 0) - F(0, \gamma_2)] \gamma_2^{-k_2} - \sum_{\gamma_2 \in GF(p^n)} [F(\gamma_1, 0) - F(\gamma_1, \gamma_2)] \gamma_2^{-k_2} \right] \gamma_1^{-k_1} \\ &= \sum_{\gamma_1 \in GF(p^n)} \sum_{\gamma_2 \in GF(p^n)} [F(0, 0) - F(0, \gamma_2) - F(\gamma_1, 0) + F(\gamma_1, \gamma_2)] \gamma_1^{-k_1} \gamma_2^{-k_2} \end{aligned}$$

follows from the property $-u = -1 \cdot u, u \in GF(p^n)$. For simplicity in notation, $f(k_1, k_2)$ will be rewritten as:

$$f(k_1, k_2) = \sum_{\gamma_1 \in GF(p^n)} \sum_{\gamma_2 \in GF(p^n)} [F(0, 0) - F(0, \gamma_2) - F(\gamma_1, 0) + F(\gamma_1, \gamma_2)] \gamma_1^{-k_1} \gamma_2^{-k_2}$$

Proceeding in a similar fashion, the following higher order partial differences can be derived and are given below.

$$\begin{aligned} f(k_1, k_2, k_3) &= \Delta_{x_1^{k_1}} \Delta_{x_2^{k_2}} \Delta_{x_3^{k_3}} F(0, 0, 0) \\ &= \Delta_{x_1^{k_1}} \Delta_{x_2^{k_2}} \left[\Delta_{x_3^{k_3}} F(0, 0, 0) \right] = \Delta_{x_1^{k_1}} \left[\Delta_{x_2^{k_2}} \left[\Delta_{x_3^{k_3}} F(0, 0, 0) \right] \right] \\ &= \sum_{\gamma_1 \in GF(p^n)} \sum_{\gamma_2 \in GF(p^n)} \sum_{\gamma_3 \in GF(p^n)} [F(0, 0, 0) - F(0, 0, \gamma_3) - F(0, \gamma_2, 0) - F(\gamma_1, 0, 0) \\ &\quad + F(0, \gamma_2, \gamma_3) + F(\gamma_1, 0, \gamma_3) + F(\gamma_1, \gamma_2, 0) - F(\gamma_1, \gamma_2, \gamma_3)] \gamma_1^{-k_1} \gamma_2^{-k_2} \gamma_3^{-k_3} \\ f(k_1, \dots, k_{i_p}) &= \Delta_{x_1^{k_1}} \dots \Delta_{x_{i_p}^{k_{i_p}}} F(0, \dots, 0) = \Delta_{x_1^{k_1}} \dots \Delta_{x_{i_{p-1}}^{k_{i_{p-1}}}} \left[\Delta_{x_{i_p}^{k_{i_p}}} F(0, \dots, 0) \right] \\ &= \dots = \Delta_{x_1^{k_1}} \left[\Delta_{x_2^{k_2}} \left[\dots \left[\Delta_{x_{i_p}^{k_{i_p}}} F(0, \dots, 0) \right] \dots \right] \right] \\ &= \dots = \sum_{\gamma_1 \in GF(p^n)} \dots \sum_{\gamma_{i_p} \in GF(p^n)} [F(0, \dots, 0) - F(0, \dots, 0, \gamma_{i_p}) \\ &\quad - \dots - F(\gamma_{i_1}, 0, \dots, 0) + F(0, \dots, \gamma_{i_{p-1}}, \gamma_{i_p}) + \dots + F(\gamma_{i_1}, \gamma_{i_2}, 0, \dots, 0) \\ &\quad - \dots * F(\gamma_{i_1}, \dots, \gamma_{i_p}) \gamma_1^{-k_1} \dots \gamma_{i_p}^{-k_{i_p}}] \end{aligned}$$

where the asterisk represents “-” if p is odd and “+” otherwise.

From the above expansions, an important theorem for multivariable Galois switching functions over the field $GF(p^n)$ can now be inferred. For notational conveniences, let $q = p^n - 1$. Also represent the vector of m 0's by $\underline{0}$.

THEOREM 2: For every function $F: GF(p^n)^m \rightarrow GF(p^n)$, there exists a unique function $f: \{0, 1, \dots, p^n - 1\} \rightarrow GF(p^n)$ such that

$$F(x_1, \dots, x_m) = \sum f(k_1, \dots, k_m) x_1^{k_1} \dots x_m^{k_m} \quad (5)$$

where the function f is given by

$$\begin{aligned}
 f(\underline{0}) &= F(\underline{0}) \\
 f(k_1, 0, \dots, 0) &= \Delta_{x_1^{k_1}} F(\underline{0}) = \sum_{\gamma_1 \in GF(p^n)} [F(\underline{0}) - F(\gamma_1, 0, \dots, 0)] \gamma_1^{-k_1} \\
 f(k_1, k_2, \dots, 0) &= \Delta_{x_1^{k_1} x_2^{k_2}} F(\underline{0}) \\
 &= \sum_{\gamma_1, \gamma_2 \in GF(p^n)} [F(\underline{0}) - F(0, \gamma_2, 0, \dots, 0) - F(\gamma_1, 0, 0, \dots, 0) \\
 &\quad + F(\gamma_1, \gamma_2, 0, \dots, 0)] \gamma_1^{-k_1} \gamma_2^{-k_2} \\
 &\vdots \\
 f(k_1, \dots, k_m) &= \Delta_{x_1^{k_1} \dots x_m^{k_m}} F(\underline{0}) \\
 &= \sum_{\gamma_1, \dots, \gamma_m \in GF(p^n)} [F(\underline{0}) - F(0, \dots, 0, \gamma_m) - \dots - F(\gamma_1, 0, \dots, 0) \\
 &\quad + F(0, \dots, 0, \gamma_{m-1}, \gamma_m) + \dots + F(\gamma_1, \gamma_2, 0, \dots, 0) - \dots * F(\gamma_1, \dots, \gamma_m)] \gamma_1^{-k_1} \dots \gamma_m^{-k_m}
 \end{aligned} \tag{6}$$

and

$$\Delta_{x_1^{i_1} \dots x_{i_p}^{i_p}} F(\underline{0}) = \Delta_{x_1^{i_1} \dots x_{i_{p-1}}^{i_{p-1}}} \left[\Delta_{x_{i_p}^{i_p}} F(\underline{0}) \right] \text{ for } p = 1, 2, \dots, m$$

where the asterisk represents “-” if m is odd and “+” otherwise. The function $F(x_1, \dots, x_m)$ has the following “power series” expansion:

$$\begin{aligned}
 F(x_1, \dots, x_m) &= F(\underline{0}) + \left[\Delta_{x_1} F(\underline{0}) \right] x_1 + \dots + \left[\Delta_{x_m} F(\underline{0}) \right] x_m \\
 &\quad + \left[\Delta_{x_1^2} F(\underline{0}) \right] x_1^2 + \dots + \left[\Delta_{x_m^2} F(\underline{0}) \right] x_m^2 + \dots + \left[\Delta_{x_m^q} F(\underline{0}) \right] x_m^q \\
 &\quad + \left[\Delta_{x_1 x_2}^{(2)} F(\underline{0}) \right] x_1 x_2 + \dots + \left[\Delta_{x_{m-1} x_m}^{(2)} F(\underline{0}) \right] x_{m-1}^q x_m^q \\
 &\quad + \left[\Delta_{x_1 \dots x_m}^{(m)} F(\underline{0}) \right] x_1 \dots x_m + \dots + \left[\Delta_{x_1^q \dots x_m^q}^{(m)} F(\underline{0}) \right] x_1^q \dots x_m^q
 \end{aligned} \tag{7}$$

Proof: We shall prove this theorem by an induction on m , the number of variables. The case $m = 1$ has already been established in Theorem 1. Assume now that Eq. (7) is true for all integers $k \leq m$ and consider the expansion of $F(x_1, \dots, x_m, x_{m+1})$ with respect to its first m variables. By the induction hypothesis,

$$\begin{aligned}
 F(x_1, \dots, x_m, x_{m+1}) &= F(\underline{0}, x_{m+1}) \\
 &\quad + \left[\Delta_{x_1} F(\underline{0}, x_{m+1}) \right] x_1 + \dots + \left[\Delta_{x_m} F(\underline{0}, x_{m+1}) \right] x_m^q \\
 &\quad + \dots + \left[\Delta_{x_1 x_2}^{(2)} F(\underline{0}, x_{m+1}) \right] x_1 x_2 + \dots + \left[\Delta_{x_{m-1} x_m}^{(2)} F(\underline{0}, x_{m+1}) \right] x_{m-1}^q x_m^q \\
 &\quad + \dots + \left[\Delta_{x_1 \dots x_m}^{(m)} F(\underline{0}, x_{m+1}) \right] x_1 \dots x_m + \dots + \left[\Delta_{x_1^q \dots x_m^q}^{(m)} F(\underline{0}, x_{m+1}) \right] x_1^q \dots x_m^q
 \end{aligned} \tag{8}$$

But $\Delta^{(p)} \cdot F(\underline{0}, x_{m+1})$ is a mapping of $GF(p^n) \rightarrow GF(p^n)$ for $p = 0, 1, \dots, m$. Hence, Eq. (3) can be used to compute

$$\begin{aligned} x_{i_1}^{k_{i_1}} \dots x_{i_p}^{k_{i_p}} \Delta^{(p)} F(\underline{0}, x_{m+1}) &= x_{i_1}^{k_{i_1}} \dots x_{i_p}^{k_{i_p}} \Delta^{(p)} F(\underline{0}, 0) \\ &+ \sum_{k_{m+1}=1}^q \left[\Delta_{x_{m+1}^{k_{m+1}}} \left[x_{i_1}^{k_{i_1}} \dots x_{i_p}^{k_{i_p}} \Delta^{(p)} F(\underline{0}, 0) \right] \right] x_{m+1}^{k_{m+1}} \\ &= x_{i_1}^{k_{i_1}} \dots x_{i_p}^{k_{i_p}} \Delta^{(p)} F(\underline{0}, 0) + \sum_{k_{m+1}=1}^q \left[x_{i_1}^{k_{i_1}} \dots x_{i_p}^{k_{i_p}} \Delta^{(p+1)} F(\underline{0}, 0) \right] x_{m+1}^{k_{m+1}} \end{aligned} \quad (9)$$

For example,

$$\Delta^{(0)} F(\underline{0}, x_{m+1}) = \Delta^{(0)} F(\underline{0}, 0) + \sum_{k_{m+1}=1}^q \left[\Delta_{x_{m+1}^{k_{m+1}}}^{(1)} F(\underline{0}, 0) \right] x_{m+1}^{k_{m+1}}$$

or

$$F(\underline{0}, x_{m+1}) = F(\underline{0}, 0) + \sum_{k_{m+1}=1}^q \left[\Delta_{x_{m+1}^{k_{m+1}}} F(\underline{0}, 0) \right] x_{m+1}^{k_{m+1}}$$

Similarly,

$$x_{i_1}^{k_{i_1}} \Delta^{(1)} F(\underline{0}, x_{m+1}) = x_{i_1}^{k_{i_1}} \Delta^{(1)} F(\underline{0}, 0) + \sum_{k_{m+1}=1}^q \left[x_{i_1}^{k_{i_1}} \Delta_{x_{m+1}^{k_{m+1}}}^{(2)} F(\underline{0}, 0) \right] x_{m+1}^{k_{m+1}}$$

and so on. Substituting Eq. (9) into Eq. (8) yields

$$\begin{aligned} F(x_1, \dots, x_m, x_{m+1}) &= F(\underline{0}, 0) + \sum_{k_{m+1}=1}^q \left[\Delta_{x_{m+1}^{k_{m+1}}} F(\underline{0}, 0) \right] x_{m+1}^{k_{m+1}} \\ &+ \left[\Delta_{x_1} F(\underline{0}, 0) + \sum_{k_{m+1}=1}^q \left[x_1 \Delta_{x_{m+1}^{k_{m+1}}}^{(2)} F(\underline{0}, 0) \right] x_{m+1}^{k_{m+1}} \right] x_1 \\ &+ \dots + \left[\Delta_{x_m^q} F(\underline{0}, 0) + \sum_{k_{m+1}=1}^q \left[x_m^q \Delta_{x_{m+1}^{k_{m+1}}}^{(2)} F(\underline{0}, 0) \right] x_{m+1}^{k_{m+1}} \right] x_m^q \\ &+ \dots + \left[\Delta_{x_{m-1}^q x_m^q} F(\underline{0}, 0) + \sum_{k_{m+1}=1}^q \left[x_{m-1}^q x_m^q \Delta_{x_{m+1}^{k_{m+1}}}^{(3)} F(\underline{0}, 0) \right] x_{m+1}^{k_{m+1}} \right] x_{m-1}^q x_m^q \\ &+ \dots + \left[\Delta_{x_1^q \dots x_m^q} F(\underline{0}, 0) + \sum_{k_{m+1}=1}^q \left[x_1^q \dots x_m^q \Delta_{x_{m+1}^{k_{m+1}}}^{(m+1)} F(\underline{0}, 0) \right] x_{m+1}^{k_{m+1}} \right] x_1^q \dots x_m^q \end{aligned}$$

and the induction is complete. The uniqueness of f follows from the fact that the total number of possible functions F is $(p^n)^{(p^n)^m}$, which is exactly the total number of possible functions f .

The existence of Eq. (5) has long been known (Refs. 2, 6, 9, 10) but not the expansion given in Eq. (6). The canonical expansion of Theorem 2 generalizes to Galois field $GF(p^n)$ a result previously formed over $GF(2^n)$ (Ref. 3).

Theorem 2, which includes Theorem 1, provides a general means of synthesizing Galois switching functions for multiple-valued logics. For example, logic elements having three-level input and three-level output voltages (Ref. 11) can be used to implement Galois switching functions in the field $GF(3^n)$. Though most studies of logic design in the past have been for the binary-valued logic, the advent of Theorems 1 and 2 may change this.

For continuity of presentation, illustrative examples, using Theorem 2, will be postponed to the next section. From Theorem 2 one can now give a formal definition of Galois switching functions.

Definition 1: A Galois switching function F of m variables v_1, \dots, v_m over field $GF(p^n)$ is a rule that associates every m -tuple of valued input variables (v_1, \dots, v_m) with an m' -tuple of valued output variables $(z_1, \dots, z_{m'})$ over field $GF(p^n)$:

$$F: GF(p^n)^m \rightarrow GF(p^n)^{m'}$$

Mathematically, a Galois switching function describes the logic performance of a "combinational" switching circuit with m input terminals v_1, \dots, v_m and m' output terminals $z_1, \dots, z_{m'}$.

If a parametrization of a function is the function obtained by replacing a subset of its variables with constants, then we can further state a more general definition of Galois functions.

Definition 2: Let $\underline{v} = (v_0, v_1, \dots, v_{m-1})$ be a sequence of length m and $\underline{f} = (f_0, f_1, \dots, f_{(p^n)^m-1})$ be a sequence of length $(p^n)^m$. A universal Galois function for \underline{v} is a Galois function $U(\underline{v}, \underline{f})$ such that each of the $(p^n)^m$ functions of \underline{v} appears exactly once among the various parametrizations of U obtained by replacing \underline{f} by a sequence of Galois field constants. (The active variables of $U(\underline{v}, \underline{f})$ are \underline{v} , while its selection variables are \underline{f} .) In other words, there exists a sequence $\underline{a} = (a_0, a_1, \dots, a_{(p^n)^m-1})$ of field elements for each function $F: [GF(p^n)]^{|v|} \rightarrow GF(p^n)$, such that

$$F(\underline{v}) = U(\underline{v}, \underline{a})$$

where $|v|$ is the length of v .

On the other hand, a general polynomial is defined as follows:

Definition 3: A general polynomial in m variables of length $\underline{q} = (q_0, \dots, q_{m-1})$ is the sum of all terms

$$a_{i_0 \dots i_{m-1}} v_0^{i_0} \dots v_{m-1}^{i_{m-1}}$$

where $0 \leq i_0 \leq q_0, \dots, 0 \leq i_{m-1} \leq q_{m-1}$:

$$\sum_{i_{m-1}=0}^{q_{m-1}-1} \dots \sum_{i_0=0}^{q_0-1} a_{i_0 \dots i_{m-1}} v_0^{i_0} \dots v_{m-1}^{i_{m-1}}$$

For example, a general polynomial in two variables of length $2^2 = (2^2, 2^2)$ is of the form:

$$\begin{aligned} \sum_{i_1=0}^3 \sum_{i_0=0}^3 a_{i_0 i_1} v_0^{i_0} v_1^{i_1} &= a_{00} + a_{01} v_1 + a_{02} v_1^2 + a_{03} v_1^3 \\ &+ a_{10} v_0 + a_{11} v_0 v_1 + a_{12} v_0 v_1^2 + a_{13} v_0 v_1^3 \\ &+ \dots + a_{20} v_0^2 + a_{21} v_0^2 v_1 + a_{22} v_0^2 v_1^2 + a_{23} v_0^2 v_1^3 \end{aligned}$$

Definition 4: A universal polynomial over field $GF(p^n)$ in m variables, each of which has length p^n , is a general polynomial of length (p^n, \dots, p^n) .

From the above definitions and Theorem 2, Corollary 1 is immediate.

Corollary 1: If the polynomial expansion is implemented in hardware such that the p^m coefficients are left unspecified, and in fact treated as the other m inputs, then such an implementation is "universal" in the sense that it can simulate any given m -argument function. It is necessary only to supply the correct values to the coefficient inputs and these values are obtainable from Eq. (6) of Theorem 2.

III. Applications

We now give an example to show how Theorem 2 can be used to find Galois switching functions for multiple-valued logic. The computational procedures will be shown explicitly. Then, Galois switching functions for realizing conventional binary-valued logic are provided to illustrate the possible varieties of the logic design using Galois field theory.

Example 1: Consider the four-input two-output specification given in Table 2. Integers 0, 1, and 2 represent three signal levels of certain three-valued logic elements. We would like to derive the Galois switching function over field $GF(3^2)$ for this truth table.

The addition and multiplication tables for $GF(3^2)$ are described in Table 1 (a derivation for obtaining these tables is discussed in Ref. 5). The truth values given in Table 2 can be realized as a two-variable input, one-variable output function by the following partition:

$$x_1 = \{u_1, u_2\}; x_2 = \{u_3, u_4\}; F = \{v_1, v_2\}$$

Representing the field elements as

$$0 = 00, 1 = \alpha^0 = 10, \alpha^1 = 01, \alpha^2 = 12, \alpha^3 = 22, \alpha^4 = 20, \alpha^5 = 20, \alpha^6 = 21, \alpha^7 = 11$$

a truth table in terms of 0, 1, and α^i can be derived from Table 2.

The Galois switching function over field $GF(3^2)$ representing the truth values of Table 2 is derivable from Theorem 2. Utilizing the field operations of Table 1, some of the computations are given as follows:

$$f(0, 0) = F(0, 0)$$

$$\begin{aligned} f(1, 0) &= \sum_{\alpha \in GF(3^2)} [F(0, 0) - F(\gamma_1, 0)] \gamma_1^{-1} \\ &= -\alpha \cdot 1 - \alpha^2 \cdot \alpha^7 - \alpha^3 \cdot \alpha^6 - \alpha^4 \cdot \alpha^5 - \alpha^5 \cdot \alpha^4 - \alpha^6 \cdot \alpha^3 - \alpha^7 \cdot \alpha^2 - 1 \cdot \alpha = \alpha \end{aligned}$$

$$\begin{aligned} f(0, 3) &= \sum_{\alpha \in GF(3^2)} [F(0, 0) - F(0, \gamma_2)] \gamma_2^{-3} \\ &= -1 - 1 - 1 - 1 - 1 - 1 - 1 - 1 - 1 = 1 \end{aligned}$$

$$f(1, 1) = \sum_{\alpha \in GF(3^2)} \sum_{\beta \in GF(3^2)} [F(0, 0) - F(0, \gamma_2) - F(\gamma_1, 0) + F(\gamma_1, \gamma_2)] \gamma_1^{-1} \gamma_2^{-1} = 1$$

Computations of this sort reveal that $f(5, 7) = f(8, 8) = 1$, and the remaining 75 functions f are all zero. Hence, the desired Galois switching function is of the form:

$$F(x_1, x_2) = \alpha x_1 + x_2^3 + x_1 x_2 + x_1^5 x_2^7 + x_1^2 x_2^8 \quad (10)$$

The fact that $F(x_1, x_2)$ realizes the truth values of Table 2 can be verified by direct substitution.

The above shows how three-voltage-level logic elements might be used to implement the truth values given in Table 2. If one had Galois PLUS and TIMES gates that were capable of performing the field operations given in Table 1, Eq. (10) could be implemented with only a few gates of these types.

Since most of present day logic elements are binary-valued type, we now provide more carefully an application of Theorem 2 in this regard.

Example 2: Consider the output table of a six-input two-output binary variable function given in Table 3 (Ref. 3). For economy of space, both the binary inputs and outputs of Table 3 are described by their decimal integer representations. The input of an output in row $n = i$ can be determined by substituting i for n in the expression given in the column of that output. For example, the input of the output 3 in row $n = 5$ and column $n + 16$ is 21. Thus, the binary output of the input 21, $u_1u_2u_3u_4u_5u_6 = 010101$, is $F_1F_2 = 11$. Similarly, the binary output of the input 10, $u_1u_2u_3u_4u_5u_6 = 001010$, is $F_1F_2 = 10$. These two outputs are encircled as shown in Table 3.

Employing either the Karnaugh map method or the Quine-McCluskey method, the minimal logical equations of the above output table are found to be as follows:

$$\begin{aligned}
 F_1(u_1, u_2, u_3, u_4, u_5, u_6) &= u_3u_4\bar{u}_6 + \bar{u}_3u_5u_6 + \bar{u}_1\bar{u}_2\bar{u}_3\bar{u}_4 + u_1\bar{u}_2\bar{u}_3u_4 \\
 &\quad + \bar{u}_1\bar{u}_2\bar{u}_6\bar{u}_0 + u_1\bar{u}_2\bar{u}_6u_0 + u_1u_2\bar{u}_3u_5 + u_1u_2u_3\bar{u}_5 \\
 &\quad + \bar{u}_1u_2\bar{u}_3u_4u_0 + \bar{u}_1\bar{u}_3\bar{u}_4\bar{u}_5\bar{u}_0 + \bar{u}_2u_3\bar{u}_4u_5\bar{u}_0 \\
 F_2(u_1, u_2, u_3, u_4, u_5, u_6) &= u_3u_4\bar{u}_0 + \bar{u}_4u_5u_0 + \bar{u}_1\bar{u}_2\bar{u}_3\bar{u}_4 \\
 &\quad + \bar{u}_1u_2u_3\bar{u}_4 + u_1u_2\bar{u}_4u_0 + u_1u_2u_4\bar{u}_0 \\
 &\quad + \bar{u}_1\bar{u}_2\bar{u}_6\bar{u}_0 + \bar{u}_1u_2u_5\bar{u}_0 + u_1\bar{u}_2u_3\bar{u}_4u_5 \\
 &\quad + \bar{u}_1\bar{u}_3u_4\bar{u}_5u_0 + \bar{u}_2\bar{u}_3\bar{u}_4\bar{u}_5\bar{u}_0
 \end{aligned}$$

where each $+$ denotes an OR operation.

These two logical equations can be implemented with 22 AND gates and 2 OR gates.

Now, either by Theorem 2 or by direct expansion, the Reed-Muller expansions of F_1 and F_2 are of the forms:

$$\begin{aligned}
 F_1(u_1, u_2, u_3, u_4, u_5, u_6) &= 1 \oplus u_1 \oplus u_1u_4 \oplus u_1u_6 \oplus u_2u_3 \oplus u_2u_4 \oplus u_2u_5 \oplus u_2u_6 \\
 &\quad \oplus u_3u_6 \oplus u_4u_5 \oplus u_4u_0 \oplus u_1u_3u_5 \oplus u_1u_3u_0 \oplus u_1u_4u_5 \\
 &\quad \oplus u_2u_3u_5 \oplus u_2u_4u_0 \\
 F_2(u_1, u_2, u_3, u_4, u_5, u_6) &= 1 \oplus u_2 \oplus u_1u_3 \oplus u_1u_4 \oplus u_1u_5 \oplus u_1u_0 \oplus u_2u_3 \oplus u_2u_5 \\
 &\quad \oplus u_3u_5 \oplus u_3u_0 \oplus u_4u_5 \oplus u_1u_3u_5 \oplus u_1u_4u_0 \oplus u_2u_3u_0 \\
 &\quad \oplus u_2u_4u_5 \oplus u_2u_4u_0
 \end{aligned}$$

where each \oplus denotes an EXCLUSIVE-OR operation. Note that in $GF(2)$, $+$ is commonly written as \oplus . Implementation of these expressions requires 20 AND gates and 2 sixteen-input EXCLUSIVE-OR gates.

Table 3 can be realized with far fewer basic gates over the field $GF(2^n)$ in the following manner. Let the input and output variables be partitioned as:

$$x_1 = \{u_1, u_2\}; x_2 = \{u_3, u_4\}; x_3 = \{u_5, u_6\}$$

and

$$F = \{F_1, F_2\}$$

Using the representation $GF(2^3) = \{0, 1, \alpha, \alpha^2\} = \{00, 11, 01, 10\}$ and Theorem 2, the Galois logic equation for the function F is derived to be:

$$F(x_1, x_2, x_3) = 1 + x_1 + x_1x_2 + x_1x_3 + x_2x_3 + x_1x_2x_3$$

Note that when $p = 2$, we have the identity: $- \equiv +$.

Two realizations of F are given in Fig. 1. If these Galois gates are comparable in cost with Boolean gates, F can be realized economically.

Examples showing more drastic savings of hardware may be found in Ref. 3.

It was shown in Ref. 3 that realizations of these types are also useful from the fault diagnostic point of view. One weak point about such a method is that it may create large delay time; this may be an important factor in certain systems. In spite of this fact, Theorem 2 can be considered as a systematic method for deriving multilevel logic networks, an alternative approach to the conventional methods—the Karnaugh map method and the Quine-McCluskey method.

IV. Points of Attraction

The following are a few points of attraction for using Galois field theory in logic design (Ref. 3).

- (1) Galois theory offers a wider choice of basic logic gates, and conceptually it can be adapted to suit each stage of an architectural development (Ref. 10).
- (2) In constructing an electronic encoder for the Bose-Chaudhuri-Hocquenghem code, Bartee and Schneider (Ref. 5) found that the decoding procedure could be economically implemented by designing the arithmetic unit based on Galois field operations.
- (3) Similar requirements for Galois field arithmetic circuits have arisen in applications of linear recurring sequences to space object tracking.
- (4) Networks derived from the concept of Galois field theory are usually composed of multioutput gates that are suitable for integrated circuit fabrication (Ref. 2).
- (5) The realization of switching functions by modular algebra has been shown to be less complex than by Post algebra (Ref. 10). When m is prime, the modulo m number system forms a finite field. For this case, its application to multiple-valued logic is promising. Example 1 illustrates this fact.
- (6) The circuit derived from Galois field theory possesses many properties that are suitable for fault diagnosis.
- (7) Conceivably, Galois logic may play an important role in telephone networks or networks of a similar nature. Specifically, each multiwire cable or bundle may be considered as a Galois variable that can assume many values.

V. Conclusion

A previously given polynomial expansion technique for single-variable functions is recognized to contain a generalized Boolean difference from which a polynomial expansion for multivariable functions is derived. The expansion is then applied to the synthesis of switching functions using multioutput blocks called PLUS and TIMES gates. This application indicates that by employing an appropriate size of the domain and a suitable representation for the elements in that domain, the synthesis of switching functions can be accomplished economically.

The amount of tedious computation required in the above application also suggests the need for good computer programs. Such programs will enable one to select an appropriate size and assignment suitable for each individual synthesis. For a given truth table having m -variable inputs and n -variable outputs, $m \geq n$, one tends to select the size of the field according to m . This would create "don't care" conditions. Whether such a selection is beneficial or not is also a subject of further research.

References

1. Reed, I. S., "A Class of Multiple-Error-Correcting Codes and the Coding Scheme," *IRE Trans. on Inf. Theory*, IT-4, Sept. 1954, pp. 38-49.
2. Menger, K. S., Jr., "A Transform for Logic Networks," *IEEE Trans. on Computers*, C-18, March 1969, pp. 241-251.
3. Benjauthrit, B., *Design and Diagnosis of Galois Logic Networks*, Ph.D. Dissertation, University of Southern California, Los Angeles, California, June 1974.
4. Lechner, R. J., "Harmonic Analysis of Switching Functions," in *Recent Developments in Switching Theory*, A. Mukhopadhyay (ed.), Academic Press, Inc., New York, 1971, pp. 121-225.
5. Bartee, T. C., and Schneider, D. I., "Computation with Finite Fields," *Inf. and Control*, Vol. 6, June 1963, pp. 79-98.
6. Van der Waerden, B. L., *Algebra*, Vol. 1, Federick Unger Publishing, 1966.
7. Reed, I. S., and Solomon, G., *A Decoding Procedure for Polynomial Codes*, Group Report 47.24, Lincoln Lab., MIT, March 1959, pp. 1-6.
8. Edwards, R. W., *Algebraic Synthesis of Switching Networks*, Stanford Electronics Lab. Tech. Report No. 2205-1, April 1963.
9. Ellison, J. T., and Kolman, B., *Galois Logic Design*, Univac Division of Sperry Rand Corp., Final Report No. AD717205, Oct. 1970.
10. Pradhan, D. K., and Patel, A. M., "Muller Like Canonic Form for Multiple Multi-Valued Functions," *Corres. IEEE Trans. on Comp.*, Feb. 1975, pp. 206-210.
11. Epstein, G., et al., "Multiple-Valued Logic Design and Applications," 1971 Symposium on Multi-Valued Logic Design, Buffalo, N. Y.
12. Berlekamp, E. R., *Algebraic Coding Theory*, McGraw-Hill Book Co., 1968.

Table 1. Field operations

Addition defined for field $GF(3^2)$										Multiplication defined for field $GF(3^2)$									
+	0	1	α	α^2	α^3	α^4	α^5	α^6	α^7	*	0	1	α	α^2	α^3	α^4	α^5	α^6	α^7
0	0	1	α	α^2	α^3	α^4	α^5	α^6	α^7	0	0	0	0	0	0	0	0	0	0
1	1	α^4	α^7	α^3	α^5	0	α^2	α	α^6	1	0	1	α	α^2	α^3	α^4	α^5	α^6	α^7
α	α	α^7	α^5	1	α^4	α^0	0	α^3	α^2	α	0	α	α^2	α^3	α^4	α^5	α^6	α^7	1
α^2	α^2	α^3	1	α^6	α	α^5	α^7	0	α^4	α^2	0	α^2	α^3	α^4	α^5	α^6	α^7	1	α
α^3	α^3	α^5	α^4	α	α^7	α^2	α^0	1	0	α^3	0	α^3	α^4	α^5	α^0	α^7	1	α	α^2
α^4	α^4	0	α^0	α^5	α^2	1	α^3	α^7	α	α^4	0	α^4	α^5	α^0	α^7	1	α	α^2	α^3
α^5	α^5	α^2	0	α^7	α^0	α^3	α	α^4	1	α^5	0	α^5	α^6	α^7	1	α	α^2	α^3	α^4
α^6	α^6	α	α^3	0	1	α^7	α^4	α^2	α^5	α^6	0	α^6	α^7	1	α	α^2	α^3	α^4	α^5
α^7	α^7	α^6	α^2	α^4	0	α	1	α^5	α^3	α^7	0	α^7	1	α	α^2	α^3	α^4	α^5	α^6

Table 2. An input-output truth table

u_1	u_2	u_3	u_4	v_1	v_2	u_1	u_2	u_3	u_4	v_1	v_2	u_1	u_2	u_3	u_4	v_1	v_2
0	0	0	0	0	0	1	0	0	0	0	1	2	0	0	0	0	2
0	0	0	1	2	2	1	0	0	1	1	2	2	0	0	1	2	2
0	0	0	2	1	1	1	0	0	2	1	0	2	0	0	2	0	2
0	0	1	0	1	0	1	0	1	0	1	1	2	0	1	0	0	2
0	0	1	1	0	2	1	0	1	1	2	2	2	0	1	1	0	2
0	0	1	2	2	1	1	0	1	2	0	2	2	0	1	2	0	0
0	0	2	0	2	0	1	0	2	0	1	1	2	0	2	0	2	2
0	0	2	1	1	2	1	0	2	1	2	0	2	0	2	1	2	1
0	0	2	2	0	1	1	0	2	2	0	0	2	0	2	2	2	2
0	1	0	0	1	2	1	1	0	0	1	0	2	1	0	0	1	1
0	1	0	1	1	0	1	1	0	1	0	1	2	1	0	1	2	0
0	1	0	2	0	1	1	1	0	2	1	2	2	1	0	2	2	2
0	1	1	0	0	2	1	1	1	0	0	0	2	1	1	0	1	0
0	1	1	1	2	2	1	1	1	1	0	0	2	1	1	1	0	0
0	1	1	2	2	1	1	1	1	2	1	0	2	1	1	2	1	2
0	1	2	0	1	2	1	1	2	0	1	0	2	1	2	0	0	2
0	1	2	1	2	0	1	1	2	1	0	0	2	1	2	1	0	0
0	1	2	2	2	2	1	1	2	2	1	0	2	1	2	2	1	2
0	2	0	0	2	1	1	2	0	0	2	2	2	2	0	0	2	0
0	2	0	1	2	1	1	2	0	1	1	1	2	2	0	1	0	0
0	2	0	2	1	1	1	2	0	2	2	0	2	2	0	2	0	0
0	2	1	0	1	1	1	2	1	0	0	0	2	2	1	0	1	0
0	2	1	1	0	2	1	2	1	1	2	1	2	2	1	1	2	1
0	2	1	2	1	1	1	2	1	2	2	0	2	2	1	2	2	2
0	2	2	0	2	1	1	2	2	0	0	1	2	2	2	0	2	0
0	2	2	1	2	1	1	2	2	1	1	1	2	2	2	1	1	1
0	2	2	2	0	0	1	2	2	2	1	0	2	2	2	2	1	2

Table 3. Truth value table for a six-input two-output binary variable function

Input n	$n + 0$	$n + 8$	$n + 16$	$n + 24$	$n + 32$	$n + 40$	$n + 48$	$n + 56$
$u_1 u_2 u_3 u_4 u_5 u_6$	$F_1 F_2$							
0	3	3	2	1	1	0	0	2
1	3	0	0	1	2	2	1	3
2	3	(2)	1	1	0	3	2	0
3	3	1	3	1	3	1	3	1
4	3	3	0	3	2	3	1	3
5	1	2	(3)	2	2	2	0	2
6	0	1	1	1	2	1	3	1
7	2	0	2	0	2	0	2	0
Output								

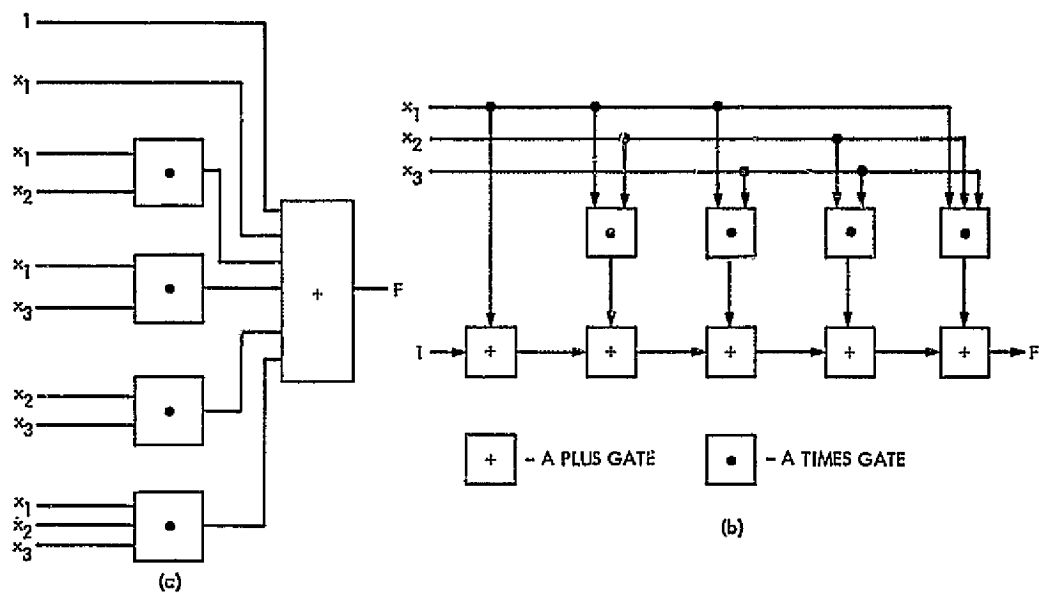


Fig. 1. Two realizations of F

ORIGINAL PAGE IS
OF POOR QUALITY

The Superior Conjunction of Mariner 10

R. M. Goldstein

Communications Systems Research Section

C. T. Stelzried

Communications Elements Research Section

The radio signals from the Mariner 10 spacecraft have been used to probe the turbulence of the north polar regions of the solar corona. Simultaneous bandwidth observations of both S- and X-band were made with a resolution of approximately 0.20 Hz during the period of May 30 to June 26, 1974, from the 64-m antenna at the Mars Deep Space Station in the Goldstone Deep Space Communications Complex.

A mathematical model is given to relate the S- and X-band spectra. It was not possible to successfully correlate the spectra with solar observations such as solar flares, solar active regions and Orbiting Solar Observatory (OSO)-7 white light coronagraph data. The bandwidths are generally narrower than previous observations but seem consistent with the reduced solar activity during this period of the solar cycle.

1. Introduction

The telemetry signals transmitted from Mariner 10 to Earth passed through the solar corona during observations taken from May 30 to June 26, 1974. Figure 1 shows a projection of the ray path intercept on a plane perpendicular to the Sun-Earth line. As the Earth-spacecraft line-of-sight approached the Sun, the downlink telemetry carrier signals, transmitted simultaneously and coherently at S- and X-bands passed through increasingly denser regions of the solar corona.

The 64-m-diam antenna of the Goldstone DSCC was used for transmitting S-band (2115 MHz) to and receiving S-band (2295 MHz) and X-band (8415 MHz) from the spacecraft for these two-way measurements. The antenna has a beamwidth of 0.14 deg at S-band and 0.040 deg at X-band. A simplified block diagram of the experiment is shown in Fig. 2. The antenna feed system is capable of simultaneous S- and X-band reception (Ref. 1). The receivers utilize separate S- and X-band masers, mixers and amplifiers which feed the computer. The computer has the capability of simultaneously computing both the S-

and X-band signal spectrograms. These data are displayed on an x-y plotter in real time and stored on magnetic tape for further processing.

II. Data

The primary data from our observations are power spectrograms of the S- and X-band carriers. The signals were sampled digitally and converted into power spectra by the discrete Fourier transform. One hundred sample pairs (in phase quadrature) per second were taken. Each spectrum was formed of 512 sample pairs, thus taking 5.12 seconds to complete, and yielding 0.195 Hz resolution.

In order to reduce the fluctuations of the result, we averaged together sets of 120 spectra. Representatives of such spectra for each of the days of observations are reproduced in Fig. 3. In every case, the X-band spectrum was the widest. The curves have all been normalized to unit height.

We have processed these spectrograms to provide three quantities of interest: area under each curve, bandwidths of the spectra, and center frequency of each.

III. Signal Power

Area, when the normalization is removed, represents received signal power. The resulting power estimates for each day are given in Fig. 4, where power is plotted against the Sun-Earth-Mariner 10 angle. Normalization of the spectrograms was with respect to background noise level, and its removal introduced most of the errors in the power estimates. Since the antenna was necessarily aimed close to the sun, minor sidelobes would cause the background noise level to vary erratically. It appears from Fig. 4 that the presence of the solar corona in the ray path did not influence the received power significantly, for either S- or X-band signals.

IV. Bandwidth

It can be seen from Fig. 3 that the bandwidths of the signals, and hence the turbulence of the solar corona, change with angular distance of the ray path to the Sun. Our measure of bandwidth is that central frequency interval which contains half of the received power.

This measure is plotted in Fig. 5, also against angular distance to the Sun. The bandwidth is seen to be a strong

inverse function of solar distance, rising sharply between 7 and 6 solar radii. The scatter of the points is not caused by systematic effects, but by the erratic nature of the corona itself. A circularly symmetric model of the corona will not fit the data.

An attempt has been made to correlate the bandwidth measurements with other observations of solar activity and coronal structure. These included flares, solar active regions and OSO-7 white light coronagraph observations. The large day-to-day variations in the bandwidth data could not be identified with any of these observations. The bandwidths measured for the Mariner 10 solar conjunction were substantially less than those measured at corresponding ray offsets for previous solar conjunction experiments such as Mariner 4, Pioneer 6 (Ref. 2), Mariner 9 and Pioneer 10. The Mariner 10 observations were taken very near to the solar cycle activity minimum while Mariner 4 was in the rising portion, Pioneer 6 was near the maximum, and both Mariner 9 and Pioneer 10 were on the declining portion. Since the solar activity during this period of the solar cycle, and in particular during the Mariner 10 observations, was largely confined to the low latitude regions while Mariner 10 probed the relatively quiet north polar region, it is not surprising that the observed bandwidths were generally narrower than those previously reported.

System tests have shown that the stability of the transmitter-programmable local oscillator-spectrum analyzer combination is generally better than 0.1 Hz. The resolution cell of the spectrum analyzer was greater than this. The data point at 13.6 solar radii still shows some influence from the corona.

Since the phase shift induced in a signal by propagation through plasma is inversely proportional to frequency, one might question the greater bandwidths of the X-band signals. We account for this phenomenon as follows:

The uplink signal passes through the solar corona and is thereby modulated in phase and amplitude. Only the phase modulation is retained by the phase-locked receiver on board Mariner 10. Figure 6 is a simplified block diagram of the system. $x(t)$ is a random signal representing the turbulence of the corona. $y(t)$ is retransmitted to Earth as the S-band signal. Simultaneously, $y(t)$ is frequency multiplied by 11/3 and transmitted to Earth as the X-band signal. We can show that the Fourier transform

$R_y(\tau)$ of the (baseband) spectrum of $y(t)$ is related to that of $z(t)$ by

$$R_z(\tau) = R_y^{n^2}(\tau) \quad (1)$$

It was not possible to observe $x(t)$ and $y(t)$ directly, but only through the corona. The effect of this complication is to change the value of the exponent, above.

Thus it should be possible to predict the X-band spectrum using only the S-band spectrum for data. Figure 7 is the result of our attempt. The S-band data from June 1 were processed according to Eq. 1, then retransformed and plotted for several values of the exponent. The actual received X-band spectrum is superimposed on the plot. It appears that this model adequately describes the broadening of the X-band spectrum.

V. Center Frequency

In order to hold the frequency of the signal centered in the receiver passband, automatic tuning was required. This removed the doppler shift caused by the motion of Mariner 10 relative to the Deep Space Station. The predictions were based on tracking data obtained over a 10-day period, May 11, 1974 through May 21, 1974, just after a trajectory adjusting rocket burn.

We have estimated the actual center frequency of the received signals as that frequency which splits the power into equal halves. The results are given in Fig. 8, where center frequency (estimated minus predicted) is plotted against date. As can be seen, the predictions were quite good, having only a small bias of about 2 Hz and, possibly, a small drift rate of about 0.02 Hz/day.

References

1. Howard, H. T., "Venus: Mass, Gravity Field, Atmosphere, and Ionosphere as Measured by the Mariner 10 Dual Frequency Radio System," *Science*, Vol. 183, p. 1297, Mar. 29, 1974.
2. Goldstein, R. M., "Superior Conjunction of Pioneer 6," *Science*, Vol. 166, Oct. 31, 1969, p. 598.

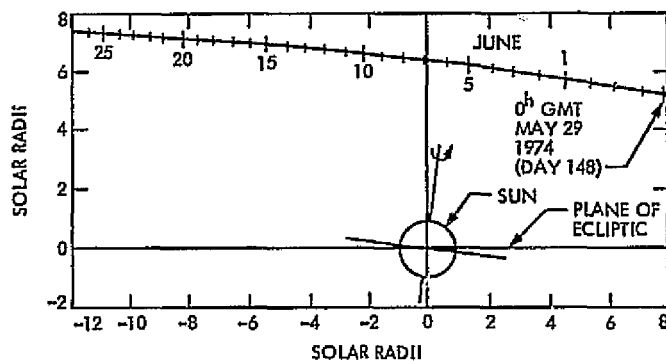


Fig 1. Plot of Mariner 10 to Earth signal ray path intercept on plane perpendicular to Earth Sun line

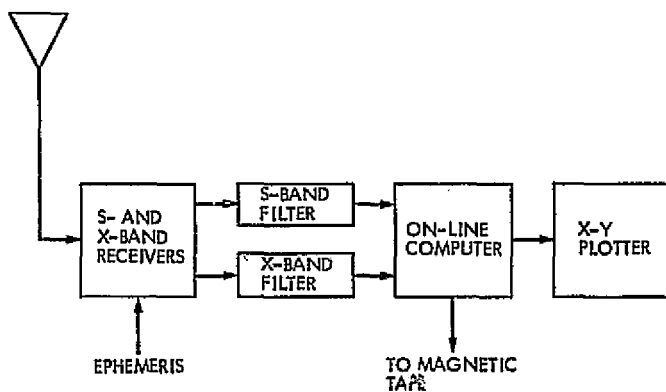


Fig. 2. Simplified block diagram of experimental system

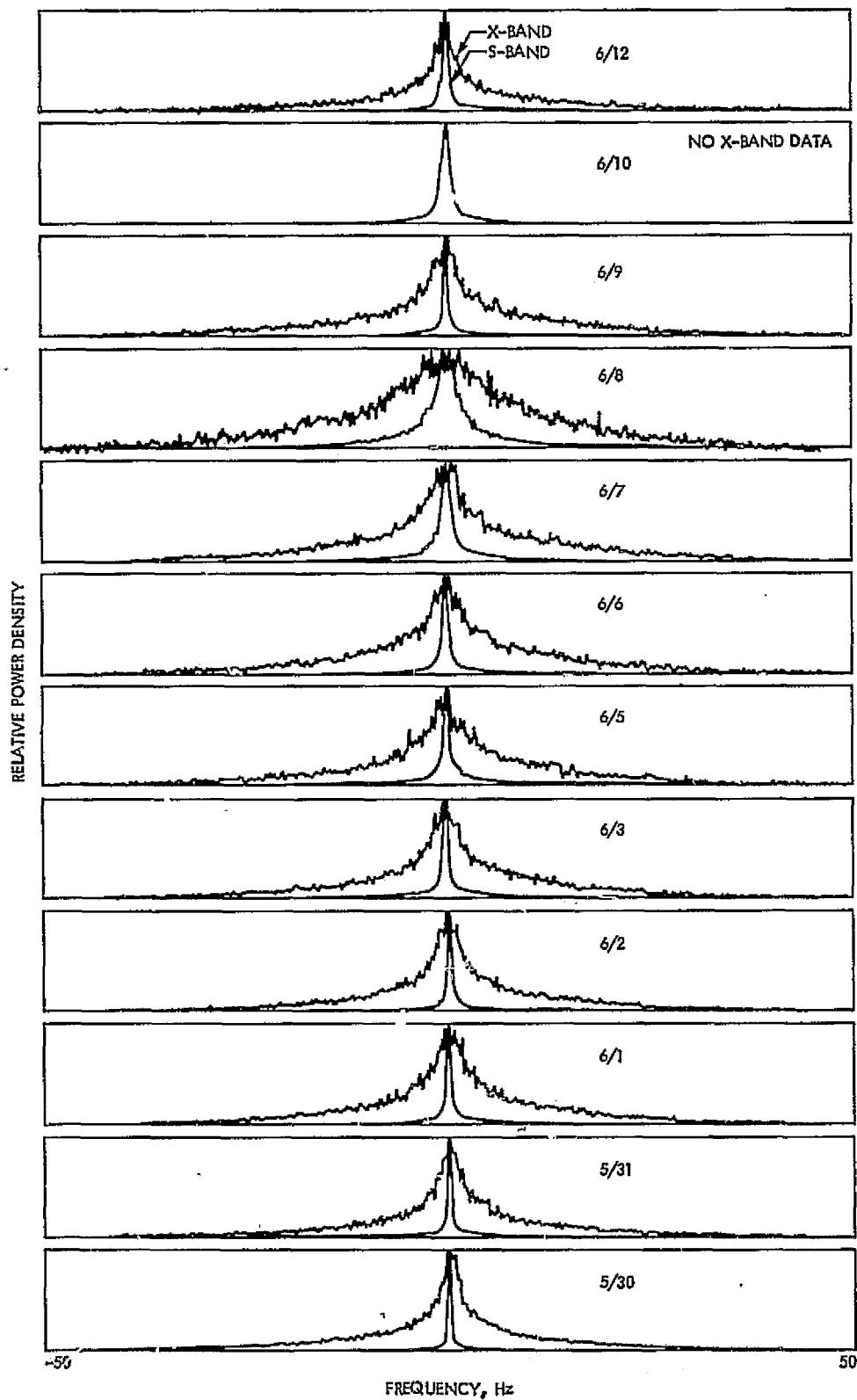


Fig. 3. Spectrograms for each day of observation. S- and X-band spectra are superposed, X always being the widest

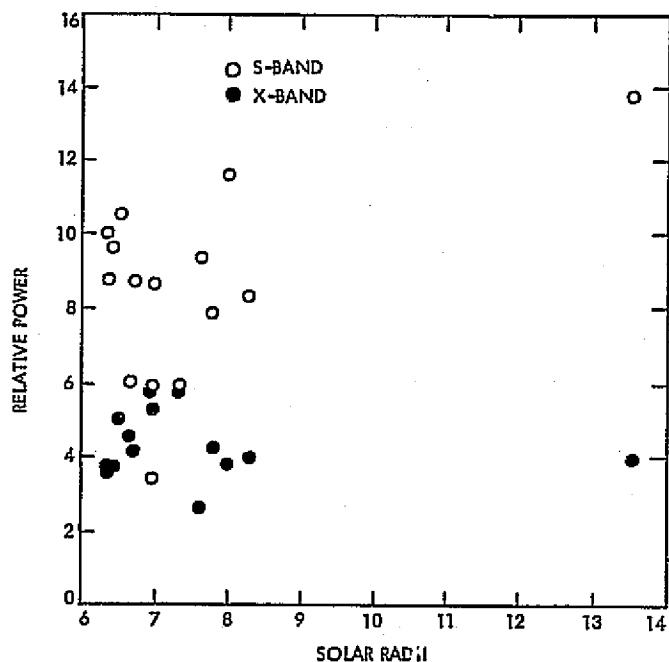


Fig. 4. Received S- and X-band power plotted against the Sun-Earth-Mariner 10 angle

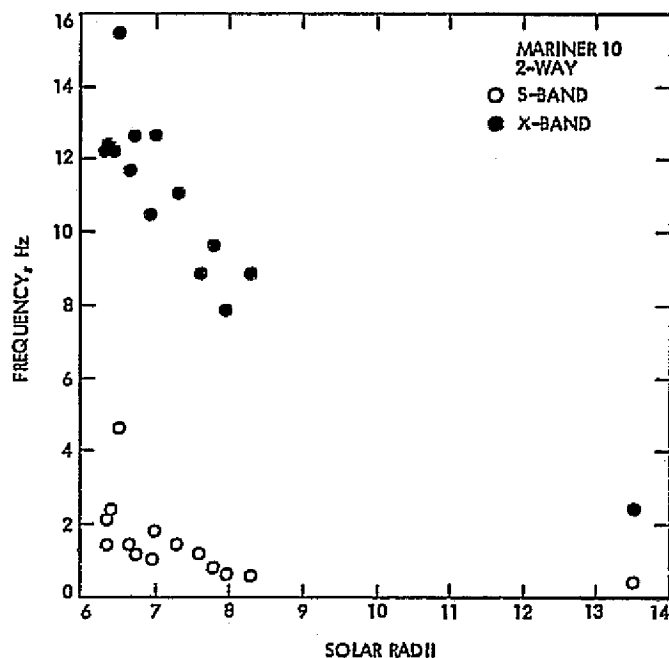


Fig. 5. Bandwidth of the received S- and X-band signals plotted against the Sun-Earth-Mariner 10 angle

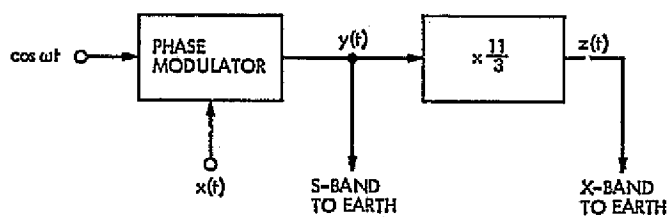


Fig. 6. Equivalent block diagram of corona-induced phase modulation

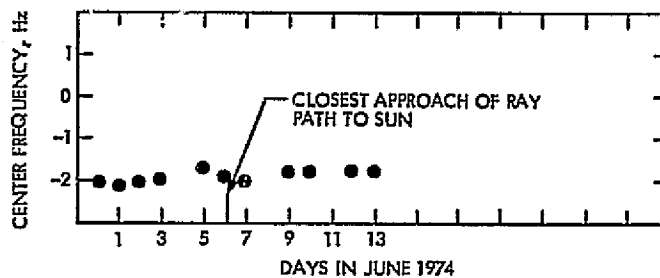


Fig. 8. Center frequency (estimated minus predicted) of the S-band signals as a function of time

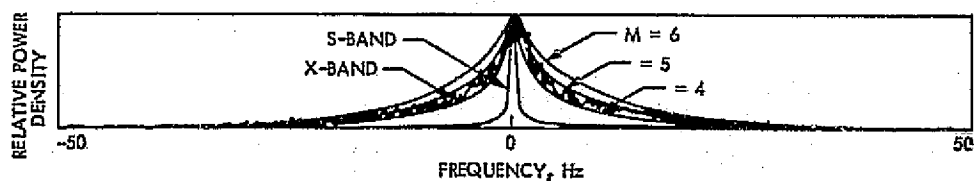


Fig. 7. X-band spectrogram plotted along with theoretical spectra derived from S-band data

S/X Band Experiment: Effect of Discontinuities on the Group Delay of a Microwave Transmission Line

R. W. Beatty¹
Consultant

T. Y. Otoshi
Communications Elements Research Section

The problem is considered of the effect of reflections from discontinuities at each end of a transmission line on the group delay at microwave frequencies. Previous work is briefly reviewed and a general analysis is made. Graphical data are presented based upon the formulas developed. Experimental results are given which confirm the theory.

I. Introduction

The effects of mismatch on the calculation and measurement of group delay or envelope delay have been investigated in the past because of the importance of delay distortion in transmission systems. In recent experiments with space probes, small variations in the delay of microwave signals have been measured in order to obtain data on planetary atmospheres and the distribution of

gaseous matter in space. Small errors in the determination of group delay have significant effects in these applications, and a need has arisen for a more thorough analysis to be carried out.

II. Background

As Lewin et al. (Ref. 1) explained in 1950, the effect of reflections from discontinuities is similar to the multipath problem (Ref. 2). A small portion of the energy traveling down the transmission line is reflected back toward the source and re-reflected to add to the energy transmitted

¹Dr. R. W. Beatty was formerly with the National Bureau of Standards. He is presently a Consulting Electronics Engineer at 2110 Fourth Street, Boulder, Colo. 80302.

to the load. In case of small reflections, one can neglect multiple reflections and consider only the dominant effect. Since the reflected wave travels farther than the main wave, its phase varies faster with frequency variations. Consequently, the resultant phase shift ψ of the transmitted wave does not vary quite linearly with frequency, but has a cyclical variation superimposed on the linear variation. The group delay τ_g is related to the phase shift variation with frequency. At a frequency f_0 , the group delay is defined as follows

$$\tau_g = -\frac{1}{2\pi} \cdot \frac{d\psi}{df} \Big|_{f=f_0} \quad (1)$$

Hence, the group delay will also undergo cyclical variations due to reflections. Such an effect was observed by Lacy (Ref. 3) in 1961.

Various analyses of this effect have appeared in the literature. In 1961 (Ref. 4), Lacy's analysis was limited to the case of reactive shunt discontinuities on lossless transmission lines and did not yield an explicit expression for group delay. In 1964 (Ref. 5), Cohn and Weinhouse gave a clear explanation of the effect and a simple analysis of the interaction phase error, stopping short of an explicit expression for group delay. In 1969 (Ref. 6), Draznyak gave an expression for the error in group delay due to reflections from test port terminations. His expression was valid for small reflections and lossless components but was limited in application. There may be other treatments of this problem in the literature, but the authors are not aware of them.

III. Theory

The following analysis is intended to be more general than previous work and will serve to clarify the assumptions made in calculating and measuring group delay of transmission lines. The analysis will be mainly useful for coaxial transmission line problems, but will be purposely kept general so as to include most uniconductor waveguide applications as well. It is not assumed that the discontinuities must be shunt susceptances, or that the characteristic impedance of the transmission line is identical to the characteristic impedances of the systems on either side. It is not assumed that the reflections from the discontinuities are small or equal. The discontinuities can be lossy or lossless and need not obey the reciprocity condition.

Consider a *uniform* transmission line of length ℓ having discontinuities at each end. A network model is shown in

Fig. 1, in which the discontinuities are represented by the 2-ports L and N and the energy is assumed to propagate in the *dominant mode* from port 1 towards port 2.

The group delay τ_g is given by Eq. (1), where ψ is now ψ_{21} , the characteristic phase shift of the model, or the argument of S_{21} , its (transmission) scattering coefficient. If we employ conventional microwave network theory (Ref. 7), we can calculate S_{21} for the three cascaded 2-ports and obtain

$$S_{21} = \frac{\ell_{21} n_{21} e^{-\gamma \ell}}{1 - \ell_{22} n_{11} e^{-2\gamma \ell}} \quad (2)$$

where $[\gamma = \alpha + j\beta]$ is the propagation constant of the transmission line and ℓ_{21} , ℓ_{22} , n_{11} , and n_{21} are scattering coefficients of the discontinuities. The attenuation and phase constants of the transmission lines are α and β , respectively. For a general transmission line such as a dominant mode uniconductor waveguide or coaxial line one can let

$$\beta = \frac{2\pi}{\lambda_g} = \frac{2\pi}{\lambda_0} \sqrt{\epsilon' - \left(\frac{\lambda_0}{\lambda_c}\right)^2} \quad (3)$$

where λ_g is the waveguide wavelength of a dielectrically filled waveguide, λ_0 is the freespace wavelength, ϵ' is the relative permittivity of the dielectric material filling the waveguide, and λ_c is the cutoff wavelength. For transverse electric (TE) and transverse magnetic (TM) waves, λ_c is dependent on the physical dimensions of the waveguide opening, but for transverse electromagnetic (TEM) waves λ_c is equal to infinity.

We can let

$$h = |\ell_{22} n_{11}| e^{-2\alpha \ell}$$

$$\theta = 2\beta \ell - \arg(\ell_{22}) - \arg(n_{11})$$

$$\phi = \beta \ell - \arg(\ell_{21}) - \arg(n_{21})$$

Then we can write

$$S_{21} = \frac{|\ell_{21} n_{21}| e^{-\alpha \ell} \cdot e^{-j\psi}}{1 - h e^{-j\theta}} \quad (4)$$

The characteristic phase shift ψ_{21} is then

$$\psi_{21} = \arg(S_{21}) = -[\phi + \arg(1 - h e^{-j\theta})] \quad (5)$$

The group delay is obtained by multiplying Eq. (5) by -1 and differentiating the result with respect to angular frequency ($2\pi f$), and is

$$\tau_g = \tau_{g1} + \tau_{g2} + \tau_{g0} + \Delta\tau \quad (6)$$

where

$$\tau_{g1} = -\frac{1}{2\pi} \frac{d}{df} \arg(\ell_{22})$$

$$\tau_{g2} = -\frac{1}{2\pi} \frac{d}{df} \arg(n_{11})$$

and if v_g is the group velocity in the dielectric filled transmission line having phase constant given by Eq. (3) and c is the velocity of electromagnetic waves in *vacuo*,

$$\tau_{g0} = \frac{1}{2\pi} \left(\frac{d\beta}{df} \right) \ell = \frac{\ell}{v_g} = \frac{\ell}{c} \left(\frac{\lambda_g}{\lambda_0} \right) \epsilon' \quad (7)$$

Furthermore,

$$\Delta\tau = \frac{1}{2\pi} \frac{h(\cos\theta - h) \frac{d\theta}{df} + \left(\frac{dh}{df} \right) \sin\theta}{1 - 2h \cos\theta + h^2} \quad (8)$$

in which

$$\frac{1}{2\pi} \frac{d\theta}{df} = 2\tau_{g0} - \frac{1}{2\pi} \frac{d}{df} [\arg(\ell_{22}) + \arg(n_{11})] \quad (9)$$

and

$$\begin{aligned} \frac{1}{2\pi} \frac{dh}{df} &= \frac{|\ell_{22} n_{11}|}{2\pi} e^{-2\alpha\ell} \\ &\times \left[\frac{1}{|\ell_{22}|} \frac{d|\ell_{22}|}{df} + \frac{1}{|n_{11}|} \frac{d|n_{11}|}{df} - 2\ell \frac{d\alpha}{df} \right] \quad (10) \end{aligned}$$

We can see in Eqs. (6) to (10) how a change with frequency of the attenuation or phase shift of the line or the reflection coefficients of the discontinuities, for example, might affect the group delay. In practical cases where the delays of the individual discontinuities are small, and we are interested in a relatively small bandwidth at microwave frequencies, we can neglect a number of terms that

would contribute an insignificant amount to the final result. Then Eq. (6) reduces to

$$\tau_g = \tau_{g0} \left[1 + \frac{2h(\cos\theta - h)}{1 - 2h \cos\theta + h^2} \right] = \tau_{g0} + \Delta\tau \quad (11)$$

One can see that $\Delta\tau$ is a function of θ which varies with frequency, so that $\Delta\tau$ varies between the following limits

$$-\frac{2\tau_{g0}h}{1+h} \leq \Delta\tau \leq \frac{2\tau_{g0}h}{1-h} \quad (12)$$

or from substitutions

$$\begin{aligned} & -2 \left[\frac{\ell}{c} \left(\frac{\lambda_g}{\lambda_0} \right) \epsilon' \right] \frac{[|\ell_{22}| |n_{11}| \mathcal{A}]}{1 + |\ell_{22}| |n_{11}| \mathcal{A}} \leq \Delta\tau \\ & \leq \frac{2 \left[\frac{\ell}{c} \left(\frac{\lambda_g}{\lambda_0} \right) \epsilon' \right] [|\ell_{22}| |n_{11}| \mathcal{A}]}{1 - |\ell_{22}| |n_{11}| \mathcal{A}} \quad (13) \end{aligned}$$

where $\mathcal{A} = e^{-2\alpha\ell}$ is the attenuation (power) ratio of the length of transmission line which has an attenuation $A = -10 \log_{10} \mathcal{A}$. The reader is reminded that in the expression given above, λ_g is for a general case single-mode dielectric filled waveguide as may be seen from Eq. (3). For an air-dielectric medium we may let $\epsilon' = 1$, and for coaxial line TEM mode, we set $\lambda_c = \infty$.

IV. Graphical Data

A graph of the limits of $\Delta\tau$ is given in Fig. 2. It is assumed for simplicity that $|\ell_{22}| = |n_{11}|$, and that $\tau_{g0} = 100$ ns. If $|\ell_{22}| \neq |n_{11}|$, one can assume that the line has equivalent identical discontinuities at each end where the equivalent discontinuity has a reflection coefficient magnitude equal to

$$\sqrt{|\ell_{22}| |n_{11}|}$$

For a transmission line having the same line attenuation but a τ_{g0} different from 100 ns, one multiplies the result obtained from the graph by the ratio of the actual τ_{g0} in nanoseconds to 100.

As an example of the use of Fig. 2, assume that a transmission line has a delay of 20 ns and a line attenuation of 5 dB prior to adding discontinuities of $|\ell_{22}| = 0.4$ and $|n_{11}| = 0.1$. Then an equivalent discontinuity placed at

each end of this line would have a reflection coefficient magnitude of $\sqrt{(0.4)(0.1)} = 0.2$. From Fig. 2, one finds that if the reflection coefficient magnitude of each discontinuity is 0.2 and the line attenuation is 5 dB for a 100-ns line, the limits of cyclical variation are ± 2.5 ns. Then the limits of cyclical variation for the above 20-ns line example are $\pm(20/100)(2.5)$ ns.

V. Experimental Results

Experimental results were obtained to confirm the theory for the case of fairly large reflections. Metal disks having a diameter of 6.12 mm (0.241 in.) and a thickness of 0.152 mm (0.006 in.) were attached to the center conductors of short sections of 7-mm coaxial line to form the discontinuities L and N in Fig. 1. The discontinuity assemblies may be seen in Fig. 3. Over a frequency range of 8.365 to 8.465 GHz, a value of 0.42 for $|l_{22}|$ and $|n_{11}|$ of the disk assemblies was calculated using computer programs developed for 2-port standards (Ref. 8). Over the same frequency range a value of 0.43 was measured using an automatic network analyzer.

The 30-ns coaxial line delay standard shown in Fig. 4 was connected between the discontinuities. Measurements of τ_g and of $-20 \log_{10} |S_{21}|$ using an automatic network analyzer are shown in Figs. 5 and 6, respectively. The group delay and the measured attenuation equal to $-10 \log_{10} e^{-2\alpha l}$ of the transmission line plus the short sections of 7-mm coaxial line with disks removed are also shown. A comparison of calculated and measured results is shown in Table I. The tabulated results show only limits near

the center of the frequency range but are typical of the results over the frequency range of 8.365 to 8.465 GHz. The calculated limits do not include the additional effects of reflections from the coaxial line connectors. Closer agreement was obtained by measuring the $|l_{22}|$ and $|n_{11}|$ taking into account the coaxial connectors.

Good agreement between theory and experiment was also obtained when additional measurements were made with different disks, different transmission line lengths, and at an additional frequency range of 2.235 to 2.355 GHz. The details are not given here but will be included in a subsequent issue of this publication.

VI. Conclusions

No attempt was made to experimentally confirm all aspects of the general theory. However, for the special case considered [identical discontinuities at each end, and negligible frequency dependence of α , $|l_{22}|$, $|n_{11}|$, $\arg(l_{21})$, $\arg(n_{21})$, $\arg(l_{22})$, and $\arg(n_{11})$ over the bandwidth of interest], adequate confirmation of the theory was obtained.

The analysis presented applies both to transmission lines operating in the TEM mode or to single-mode propagation in waveguides in general. The graphical data presented can be useful for: (1) estimating the limits on the variation of group delay with frequency or (2) determining how much reduction of discontinuities is necessary in order to achieve a given accuracy in predicting group delay.

Acknowledgment

The experimental work was expedited by the capable assistance of A. Rosenzweig and M. Culbertson of the Western Automatic Test Services at Sunnyvale, California.

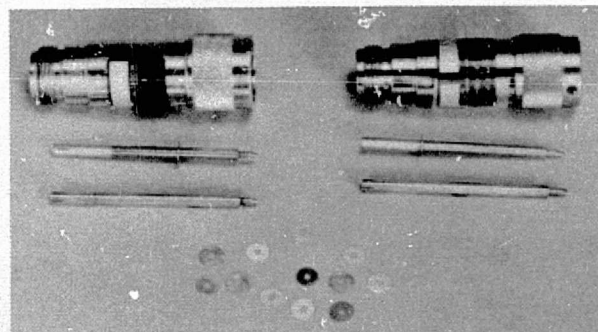
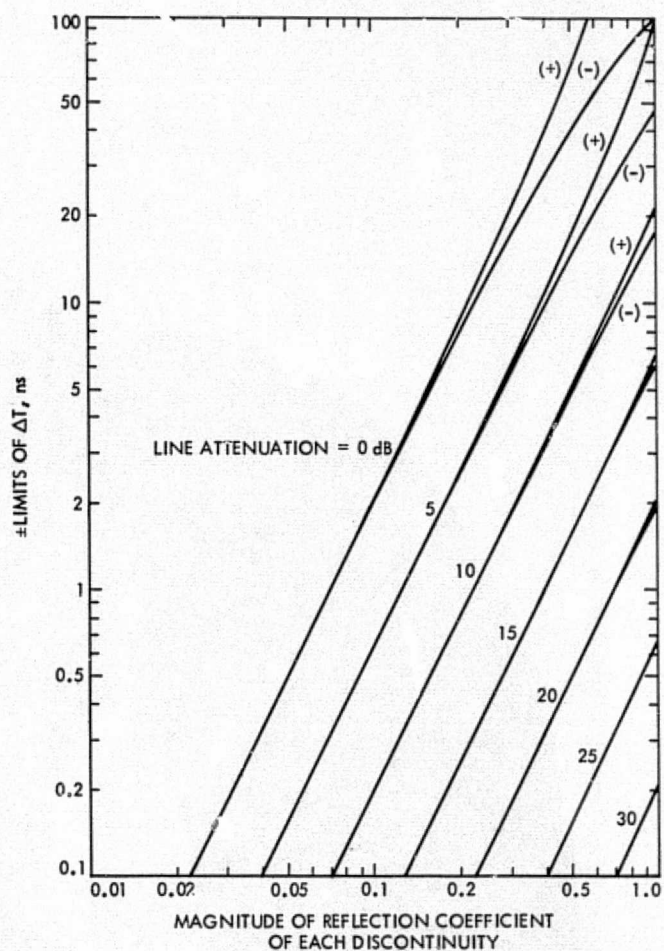
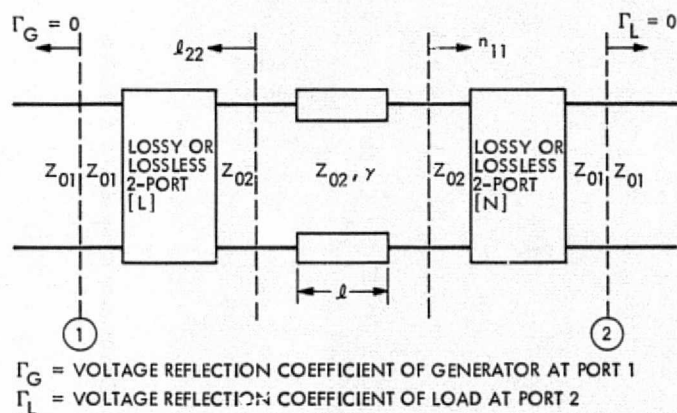
References

1. Lewin, L., Muller, J. J., and Basard, R., "Phase Distortion in Feeders," *Wireless Engineer*, pp. 143-145, May 1950.
2. Otoshi, T. Y., "S/X Band Experiment: A Study of the Effects of Multipath on Two-Way Range," *The Deep Space Network Progress Report 42-25*, pp. 69-83, Jet Propulsion Laboratory, Pasadena, California, Feb. 15, 1975.
3. Lacy, P., "Measuring Transmission Delay Distortion," *Microwaves*, Vol. 3, No. 7, pp. 22-25, July 1964.
4. Lacy, P., "Analysis and Measurement of Phase Characteristics in Microwave Systems," 1961 WESCON Reprints, paper 23/3.
5. Cohn, S. B., and Weinhouse, N. P., "An Automatic Microwave Phase-Measurement System," *Microwave J.*, Vol. 7, No. 2, pp. 49-56, February 1964.
6. Drazy, E. J., "The Practical Use of Test Equipment for Microwave Filter Measurement," 1969 *NEREM Record*, Technical Applications Sessions, pp. 1-5, Nov. 1969.
7. Kerns, D. M., and Beatty, R. W., *Basic Theory of Waveguide Junctions and Introductory Microwave Network Analysis*, Pergamon Press, New York, New York, 1967.
8. Beatty, R. W., "Calculated and Measured S_{11} , S_{21} , and Group Delay for Simple Types of Coaxial and Rectangular Waveguide 2-Port Standards," *NBS Tech. Note 657*, December 1974.

Table 1. Comparison of calculated and measured upper and lower limits of group delay and loss of a 30-ns line with a discontinuity assembly at each end

Parameter	Calculated value	Measured value ^a	Difference
Maximum delay	34.60 ns	34.38 ns at 8.407 GHz	0.22 ns
Minimum delay	26.56 ns	26.70 ns at 8.415 GHz	-0.14 ns
Maximum loss	6.51 dB	6.42 dB at 8.415 GHz	0.09 dB
Minimum loss	5.36 dB	5.25 dB at 8.407 GHz	0.11 dB
^a The frequency interval between successive upper and lower limits is $1/(4\tau_{go})$			

C-2



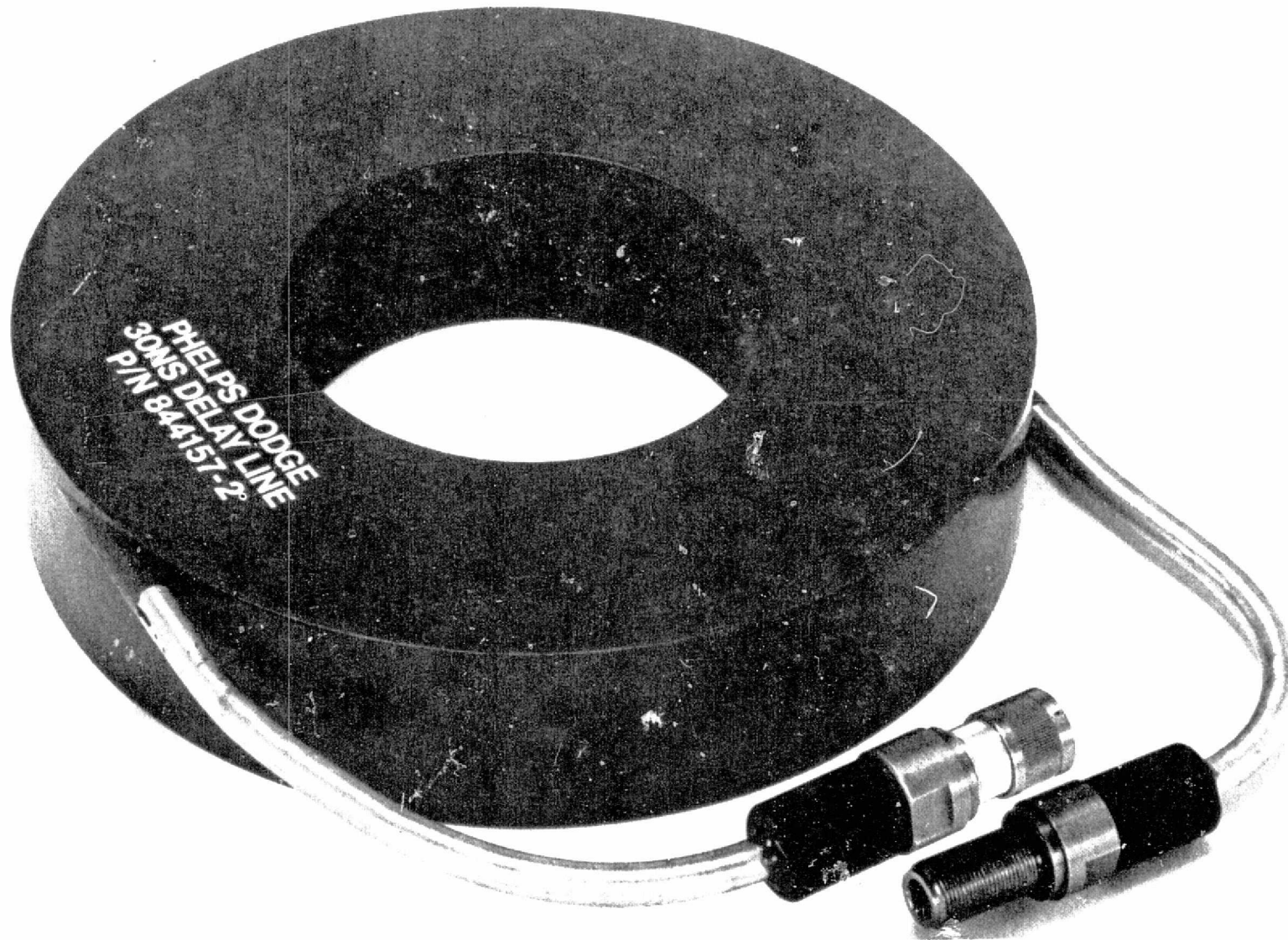


Fig. 4. Coaxial line delay standard of 30 ns

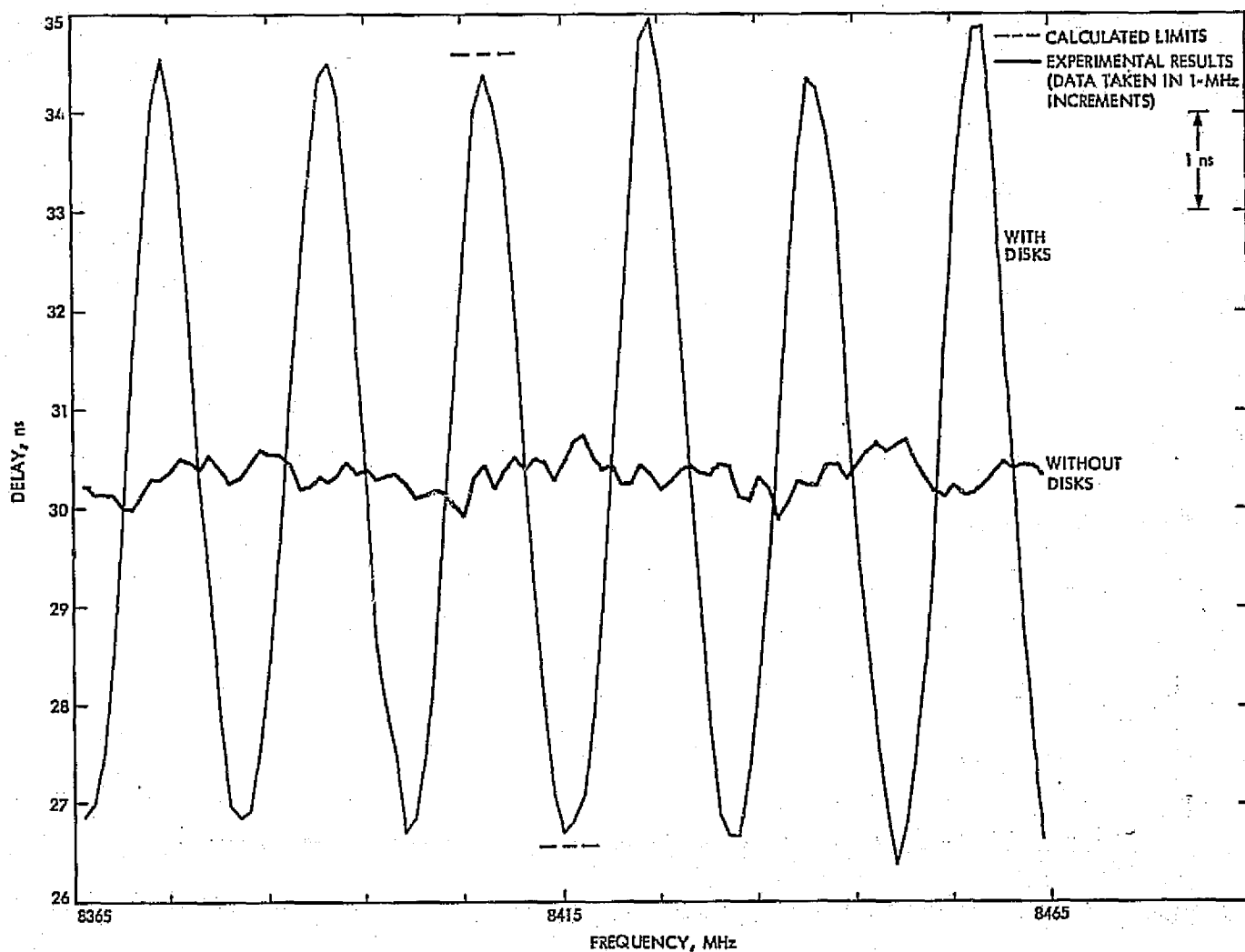


Fig. 5. Measured group delay of a 30-ns transmission line plus short end sections of 7-mm lines with and without 6.12-mm (0.241 in.) diam disks

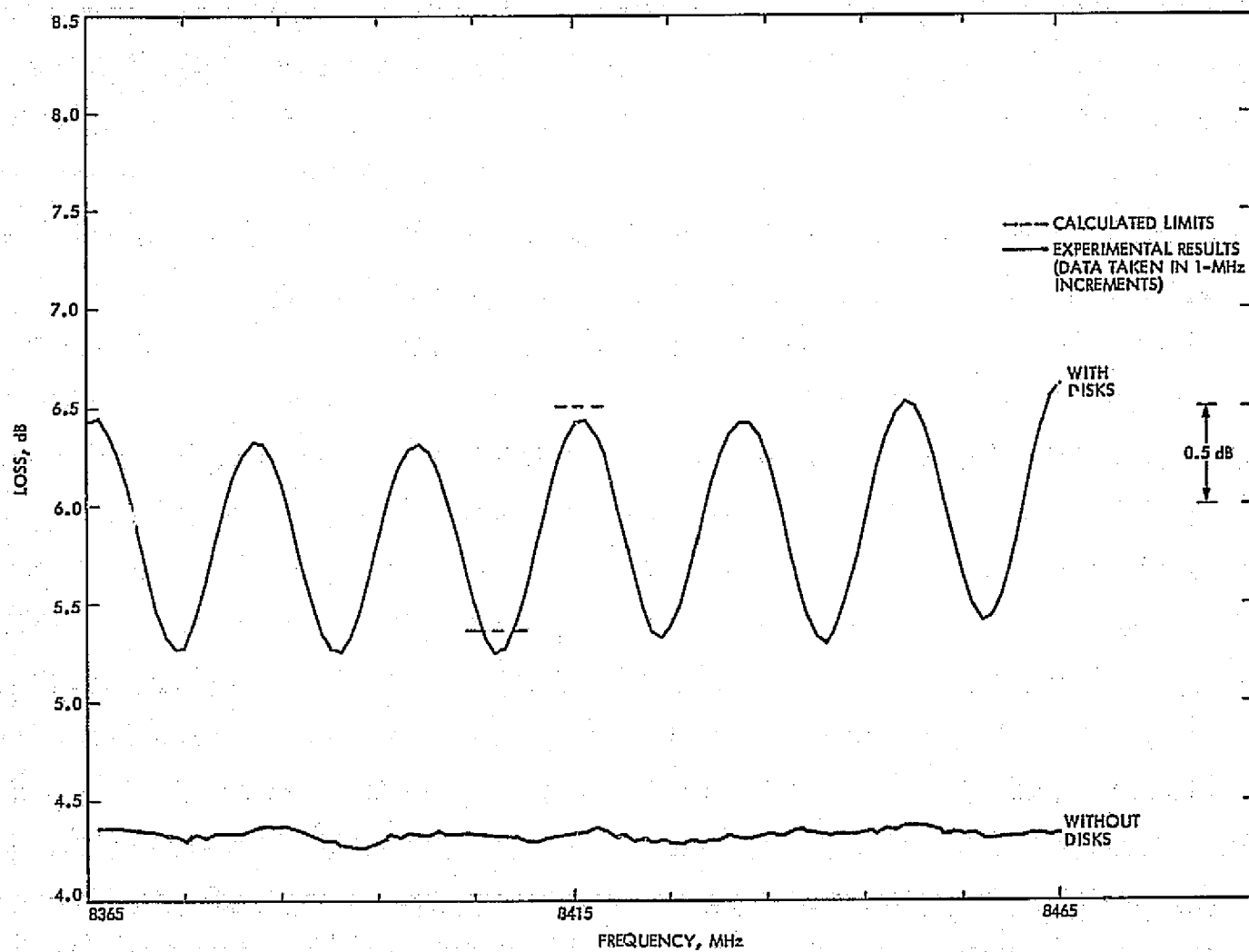


Fig. 6. Measured $-20 \log_{10} |S_{21}|$ of a 30-ns transmission line plus short end sections of 7-mm lines with and without 6.12-mm (0.241 in.) diam disks

Graphs With Multiplace Nodes for Printed Circuitry

H. Taylor

Communications Systems Research Section

A problem in the design of printed circuits is recast into a problem in applied graph theory. A catalog of diagrams that can be used to obtain efficient realizations of many circuit diagrams is presented.

I. Introduction

Arranging the terminals of a printed circuit so that none of the connecting lines cross each other can be taken as a problem in applied graph theory.

To agree with the terminology of graph theory let us call terminal codes nodes, connecting lines edges, and when some nodes and edges are given let us call the resulting collection a graph.

A given graph, then, presents a question as to whether or not it is possible to draw a picture of the graph on one side of one sheet of paper, for example, with no edges crossing.

Usually the answer is no. So the next question is how to get around it. One possibility is to draw a picture with the number of crossings minimized and then drill holes in the board. The literature has a few studies of the

problem of minimizing the number of crossings (Ref. 1) but these results may still be far from best possible.

Another possibility is to use several sheets of paper, picturing the nodes over again on each sheet but each edge on only one sheet. Here the problem is to minimize the number of sheets. The literature has better results on this problem, and in some cases the best possible (Ref. 2).

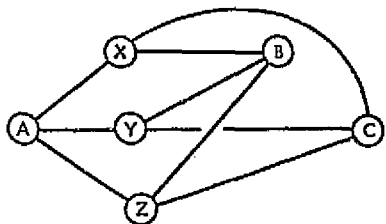
A third possibility is the subject of the present study. It is to picture the graph on only one sheet of paper by allowing each node to appear in several places. Thus by using multiplace nodes any graph can be pictured on one sheet with no edges crossing. The problem is to minimize the number of places. There seems to be little mention of this problem in the literature between 1890 when Heawood (Ref. 3) drew the basic example of 12 two-place nodes with all 66 edges, and quite recently (Ref. 4) when some interesting cases are mentioned as unsolved, but with no new results since Heawood.

In actually realizing some circuitry there is also the question of making connection to the nodes from the outside, and presumably this could present real difficulties if the circuitry is to be miniaturized. One separate sheet for the nodes would be enough if each node could be spread out in a strip of conducting material, and then connected at certain places to the sheet on which the graph is pictured.

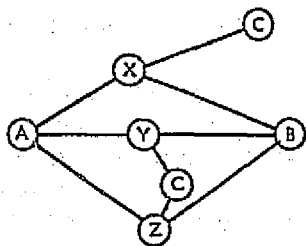
Two sheets will suffice for any graph: one sheet for access to the nodes from the outside, and one sheet to picture the graph with multiplace nodes.

These are the first entries for a catalog of pictures that hopefully will be of use to the circuit designer. Any one of these graph picturing problems is quite likely to be very troublesome by itself. The designer can look in the catalog and find a picture close enough to what he needs to at least keep it on only two sheets and maybe economize on multiplace nodes as well.

To start with a well-known example, suppose it is required to draw all the edges from nodes A,B,C to nodes X,Y,Z. After a few trials it will look impossible as in this sketch:



But if we allow C to be a 2-place node, it looks too easy, as in this sketch:



So to have a more difficult example, suppose we require all the edges from nodes A,B,C,D,E,F,G to nodes 1,2,3,4,5,6,7,8 allowing each node to be 2-place. This graph is designated $K_{7,8}$ and pictured 2-place in Fig. 1.

The notation $K_{a,b}$ refers to a graph having $a + b$ nodes with all the edges from a of them to b of them. Figure 1 shows $K_{7,8}$ pictured with 2-place nodes and that will go into the catalog. What makes it interesting is the fact that, with nodes allowed no more than 2 places each, $K_{8,8}$ is impossible. This bounding impossibility, and most of the others like it, will become easy to prove using the famous formula $V - E + F = 2$, often called Euler's formula.

II. $V - E + F = 2$

By common usage E is the number of edges, F is the number of faces, and V is the number of vertices. In the present context one place at which a node is pictured will count as one vertex.

An undivided region will count as one face. A line segment drawn with a vertex at each end will count as one edge. Let it be understood from here on that an edge is not meant to cross, nor even touch, another edge in the picture.

The formula holds for any connected configuration of vertices, edges, and faces on a surface like the sphere, plane, or one side of a sheet of paper. This is one of those situations where minimum conditions result in the simplest proof. So here is proof by induction that $V - E + F = 2$ holds for any connected configuration of vertices, edges, and faces satisfying conditions 0 and 1:

0. An edge which has both ends on the same vertex will divide the surface into two regions.

1. $V > 0$.

The induction is on the number of edges. When $E = 0$, connectedness requires $V < 2$; so, we can only have $V = 1$, $F = 1$, and $V - E + F = 1 - 0 + 1 = 2$. When $E = 1$ there are two possible configurations, namely, $\textcircled{A} - \textcircled{B}$ with $V = 2$, $E = 1$, $F = 1$, and \textcircled{A} with $V = 1$, $E = 1$, and as we know by conditions 0, $F = 2$.

Now for the inductive step let us be given a connected configuration with E edges, V vertices, and F faces and presume the formula holds for all connected configurations with fewer than E edges, under condition 0 and 1. Select any edge and consider two cases.

Case I. The selected edge has different vertices at its two ends. In this case we shrink the edge to nothing and merge the two vertices into one vertex, thereby reducing

the number of edges by one and reducing the number of vertices by one. This keeps the configuration connected and preserves conditions 0 and 1 so by the inductive presumption $(V - 1) - (E - 1) + F = 2$, and $V - E + F = 2$.

Case II. The selected edge has the same vertex at both ends. In this case erasing the edge will reduce the number of edges by one and reduce the number of faces by one because of condition 0. But the configuration will remain connected and conditions 0 and 1 will be unaffected. So by our inductive presumption $V - (E - 1) + (F - 1) = 2$ and therefore $V - E + F = 2$.

Thus $V - E + F = 2$ for any connected configuration on a surface which satisfies condition 0.

Observe that a configuration with several parts on a surface satisfying condition 0 would still satisfy the inequality $V - E + F \geq 2$, because it would still have $V - E + F = 2$ for each connected part.

III. $K_{a,b}$ with 2-place Nodes

We can lose no generality by considering only pictures in which every face has three or more edges, and now that we want to find bounds on the most that can be pictured with $K_{a,b}$ we can derive even more limitation. In $K_{a,b}$ an edge only connects one of the a nodes with one of the b nodes so that a face will have an even number of edges. Thus for $K_{a,b}$ we can count the number of incidences of a face with one side of an edge and find from the edges that the number is $2E$, while from the faces the number is $\geq 4F$.

The inequality $2E \geq 4F$ together with $4V - 4E + 4F \geq 8$ boils down to a very useful relationship: $E \leq 2V - 4$, which applies to $K_{a,b}$ as long as $a + b > 2$. Again, counting edges is easy for $K_{a,b}$, and we have $E = ab$.

Now here are some bounding examples of what graphs $K_{a,b}$ can be pictured using m -place nodes in case we require $m \leq 2$. It makes $V \leq 2(a + b)$ and so it would be not impossible only for values of a and b satisfying:

$$ab \leq 4(a + b - 1)$$

The impossibility of picturing $K_{a,b}$ with 2-place nodes is now established because the formula is not satisfied with a and b both ≥ 8 .

The values allowed by the formula are as follows:

$$a = 7 \text{ requires } b \leq 8$$

$$a = 6 \text{ requires } b \leq 10$$

$$a = 5 \text{ requires } b \leq 16$$

and then $a \leq 4$ allows b as large as space permits.

With Fig. 2 showing $K_{7,8}$, Fig. 3 showing $K_{6,10}$, Fig. 4 showing $K_{5,16}$, and Fig. 5 showing a scheme for $a \leq 4$ and arbitrary b , we have sharp bounding examples.

IV. K_n , One of the Worst Cases

The complete graph, denoted K_n , has n nodes with an edge for every pair of distinct nodes. Regarding an arbitrary graph as a subgraph of the complete graph on the same nodes makes it clear that no graph on n nodes can demand more vertices than K_n to be pictured with multiplace nodes.

Thus we get a rough outline by asking for the minimum number of vertices needed for K_n . Table 1 and the corresponding figures show the best obtained so far.

The question marks in Table 1 indicate tried without success, whereas the blank spaces just mean not tried yet.

Now to explain the column headings in Table 1. The numbers under t are taken from Ref. 2. Given n the number of nodes in the complete graph, t is the minimum number of sheets that would be needed. Beineke gives

$$\left\lceil \frac{n+7}{6} \right\rceil$$

for large n except for the question marks when $n \equiv 4 \pmod{6}$ or $n = 9$. We could put the separate sheets side by side on one sheet and always have true $\min V \leq nt$.

The true $\min V$ is the actual minimum number of vertices for any picture of K_n using multiplace nodes.

The number in the picture V column gives the number of vertices in a multiplace picture of K_n which has actually been drawn.

The formula V has been calculated from $E = \binom{n}{2}$ as the smallest integer satisfying

$$V \geq \frac{E + 6}{3}.$$

This lower bound for the minimum V has been derived from our formula $V - E + F = 2$ as follows.

A picture minimizing V will need at least $E = \binom{n}{2}$ edges, and any more edges could only get in the way. So, without loss of generality, we can erase any edge with the same vertex at both ends, or any extra edges between the same pair of vertices—with the result that any face will touch at least three edges. Counting edge-face incidences gives us the inequality $3F \leq 2E$. Putting this together with the formula $3V - 3E + 3F \geq 6$ gives us $3V - 3E + 2E \geq 6$ which says $3V \geq E + 6$. Thus in general we have formula $V \leq \text{true min } V \leq nt$.

A word of explanation about the figures. $w \cdot 1 + x \cdot 2 + y \cdot 3 + z \cdot 4 = V$ means that the picture is using w 1-place nodes, x 2-place nodes, y 3-place nodes, and z 4-place nodes, where of course, $w + x + y + z = n$.

When the same figure is listed for several values of n it means that a picture for the smaller case can be obtained by simply erasing some vertices and edges. For example to get a picture of K_6 with $V = 3 \cdot 1 + 6 \cdot 2$ just erase the 3 vertices each, of nodes A, B , and C from Fig. 8, together with the edges which end on A, B , or C .

V. The Impossibility Proofs

Proof is required when the true min V is larger than the formula V .

For K_6 it is almost immediate that $V = 7$ is impossible. It could only be pictured with $V = 5 \cdot 1 + 1 \cdot 2$; but then erasing the 2-place node and edges to it would leave K_5 pictured with $V = 5$. Similarly the impossibility of picturing K_7 with $V = 9$ is proved by reducing to the previous case.

By contrast the proof for K_8 is difficult—in fact, it is mentioned as an unsolved problem in (Ref. 4). Since a more elegant proof may be presented in part II, only a brief sketch is given here, as follows.

First, the previous cases would force a picture of K_6 to have $V = 4 \cdot 1 + 5 \cdot 2$.

Next, naming the 1-place nodes W, X, Y, Z , and the 2-place nodes 1, 2, 3, 4, 5, the result in (Ref. 5) helps to rule out all but a few apportionments of the numbered vertices into the four regions formed by the six edges connecting the lettered vertices.

Then an exhaustive comparison of the valences reduces it to the two partial pictures in Fig. 1C. And by some further direct exhaustion, it turns out that these cannot be completed.

References

1. Saaty, T. L., "On Polynomials and Crossing Numbers of Complete Graphs," *J. Combin. Theory*, Vol. 10, No. 2, March 1971.
2. Beineke, L. W., "The Decomposition of Complete Graphs into Planar Sub-Graphs," in *Graph Theory and Theoretical Physics*, pp. 139-153, F. Harary, ed., Academic Press, 1967.
3. Heawood, P. J., "Map-colour Theorem," *Quart. J. Math.*, Vol. 24, No. 1890, pp. 332-338.
4. White, A. T., *Graphs, Groups, and Surfaces*, North Holland Pub. Co., distributed by American Elsevier Pub. Co., Inc., New York, 1973.
5. Battle, J., Harary, F., and Kodama, Y., "Every Planar Graph with 9 Points has a Non-Planar complement," *Bull. Amer. Math. Soc.*, Vol. 68, pp. 569-571, 1962.

Table 1. Compared bounds for K_n

t	n	E	Formula V	Picture V	True min V	Reference
1	4	6	4	4	4	Fig. 5
2	5	10	6	6	6	Fig. 7
2	6	15	7	8	8	Fig. 7
2	7	21	9	10	10	Fig. 7
2	8	28	12	12	12	Fig. 7
3	9	36	14	15	15	Fig. 8
3	10	45	17	18	?	Figs. 8 and 9
3	11	55	21	21	21	Fig. 8
3	12	66	24	24	24	Figs. 8 and 6
3	13	78	28	28	28	
3	14	91	33	33	33	
3	15	105	37	38	?	
?	16	120	42			
4	17	136	48			
4	18	153	53	53	53	Fig. 11
4	19	171	59	59	59	Fig. 11
4	20	190	66			
4	21	210	72			
?	22	231	79			
5	23	253	87			
5	24	276	94			
5	25	300	102			

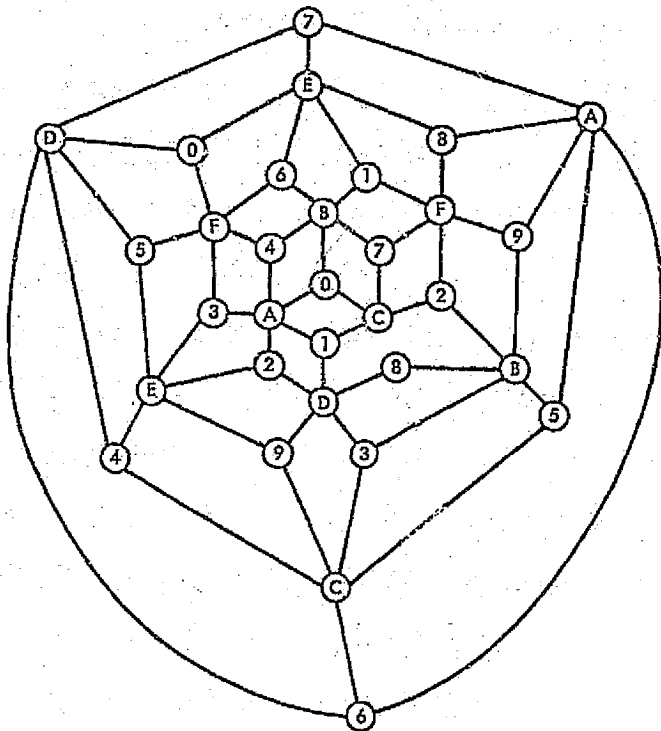


Fig. 1. $K_{7,8}$ with 2-place nodes

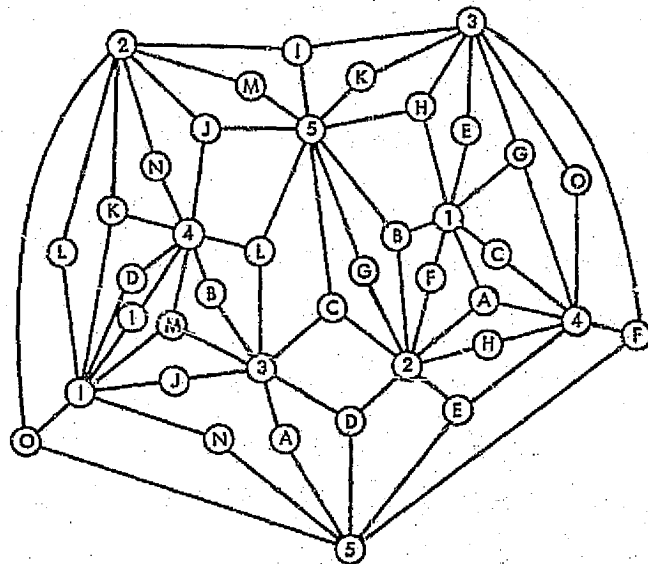


Fig. 3. $K_{5,16}$ with 2-place nodes

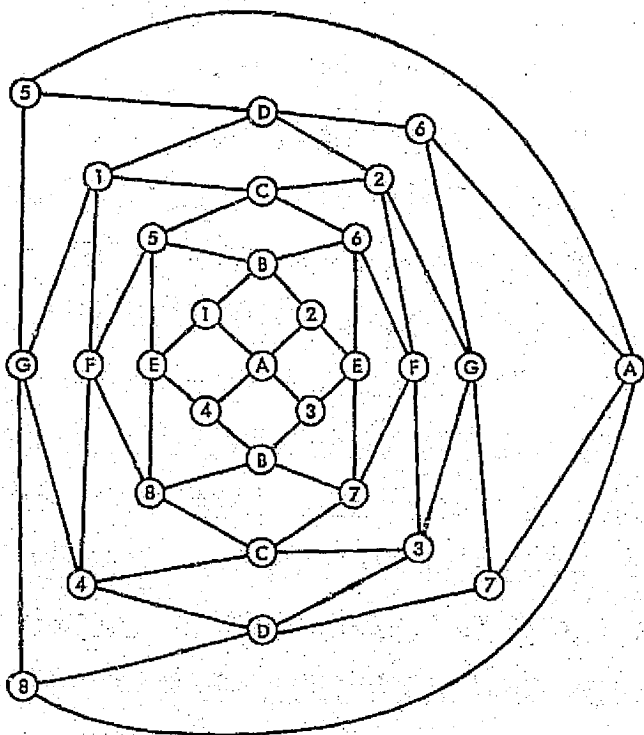


Fig. 2. $K_{8,10}$ with 2-place nodes

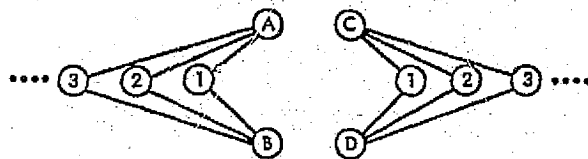


Fig. 4. $K_{4,4}$ with 2-place nodes

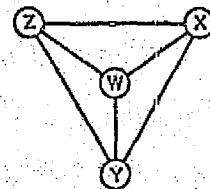


Fig. 5. $V = 4 \cdot 1$

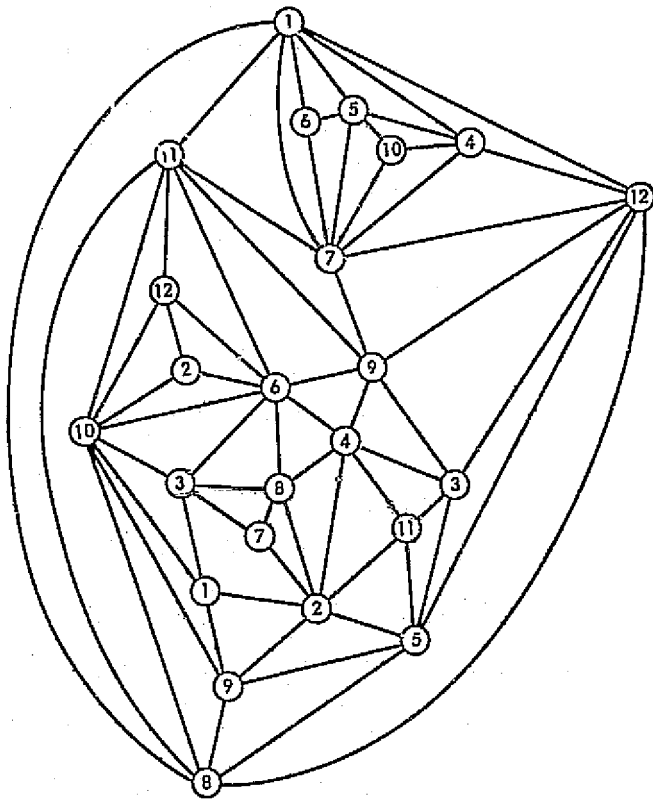


Fig. 6. $V = 0 + 12 \cdot 2$

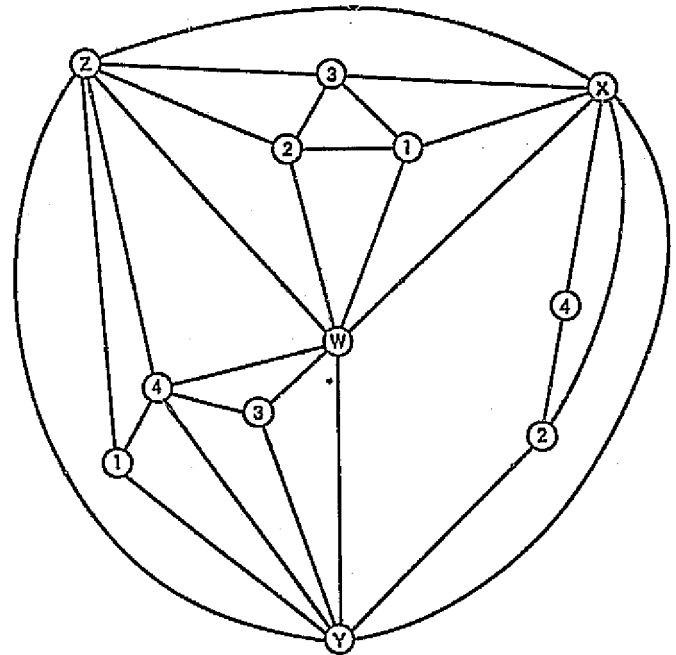


Fig. 7. $V = 4 \cdot 1 + 4 \cdot 2$

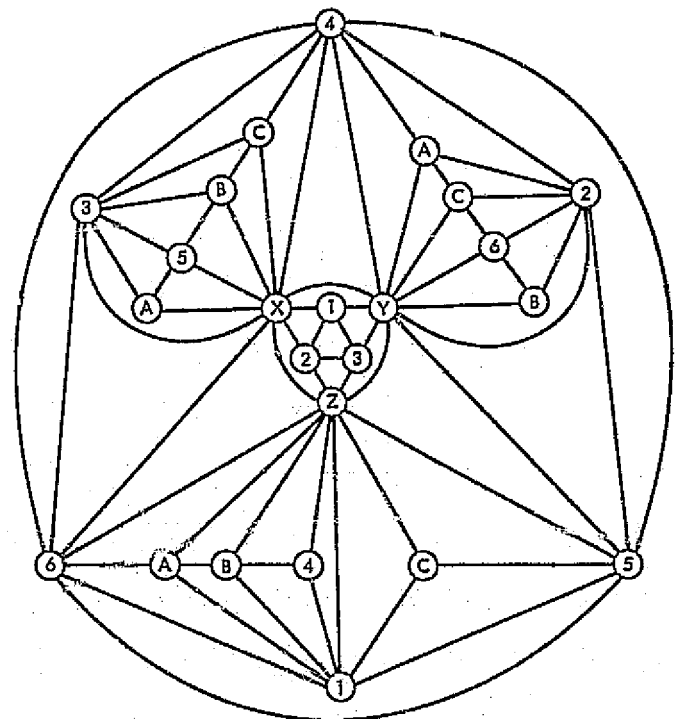


Fig. 8. $V = 3 \cdot 1 + 6 \cdot 2 + 3 \cdot 3$

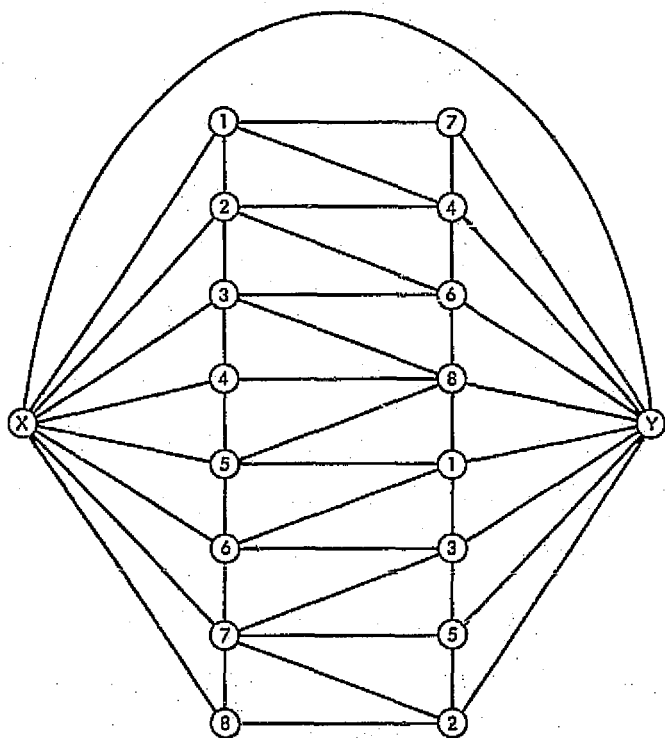


Fig. 9. $V = 2 \cdot 1 + 8 \cdot 2$

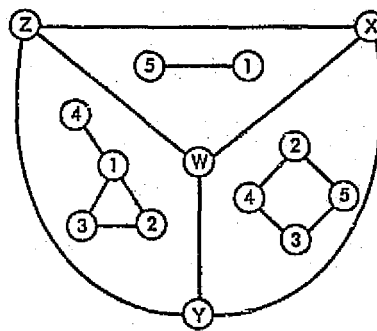


Fig. 10. Last stage of the impossibility proof for K_8

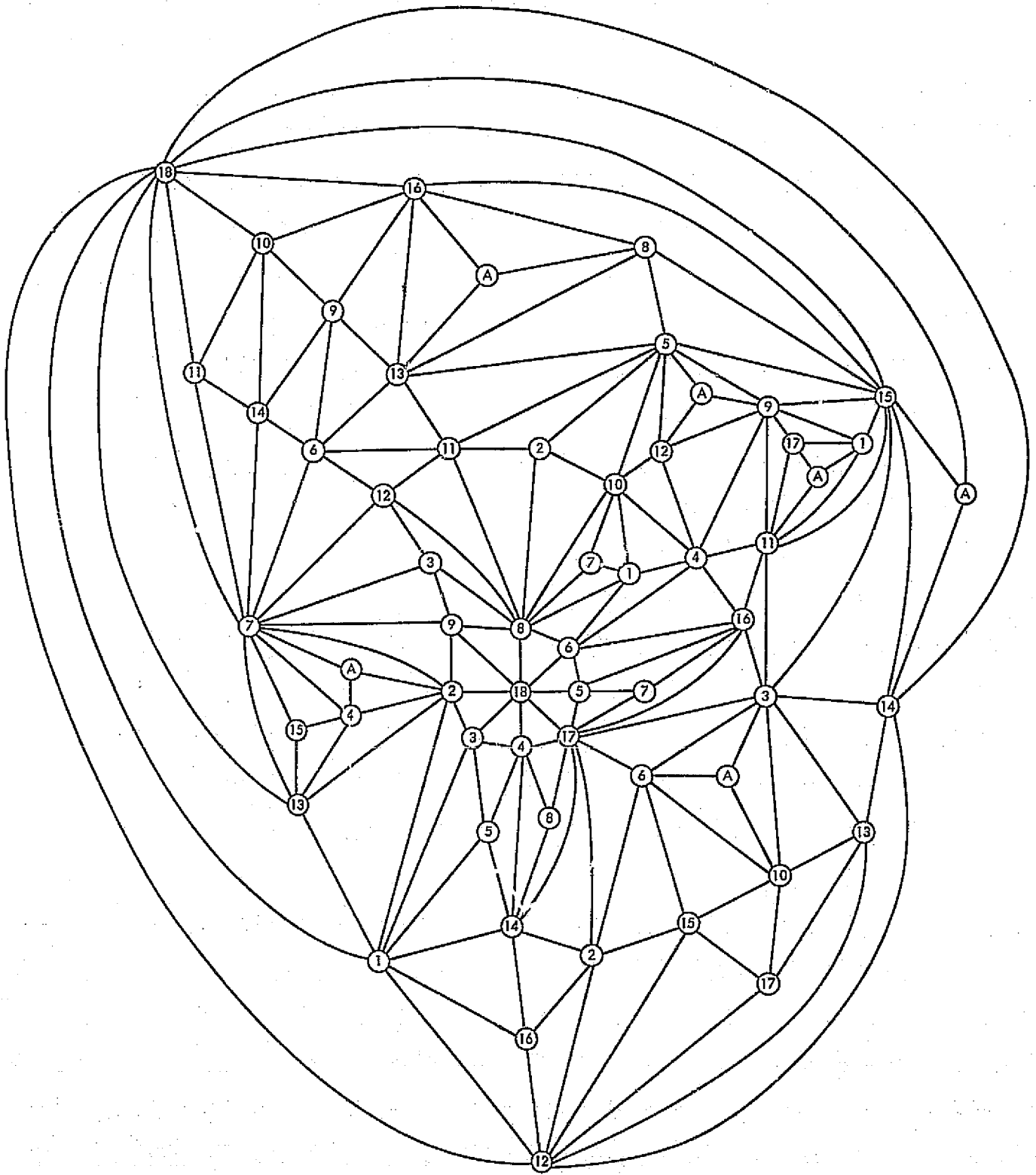


Fig. 11. $V = 0 + 1 \cdot 2 + 17 \cdot 3 + 1 \cdot 6$

DSN Research and Technology Support

E. B. Jackson and A. L. Price
R. F. Systems Development Section

The activities of the Development Support Group in operating and maintaining the Venus Station (DSS 13) and the Microwave Test Facility are discussed and summarized and progress noted during the period February 16 through April 15, 1975. Major activities include testing of hardware/software for a planned "automated station" demonstration, observation of rotational constancy of various pulsars, antenna gain standardization measurements, Block IV Receiver/Exciter testing at DSS 14, differential very long baseline interferometry (VLBI) observations, and further electromagnetic compatibility testing with the proposed Goldstone Operations Support Radar. Routine clock synchronization transmissions as well as clock synchronization system preparation for Viking and Radio Science Support activities are also discussed.

During the two-month period ending April 15, 1975, the Development Support Group, in operating the Venus Station (DSS 13) and the Microwave Test Facility (MTF), made progress on various programs as discussed below.

I. Station Automation

An automated station will be demonstrated by performing a pulsar track at DSS 13 under remote computer control. In support of this demonstration, the Development Support Group provided 24-1/2 hours of testing. The software and hardware for use at DSS 13 are complete and functioning; the first demonstration awaits

the completion of the remote (JPL in Pasadena) computer software. As part of the testing done for this program, pulsar data are being recorded onto magnetic tape for later review.

II. Pulsar Observations

In support of Pulsar Rotation Constancy (OSS-188-41-52-09), we provided 45 hours of pulsar observations, during which we recorded data on the pulsars tabulated in Table I. These recorded data, from observations made at 2388 MHz, left-circular polarization (LCP), are used to determine precise pulse-to-pulse spacing, pulse shape, and pulse power content.

III. NAR Reliability Testing

Using the 26-m antenna, the station receiver, and the noise-adding radiometer (NAR), data are automatically collected at night and during weekend hours when the station is unmanned. The antenna is fixed in position, and recordings are made of total system temperature. Inasmuch as Earth's rotation causes the antenna to sweep a segment of the sky, data are collected on background temperature as well as radio sources which pass through the beam. During this period, data were collected for a total of 358-1/4 hours, at either 180- or 0-deg azimuth and at elevations of 81.9 through 82.4 deg, in 0.1-deg increments; some data were collected at 80-deg elevation. Data are measured at a frequency of 2295 MHz, right-circular polarization (RCP).

IV. Antenna Gain Standardization

To provide transfer gain standards, observations are made at DSS 13 to determine the received flux density of some calibration radio sources. During this period, measurements at 2278.5 MHz, RCP, of Cygnus A, 3C123, and Cassiopeia A were made using the 26-m antenna, the station receiver, and the NAR. Measurements were made for a total of 21-3/4 hours with the NAR providing a semi-automated data taking cycle inasmuch as it has control of antenna offsets as well as taking and recording the data.

V. Solar Energy Instrumentation

No additional sensors have been added to the Solar Energy Instrumentation Data Acquisition System (SEIDAS) (Ref. 1), but data are being collected and recorded onto magnetic tape, chart recordings, and printed paper tape. However, difficulty has been experienced with the magnetic tape data collection system, and assistance from the system supplier (Instrumentation Technology Company) has been necessary.

VI. Microwave Power Transmission

The collimation tower has been strengthened by replacing the tower side braces with stronger diagonals, and the "rectenna" mounting frame has been installed on the collimation tower. Final electrical work, which includes the installation of the dc load box, monitoring cabling, and the sub-array load lights (36 of them) is underway, pointing toward a final system test and demonstration in May-June of 1975. The rectennas have arrived on site, along with the dc load box, and the

operational desk/console for installation into the operating area.

VII. X-Band Radar

The buffer amplifier was delivered by the contractor and testing is underway. Fabrication of final system elements (combiner control printed circuit cards, power supplies, bracketry, etc.) is underway, pointing toward a system test with all "transferable" equipment in late May 1975.

System documentation (test procedures, instruction manuals, etc.) preparation is underway and some deliveries have already been made to the documentation contractor.

VIII. Block IV Receiver/Exciter, DSS 14

In support of the implementation of the Block IV Receiver/Exciter at DSS 14 (as required for the Viking mission), we provided a total of 225 manhours in the following areas:

- (1) **Qualification Tests.** Testing is now 75% complete with final testing awaiting the installation of the production voltage-controlled oscillator (VCO)/mixer modules and a new doppler mixer module.
- (2) **System Tests.** Provided Block IV support for the following tests: Planetary Ranging System Performance Tests (SPT), Viking Mission Configuration Tests (MCT), Viking Operational Verification Tests (OVT), System Integration Tests, Zero Delay System Tests.
- (3) **Training.** Assisted in the familiarization of and informal training of DSS 14 subsystem operations personnel.
- (4) **Subsystem Testing.** As the DSS 14 tracking schedule permitted, troubleshooting and testing of the remaining subsystem problems were continued. These problem areas are: hardware replacement, system monitoring interface, doppler quality and QA acceptability.

IX. Goldstone Operations Support Radar

Initial testing had disclosed no interference with telemetry demodulation with a simulated radar signal into the maser at a -10-dBm level. Further testing has been accomplished using a simulated radar maser input signal of +17 dBm at a telemetry demodulation signal-to-noise

ratio (at the Symbol Synchronizer Assembly (SSA)) of 1.0 dB. No detectable difference, radar signal on/off, can be found in the telemetry error rate under these conditions. We conclude that, if the interfering signal at 2850 MHz does not exceed +17 dBm at the maser input, no interference will be experienced with normal DSN operations from the Operations Support Radar.

X. Block IIC Receiver/Exciter, DSS 13

Preparation for the planned Block III Receiver/Exciter Subsystem installation at DSS 13 is underway. This includes the relocation of equipment in the Operations Building and the modification of the present Mod IV R&D receiver. This modification includes reducing the present three-bay receiver into a one-bay unit. The new receiver will provide one wideband open-loop channel and one phase-locked channel. The open-loop operation will still be used in conjunction with a programmed local oscillator mounted in a separate cabinet.

It is planned to incorporate all necessary ECOs to update the Block III subsystem to the present DSN status.

XI. Differential VLBI

In support of the differential VLBI experiment (OTDA 310-10-60-56), DSS 13 in cooperation with the portable ARIES station and the Robledo Deep Space Station (DSS 63) provided 27-1/2 hours of observation, during which data from 132 radio sources were recorded using the special video tape recorder. Observations were made at 2290 MHz using the 26-m antenna adjusted to receive RCP signals and coupled into the station receiver.

XII. Clock Synchronization Transmissions

As arranged by DSN Scheduling, one transmission of one-hour duration was made to DSS 63. During system performance tests, the transmitter water load failed due to a cracked waveguide window. This allowed coolant water to enter and contaminate the waveguide system. The water did not, however, reach the power amplifier output window and the klystron does not appear to be damaged. The waveguide switch and forward/reverse power directional coupler were replaced with spares.

One possible explanation of the water load failure is the possibility of plating or coating of the load cavity or input window by contaminated water, creating a poor impedance match between the waveguide and the load. This would result in heating at the load window, producing a fracture.

To reduce the possibility of this failure recurring, the entire coolant system has been thoroughly examined. Some ferrous piping was found and replaced. One potential trouble source remains, however. This is the antenna-mounted storage surge tank, which is constructed of steel with an internal plastic coating. The cognizant design engineer for the coolant system indicates that the tank has a typical five-year life before the plastic starts to crack, allowing the tank to introduce rust into the system. Although the tank was inspected visually at this time and found to be satisfactory, it is five years old. In view of the Viking Project commitment for this system, replacement with a stainless steel tank is being considered.

Other problems during this period included a control cable failure and a logic section power supply failure in the Programmed Oscillator Assembly. This assembly provides the radio frequency drive and modulation for the transmitter. The faulty components have been replaced with spares.

An additional safety feature has been installed in the transmitter system. An antenna elevation angle actuated cutoff relay now removes the radio frequency drive to the transmitter whenever the antenna elevation angle is less than +10 deg.

XIII. Planetary Radio Astronomy

In support of the Planetary Radio Astronomy experiment (OSS 196-41-73-01), we observe the planet Jupiter and various radio calibration sources. Total receiving system temperature, on and off source, is measured from which received flux density of the radio source can be calculated. These measurements are made at 2295 MHz, LCP/RCP, and utilize the 26-m antenna, the station receiver, and the NAR. Observations, in addition to Jupiter, were made of the sources tabulated in Table 2, and the data were collected semi-automatically under the control of the NAR for a total period of 55 hours.

Reference

1. Jackson, E. B., "DSN Research and Technology Support," in *The Deep Space Network Progress Report 42-26*, p. 120, Jet Propulsion Laboratory, Pasadena, Calif., Apr. 15, 1975.

Table 1. Pulsars observed at DSS 13
(Feb. 16 through Apr. 15, 1975)

0031-07	1237+25	1749-28	2021+51
0329+54	1604-00	1818-04	2045-16
0355+54	1642-03	1911-04	2111+46
0525+21	1706-16	1929+10	2218+47

Table 2. Radio calibration sources observed at DSS 13
(Feb. 16 through Apr. 15, 1975)

3C17	3C138	3C348
3C48	3C147	3C353
3C58	3C286	NGC 7252
3C123	3C309.1	NGC 7332

Instrumental Polarization of the Goldstone 64-m Antenna System at 2388 MHz

G. S. Downs and P. E. Reichley
Communications Systems Research Section

Transmission of a signal in the right-circularly polarized mode using the Polarization Diversity S-Band (PDS) cone in fact results in a slightly elliptically polarized wave. After reflection from a distant surface and return to the antenna, the expected wave polarization is left-circular. Upon reception, a small component of right-circular polarization is present, and is partly the result of transmitting a small left-circular component. A similar fraction of the received left-circular wave is coupled into the received right-circular polarization. The total power in the received right-circular component is $1.2 \pm 0.2\%$ of the power in the received left-circular component. The instrumental polarization is then $0.6 \pm 0.1\%$. The data leading to this result were obtained between July and November 1973 by transmitting radar signals to the planet Mars and subsequently measuring the power in the reflections.

I. Introduction

An electromagnetic wave transmitted by an antenna system is usually not perfectly polarized. This deviation from a perfect polarization is an instrumental effect. This deviation is present, for example, when we wish to transmit a presumably circularly polarized wave that in fact is slightly elliptically polarized. The reciprocal situation will occur in which a perfectly circularly polarized wave is intercepted by the antenna system, now used as a polarimeter. The measurement of the power in each polarization then indicates the wave is elliptically polarized. The main causes of this instrumental effect are reflection from the subreflector supports, imperfect isolation between

feeds of orthogonal polarization, and internal reflections in waveguides. The ratio of the power in the undesired polarization to the total power in the wave is called the instrumental polarization.

The measurement of instrumental polarization is usually difficult. Many experimenters have measured the polarization of radiation from natural radio sources believed to be unpolarized. The measured polarization is then considered to be instrumental in origin. Difficulties are caused by possible polarization in the radio sources, random amplitude fluctuations in the received signal, and by the additive receiver noise. Often the desired accuracy of the measurements is less than the uncertainties caused

by the random fluctuations. Hence one is tempted to measure the polarization by transmitting a strong signal with the antenna system to a colleague standing in the far zone with a polarimeter (another antenna followed by a receiver). If the curvature of Earth does not ruin the measurement attempt, polarized reflections from Earth's surface will. Placing a polarimeter in a satellite orbit has its special problems, including not knowing the instrumental effects of the polarimeter itself. Perhaps, then, a large spherical reflector placed in synchronous orbit would suffice. The antenna system is then used to transmit a polarized signal toward the reflector. The reflected signal is then received by the same antenna system now used as a polarimeter. The ratio of the power in the undesired component to the total power, called the radar instrumental polarization, is twice the one-way (transmit only or receive only) instrumental effect.

The planet Mars has been used recently in lieu of a spherical reflector. Between July 12 and November 24, 1973, radar signals were reflected off isolated regions approximately 8 km (E-W) by 110 km (N-S). A narrow band right-circularly polarized (RCP) wave was transmitted at 2388 MHz toward Mars using the Goldstone 64-m antenna fitted with the polarization diversity S-band cone. A perfectly smooth dielectric surface would convert the reflected signal into a specular component that is polarized in left circular polarization (LCP) near normal incidence. If some of the received signal were reflected twice by a rough terrain, or if asymmetrical rubble suppressed one component of linear polarization, the received signal would contain a small, diffuse RCP component. Also, if the transmitted signal is in fact elliptically polarized it would contain a small LCP component. This LCP deviate, when reflected, would return as an RCP wave. Hence in this series of measurements the two main difficulties were (1) the separation of the component of the received RCP signal induced by the surface of Mars from that inherent in the wave at transmission, and (2) the relatively large random fluctuations superimposed by receiver noise onto the weak received RCP signal.

II. Measurement of Signal Power

Imagine that the planet Mars is a stationary, perfectly conducting sphere. The narrow band radar signal, reflected from the sphere and then received at Goldstone, will contain a predictable amount of power. The strength of the signal depends on transmitting power, distance to the target, the gains of the transmitting and receiving

antennas, the wavelength of the radar signal, and the size of the spherical target. The measured power is generally expressed in square meters of radar cross section when the wave incident on the planet has an intensity of 1 W/m^2 . The radar cross section for a sphere of the same radius as Mars is πa^2 , where $a = 3393 \text{ km}$. The reflections from this perfect planet are obtained primarily from a small region about the subradar point (a surface point on the line of sight between the antenna and the center of the planet). In this ideal case the measurement of the instrumental polarization would consist of transmitting an RCP signal, then measuring the fraction of the total received power in the expected (LCP) mode and the fraction in the orthogonal (RCP) mode. The fraction in the RCP component, called the radar instrumental polarization, is two times the one-way effect. The one-way effect is merely called the instrumental polarization.

The surface of the planet Mars is made up of rough regions. Therefore, reflections can be obtained from regions well outside the subradar point. The only restriction is that these rough regions contain elements whose surface normal points in the direction of the radar antenna. Since the surface is curved, the time-delay from all regions is not necessarily the same. The delay difference between the closest point on Mars and a region on the limb is 23 ms. In the case of the perfect sphere the observed spread in delays would be many orders of magnitude less than $1 \mu\text{s}$. Also the planet Mars spins on its axis. A signal reflected from a spinning target is subject to doppler broadening of its spectrum. A narrow-band signal transmitted at 2388 MHz can be spread over 7400 Hz when reflected from Mars. A perfect sphere spinning at the same rate would produce no broadening.

Examples of the radar data obtained in the course of these measurements is presented in Fig. 1. Signal power was measured for a series of 32 time delays, each separated by $3 \mu\text{s}$. The signal is not narrow band, but spread in frequency as described above, so the distribution of the signal power in doppler shift frequency is presented at each time delay. In this case the subradar point was at a latitude of -15.5° . Its longitude was 100.6° . The radar signal was transmitted in the RCP mode and received in the LCP mode. The next day, when the longitude of 100.6° was again visible to the radar system, the experiment was repeated with reception being in the RCP mode. The bright specular reflection at low time delays corresponds to the region closest to the receiver. The parabola denotes the doppler equator, or the locus of maximum doppler shift possible at each time delay. This dashed

curve is essentially a parallel of latitude at -15.5° . The wide-band component caused by receiver noise has been subtracted in this display. The scale in Fig. 1b is 30 times larger than that in Fig. 1a, so the system noise has been brought into view. The distribution of the power in the RCP mode in delay and Doppler shift is similar to the distribution of power in the LCP mode.

If the RCP component had been produced by (1) multiple reflections on the Martian surface or by (2) small asymmetrical rocks on the surface, the power in Fig. 1(b) would be spread nearly uniformly in the region lying about the parabolic curve. It was assumed in the results presented here that an RCP component induced by the planet is tied to the presence of a diffuse scattering component and decreases slowly with an increasing angle of incidence. However, the RCP component due to instrumental effects will be subject to the same doppler shift and time delay effects as the LCP component. The instrumental RCP component will then be a constant fraction of the LCP component at all doppler shifts and time delays.

It was concluded that the RCP component is due to instrumental effects and represents a radar instrumental polarization of 1.4%. If Mars were replaced with the perfectly conducting, rotating sphere, the received LCP and RCP signals would appear in Fig. 1 as sharp spikes at a delay of 15 s. The ratio of the power in the RCP component to the total power (both components) would be 0.014.

III. An Estimate of the Instrumental Effect

Another view of the reflected power is shown in Fig. 2. By choosing to measure power only along the parabolic curve of Fig. 1, particular regions are viewed at a variety of angles of view. That is, the reflected power for a particular region is measured for different angles of incidence. The region from which the radar signals were reflected in Fig. 2 was effectively $8 \text{ km} \times 110 \text{ km}$ centered at longitude 99.52° and latitude -15.5° . The transmitted signal was polarized in RCP so the expected polarization upon reception is LCP. The power is expressed in units of radar cross section. Note that the ratio of RCP power to LCP power does not vary significantly with angle of incidence. The RCP component is approximately 1.4% of the LCP component. This is the behavior expected from instrumental polarization, where the undesired component is proportional to the total power in the wave. If the RCP component had been induced by surface roughness, the RCP power would be nearly independent

of the angle of incidence. An upper limit to the cross section of such an RCP component, provided by the lowest values of the RCP component presented in Fig. 2, is 3×10^{-6} . The peak RCP and LCP cross sections of Fig. 2 are 3.3×10^{-5} and 2.4×10^{-3} , respectively. Therefore the maximum radar instrumental polarization is 1.38% and the minimum is 1.25%. This represents only one estimate of several possible estimates of the radar instrumental polarization. The entire ensemble of measurements is considered next.

IV. An Estimate Based on all Available Data

In the absence of an RCP component induced by a rough planet, the estimate of the peak power A_p (RCP) in the RCP component divided by the estimate A_p (LCP) is approximately the radar instrumental polarization. Estimates of A_p (RCP) and A_p (LCP) were made for reflections from 193 small regions. The signal-to-noise ratio of the RCP component was not always as high (about 10) as that exhibited in Fig. 2. In some cases the RCP component was buried in the receiver noise. In the absence of noise one would expect to obtain, for small regions of differing cross sections A_p (LCP), an RCP cross section A_p (RCP) that is a constant fraction of the LCP cross section. Hypothetical results are presented in Fig. 3(a) in which the LCP cross section is continuously increased, corresponding to increasing reflectivity or smoothness. Curves of the expected RCP cross section A_p (RCP) for radar instrumental polarizations R_i of 0.5, 1.0 and 2.0% are shown.

If, in addition to the instrumental effect, significant RCP power were produced by the planet, the measured cross section would lie above the line corresponding to the true value of R_i . To illustrate how the planet might affect the measured ratios, break the transmitted wave into the dominant RCP component and the perturbing LCP component. The vector P_{TX} , representing the transmitted wave becomes

$$P_{TX} = (1 - \alpha) P_T U_L + \alpha P_T U_R$$

where P_T is the transmitter power, α is close to 1.0, and the orthogonal vectors U_L and U_R represent the two components of the wave. Upon reflection from the planet, the polarization of each component will be reversed. Extreme roughness will perturb the wave by converting a small amount of incident RCP power into diffusely scattered power in LCP and RCP. The same effect will perturb the RCP wave. A fraction $p_o + p_{10}$ of the incident

circularly polarized wave will be of the opposite polarization upon reflection. The coefficient ρ_o is associated with the specular component and ρ_{do} with the diffuse component. A fraction ρ_{ds} , associated with the diffuse scattering, will be reflected into the same polarization as the incident wave. The reflected wave P_{REF} is then, letting $\beta = 1 - \alpha$,

$$P_{REF} = [\alpha\rho_o + \alpha\rho_{do} + \beta\rho_{ds}] P_T \bar{U}_L \\ + [\beta\rho_o + \beta\rho_{do} + \alpha\rho_{ds}] P_T \bar{U}_R$$

After reception, and hence after the experiencing of further perturbation by the antenna, the received wave P_{REV} becomes

$$P_{REV} = [(\alpha^2 + \beta^2)(\rho_o + \rho_{do}) + 2\alpha\beta\rho_{ds}] P_T \bar{U}_L \\ + [2\alpha\beta\rho_o + (\alpha^2 + \beta^2)\rho_{ds} + 2\alpha\beta\rho_{do}] P_T \bar{U}_R$$

The ratio $A_p(RCP)/A_p(LCP)$ is then given by

$$\frac{A_p(RCP)}{A_p(LCP)} = \frac{2\alpha\beta(\rho_o + \rho_{ds} - \rho_{do}) + \rho_{ds}}{\rho_o + \rho_{do} - 2\alpha\beta(\rho_o + \rho_{do} - \rho_{ds})}$$

where use is made of the relation $\alpha + \beta = 1$. In one extreme case of depolarization one expects $\rho_{ds} = \rho_{do} = \rho_d$.

Then

$$\frac{A_p(RCP)}{A_p(LCP)} = \frac{2\alpha\beta\rho_o + \rho_d}{(1 - 2\alpha\beta)\rho_o + \rho_d}$$

In another extreme case, $\rho_{do} = 0$, $\rho_{ds} = \rho_d$, and

$$\frac{A_p(RCP)}{A_p(LCP)} = \frac{2\alpha\beta\rho_o + (1 + 2\alpha\beta)\rho_d}{\rho_o - 2\alpha\beta(\rho_o - \rho_d)}$$

If the diffuse component of the received RCP is small compared to the specular component, as in Fig. 2, and if $\beta \ll 1$, so $\alpha \approx 1$, then the ratios above approach 2β , the true radar instrumental polarization. However, the diffuse component of RCP may not be comparably small at

lower LCP cross sections. Both of the ratios above will then be larger than if the diffuse components were comparably small. The effect is to induce a curvature into the straight lines of Fig. 3(a) such that a straight line, when fit to the data in a least-squares sense, will not pass through the origin. The y -intercept will be greater than zero.

The results for the planet Mars are presented in Fig. 3(b). A weak but definite correlation appears in Fig. 3(b) between the power in the RCP component and that of the LCP component. Ideally, in the absence of noise, the data pairs would be confined to a straight line of the form $y = mx$. The instrumental effect to be measured would then be m . Therefore a straight line was fit to the data in a least-squares sense. The result, the dashed line of Fig. 3(b), was a line of the form $y = mx + b$ where

$$m = (0.96 \pm 0.10) \times 10^{-2}$$

$$b = (1.0 \pm 0.3) \times 10^{-5}$$

(one-sigma errors are quoted). Since $b \neq 0$ there may have been a planetary effect present. The solid line in Fig. 3b was then fit with $b = 0$, obtaining

$$m = (1.19 \pm 0.10) \times 10^{-2}$$

V. Conclusion

All the possible values of radar instrumental polarization presented above are included in the adopted value of $1.2 \pm 0.2\%$. This is considered to be a conservative estimate of the two-way instrumental polarization that is introduced in a signal transmitted at 2388 MHz using the 64-m antenna, then, after reflection from a distant object, received by the same antenna. The one-way effect is then $0.6 \pm 0.1\%$. This result is dependent on the belief that an RCP component induced by the planet is tied to a diffuse scattering component.

Acknowledgement

The authors are grateful to D. A. Bathker, R. R. Green, and R. M. Goldstein for their helpful comments.

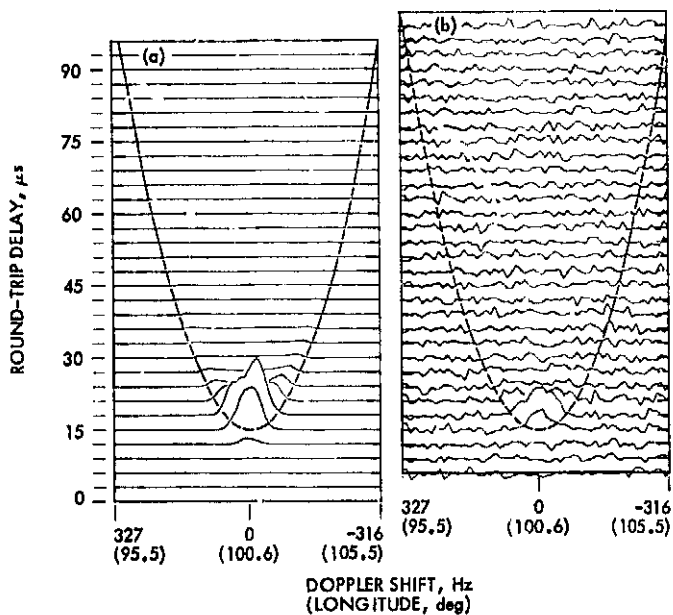


Fig. 1. Examples of reflected signal power arranged by time delay and doppler shift: (a) the antenna polarization is in LCP, (b) reflected RCP power from the same region as in (a)

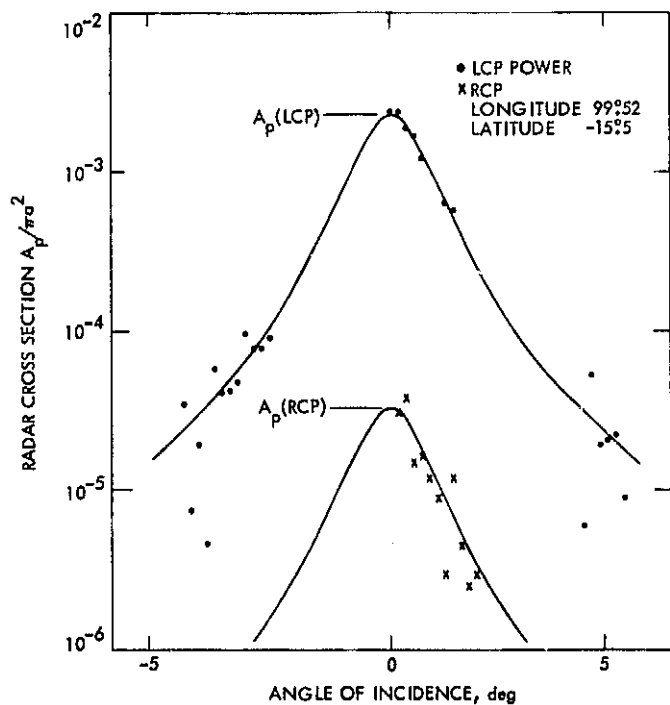


Fig. 2. Reflected power versus angle of incidence for a small Martian region 8×110 km

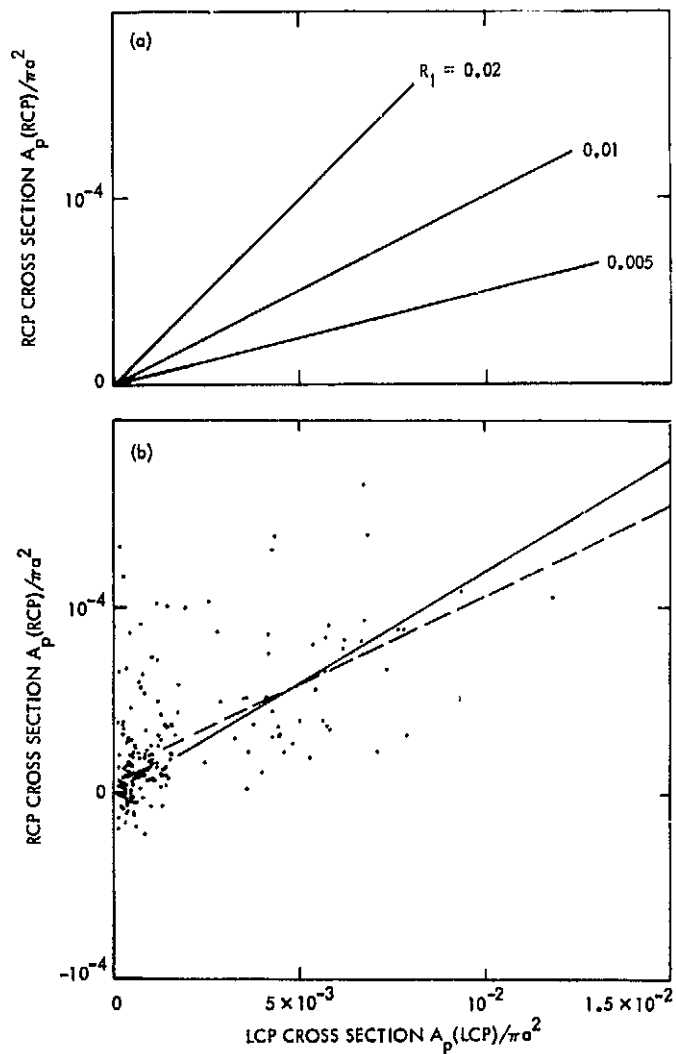


Fig. 3. RCP cross sections vs corresponding LCP cross sections: (a) expected RCP cross section vs the LCP cross section for radar instrumental polarizations R_i of 0.005, 0.01, and 0.02, (b) the peak radar cross sections (power) measured in the RCP component vs the corresponding power in the expected (LCP) polarization when the transmitted signal was right-circularly polarized

An NCS Standard Interface for the XDS 900 Series Computers

W. Lushbaugh
Communications Systems Research Section

The Network Control System standard interface has been adopted as a standard computer interface for all future minicomputer-based subsystem development for the Deep Space Network. This article describes a standard interface adapter for existing XDS 900 series computers that will enable the design of equipment compatible with the presently available machines and easily transferable to new minicomputers as they become available.

I. Introduction

The Network Control System (NCS) standard interface has been adopted as a standard computer-interface for all future minicomputer-based subsystem development for the DSN. In order to design and test equipment for currently existing 900-series machines and be able to transfer that equipment conveniently to new minicomputers as they become available, a standard interface adapter (SIA) is needed which can be attached to the 900 series machines. The following article provides a design overview of such an SIA.

II. Review of 900 Series I/O Structure

The 900 series XDS computers are 24-bit machines with input/output (I/O) performed in the register mode, i.e., transfers to and from an external piece of equipment

are on a 24-bit basis. An energize output machine (EOM) instruction and parallel input (PIN) and parallel output (POT) instructions perform I/O on a word-by-word central processing unit (CPU) controlled basis. Executing an EOM-POT (or PIN) sequence delivers (or receives) data from the device addressed by the EOM. An EOM-POT (or PIN) sequence cannot be interrupted by an external interrupt.

Two interrupts are typically used in an I/O sequence. One is a data interrupt to signify that the input/output buffer is full/empty, while the other interrupt is used to signal special conditions such as end of message or errors.

Reference 1 gives a detailed description of the XDS 900-series computer interfacing for those who find the above description too brief.

III. Review of the Standard Interface Format

The NCS standard interface output consists of fourteen signals and a power sense line. The fourteen signals consist of eight data signals, two function code signals and four control or handshaking signals. Three of the four combinations of function codes are available for tagging data transmission while the fourth, the 1-1 condition, is reserved for commands out of the computer or status in from the device connected to that computer. Two of the control signals are used as stimulus signals; one from computer (STC) and one from the device (STD). Both of these signals are unidirectional and go true for the complete duration of a message. The remaining two signals are bidirectional control signals called response (RSP) and ready (RDY), which control the handshaking of data across the interface. Response and ready each make one complete cycle (false to true to false) for each byte transferred across the interface.

IV. Programming Characteristics of the Interface

To the programmer, the standard interface appears to be a device, with two associated EOMs. One EOM is used to channel the input or output of the data to the interface while the other is used to communicate status information to and from the program.

A typical data-out sequence is as follows. A status EOM-POT sequence is executed by the program to alert the interface that the data output mode is starting. The hardware will generate a data interrupt at this point to notify the software that the output buffer is empty. The software responds to this interrupt by executing an EOM(DATA)-POT sequence which fills the output buffer and clears the interrupt. This sequence of data interrupts and data POTs will be continued until the desired number of words has been transferred from the computer. There will be one last data interrupt telling the program that the buffer is empty, at which time a status EOM-POT sequence is executed, which terminates the data output mode and automatically clears the data interrupt. This normal data-out mode only uses one of the two interrupts, i.e., the data interrupt. If at any time during this mode, the device connected to the other end of the SIA interrupts the data out mode by either a status insert or by turning the data transmission around by initiating the data input mode, the program would be notified by a service interrupt.

The data-in mode is started by the device. The hardware in the SIA holds the data-in buffer ready when not in use so that three bytes will be transferred to the computer before the first data interrupt occurs. This data interrupt is the same physical interrupt as used in the data out mode, but no confusion can result if the interface is programmed properly. For example, the status of the device can be read at any time to clarify which type of data interrupt is occurring.

V. Status Register

The status register is the means by which software and hardware communicate. The software delivers commands to the SIA via the output status register and reads back various status information from the input status register. Despite this split input/output function, the status register is a single 24-bit register.

A list of input and output bit assignments is given in Table 1. Following is a detailed description of each signal.

C₂₃-C₁₆ Command Byte/Status Byte. These 8 bits are used to communicate to the device connected to the SIA. When a command is to be sent from the computer to the device (see bit 15) the contents of these 8-bit locations are stored in the SIA and transmitted to the device at the proper time in the handshaking sequence.

When the device delivers an 8-bit status byte to the computer, these 8 bits are stored in the SIA and delivered to the computer following an EOM (STATUS)-PIN sequence. These bits are only changed when a new status byte is delivered and so are meaningless unless C₇ is set (see C₇).

C₁₅ Command Flip Flop. Setting this bit via an EOM POT STATUS sequence, causes the hardware to interrupt (at the proper time) whatever I/O process is happening and send a command to the device. If this bit is not set, the contents of C₂₃ through C₁₆ do not get copied into the SIA.

C₁₄-C₁₃. These two bits are the two function codes to be used in the data output mode or the received function codes in the data input mode. These two bits must be set to the desired value at the beginning of each data transmission AND MUST NOT BE CHANGED until the next message.

When the hardware in the SIA detects the data input mode, it switches these two inputs from the output function code flip-flops to the input function code flip-flops, so that these two bits have different meanings depending upon what the hardware is doing.

C₁₂ Data Request. Setting this bit causes the hardware to attempt the data output mode to the device. This request will be honored as long as the device does not override it. Resetting this flip-flop terminates the data output mode.

C₁₁, C₁₀ — B₁, B₀. B₁, B₀ are interpreted in the hardware as a binary number (B₀ = LSB) giving the number of bytes per word to be transferred in the data output mode, or the number of bytes received before a data interrupt is generated, in the data input mode. It is possible to change these bits during a message, but this should only be done during a data interrupt.

C₉ Reset SIA. Setting a 1 in this position triggers a 100-ns pulse that resets the SIA.

C₈ Reset Device. Setting a 1 in this position sets a flip-flop which sends a RESET COMMAND to the DEVICE. This device reset flip-flop is cleared after the RESET COMMAND has been delivered to the device.

C₇ Status Byte Here. A one read in at this position means that a status byte was received from this device. This bit causes a status interrupt and may be reset by putting a one in this position or by RESET. When this bit is set, data output mode is temporarily cut off.

C₆ ASTD. This bit is set to 1 when STD (stimulus from the device) makes a 1 to 0 transition. This bit causes a status interrupt and can be reset by putting a 1 in this position or by RESET.

C₅ STD. This is a raw copy of the signal stimulus from device (STD).

C₄ Device Power. This bit = 1 when device power is off. This will cause a status interrupt to be generated as long as this signal is set, but this can be masked out of the interrupt by a 1 in this position. Setting a 1 in this position does not affect the value read in during a status PIN.

C₃ Device Override. This bit is set to 1, causing a status interrupt when a data byte is received while the data request (see C₁₂) is set.

C₂, C₁, R₁, R₁₁, Respectively. These two bits give the number of received bytes in UNARY. Both are reset to "0" on an EOM-PIN of data (or start or reset). A data interrupt is developed when R₁ = R₁₁ = 1 and a third byte has arrived.

C₀ Data Interrupt. This bit is a copy of the data interrupt.

VI. Design Philosophy

Since it was felt that most noise pulses encountered in practice are high-energy short-duration voltage spikes, and furthermore that most system noise is synchronous with a system clock, it was decided to investigate the possibility of building an asynchronous (clockless) SIA. There was a further line of thought leading to this investigation, i.e., that there is no inherent demand at either end of the interface to have a clock. Certainly the 900-series computer end of the link could use computer timing signals where necessary and the interface would supply other necessary timing signals, e.g., data here, data taken, etc. There also is no need to supply a clock at the device end, for if the device does have a clock, it will not necessarily be the 5-MHz reference required in the DSN specification.

VII. Design Results

The design objectives were completely met in that, a completely clockless interface was built and demonstrated. The heart of the system is the low-pass filtered line receiver shown in Fig. 1. The line receiver is National Semiconductor's DM8820A, a dual line receiver in a 14-pin package. Figure 1 shows one of the control signals terminated in the standard 220/330 Ω terminator and feeding an RC network consisting of the 1 k Ω resistor and the 220 pF capacitor. This RC network forms part of the low-pass filter, as the device itself with the feedback as shown also has an inherent filtering capability of about 10 MHz. The 4.3 k Ω resistor to ground from pin 3 of the DM8820A causes the device to compare the signal on pin 1 to approximately 1.7 V when the output is high, while the 1 k Ω and the diode to the output drops the comparison voltage to about 1.1 V when the output is low. The combined effects of these external components is to add hysteresis, and increase the noise rejection to greater than half the voltage swing in both the high and low signal states.

Laboratory tests of the combined filter and line receiver gave the following results: (a) A square wave input varying between 0.3 and 3.0 V of 3 MHz or higher did not get through the line receiver; (b) A single positive-going pulse of less than 200 ns never got through the line receiver, and some circuits rejected pulses as wide as 250 ns; (c) A single negative going pulse (i.e., signal normally 3 V pulsing to 0.3 V) of less than 200 ns would never trigger the output of the line receiver, and some circuits rejected pulses of 250 ns. The variation in pulse widths rejected can be attributed to variations in external components as well as variations in the line receivers themselves.

Figure 2 shows \overline{RSP} (on the upper trace) and \overline{RDY} (on the lower trace) of an actual handshaking sequence between the SIA for a 900-series computer as it was connected to an external test box which had the full complement of handshaking logic. The signals are as they appear inside of a short (negligible delay) cable. The horizontal calibration is 500 ns/cm, while the vertical scale is 1 V/cm, with ground at the bottom reticle and center reticle for the lower and upper traces, respectively. The upper trace showing \overline{RSP} from the test box (a device), starts the sequence asserted, as the SIA on the 910 computer does not have any data ready. When the 24 bits of data are loaded into the SIA, \overline{RDY} is asserted by the SIA, as seen on the lower trace of Fig. 2. Approximately 300 ns later, the device recognizes the assertion of \overline{RDY} and generates a 100-ns data strobe pulse (not shown) after which \overline{RSP} goes high. Approximately 250 ns later the SIA recognizes the raising of \overline{RSP} , and it completes the cycle by raising \overline{RDY} . A new cycle is then initiated by the device about 350 ns later, when it observes the raising of

\overline{RDY} when it again lowers \overline{RSP} . The total length of the handshaking sequence is about 1.3 μ s. Three handshaking cycles are shown in Fig. 2, the sequence ending there, since the buffer in the SIA is now empty. All three pulses on both traces appear synchronously in Fig. 2, since the relative timing of each is derived from fixed delays rather than a system clock. This synchronous feature considerably aided in the speedy debugging of the initial design and will certainly be helpful in repairing a malfunctioning SIA or device in the future.

VIII. Conclusions

An SIA for XDS 900-series computers has been built without using a system clock. Rather than validating the signal by interrogating it with two clock pulses, the signal is assumed valid only when it is present long enough (200 to 250 ns) to pass through a low-pass filter. The resulting SIA has a peak data transmission rate of approximately 770 kilobytes/s (minus software I/O time). The unit has been successfully tested using a completely functional clockless test unit. The unit has also been successfully tested over 100 m (300 ft) of cable and connected to the precision signal power measurement unit (PSPM). The PSPM is a device with an SIA adaptor, developed by the Digital Projects Group, which uses the double clocking method of filtering the received signals.

A device is now under development which will convert the twin-coax intercomputer communications link (Ref. 2) to a device with an SIA adaptor. This will enable any computer with an SIA adaptor to communicate via coaxial cable to another computer up to 600 m away.

References

1. Martin, W. L., "Digital Communication Tracking: Interfacing with SDS 900 Series Computers," in *The Deep Space Network, Space Programs Summary* No. 37-39, Vol. III, pp. 52-65. Jet Propulsion Laboratory, Pasadena, Calif., May 31, 1966.
2. Lushbaugh, W. A., "A Driver/Receiver Unit for an Intercomputer Communications Link," in *The Deep Space Network Progress Report*, Technical Report 32-1526, Vol. XV, pp. 109-113, Jet Propulsion Laboratory, Pasadena, Calif., June 15, 1973.

Table 1. XDS 900-Series 14 line interface status register

900-Series Bit Number				
23	Least sig. bit }	Command byte on pot Status byte on pin	D1 D2 D3 D4 D5 D6 D7 D8	Line of 14 line interface
22				
21				
20				
19				
18				
17				
16				
15	CMD F.F. Set one EDM Pot status. Reset by start and when CMD sent			
14	F_0 } Function codes to be used in data out mode, or			
13	F_1 } Received function codes			
12	DAT RQST. Indicates data output mode (not needed for CMD out)			
11	B_0 } B_1, B_0 are interpreted in the hardware as a binary number ($B_0 = \text{LSB}$) giving the number of bytes per word to			
10	B_1 } be transferred in output mode, or the number of bytes received before a data interrupt is generated, in input mode			
9	Reset. Setting a one in this position triggers a one-shot pulse to reset the 900 series end of the comm. link			
8	Reset device. Setting a 1 in this position sets a flip-flop which sends a reset CMD to the device. This device reset flip-flop is cleared after the reset command has been delivered to the device.			
7°	Status byte here. Cuts off data out transfer until cleared			
6°	ASTD. Set to 1 when STD makes a 1 to 0 transition			
5	STD. Raw copy of STD line			
4°	Device power = 1 when device power is off, masked out of status interrupt by entering a 1 in this position			
3°	Device override. Set to one when a data byte is received when the hardware is in data out mode			
2	R_1 } Number of data bytes received in unary. Both are reset to 0 on EOM-PIN data or start. A data in interrupt is			
1	R_{11} } developed when $R_1 = R_{11} = 1$ and a third byte has arrived			
0	Data interrupt			

*Status bits 3, 4, 6, and 7 are either masked or reset by potting a 1 in the corresponding position of the status register. Any one of these bits set generates a status interrupt.

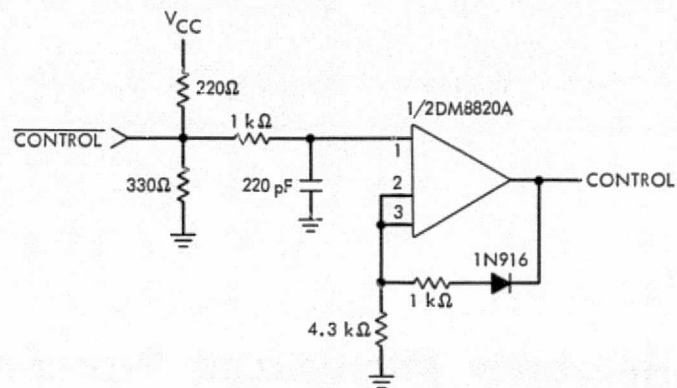


Fig. 1. Filtered line receiver with hysteresis

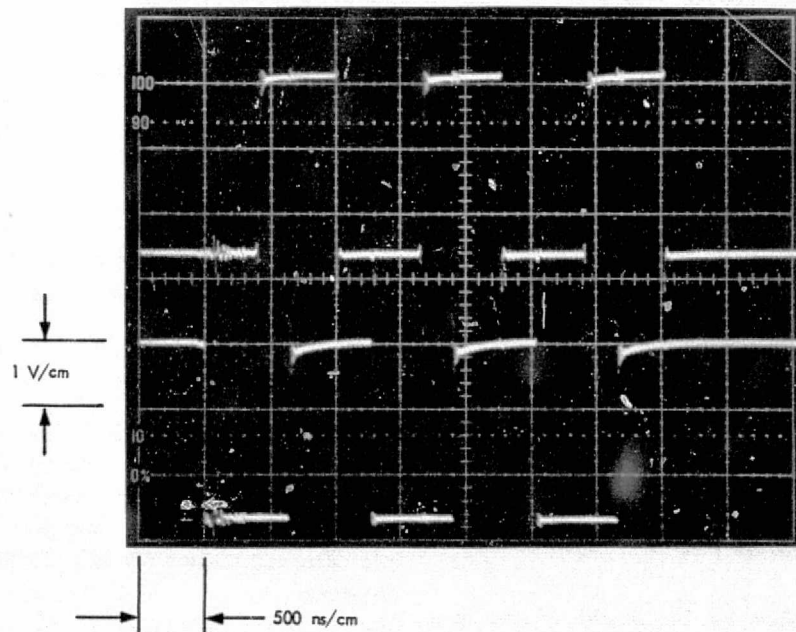


Fig. 2. \overline{RSP} (TOF) \overline{RDY} (BOT)

High-Reliability Microcircuit Procurement Program in the DSN

E. F. Zundel

DSN Data Systems Development Section

A description of the high-reliability microcircuit procurement program is discussed, together with the status and accomplishments in cost reduction and detection of problems which would otherwise go unrecognized. Planned changes and program effectiveness are also discussed.

I. Program Description

The DSN Data Systems Development Section has implemented a program for the procurement of microcircuits screened to a reliability level consistent with the needs of the DSN. Specifications have been prepared which place emphasis on selected process controls to minimize the most frequent industry failure mechanisms, and also to give JPL sufficient visibility into manufacturing operations to insure compliance with JPL requirements.

The program also provides for the establishment of a standard set of logic device types and for constraints which limit designers to their use except in extraordinary justifiable cases. This affords the advantages of:

- (1) A logistical simplification of supply and spares.
- (2) Quantity buys at reduced unit prices.
- (3) Creation of a modest inventory which can adequately support design changes, or management

changes without the penalty of unfavorable procurements to cover the changes.

II. Program Status

Approximately 70,000 devices have been received under this program. Approximately 60,000 are now in production and will be received by October 1975, and additional procurements are planned. Of the total received to date, approximately half (39,000) have been installed in systems.

III. Program Accomplishments

A. Unit Cost

The average unit cost per device has been reduced from \$7.00 on the first procurement to \$3.00 on the current order. There are two major reasons for this reduction in costs: the pooling of orders has resulted in significant quantity discounts, and the test procedures have been

modified in cooperation with the manufacturer. This modification has reduced costs and shortened delivery time with no apparent reduction in reliability.

B. Identified Problem Areas and Corrections

The following problem areas were identified solely because of the JPL specification and the visibility it provides into the manufacturing process. Had the devices been purchased as commercial products or even as supplier-processed MIL-STD parts, the problems would have gone undetected.

1. Foreign material on die (detected at Pre-Cap Visual). This consisted of opaque material on the surface of the die. The supplier's contention that it was on the glass passivation surface only and therefore could do no damage was proved questionable when it was observed also in pre-assembly operations. The supplier agreed to remove all devices that exhibited this condition, until a better understanding of its origin and consequences could be obtained.

2. Lead bonding irregularities (detected at Pre-Cap Visual). Excessive rebond attempts are not permitted by the JPL specification. Since the supplier's requirement was less stringent, many rejects began to appear. A discussion of the condition led to the discovery that the lead frame had been coated with an oily substance which made bonding more difficult. This resulted in a new cleaning procedure to remove the residue.

3. Burn-in deficiencies. Procedures issued by the supplier were not followed completely, permitting devices to be placed in the temperature oven with no electrical stress applied. In another instance, a subcontractor of burn-in services failed to provide required monitoring procedures. In each case, corrective action was taken to insure that all devices would receive full stress for the full time period.

4. Electrical test deficiencies. JPL specifications require 100% testing of each device with variables data furnished. A study of the data revealed the following discrepancies on many occasions:

Discrepancy	Corrective action
Tester malfunction	Retest entire lot
Failed units not removed from test lot	Review each data entry and remove failures
Devices tested twice while next serial number not at all	Review each data entry and remove all suspected failures
Data/device identity lost at post-burn-in tests	Review each data entry and remove all suspected failures or re-test lot

IV. Program Changes

A study of the data submitted with each shipment is being made and, where desirable, the JPL specification limits will be adjusted to agree with the normal data distribution.

V. Program Effectiveness

The objective to provide a procurement program for microcircuits that is cost effective and yields a reliable product has been realized. Of the 39,000 devices withdrawn for system use, only three failures that were not induced are known. One of the three has been verified as a failure, while the other two are under investigation.

Generally speaking, the supplier devotes attention to process details in direct proportion to the interest and concern shown by the customer. The program will continue to be effective as the supplier comes to know that he will be required to demonstrate his compliance with the specifications.

Simulation Time Switch Assembly: A New Conjoint Station Time Switching Capability

M. J. Galitzen

DSN Data Systems Development Section

The DSN conjoint stations located in Spain and Australia have been operating with a tracking and telemetry simulation restriction. The Frequency and Timing Subsystem is able to provide either a real-time output or a simulation time output to the 64-m and 26-m station wings of the conjoint stations at any time, but not both simultaneously. During various tracking schedules, it is useful to be able to conduct a simulation run or training exercise with the non-tracking wing. This station utilization is restricted with the present system. The solution to this problem is to provide a separate real-time and simulation time interface to each of the two stations and to the three Telemetry and Command Processor strings. The simulation time switch assembly will provide the switching capability to drive independently the 64-m, 26-m, and processor interfaces with binary coded decimal time, 1 pulse per second, 100 pulse per second, and 1000 pulse per second Greenwich Mean Time (GMT) real time or simulation/tape time sources.

I. Introduction

The 64-m/26-m conjoint stations have one Frequency and Timing Subsystem (FTS) digital clock system which provides Greenwich Mean Time (GMT) real time, and clock pulses to clock the dual control room telemetry systems. The station configuration required that the two stations and the Telemetry and Command Processors (TCPs) be driven together from the single FTS for a simulation or training exercise, or for a spacecraft track. The subsystem to processor interface is shown in Fig. 1. Figure 1 shows that the present subsystem can be

switched to either the real-time mode or the simulation mode. The real-time input to the subsystem is amplified and distributed to the TCP 1, 2, and 3 equipment. The simulation input to the real-time switch is derived from a serial to parallel time code translator (TCT) which is a part of the Pre-Post Recording (PPR) Subsystem. The input to the time code translator is a 36-bit serial NASA time code. This code is switched at the Pre-Post Recording Subsystem and is used to drive the time code translator. The inputs to the translator are derived from either the Simulation Conversion Assembly (SCA) time code generator (TCG) or the 64-m/26-m tape recorder

time playback channels. The 30-bit binary coded decimal (BCD) time codes and a 1-pulse-per-second (pps) signal are provided by the time code translator for the FTS simulation channel. The binary coded decimal signals are distributed to all complex equipment when the FTS is in the simulation switch mode. The time code translator 1 pps is used to reset the subsystem timing pulse outputs before they are distributed. The subsystem outputs are reset only when in the simulation mode.

The TCP 2 presently has a special time switch assembly. This assembly switches the 30-bit binary coded decimal, 1-pps and a 1-kpps signal from either the time code translator or the FTS. The TCP 2 time switch assembly reamplifies and distributes the 30 binary coded decimal real time or simulation binary coded decimal and the 1-pps, 1-kpps pulse inputs to the TCP 2 computers. The TCP 1 and 3 computers can only be used for simulation if the FTS is in the simulation position. A summary of the configuration and constraints of this system is given in Fig. 2. Line A shows the operational modes when the FTS GMT switch is on GMT. Line B shows the lack of flexibility when the subsystem GMT switch is in the simulation position.

II. New Configuration

The simulation time switch assembly (STSA) was built to replace the time switch assembly and to expand the FTS GMT time distribution. Figure 3 is a functional diagram of the FTS, Pre-Post Recording Subsystem, simulation time switch assembly, and station configuration. The simulation time switch assembly receives inputs from the FTS and the Pre-Post Recording Subsystem time code translator. The FTS input consists of the 30-bit GMT binary coded decimal time bits, 1 pps and 1 kpps. The assembly time code translator also provides the binary coded decimal and pulse outputs for a tape playback mode. The assembly uses the simulation and tape 1 pps and 1 kpps to generate internally a 100-pps signal for the simulation and tape channels. The assembly can then independently switch the real-time and nonreal-time input pulses and binary coded decimal GMT to the 64-m station FTS distribution system, the 26-m station FTS distribution system, and each of the three Telemetry and Command Processors. This capability then allows the 64-m station and the 26-m station to operate independently. The basic capability of the new system can be summarized in the following two statements:

- (1) The simulation time switch assembly provides real-time and simulation time buses which allow each

telemetry string and station to connect to either bus independently.

- (2) The simulation time switch assembly also provides sufficient distribution amplifiers to drive multiple-telemetry processing strings and station loads which are to be switched on to the assembly buses.

A. Tape Time Mode

The real-time/simulation inputs to the simulation time switch assembly originate at the FTS GMT/SIM switch and the assembly time code translator. The GMT/SIM position of the FTS is driven by 30 binary coded decimal bits from the time code translator mounted within the simulation time switch assembly. The input to the time code translator would normally be from 64-m or 26-m station tape recorder time channels. This input provides a means of switching tape playback time on to the FTS simulation time switch assembly real-time bus. In this tape playback mode, the FTS real-time bus then becomes a nonreal-time (tape time) bus. Control switches connected to the assembly will be used to activate the assembly time code translator tape pulse outputs in conjunction with the FTS simulation switch.

B. Dual Time Operation

The Pre-Post Recording Subsystem time code translator would be used to provide the simulation time bus with simulation time. By using the frequency and timing/simulation bus and the simulation time switch assembly simulation bus, the stations can conduct a tape playback verification and a simulation or training exercise simultaneously. The control of both of these buses is from a central control panel mounted in the Station Monitor and Control (SMC) Subsystem. This panel provides the switching point for the simulation time switch assembly. The assembly has an independent single status monitor output. This output will provide digital information to the Monitor Subsystem. This information will be input to the station monitor computers which would record or display the assembly switching status.

III. Simulation Time Switch Assembly System Design

The assembly requires a standard equipment rack. Mounted within this rack are pulse amplifiers, amplifier power supplies, a time code translator, a control and status assembly, coaxial switch assembly, a binary coded decimal relay assembly, and a signal distribution assembly.

The block diagram of the simulation time switch assembly binary coded decimal switching is shown in Fig. 4. The 30 binary coded decimal bits from the FTS simulation bus are distributed to five 51-pole relays. One relay is provided for each of the five outputs. These channels, as stated before, are for the 64-m and 26-m station Frequency and Timing Subsystems, and for the three Telemetry and Command Processors.

A. Failure Isolation

The FTS binary coded decimal signals are amplified and sent to the FTS distribution system. This series amplifier protects the simulation time switch assembly FTS/GMT bus from 64-m station binary coded decimal line failures or feedback. The signals to the 26-m station FTS distribution are re-amplified and isolated within the 26-m station FTS distribution system. The Telemetry and Command Processor outputs are also amplified, isolated, and distributed to the three processors through their respective relays. Each of the five relays has an external independent control and monitor interface. This is represented by the circled capital R on Fig. 4.

B. Timing Pulse Distribution and Switching

The distribution and generation system for the 1 pps, 100 pps, and 1 kpps is shown in Fig. 5. The Frequency and

Timing Subsystem provides a 1-pps, 100-pps, and 1-kpps timing pulse input. These signals are amplified, isolated, and distributed to five coaxial relays. The time code translator from simulation and the time code translator within the simulation time switch assembly each provide a 1-pps and a 1-kpps input. These signals are used to generate a synchronized 100 pps for the simulation and tape channels. The simulation tape 1 pps, 100 pps and 1 kpps are switched within five sets of three coaxial relays. The relays have three inputs, one each for FTS, simulation, and tape pulses. The output of the coaxial relays is controlled by the external monitor and control panel within the Station Monitor and Control Subsystem. Status lines are sensed and are part of the remote monitor interface. This interface is combined with the binary coded decimal status lines to form an interface which can be sensed by the station monitor computers.

IV. Conclusions

The simulation time switch assembly will support the Viking multiprobe mission. This system will allow tracking, training, and simulation in a dual station simultaneously. This will increase the utilization of the dual station configuration. In future years the tape playback channel will be used for tape verification as well as for simulation from prepared test tapes.

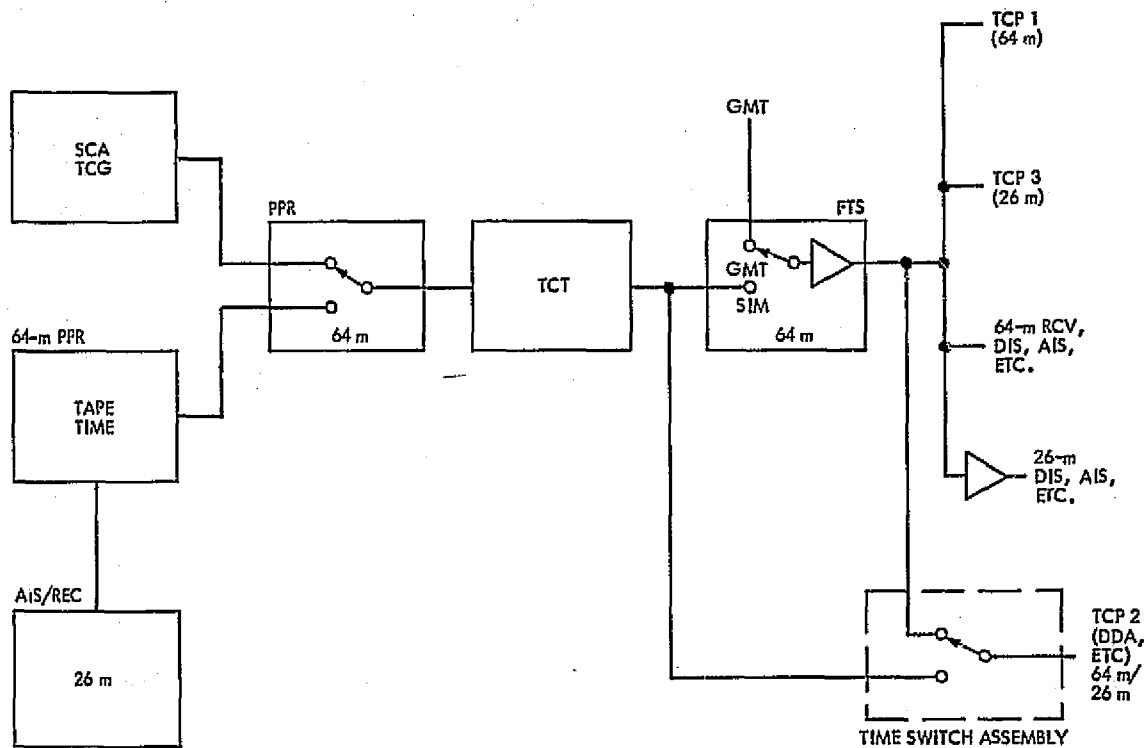


Fig. 1. Present configuration for DSSs 43/42, 63/61

LINE	TLM STRING 1	TLM STRING 2	TLM STRING 3	STATION EQUIPMENT	
				64 m	26 m
A	GMT	GMT OR SIM	GMT	GMT	GMT
B	SIM	SIM	SIM	SIM	SIM

Fig. 2. Present capabilities of dual station time switching

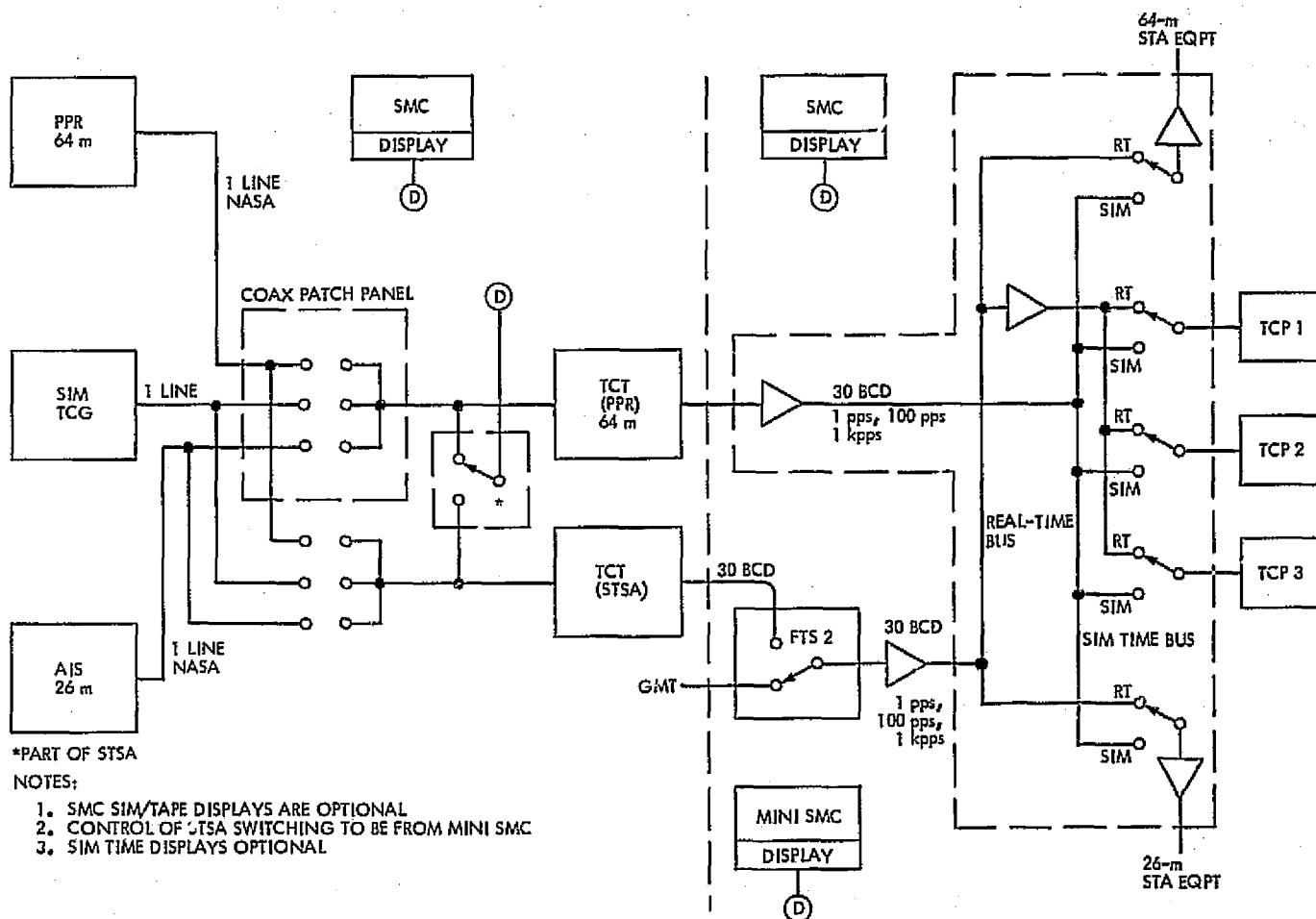


Fig. 3. Simulation time switch assembly configuration

ORIGINAL PAGE IS
OF POOR QUALITY

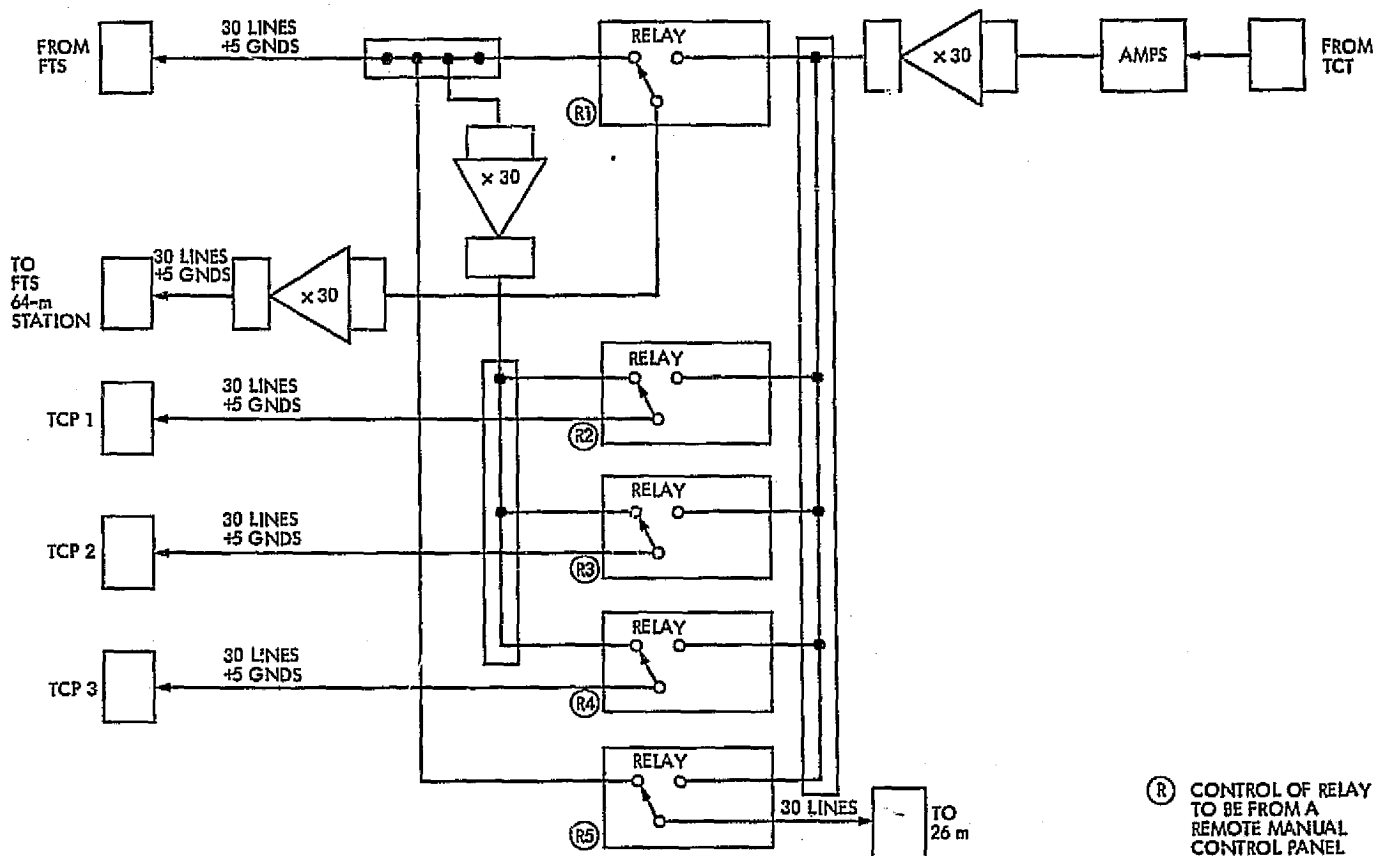


Fig. 4. Block diagram of simulation time switch assembly BCD switching

ORIGINAL PAGE IS
OF POOR QUALITY

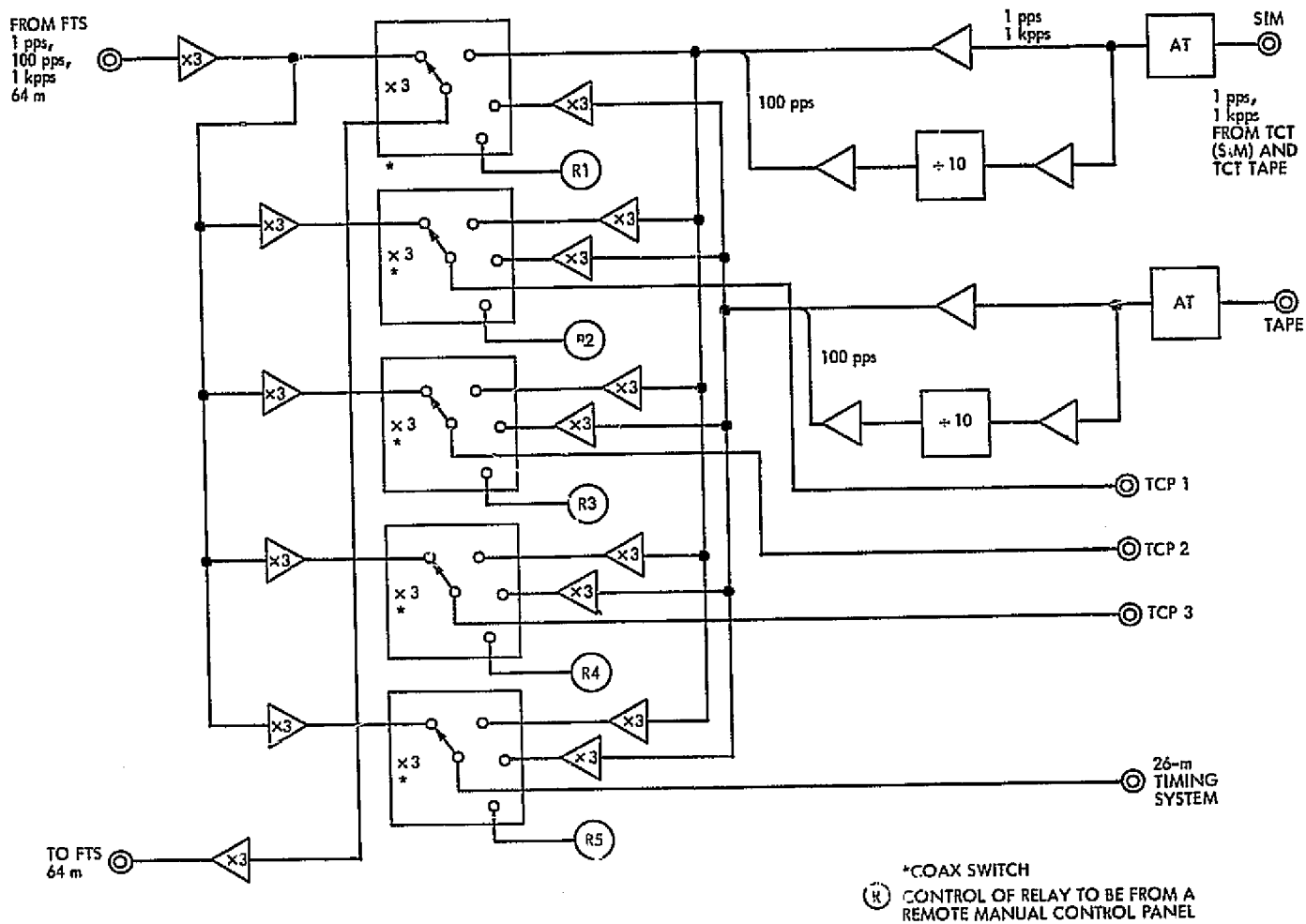


Fig. 5. Block diagram of simulation time switch assembly for 1 pps, 100 pps, and 1 kpps

Automatic Space Noise Recorder

R. W. Livermore

Tidbinbilla Deep Space Communications Complex

A method is described of adding hardware and software to the Antenna Pointing Subsystem (APS) for star tracking and to check pointing. The addition is also designed as an aid in using the antenna for radio astronomy. The antenna will automatically scan radio stars in hour angle and declination. Noise is sampled by an analog-to-digital (A-D) converter and recorded (along with other parameters) onto magnetic tape.

I. Introduction

Present methods of star tracking require careful operation and recording of levels, usually on a chart recorder. Operationally, this method is tedious and liable to errors. This article describes an automatic method which records all data on magnetic tape for future processing. It is proposed to deal with processing in a later article, however an initial program using a least squares curve fitting technique to a normal curve has proved very accurate in obtaining a measure of antenna accuracy. Recording errors should be eliminated, and a minimum of operator supervision is required to continuously star track. The program has been written with selectable modes of operation with a view to easily adding any extra scanning or data collection methods.

II. Additional Hardware

An XDS TM4 magnetic tape recorder is connected to the W buffer of the APS. Records are written on magnetic

tape in 480-word blocks using interlace. A 10-bit A-D converter is connected to a spare 24-bit parallel input of the APS which uses EOM 30020. The A-D converter is triggered 50 times per second in parallel with the normal 50 PPS supplied to the APS. Bits 0 to 9 of the 24-bit word input are used to allow use of the sign bit 0 when processing within the XDS 910 computer. The analog input to the A-D converter is obtained from the 2-volt output 0.1-second time constant of the broadband square law detector.

III. Additional Software

The program was written as an overfill for program DOI-5047-OP, which is the antenna pointing program for the 64-meter antenna at DSS 43. The overfill uses about 2000 extra octal locations and was allocated locations 13000 and up. A new declination rate offset interrupt routine has been written to select the mode of operation and initialize counters and scan rates. A real-time auto-track facility has recently been added and has been tested

on a star of about 40 flux units. Briefly, the method is to keep a running mean of 10 seconds worth of data, and to optimize by automatic entry of offsets; hour angle and declination are adjusted alternately at one-minute intervals. Examination of the digi-switch input is made to determine the program selected. There are 20 remaining bits left, which will be useful for other information that may be required at a later stage.

IV. Program Operation

A normal hour angle and declination star input is made at the APS control panel, and the antenna is pointed at the star. To commence an automatic scanning star track, magnetic tape unit No. 1 is made ready and the declination rate offset interrupt switch is operated with the declination rate offset value set to zero. The antenna then goes into continuous declination scans followed by hour angle scans. The drive off and on is at 5 times sidereal rate and the scan is at sidereal rate (sidereal rate = 0.004178 degrees per second). It is intended to be able to increase scanning rates up to 5 times sidereal rate with a later version of the program. The A-D converter samples 50 times per second and data are recorded only during the sidereal rate scans. The declination scan is over a local declination of one degree. The hour angle scan is over $1/\cos$ declination degrees. Data are written on the magnetic tape in binary records of 480 words, once per minute.

V. Magnetic Tape Data Formats

The 480-word record is divided up into 60 sections. Each section of 8 words is allocated the following values: DOY, GMT, sample, hour angle, declination, azimuth, elevation and sum of squares.

- (1) DOY (day of year) is in 4-bit BCD (binary coded decimal).

- (2) GMT is in 4-bit BCD.
- (3) The value of the sample is the sum of the previous 50 samples per second.
- (4) Hour angle, declination, azimuth, and elevation are all commanded angles in $1/1000$ of a degree with binary point at bit 024 (octal).
- (5) The sum of the squares of the sample is also available to allow calculations of the standard deviation.

To assist in processing to find accuracy of the antenna, the two most significant bits of the DOY word are used to indicate zero offsets in either hour angle or declination. This occurs when the antenna is being commanded to point at the source. Bit 0 is true for the center of the declination scan. Bits 0 and 1 are true for the center of the hour angle scan.

VI. Printing and Graphing Results

A sample of the type of result obtained is shown in Table 1 for Virgo, Day 63. Other parameters can be listed, such as right ascension and declination, local hour angle and local declination, DOY and GMT, azimuth and elevation, and value of the least sum of squares.

VII. Conclusions.

Initial processing of the magnetic tape recordings has been good. Filtering of the samples is necessary, and accurate estimations of antenna pointing accuracy can be made. Processing is not done in real time, therefore longer routines can be employed. Curve fitting equations can be used with greater accuracy than that of the pointing program itself which is ± 0.001 degrees. It is feasible to record angle tracking data at the APS, together with sampling an analog input. This could be done at a rate of 50 times per second, without impairing normal pointing facilities while tracking a spacecraft.

Acknowledgment

Thanks are due to D. L. Jauncey (Australian Commonwealth Scientific Industrial Research Organization) for valuable advice on desirable methods of star tracking.

Table 1. Antenna offsets in 1/1000ths of degree

Hour angle	-20	-10	0	+10	+20
344.197	I	I	I	D ^b	I
345.484	I	H ^a I	I	I	I
346.761	I	I	I	D	I
348.048	I	HI	I	I	I
349.320	I	I	I	D	I
350.612	I	HI	I	I	I
351.890	I	I	I	DI	I
353.177	I	HI	I	I	I
354.455	I	I	I	DI	I
355.741	I	HI	I	I	I
357.019	I	I	I	DI	I
358.306	I	HI	I	I	I

^aD = declination.
^bH = hour angle.

An Evaluation of the Use of a Cathode Ray Tube Light Pen Option Within the Deep Space Station Monitor and Control Subsystem

J. Thomson

DSN Data Systems Development Section

A routine has been written and tested to provide a run-time environment to evaluate the feasibility of using a cathode ray tube light pen option to simplify the operator interface with the Deep Space Station Monitor and Control Subsystem. This routine introduces two new concepts within the scope of the operator/program interface. First is the idea of using a selection list to aid the operator in executing the available commands. Second is the concept of using a tree-like hierarchy of information display for improved fault detection and isolation.

I. Introduction

During the previous year, a routine was written and tested to provide an environment to evaluate the feasibility of using a light pen option within the DSN Monitor and Control Subsystem. The light pen, along with the current cathode ray tube (CRT) terminal, would be used to simplify the operator interface with the Station Monitor and Control Subsystem. The routine was written to operate within the station Monitor and Control

Subsystem Operational Program, for purposes of the evaluation.

II. Hardware Description

The Monitor Program resides in a Xerox Data Systems (XDS) 920 computer contained within the Digital Instrumentation Subsystem. This subsystem is connected to the other Deep Space Station subsystems via several

types of communication links. The current operator/program interface uses a CRT station to display the status of the DSS and to allow input of control messages (commands).

The light pen option can be added to the CRT station and consists of the following:

- (1) Two circuit boards fitting within the CRT controller.
- (2) A light pen holder assembly plugged into the controller and connected to the light pen.
- (3) A light pen; a small hand-held device with a photo sensor at its end.

III. Hardware Operation

The light pen system functions as follows: When the pen is held up to a character displayed on the CRT, its photo sensor receives an impulse every time the character is refreshed. This impulse causes the light pen controller to copy the contents of the CRT refresh address register into the light pen address register. Thus, the location of the character selected by the pen can be saved. If the address remains constant, the light pen controller causes a blotter character to flash at the selected location. At this point, the light pen switch can be pressed causing the CRT controller to enter the interrupt mode.

IV. Monitor Input and Data Display

The Monitor Program uses the CRT as an interactive terminal for the input of commands and to display the current status of a Deep Space Station in the form of a grid of 20 parameters. Each of the 110 available parameters gives the status of some subsystem or value by displaying the parameter's name and its value. The value's color is used to give parameter status. For example, a value displayed in red indicates an alarm condition, and a value displayed in yellow indicates a warning condition. Normal or good values are displayed in green or blue. Commands may be keyed on line 0 of the CRT screen and executed by pressing the interrupt key. The commands are used to control operational features of the Monitor and may be used to select a single parameter or a set of 20 parameters, called a format, for CRT display.

V. Purpose

The task can be divided into two main goals:

- (1) To develop the essential software for communication between the light pen and the XDS 920 computer, and to test the available hardware for any defects and for ease of physical manipulation.
- (2) To develop the software needed to provide a run-time environment for evaluating the use of the light pen to simplify the operator interface with the Monitor Program.

VI. Program Description

This routine introduces two new concepts within the scope of the operator interface. First is the idea of using a selection list to aid the operator in executing the available commands. Second is the concept of using a tree-like hierarchy of information display for improved fault detection and isolation.

Each time the light pen switch is pressed, two pieces of information must be obtained: first, if necessary, the source of the interrupt can be determined by requesting the "status word" which contains a 1-bit flag if the interrupt was from the light pen rather than the keyboard; second, the light pen address must be requested—once translated, the address yields the row and column of the selected character.

Once this information is obtained, the program can be made to react in any given way. This program is actually made up of two separate subprograms. The first has been written as a means of creating the commands used by the monitor with a minimal use of the keyboard. The commands can be divided into two or three fields. Since there are a limited number of choices for field-1, they can be displayed within a "selection list." After field-1 is selected, the corresponding field-2 choices can be listed, etc. Once the command has been determined (and created on line 0), it can be processed and executed by the Monitor software.

The second subprogram has been provided as an alternative to the formatted display of parameters. All of the approximately 110 parameters displayed by the Monitor program have been separated into several groups—and some groups have been separated into smaller subgroups. Each group has a "header" parameter associated with it. The color of the header is determined by worst status of any of the parameters within the group. For example, if one parameter turns yellow and one turns red, the header will turn red, indicating an alarm condition within the group. The headers are grouped together in a similar fashion so that all parameters together form a

"tree." If any single parameter turns red, the root of the tree will also turn red, indicating trouble. Thus, only one parameter needs to be displayed.

A "page" of information about any subtree (a header and its group) can be accessed by using the light pen to call the subprogram and then advancing and/or retracing through the tree to the proper subtree. Since this was a sample program, the pages were simple and consisted of a title, a list of parameters or headers within the group, some information messages pertaining to the group, and a return list of the previous pages that could be recalled. The user could advance to a subtree by selecting a header parameter displayed on the current page and retrace to a previous page by selecting a page title within the return list.

VII. Results

There were several problems which involved the particular hardware used. The light pen lacked sensitivity to certain characters and could only respond to characters in blue. This tended to slow down an inexperienced user. Another difficulty was that wherever messages were being output onto the CRT screen, both the light pen and keyboard were disabled. This tended to cause less difficulty with the light pen than with the keyboard, since keyed-in commands with a dropped character resulted in an error.

Pressing the light pen switch twice in close succession sometimes caused the command to be erased. Minor

improvements in the light pen hardware and the CRT routine should help to alleviate these problems.

The basic light pen operating system required to find the light pen row and column used 160 24-bit locations in addition to the CRT routine. The page handling routines used 270 locations. Most of the 2000 locations were used to create the Monitor commands. With this much core usage, it became necessary to delete part of the Monitor Program to make space available. New computer hardware with increased core memory and a disk operating system would alleviate this problem. This would allow room for a complete monitoring and diagnostic system using the page display subprogram. This program would also be ideal for a disk operating system, since only a small amount of data is needed in core for the displayed page of information.

VIII. Conclusions

The concept of a selection list helped to make the user aware of the full scope of commands available and simplified their execution. The page display subprogram produced successively higher degrees of diagnostic information and thus provided a fast and accurate means of pinpointing a problem area in the system. The simple tree structure also helped an unfamiliar user to understand the structure of the DSS and its subsystems. These simplifications in the operator interface could be used to lower the level of training required for operational personnel and thus could provide a savings in operational costs for the DSN.

Computation of Gravity RMS for HA-DEC Antennas

M. S. Katow and R. Levy
DSN Engineering Section

The gravity load distortion rms (half path length) values are calculated for the hour angle-declination angle (HA-dec) antenna by computing the positions of the three principal axes fixed on the reflector structure, but rotating in declination and hour angle. For a symmetric structure, the rms values are equal to the results from the standard square root of the sum of the squares equation. For unsymmetric structures, the required modifications to the equation are described. Contour level plots for a sample 27.4-m HA-dec antenna show the variations of the rms with respect to selected surface panel setting positions. Also plotted are the X, Y, and Z load components for the panels set at zenith look.

I. Introduction

To compute the gravity loading distortions of a ground radio antenna structure, a model is created that is input to the NASTRAN or IDEAS program and the displacements of the surface panel mounting points are best fitted with a paraboloid and the rms of the residuals becomes an index useful for determining the RF performance.

A practical structural model will usually be described by using a rectangular or cylindrical coordinate system fixed on the reflector with the three principal axes (1) "X" parallel to the elevation axis, (2) "Y" normal to X and (3) "Z" normal to the X-Y plane and coincident with the centerline of the reflector structure.

For the azimuth-elevation (az-el) axes configuration, the angle between the gravity vector and the Y and Z axes is either the elevation angle or its complement. However, for the hour angle-declination angle (HA-dec) axes configuration, the angle between the gravity vector and the principal axes of the structural model becomes a function of the declination, hour, and latitude angles.

The standard coordinate conversion equations from the HA-dec system to the az-el system are used to solve for the components of the gravity vectors along the principal axes of the structural model.

Gravity loadings applied in the directions of the three principal axes are the basic loadings of the structural

model. The associated three rms values can then be combined by superposition with the geometric relationships to determine the resultant rms for a particular pointing direction of the antenna.

The rms is computed in this report, as described above and detailed below, by superposition. However, an alternative rms value can be computed for any particular pointing direction with the rms program (Ref. 1) by adding three component displacements for the three basic loadings into a single displacement vector before the best fit by the paraboloid is made. Some comparisons using the results from both methods are presented together with the explanations of the accuracies of the superposition method.

The sample antenna is a modified reflector structure of the Caltech 27.4-m (90-ft) HA-dec antenna.

II. Calculations

The motion of the RF boresight of a HA-dec antenna may be described by the equatorial coordinates system. The two axes of rotation are centered at point "O" of Fig. 1. The polar axis is OP and the rotation about this axis is measured in hour angle " t " from the meridian circle. The rotation of the declination axis is measured as declination angle " δ " from the equator $OUQR$. The resultant direction of the RF boresight is along the radial line OM , which intersects the spherical surface at M .

The computer model is assumed to use the coordinate system described in the second paragraph. The Z axis of the reflector structure is coincident with radial line OM and the RF boresight direction line. The azimuth measuring vertical plane $OZMH$ contains these lines and the vertical gravity vector MG . As shown in Fig. 2, the X and Y principal axes of the reflector are rotated with respect to this azimuth measuring plane as the Y axis is coincident with the hour angle great circle. This angle of rotation measured at point M is β , the angle between the hour angle circle and the azimuth measuring circle ZMH .

Spherical triangle PZM may then be used to compute angle β . That is, given

A = azimuth angle

PZ = 90-deg - polar angle ϕ

t = hour angle

PM = 90-deg - declination angle δ

then compute

ZD = zenith distance

from

$$\cos(ZD) = \sin(\phi) \sin(\delta) + \cos(\phi) \cos(\delta) \cos(t)$$

which is a standard astronomical formula.

Using half angle relations of the sides and angles of a spherical triangle to minimize sign anomalies, the following equations were used:

$$1/2[A + \beta] = \tan^{-1} \left[\frac{\cos\left(\frac{PM - PZ}{2}\right) \cos\frac{t}{2}}{\cos\left(\frac{PM + PZ}{2}\right) \sin\frac{t}{2}} \right] \quad (1)$$

$$1/2[A + \beta] = \tan^{-1} \left[\frac{\sin\left(\frac{PM - PZ}{2}\right) \cos\frac{t}{2}}{\sin\left(\frac{PM + PZ}{2}\right) \sin\frac{t}{2}} \right] \quad (2)$$

β and A may be resolved from the above equations by computing the right sides of the equations. Then

$$\beta = \text{right sides } ((1) - (2))$$

$$A = \text{right sides } ((1) + (2))$$

The antisymmetric gravity vector component MJ acts at angle β to the X and Y axes of the reflector. Therefore the resultant component factors with respect to the unit gravity vector for the two X_c and Y_c axes are:

$$X_c = -\sin(ZD) \sin(\beta) - X'_c \quad (3)$$

$$Y_c = -\sin(ZD) \cos(\beta) - Y'_c \quad (4)$$

For the Z component, since gravity is on or working at any position and our primary interest is that due to the change in the direction of the Z gravity vector, it follows that

$$Z_c = 1.0 - \cos(ZD) - Z'_c \quad (5)$$

1.0 is the unit gravity vector value at zenith look where ZD -zenith distance is equal to 0.

X'_c , Y'_c and Z'_c are the component values at the surface panels setting position. The rms for a particular pointing direction may then be computed by

$$rms = \sqrt{(rms_x)^2(X'_c)^2 + (rms_y)^2(Y'_c)^2 + (rms_z)^2(Z'_c)^2} \quad (6)$$

When the antenna structure is symmetric about the three axes, the above equation may be used. When the structure is not symmetrical, the method of resolution described in the Appendix will be necessary. The Appendix also illustrates the use of vector analysis to compute the load components.

III. Results

A computer program was coded to solve for the load components and for the rms distortions for a range of declinations and hour angles. A JPL library subroutine was used to output contour level plots of the results.

First, the surface panels of the antenna were assumed to be set to a perfect paraboloid at zenith look, with hour angle = 0 and declination angle = 37 deg (the polar angle = 37 deg). Then the surface panels setting position was changed to 0 deg declination 0 deg hour angle and to -10 deg declination. The rms were computed and output on contour level plots (Figs. 3, 4, and 5 respectively).

The X, Y, and Z load components for only the zenith look panels setting cases are plotted where the X'_c , Y'_c and Z'_c components are equal to 0 (Figs. 6, 7, and 8, respectively).

For other surface panels setting angles, the particular load components at the setting angle may be subtracted

from the curves for the zenith look case to obtain the resulting changes from the setting position.

Table 1 lists some computed rms values for using the superpositioning method and the displacement adding and best fitting rms program.

IV. Summary

The rms values in this report are only for the surface panel mounting points of the reflector structure. Errors of the surface panels, for setting, etc., must be added to obtain the rms values the RF uses.

For DSN use, the celestial targets are close to the ecliptic plane. Inspection of the rms values along the 0 deg declination angle vs. hour angles shows that the minimum degradation due to gravity loads results when the surface panels are set with the reflector close to 0 deg declination angle.

For the northern hemisphere locations, in the next decade, the far out planets will be below the ecliptic. For this condition, better performance under gravity loads can be expected with the initial setting of -10 deg or lower elevation angles.

It is interesting to note that the setting of the surface panels at 0 deg declination minimizes the Y-component changes. Referring to Fig. 7, the Y-component does not change throughout the hour angle change; it starts with about 0.6 and remains at this figure. For surface panels set at 0 deg declination, the gravity distortions contribution by the Y component is zero for targets along the ecliptic.

Appendix

General Formula for RMS Computation

In the foregoing, relationships have been given to express the loading components in the direction of the reflector coordinate axes, and an equation has been supplied for computation of the rms in terms of the three rms values computed independently for the loadings along each of the three reflector axes. The equation given, however, is correct only for the case of a reflector structure that is symmetric about its own X-Z and Y-Z planes. In the general case where this symmetry does not occur, the equation must be modified to account for coupling of the loading. In Ref. 2 relationships have been given to compute the rms for a general, unsymmetric az-el antenna. That development will be extended to the HA-dec type of axes arrangement.

We will consider a moving set of X, Y, and Z axes attached to the reflector as described previously and a set of reference axes fixed on the ground. For the reference set of axes let X_0 and Y_0 establish the horizon plane

where

X_0 points east

Y_0 points north

and let

Z_0 point to the zenith

If we consider a set of unit vectors $\{e_r\}$ aligned with the reflector's X, Y, and Z axes, and set of unit vectors $\{e_0\}$ aligned with the X_0 , Y_0 , and Z_0 axes, then the transformation from the reflector to the ground axes can be made by

$$\{e_r\} = [T] \{e_0\}$$

The components of the transformation (orthogonal) $[T]$, in terms of the latitude, ϕ , the declination, δ , and the hour angle t , can be shown to be

$$[T] = \begin{array}{ccc} \cos t & -\sin t \sin \phi & \sin t \cos \phi \\ \sin \delta \sin t & \cos \delta \cos \phi + \sin \delta \sin \phi \cos t & \cos \delta \sin \phi - \sin \delta \cos \phi \cos t \\ -\cos \delta \sin t & \sin \delta \cos \phi - \cos \delta \sin \phi \cos t & \sin \delta \sin \phi + \cos \delta \cos \phi \cos t \end{array}$$

The components of the third row of the transformation are the components of a unit vector in the direction of the reflector Z axis, which is the pointing vector. Consequently, in azimuth-elevation coordinates, the elevation angle α , (the complement of the zenith distance) is given by

$$\sin \alpha = T_{3,3} = \sin \delta \sin \phi + \cos \delta \cos \phi \cos t$$

Similarly, the azimuth angle, A , can be found from T as

$$\cos A = T_{3,2} / \cos \alpha = (\sin \delta \cos \phi - \cos \delta \sin \phi \cos t) / \cos \alpha$$

As an alternative to computing the gravity load components according to relationships given previously, we can take the vector scalar product of a unit vector in the

direction of gravity loading (components 0.0, 0.0, -1.0) with each of the three components of $\{e_r\}$ in turn to obtain the projections \underline{X} , \underline{Y} , \underline{Z} on the reflector X, Y, and Z axes. As the result, we find:

$$\underline{X} = -T_{1,3} = -\sin t \cos \phi$$

$$\underline{Y} = -T_{2,3} = -\sin \delta \cos \phi \cos t - \cos \delta \sin \phi$$

$$\underline{Z} = -T_{3,3} = -\sin \alpha$$

The panel setting position is defined by the elevation rigging angle γ . When the setting angle has declination $\underline{\delta}$ and zero hour angle, then γ can be found from

$$\gamma = 90 - \phi + \underline{\delta}$$

At the setting position, the unit loading vector has the following projections, \underline{X}_s , \underline{Y}_s , \underline{Z}_s , on the reflector axes

$$\underline{X}_s = 0.0$$

$$\underline{Y}_s = -\cos \gamma$$

$$\underline{Z}_s = -\sin \gamma$$

Consequently the net projections of the unit loading vector are

$$\xi = \underline{X} - \underline{X}_s = -\sin t \cos \phi$$

$$\eta = \underline{Y} - \underline{Y}_s = \cos \gamma - \cos \delta \sin \phi + \sin \delta \cos \phi \cos t$$

$$\zeta = \underline{Z} - \underline{Z}_s = \sin \gamma - \sin \alpha$$

From the linearity of the antenna structure response to gravity loading it follows that the displacements of the structure at any orientation (δ, t) are a linear combination of the separate displacements caused by gravity loading in the directions of the X, Y, and Z axes. That is, let

$$\{u(\delta, t)\} = \text{the displacement vector at } \delta, t$$

and

$$\{u_x\}, \{u_y\}, \{u_z\} = \begin{array}{l} \text{displacement vectors for gravity} \\ \text{applied in the X, Y, Z, directions} \\ \text{respectively} \end{array}$$

then we have

$$\{u(\delta, t)\} = \xi \{u_x\} + \eta \{u_y\} + \zeta \{u_z\}$$

Since the pathlength deviations of the reflector surface from a paraboloid are linear functions of the displacements and the geometry of the surface, the foregoing equation for superposition of displacements also applies to pathlength deviations.

Furthermore, as shown in Ref. 2, the pathlength deviations from the best-fitting paraboloid are also a linear function of the displacements. Therefore it follows also that pathlength deviations from the best-fit paraboloid at any reflector attitude can be obtained by superposition of the deviations for the three sets of gravity loadings applied independently in the X, Y, and Z directions.

Therefore, if we let

SSX , SSY , SSZ be the mean square half pathlength deviations from the best fitting paraboloids for gravity loadings in the X, Y, Z directions respectively

and

SXY , SXZ , SYZ be the mean inner product of the half pathlength deviation vectors for X and Y, X and Z, Y and Z, gravity loading respectively,

then the mean square pathlength deviation SS at any reflector orientation is given by

$$SS = \xi^2 SSX + \eta^2 SSY + \zeta^2 SSZ \\ + 2\xi\eta SXY + 2\xi\zeta SXZ + 2\eta\zeta SYZ$$

To make this equation represent the mean square pathlength deviation for an az-el antenna, set

$$\xi = 0$$

$$\eta = \cos \gamma - \cos \alpha$$

For a reflector structure that is symmetric about the X-Z plane, SYZ and SXY are zero. For a reflector that is symmetric about the Y-Z plane, SXZ and SXY are zero.

Finally, take the square root of the mean square to obtain the rms half pathlength deviation.

References

1. Katow, M. S., and Schmele, L. W., "Antenna Structures: Evaluation Techniques of Reflector Distortions." *Space Programs Summary 37-40*, Vol. IV, pp. 176-184. Jet Propulsion Laboratory, Pasadena, California, Sept. 30, 1968.
2. Levy, R., "A Method for Selecting Antenna Rigging Angles to Improve Performance." *Space Programs Summary 37-65*, Vol. II, pp. 72-76. Jet Propulsion Laboratory, Pasadena, California.

Table 1. RMS vs antenna position for 27.4-m (90-ft) HA-dec antenna^a

Panels set position		Antenna attitude		Reflector principal axes load components			Reflector distortion - rms, mm ^b	
Dec, deg	HA, deg	Dec, deg	HA, deg	X _c	Y _c	Z _c	Superposition	Rms program
37	0	-53	0	0.	-1.0	1.0	1.29	1.29
0	0	-53	0	0.	-0.39819	0.79864	0.87	0.87
-10	0	-53	0	0.	-0.26865	0.66200	0.73	0.73
37	0	0	90	-0.79864	-0.60182	1.0	1.23	1.23
0	0	0	90	-0.79864	-0.	0.79864	0.95	0.95
37	0	-10	50	-0.61179	-0.68181	0.59895	0.90	0.90
0	0	-10	50	-0.61179	-0.08000	0.39759	0.56	0.56
-10	0	-10	50	-0.61179	-0.04954	0.28095	0.48	0.48

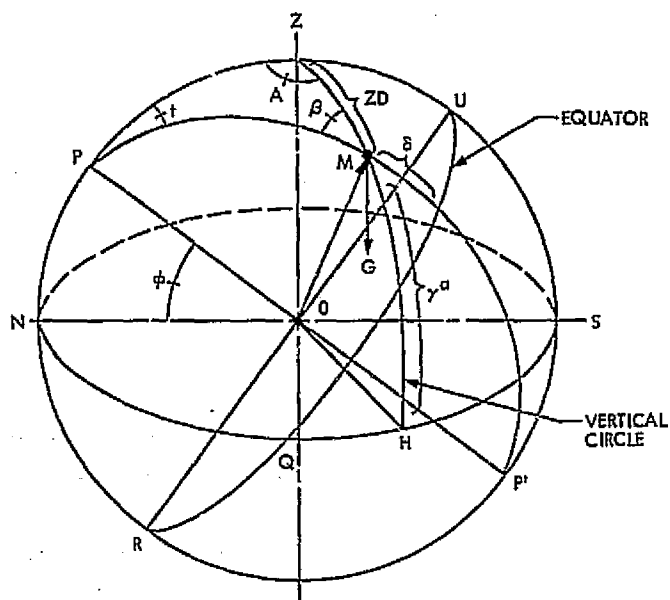
^aGravity - off/on - rms values

$rms_x = 0.626237$ mm (0.024655 in.)

$rms_y = 0.787527$ mm (0.031005 in.)

$rms_z = 1.018235$ mm (0.040088 in.)

^bRms, mm = ½ pathlength errors.



^a GAMMA IS DEFINED IN THE APPENDIX

Fig. 1. Topocentric coordinates

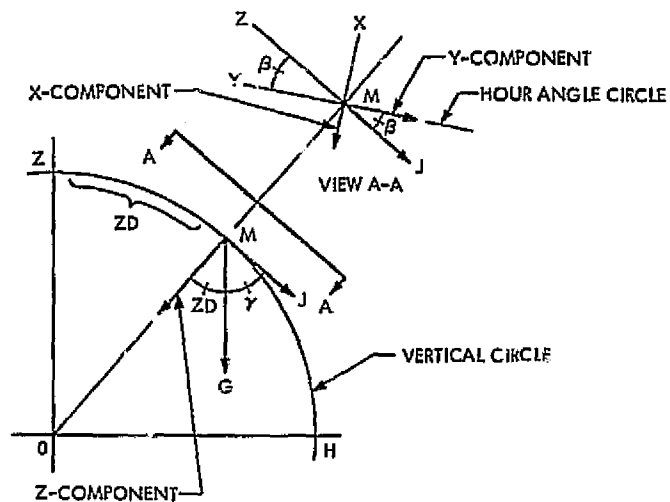


Fig. 2. Azimuth measuring plane

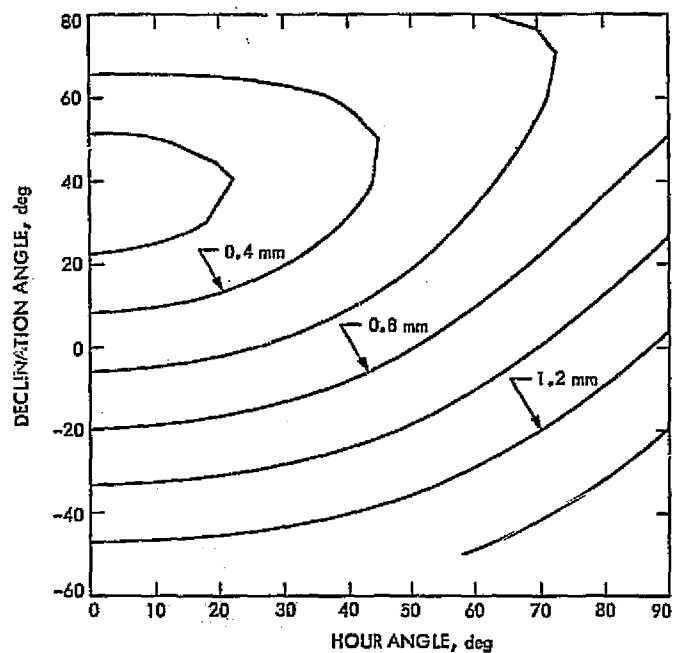


Fig. 3. RMS, mm (panels set at zenith look)

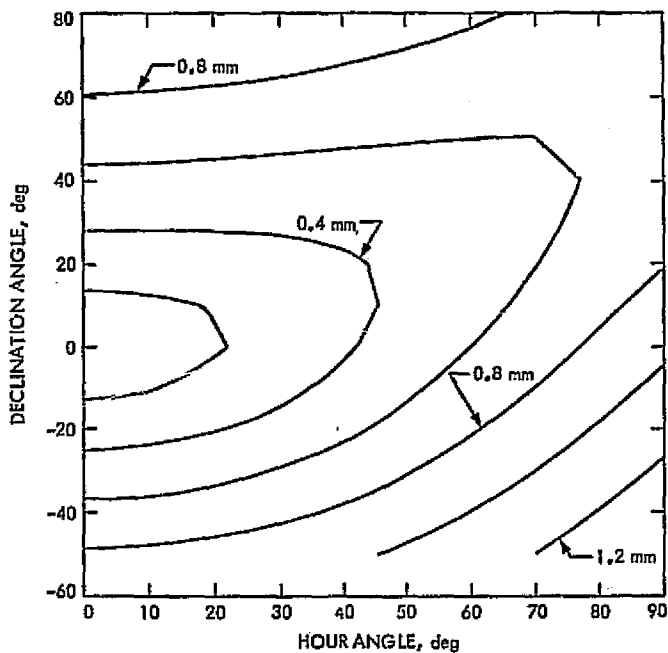


Fig. 4. RMS, mm (panels set at 0 deg declination)

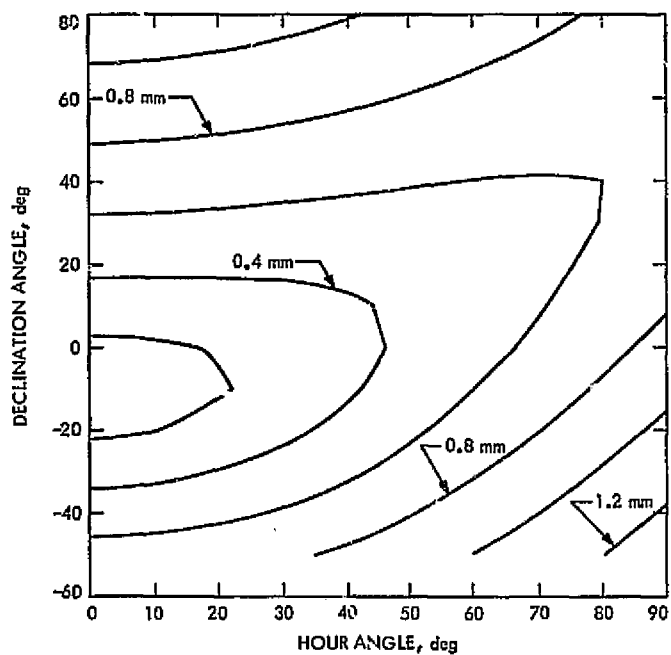


Fig. 5. RMS, mm (panels set at -10 deg declination)

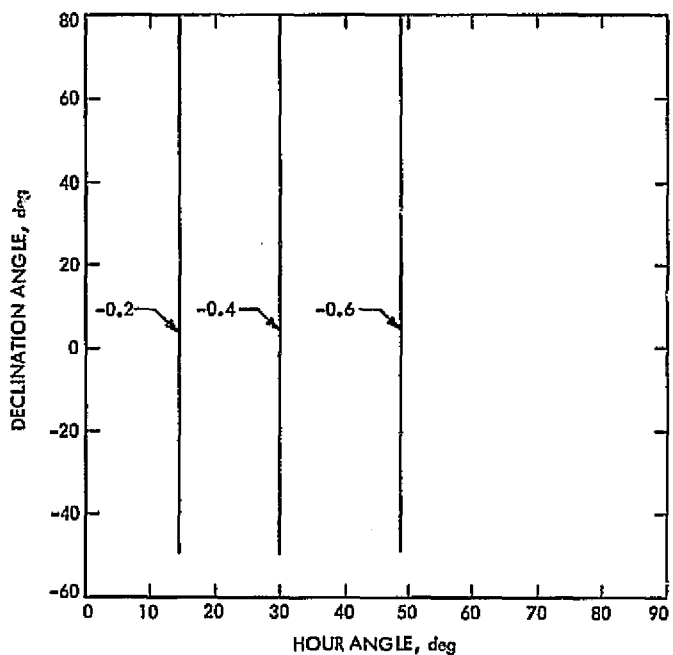


Fig. 6. X_c loading component

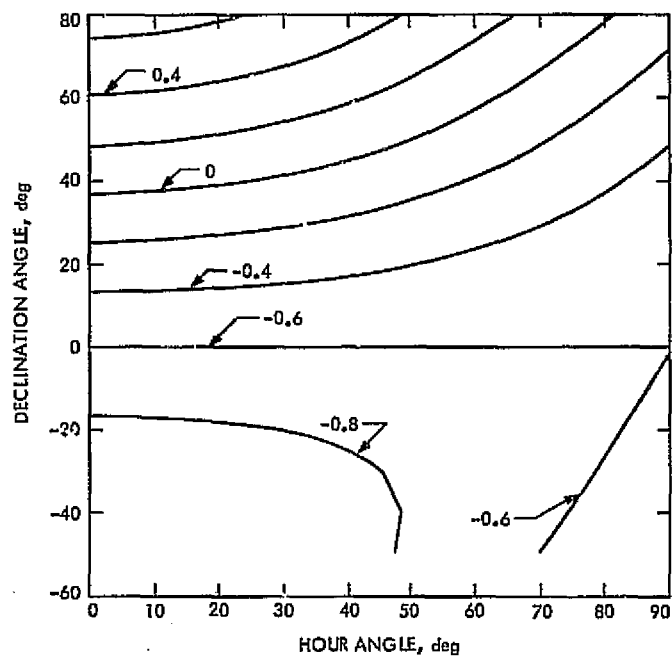


Fig. 7. Y_c loading component

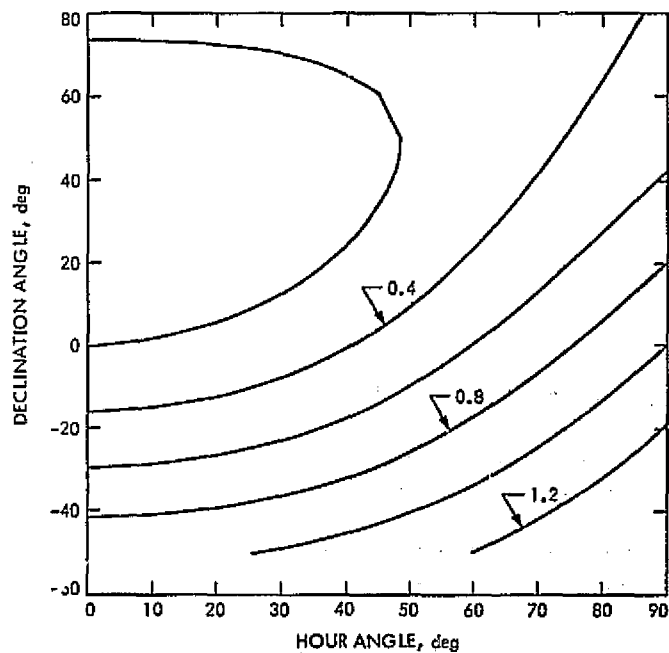


Fig. 8. Z_c loading component

Structural Data Checks With Computer Graphics

M. S. Katow

DSN Engineering Section

R. H. Patton

Science and Engineering Computing Section

Previous reporting described the use of Computer Graphics for generating and checking of the bulk input data required by the NASTRAN or IDEAS structural analysis programs. Modifications to the checking method are described in this reporting. A new version of the Object Inspection Program now resides in the Graphics 1557 Controller so that multiple sets of line directives that outline the elements of the structure may be inserted at one time. Then each group of elements, limited in numbers to ease the visual observation, may be checked individually or added to the other groups so that assemblies of these groups can be viewed in one display for checking. A sample sequence of the displays is described.

I. Introduction

A new version of the Object Inspection Program was coded to reside in the Graphics 1557 Controller or Minicomputer which controls the 1558 console with the cathode ray tube and a keyboard for inserting directions into the 1557 controller.

To improve the checking of structural elements used to model a complete structure in the NASTRAN or IDEAS structural analysis programs (Ref. 1), modifications were made in the Object Inspection Program so that multiple sets of elements consisting of individual elements or

combinations of elements could be transmitted into the 1557 controller from the 1108 computer with a single transferring call.

This allowed inspection of one element at a time (useful for checking solid elements) by rotation of the object on display to allow a three dimensional check. The new capability for adding one element to another then allowed a buildup of the elements in order to check the assemblies of elements. Also, the 1108 computer costs were minimized with the decrease in the number of required accesses to the 1108 computer.

Smaller assemblies of bar-trusses could also be displayed one at a time and added to check their mated assembly.

II. Description

A set of line directives that describes a structural truss consisting of bars is shown in Fig. 1. This display has 57 line directives and 20 nodes or joints. Depressing key W brings up to display the second set of bars with the same number of line directives and nodes as shown in Fig. 2.

Figure 3 shows three sets together, Fig. 4 shows four sets, and Fig. 5 shows eight radial sets plus three sets comprising the elevation bearing supporting truss.

Each unit may be inspected in turn by the rotation controlling keys on the 1558 console. The rotation motion seems to accent the 3-dimensional view of the structure. Depressing the S key produces two images in perspective geometry, which, by use of two lenses about three feet from the cathode ray tube, may be viewed as a three-dimensional object with true depth perception. It should be obvious that checking of a unit or set with fewer line

directives as in Fig. 1 should be easier than the checking of a unit like Fig. 5 or even Fig. 4.

Figure 5 includes all of the sets. (11 sets, 180 nodes, 589 line directives with duplications at the joint planes of the sets) and the complete picture is based on a scaling factor which uses about 80% of the 30 × 30 cm of the cathode ray tube face. This scaling factor is not critical as shown by Fig. 6 where the scaling factor was multiplied by 2. At the borders of the frame, the Object Inspection program replaces all nodes outside of the frame by the intersection point of the line directives with the border line. This results in a true display up to the border of the frame with indications of the line directives outside of the border coincident with the border. As the display is rotated, the line directives appear to come out of the border with the correct geometry of the display as it rotates.

These figures are reproductions of the hard copies made by the Stromberg Carlson 4020/F80 camera using the plot stacking tape written by the 1108 main computer. The 1108 was directed to write on this tape by an 1108 software package actuated by keys on the 1558 display console when the desired display was stopped on the cathode ray tube.

Reference

1. Katow, M. S., and Cooper, B. M., "NASTRAN Data Generation and Management Using Interactive Graphics," NASTRAN: Users Experiences, NASA Tech. Memo TM x-2637, Sept. 1972, pp. 399-406. Also appears in *The Deep Space Network Progress Report*, Technical Report 32-1526, Vol. XI, pp. 104-107, Oct 15, 1972.

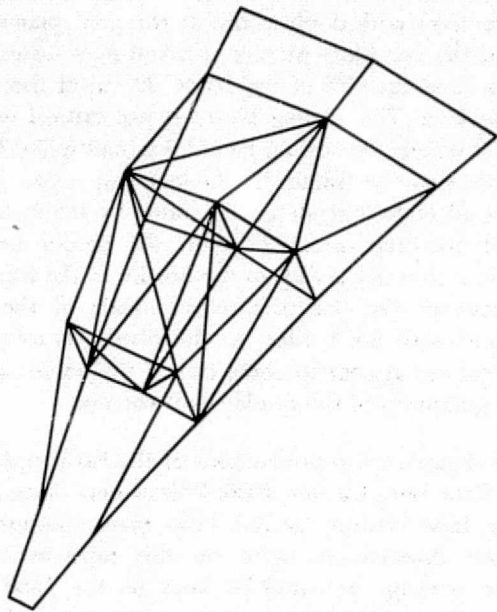


Fig. 1. First set of bars

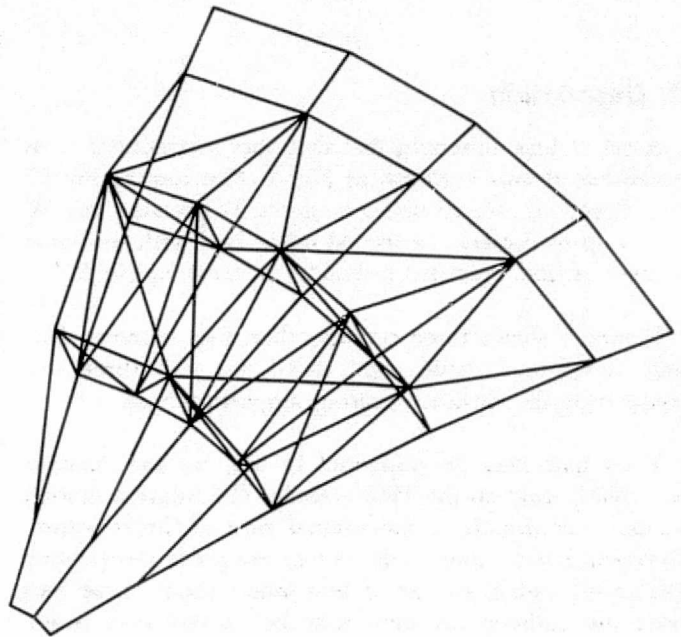


Fig. 2. 2 Combined sets of bars

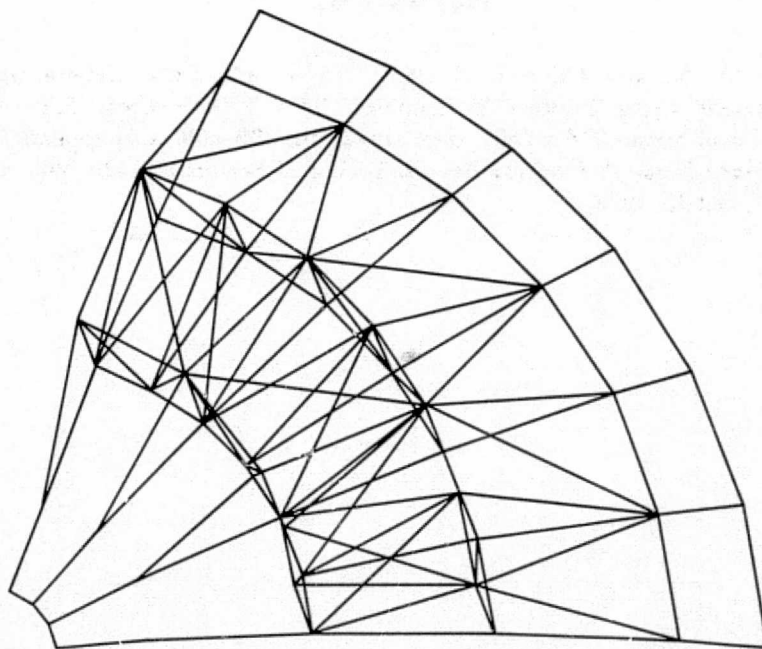


Fig. 3. 3 Combined sets of bars

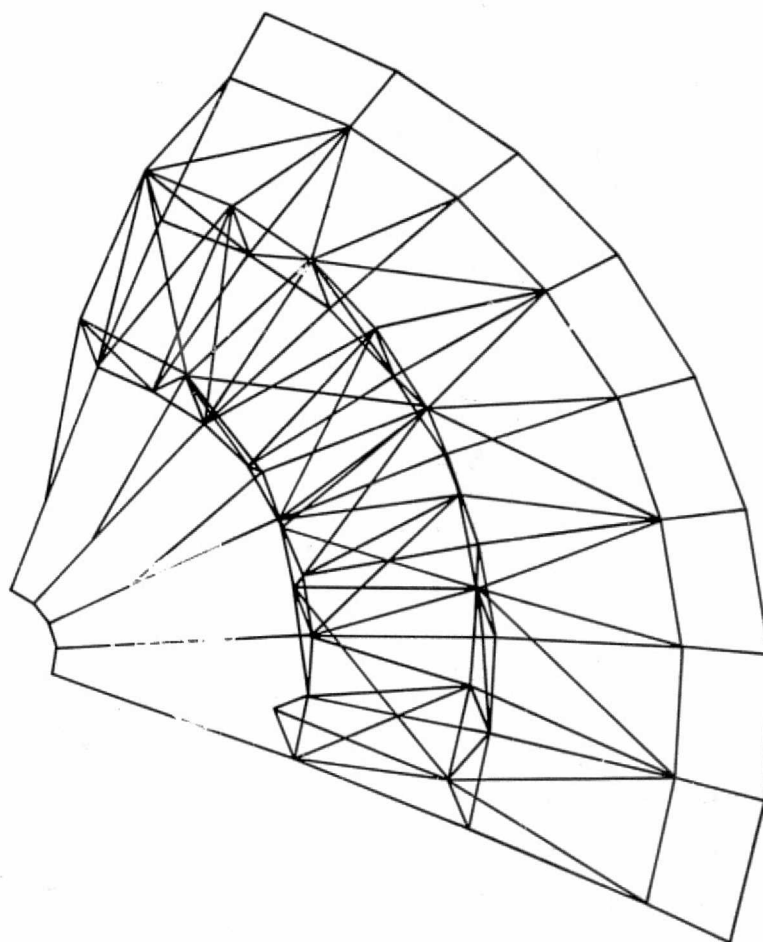


Fig. 4. 4 Combined sets of bars

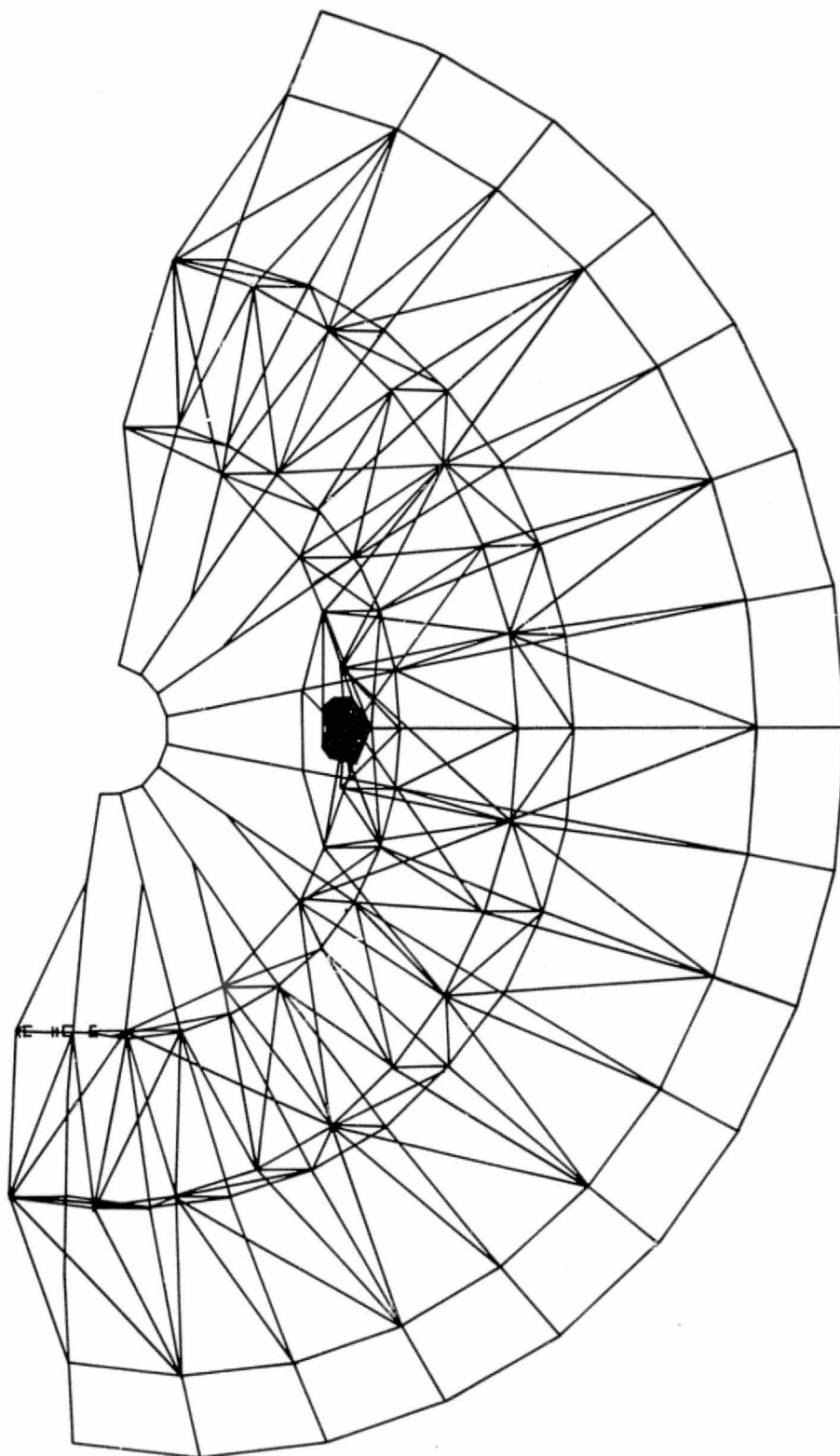


Fig. 5. 8 Combined sets of bars

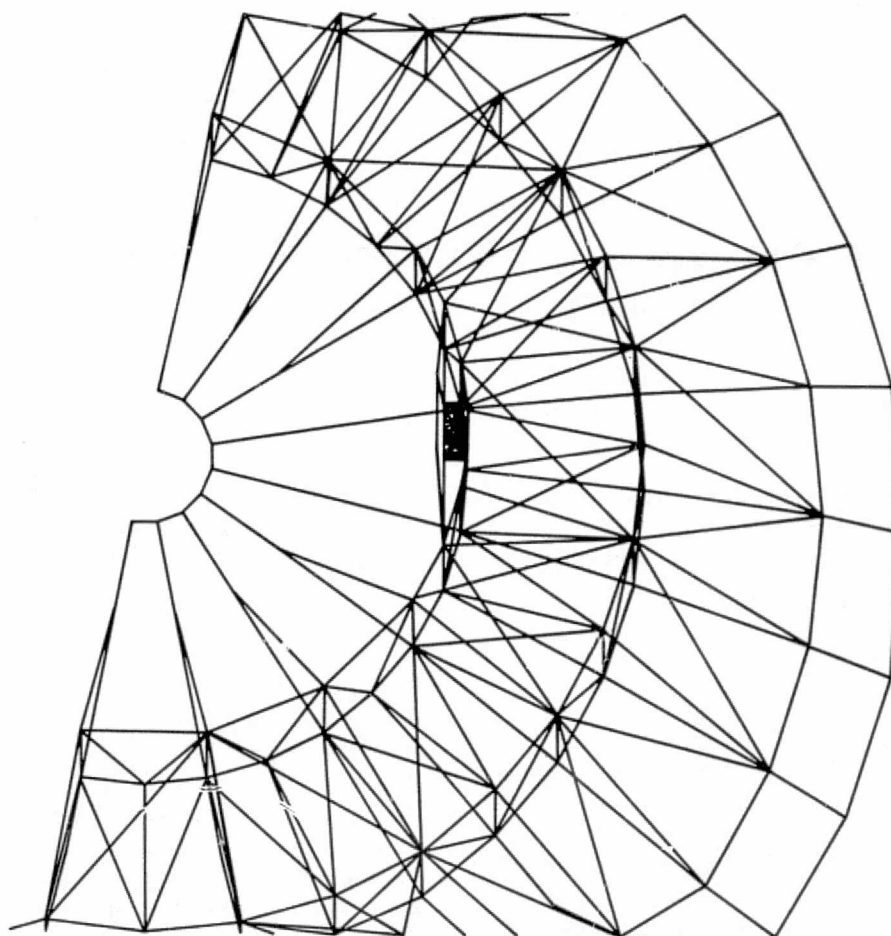


Fig. 6. Enlarged view

Magnetic-Tape Module Copy and Verification System

R. Billings and M. Martin
Network Operations Office

The Magnetic-Tape Module Copy and Verification System consists of three programs, DOI-5431-SP, DOI-5378-SP, and DOI-5428-SP. These three programs are used to copy module type software on magnetic tape for distribution and to verify these copies for accuracy.

I. Introduction

The problem of copying and verifying module-type programs on magnetic tape by the DSN Program Library for distribution to Deep Space Stations was solved in a three-stage sequence involving three progressively complex computer programs. The first of the three, a simple checksum verifier, was written to satisfy an immediate need for verifying that a modular tape is copied correctly. Modular tapes are copied initially with Telemetry and Command Subsystem (TCD) Multimission Software Update Program DOI-5414-SP in lower core. Module Checksum Verifier DOI-5431-SP, in upper core, is then operated to obtain a checksum for both the master tape and the copy. In use, the checksum for the master tape is computed first; the checksum for each copy is then computed and compared visually with the checksum of the master.

In the next stage, a more sophisticated program, Magnetic-Tape Module Verifier DOI-5378-SP, was written to perform a bit-by-bit comparison between the master

and copy tapes, thus assuring 100% accuracy. The program also computes a checksum and total word count. Again, the tapes are copied with TCD Multimission Software Update Program DOI-5414-SP, and Magnetic-Tape Module Verifier DOI-5378-SP is operated in upper core to verify in a second pass that the copy is accurate. In addition to the bit-by-bit comparison between the two tapes, the checksums and word counts are compared by the program not only to provide additional assurance of accuracy but also to establish checksum and word-count figures against which a tape can be measured at any subsequent time to determine its usefulness.

It was thereupon established that copying a modular tape with TCD Multimission Software Update Program DOI-5414-SP and verifying the copies with Magnetic-Tape Module Verifier DOI-5378-SP was a sound, accurate procedure. However, the update program required many type-ins by the operator, and switching between the two programs required continual operator intervention. Therefore, to speed the process, a third program was written

which copies all records from a master tape up to a double end-of-file mark (or two meters of blank tape) onto the copy tape on the first pass, and then performs a bit-by-bit comparison, word count, and checksum computation on the second pass. In this program, Magnetic-Tape Module Copy/Verify Program DOI-5428-SP, both passes are completely under program control. The operator has only to observe type-outs and to clear halts between tapes. Operation is sufficiently fast so that 20 copies of a modular tape can be made in less than 2 hours. The typewriter type-outs provide a log showing how many tapes were copied without error.

II. Description of Programs

The purpose of the simplest of the three programs, Module Checksum Verifier DOI-5431-SP, is to compute an exclusive-or checksum of the data file on a magnetic tape. It operates in upper core, with the copying routine DOI-5414-SP in lower core, so that the operator may switch between programs as he copies and verifies magnetic tapes.

Magnetic-Tape Module Verifier DOI-5378-SP also computes a checksum, but in addition it tallies the words on both tapes and performs a bit-by-bit comparison of the data on the tapes. It differs operationally from DOI-5431-SP in that it works with two tapes. A functional flow chart is shown in Fig. 1. The program is seen to test for a buffer error when it reads and stores a record from Tape 1 and to test for a comparison error when it reads Tape 2. If either type of error is encountered, the tape is backspaced over one record and another attempt is made. After three attempts, an error message is typed out. If the tapes reach the end of data without an error, the checksums and word counts are compared. If these values agree, the program branches back to the copy routine DOI-5414-SP after typing out the checksums and word counts.

The significant difference between Magnetic-Tape Module Copy/Verify Program DOI-5428-SP and its forebears is that DOI-5428-SP adds a copy routine to its functions. In the copy routine, the master tape is read under interrupt control and the copy tape is written with interlace. On the second pass, both tapes are read under interrupt control, their contents are compared bit-by-bit, and checksums and word counts are computed for both tapes. As with DOI-5378-SP, agreement must be reached in all three areas in order to obtain a "Verification OK" typeout. In any case of error, the program branches back to the start of the copy routine to make another attempt at writing an accurate copy of the master.

The flowchart in Fig. 2 shows the main functional elements of the program. With the master modular tape on tape unit 1 and a blank tape on unit 2, the program begins by reading and storing a record from the master tape. This record is then written on the blank tape on unit 2. This process continues until an end-of-file mark or one or two meters of blank tape is encountered, at which time both tapes are rewound to loadpoint.

The program next checks the accuracy of the copied tape by reading and storing records from both tapes, comparing the records bit-by-bit, and computing a checksum and word count for each. If a comparison error is found, an error message is typed out and the program branches back to the copy routine for another attempt. Otherwise, the procedure repeats until an end-of-file mark or blank tape is found. The checksums and word counts of the two tapes are then compared and appropriate error messages are typed out if they differ.

If no errors are found, the program types out a success message, listing the checksum and word-count values of both tapes. Finally, it branches back to the start of the program to make and verify another copy of the master modular tape.

With this program, the task of copying modular magnetic tapes is reduced to a fairly simple operation which can be handled by an operator with little training. Operation requires only that the operator ascertain that a "Verification OK" message is obtained before removing and labeling each copy. The typewriter messages comprise a log which indicates exactly how many accurate copies of the master were made. This program has been in use for almost a year with no indications of difficulty or deficiency in its operation of copying and verifying modular magnetic tapes.

III. Procedure

With new modular tapes, the following procedure is used: The first copy is made with TCD Multimission Software Update Program DOI-5414-SP and verified with Magnetic-Tape Module Verifier DOI-5378-SP. Another copy is then made using Magnetic-Tape Module Copy/Verify Program DOI-5428-SP. If the checksums and word counts of the two copies agree, subsequent copies are made with DOI-5428-SP to take advantage of that program's facility. If checksums or word counts do not agree, copies are made with DOI-5414-SP and verified with DOI-5378-SP until the reason for the discrepancy is found and reconciled. This procedure obviates errors in

copying which may be beyond the capability of DOI-5428-SP.

The computation of checksums and word counts with these programs provides an extra dimension of reliability in that if a program tape is suspected of possible damage, it may be verified at the Deep Space Stations using Magnetic-Tape Checksum Verifier DOI-5344-SP. The checksum value and word count obtained with DOI-5344-SP must agree with those values on the tape label, which were established when the tape was copied.

IV. Conclusion

The problem of copying and verifying modular magnetic tapes was resolved in a time-effective manner by preparing programs in three steps, progressing from a simple checksum verifier to a program which copies tape from the master and performs a bit-by-bit verification between the master and the copy. The checksum verifier sufficed at the outset, but it was replaced as soon as possible by a program which compared the two tapes bit-by-bit to insure 100% accuracy. This latter program was then updated to perform the entire task of copying and verifying modular magnetic tapes.

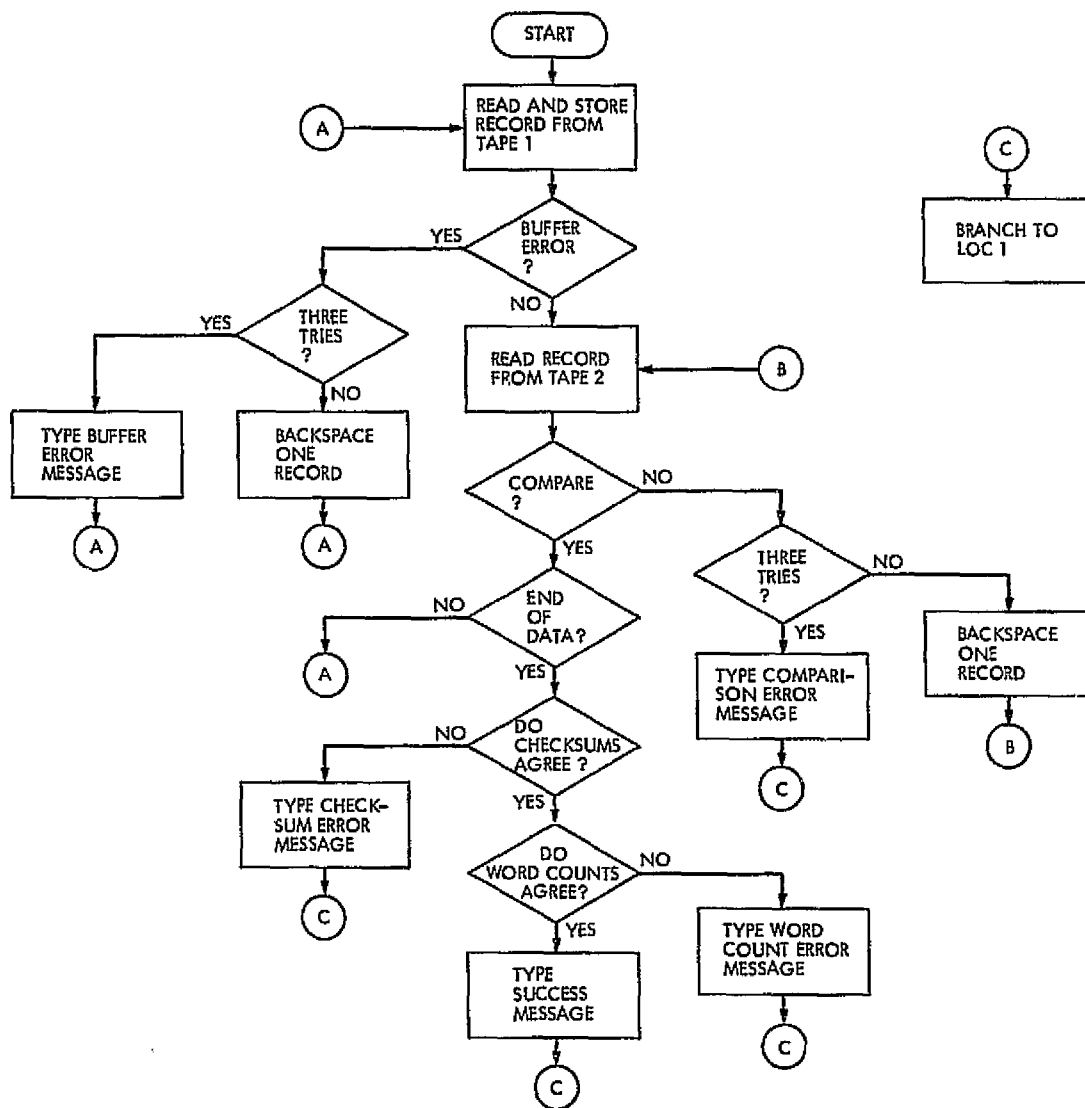


Fig. 1. Magnetic-tape module verifier program DOI-5378-S²

ORIGINAL PAGE IS
OF POOR QUALITY

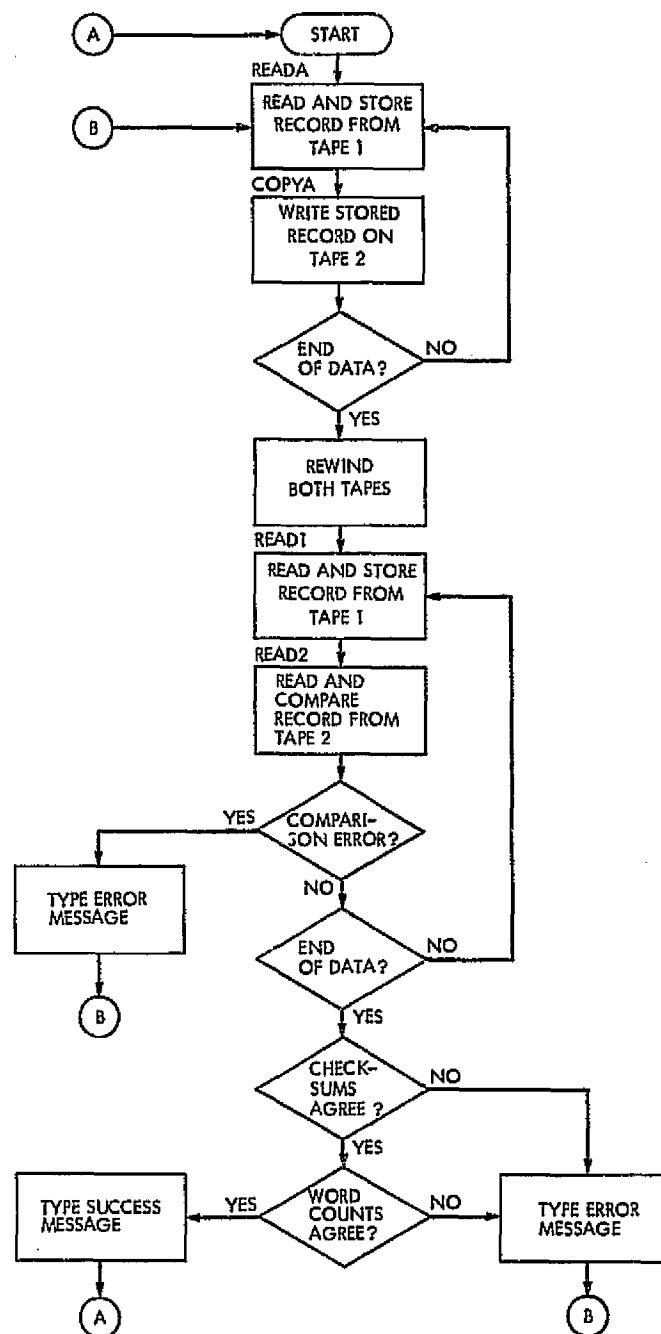


Fig. 2. Magnetic-tape module copy/verify program DOI-5428-SP

Deep Space Network Sequence of Events

M. Puchalski
Network Operations Office

In January 1975 the Network Operations Control Group began generating the Deep Space Network Sequence of Events with a new software system designed for use in the Network Data Processing Area's Sigma 5 computer system. This article provides an overview of the DSN Sequence Generation (DSNSG) Generator capability by describing the inputs, software, and system flow required to construct an SOE.

I. Introduction

The DSN Sequence of Events (SOE), ordinarily prepared on a seven-day basis as an adjunct of the DSN Seven-Day Schedule, provides milestone data for the handling of routine and/or critical daily network operations. It is published as a chronological listing of events and released in both printed text and output file form. The printed text is generated as hard copy (Fig. 1) via a Network Data Processing Area (NDPA) line printer. The output file is maintained on magnetic tape (high-speed data). The high-speed data tape is re-written to a second magnetic tape that is formatted as an output file message for transmission to DSN stations and other NASA facilities having suitable receive capability. The request for transmission of the DSN SOE is at the discretion of the Network Operations Chief.

II. Inputs

The Network Operations SOE coordinator is responsible for the production of an acceptable DSN SOE. He

begins the generation process by collecting and/or creating the following inputs:

- (1) Event data
- (2) SOE Subsequence file
- (3) Trigger data
- (4) Seven-Day Schedule data
- (5) Master SOE

A description of the above inputs follows.

A. Event Data

The basic unit of data used in the SOE is an event. Each event consists of time, options and text. Time may be either GMT (absolute) or reference time (relative). Options include mission reference symbols, cross reference

symbols, and time symbols. The text consists of statements explaining the DSN station activity to be performed.

Events can be input to the DSN Sequence Generator from cards and/or magnetic tape. The SOE coordinator normally creates this data on cards from information supplied by the DSN project representatives. Project users can supply events on magnetic tape via a machine interface file.

B. SOE Subsequence File

The Subsequence file is a collection of events stored on magnetic tape. Events held in this file differ from the Event data description above in that a subsequence can receive variable information from trigger records at the time of SOE generation. The main attraction to the subsequence file is in the customary benefits derived through the standardization processes. The file is created and updated by the SOE coordinator from inputs supplied by the DSN project representatives.

C. Trigger Data

Trigger records are created from information supplied by the DSN Scheduling Office and the SOE coordinator. These records are generated by the SOE coordinator on cards or magnetic tape. Triggers are used by the DSN Sequence Generator to access and complete the appropriate events from the subsequence file. A trigger file can be supplied to project users for incorporation into a project SOE file.

D. Seven-Day Schedule Data

The Network Operations Scheduling Group supplies the SOE coordinator with card information relating to future station activities; such as start and stop times with calibration requirements. The data usually covers a seven-day period within the following week. The Seven-Day cards are used by the coordinator to create trigger records.

E. Master SOE

The SOE coordinator has the option of declaring the creation of a Master SOE following the generation of an SOE. The Master SOE is stored on magnetic tape and can be input to future DSN Sequence Generator runs. The coordinator may elect to input the Master SOE for generation of additional reports or updated SOEs.

III. Software System

The SOE coordinator has access to three programs for use in creating the DSN SOE. The Preliminary and Final

File programs create triggers that can be used for input to the SOE generation program.

A. Preliminary File Generator

The purpose of this program is to create a tape file of trigger records which contain DSN station tracking information needed to generate the SOE. Trigger records are generated from Seven-day Schedule and user input cards (Fig. 2). Each seven-day record produces two trigger output records. One trigger will contain the scheduled time that a station is to begin tracking (acquisition of signal) while the other reflects the scheduled time that the track will end (loss of signal). Both triggers carry information that is needed to access and complete the appropriate statements from the subsequence library. All triggers generated by this program make up the Preliminary file which will be used as input to the Final File Generation program. The file can also be input to the Network Sequence of Events Generation (NSG) program or to project-designed programs that maintain independent SOE files.

B. Final File Generator

The function of this program is to create a Final Trigger File and to provide file maintenance capabilities to the user. The Final File contains all triggers from the Preliminary File plus any triggers generated by this program. The triggers created by this program consist of two types; transfer and nontransfer. Transfer triggers are generated for conditions where the tracking times for two stations, following the same spacecraft, overlap with sufficient time to adequately complete handover operations. Nontransfer triggers will be created whenever there is either a gap in the tracking of a spacecraft between two stations or the times do not overlap with enough time to complete the handover. Transfer triggers contain the scheduled GMT that the receiving station is to begin tracking, while nontransfer triggers carry either the end of track GMT of the losing station or the start track GMT of the receiving station. Both triggers contain data that are needed to access and complete the appropriate statements from the subsequence library. The Final File is generated through the processing of user and Preliminary File inputs (Fig. 3) and is used as input to the Sequence of Events Generation program.

The file maintenance feature of this program gives the user the ability to add, change, or delete any trigger record held in the Preliminary or Final files. With this processor an updated trigger file tape is produced using update card and (old) trigger file inputs (Fig. 4).

The updating and generation features of this program can be utilized within one processing run as well as in separate runs. (Fig. 5)

C. Sequence of Events Generator

The basic purpose of this program is to generate from inputs a time-ordered Sequence of Events (Fig. 6) and to output it in formats convenient to the users. There are a number of potential inputs to the Sequence of Events generation. They are:

- (1) Events cards (either in card form or on tape)
- (2) Trigger cards (either in card form or on tape)
- (3) Subsequence library
- (4) Master SOE tape from a prior generation

There are also three possible outputs from the Sequence of Events generation. The possible outputs are:

- (1) Listing of the sequence of events
- (2) A data tape suitable for formatting into high-speed data blocks for transmission
- (3) Master SOE tape for input to other SOE generation runs

IV. SOE Generation

The following is a description of the procedure normally used to produce a DSN SOE and is graphically displayed in Fig. 7.

The SOE coordinator usually receives the Seven-Day Schedule cards first. The deck is input to the DSNSG which produces the Preliminary file. A duplicate can then be passed to projects that have established a machine data file interface. The Preliminary file tape is then input to the DSNSG for production of the Final file.

While performing the above task the coordinator is also receiving inputs from the various projects. He must code information on cards for those projects that have not established a machine data file interface.

After the coordinator has collected and created all the various inputs necessary to the SOE, he then generates the final product. The output listing must be reviewed by each DSN Project Representative before the tape is released to the NDPA and the Network Operations Chief can be notified of its availability.

V. Conclusion

The DSNSG which is a major redesign of the Sequence of Events Generator (SEG), residing in the Mission Control and Computing Center IBM 360/75 system, allows the Network Operations Section to create a DSN SOE with much less procedural complications and provides greater flexibility on the part of the DSN toward establishing acceptable project interfaces.

PRINTED ON DAY 151 PAGE 1

DSN WEEKLY SCE FOR PERIOD 154/00002 TO 161/03302 TAPE 12402

ITEM NO.	MISSION TIME 000 HH MM SS	GMT TIME 000 HH MM SS	ACTION BY TO	USER S/C ID	DSN	TRM	CMD ERT	EVENTS	SORT
402.0		156 14 00	ARC	PNF-23				PA303	
403.0	EM + 067 17 13 07	156 14 00 00	14 TRK	M73-76	62->14			2-WAY TRANSFER FROM DSS 62 TO DSS 14	RX4T
404.0	EM + 067 17 18 07	156 14 05 00	14 TRK CPCH ACE1	M73-76	14			DSS 14 CMD MOD ON (AFTER TUNING)	RX4T
406.0	EM + 067 17 42 01	156 14 28 54	14 TRK 62 TRK	M73-76	14 62			DSS 14 2-WAY DSS 62 3-WAY	RX4E
408.0	EM + 067 18 34 03	156 15 20 56		M73-76				**OWLT = 14M 27S (867 SEC) **	MA4N
409.0		156 15 50 00	DSS 44	PNG-24				START PRE-COUNT LEVEL 303343 - CONF 1000	
410.0		156 16 20 00	CMCH	PNG-24				TURN OVER DSS 44 CKTS TO NETWORK OPERATIONS	4
412.0		156 16 25 00	NOC TRK	PNG-24				VERIFY DSS 44 HAS PROX FOR PASS	
413.0		156 17 00 00	ARC	PNG-24				FGM201	
414.0		156 17 20 00	NOC ALL	PNG-24				START DSN DATA VERIFICATION TEST FOR DSS 44	
415.0		156 17 20 00	44 TRK	PNG-24	44 ACS			DSS 44 ACS - RPT ACQ PARAMETERS AS RCV'D REPORT SCA BEST LOCK FREQ	4
416.0		156 17 20 00	NOC TRK NOC ARC11	PNG-24 PNG-24				PREPARE FOR 2-WAY XFER OF S/C FROM DSS 11 TO DSS 44 PASS 427 IN 20 MIN PER SOP 8 3-32-31-62/REV 8	
417.0		156 17 35 00	TRK	PNG-24				TURN CMD MOD OFF	
418.0		156 17 35 00	NOC ARC11	PNG-24				REPORT CMD MOD OFF - DSS 11	
419.0		156 17 40 00	TRK NOC	PNG-24	11 TO 44			2-WAY XFER FROM DSS 11 TO DSS 44	
420.0		156 17 40 00	DSS 44	PNG-24				PERFORM PROCEDURES IN TABLE 6-2 616-20 REV-A VOL. VII	
421.0		156 17 45 00	TRK 44	PNG-24				TURN CMD MOD ON	
422.0		156 17 45 00	NOC ARC11	PNG-24				REPORT CMD MOD ON - DSS 44	
423.0		156 17 50 00	NOC CMCH	PNG-24				AT COMPLETION OF DATA VERIFICATION TEST BRIDGE DSS- NET (T/L) TO 44 VOICE CKT AND PERFORM ARC11 VOICE CHECK	4
424.0		156 17 50 00	NOC TRK	PNG-24	11 LOS			DSS 11 LOS - INITIATE 1 HR POST PASS AS SPECIFIED	4
425.0		156 17 50 00	NOC ARC11	PNG-24				DSS 11 END TRACK	4

Fig. 1. Typical DSN sequence of events page format

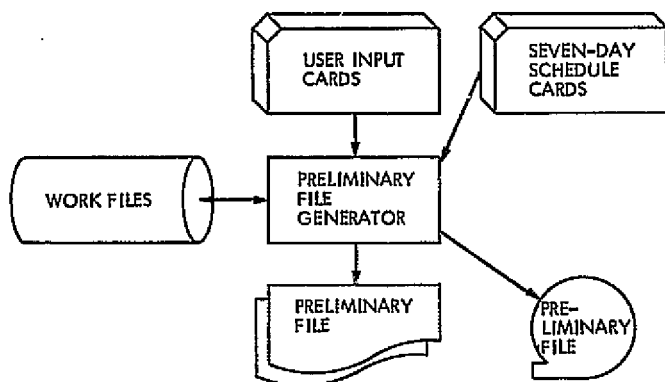


Fig. 2. Preliminary file generation

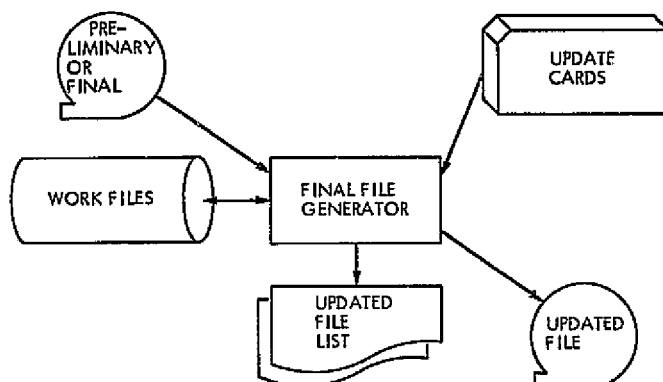


Fig. 4. Preliminary or final file update

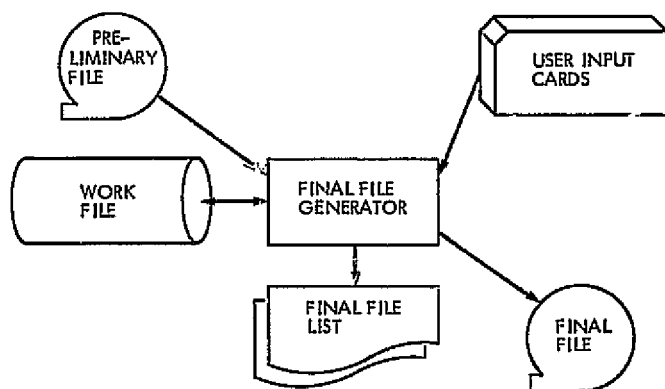


Fig. 3. Final file generation

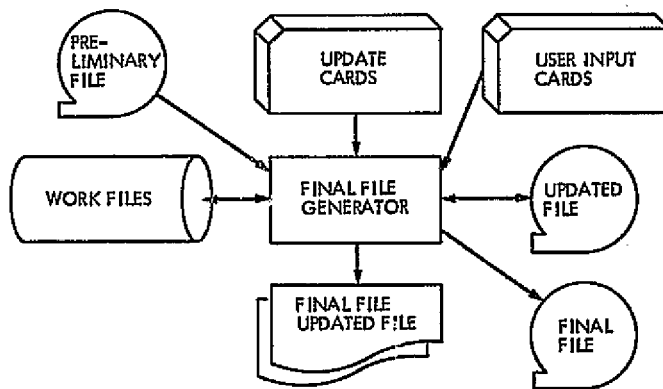


Fig. 5. Preliminary file update and final file generation

ORIGINAL PAGE IS
OF POOR QUALITY

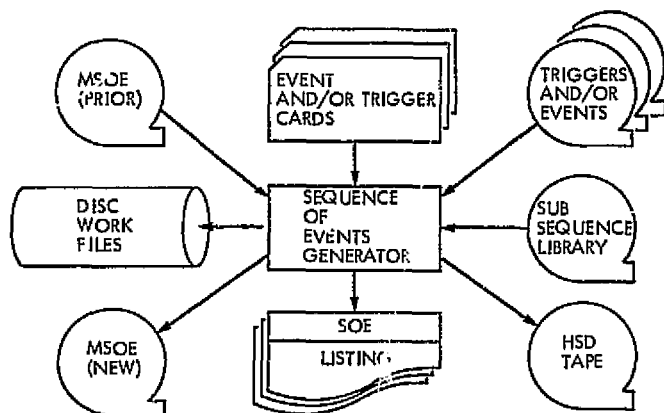


Fig. 6. Sequence of events generation

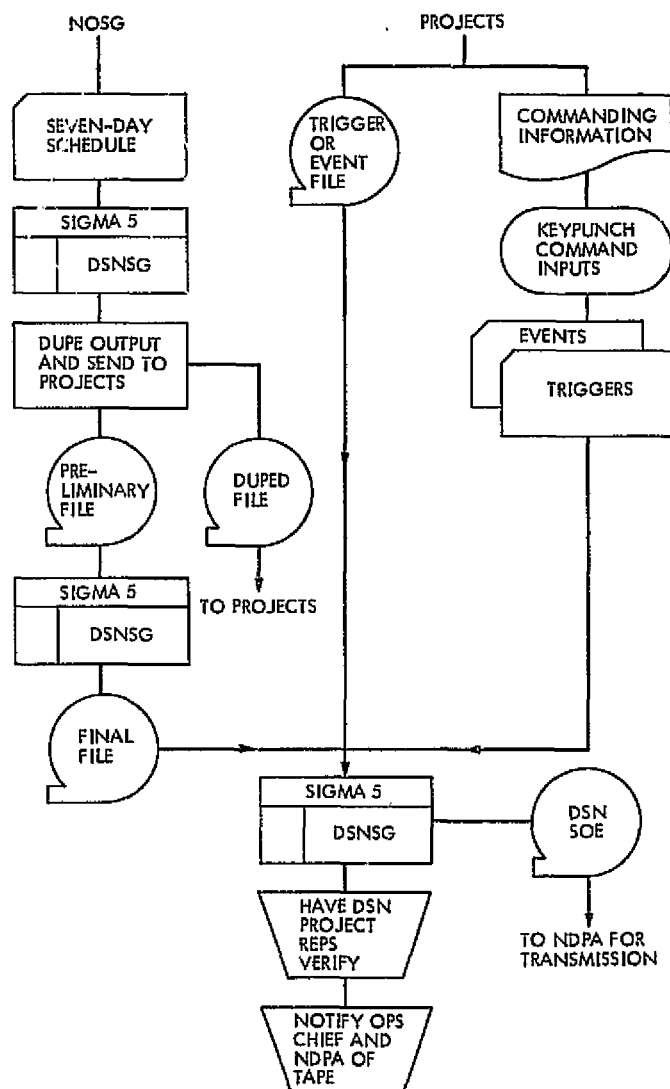


Fig. 7. System flow (overview) of normal SOE generation

X-Band Tracking Operations During the Viking Orbital Phase

A. L. Berman
Network Operations Section

X-band tracking of the Viking spacecraft in orbit around Mars will be complicated due to the combination of high periapsis doppler rates and low downlink carrier margin. This report presents methods to implement X-band tracking of the Viking spacecraft by ramping either the ground transmitter frequency or the ground receiver frequency. The operational impact of the two methods is assessed.

I. Introduction

Tracking at the 64-m deep space stations with the Block IV X-band receiver in a 10-Hz tracking loop filter setting will be quite difficult at Viking Orbiter periapsis because of high doppler rates. As an alternative, use of the 30-Hz tracking loop filter during Block IV X-band tracking is not promising because there is only marginal carrier power above threshold (~ 8.7 dB) in this mode. Additionally, it had been thought (Ref. 1) that in order to maintain a reasonably small phase error while tracking with the Block IV X-band receiver in a 10-Hz tracking loop filter setting, as many as 20 digital controlled oscillator (DCO) ramps (frequency rates) per periapsis pass might be required. It is therefore the intent of this report to analyze in greater detail the operational capabilities and constraints while tracking a Viking Orbiter with the Block IV X-band receiver(s) in a 10-Hz tracking loop filter setting.

II. Orbits Utilized in the Analysis

Reference 2 analyzed in great detail four separate orbits. These consisted of permutations of periapsis altitudes of 1200 and 500 km and of lines of apsides either normal to or parallel to the Mars-Earth vector. These can be abbreviated as 500 km/N, 500 km/P, 1200 km/N and 1200 km/P. The highest periapsis doppler rates are encountered with the 500 km orbits, so it was considered adequate to limit this analysis to the 500 km/P- and 500 km/N-type orbits. The periapsis doppler rates (X-band, two-way) for these two orbit types can be seen in Figs. 1 and 2, respectively.

III. Consideration of Static and Dynamic Phase Error

In the initial consideration of the adequacy of a given receiver to track a given signal, one is concerned with both the static phase error (SPE) due to frequency dis-

placement and dynamic phase error ($\Delta\theta$) due to frequency rate. As it turns out, the pacing criterion for the worst Viking orbital case (the 500-km/P-type orbit), in terms of necessary ramping of the X-band receiver, is the dynamic phase error, and hence this study will be mostly focused on this particular parameter. Also, any receiver ramping schemes which will alleviate the dynamic phase error problem, coupled with judicious choices of starting receiver frequencies, will almost automatically keep the total frequency displacement small, and hence negate most static phase error buildup. Quite simply, if one is ramping the receiver to keep the received frequency rate within certain bounds as in Fig. 3, the cumulative frequency displacement

$$\sum_{n=1}^i \int_{n-1}^n \left\{ R_n - \frac{d}{dt}(D2) \right\} dt \sim 0$$

(where R_n is the receiver ramp rate and $d/dt(D2)$ is the received doppler rate) is relatively small when compared to that frequency displacement which would result from no ramping of the receiver.

IV. Analysis of Receiver DCO Ramps to Maintain Dynamic Phase Error Below 13 deg

Rather arbitrarily selecting a (conservative) objective of maintaining the phase error ($\Delta\theta$) at 13 deg or less, one has the following pertinent information from the DSN/Flight Project Interface Design Handbook (Ref. 3) and from Ref. 1:

Block IV X-band receiver carrier margin at 10 Hz tracking loop filter ≈ 13.51 dB

Downlink frequency rate required to produce $\Delta\theta = 13$ deg at a carrier margin of 13.5 dB $\approx \pm 15$ Hz/s.

The periapsis 2-way X-band doppler frequency rates versus time for the 500-km/P-type and 500-km/N-type orbits are shown in Figs. 1 and 2, respectively. Overlaying the doppler frequency rates in Figs. 1 and 2 are the required receiver ramps to keep the dynamic phase error approximately equal to or less than 13 deg, and hence from the information above, to keep the (relative) frequency rate at the receiver (= downlink frequency rate minus receiver ramp rate) approximately equal to or less than ± 15 Hz/s. As can be seen in Fig. 1, the 500-km P-type orbit is the more extreme case, requiring 11 re-

ceiver DCO ramps during the periapsis period. The 500-km/N-type orbit (see Fig. 2) is only slightly less difficult, requiring 8 receiver DCO ramps during the periapsis period.

V. Error Analysis

In the previous section the number of receiver DCO ramps required to produce a $\Delta\theta$ of 13 deg or less was analyzed; however, this (implicitly) assumed that the predictions used to generate the required ramp parameters would be perfectly matched to the actual data. At this point it would be reasonable to briefly examine the effect of using (slightly) inaccurate predictions.

Let one assume that a reasonable goal would be the generation of a ramp scheme designed to keep $\Delta\theta$ at 13 deg or less, but that one would tolerate occasional $\Delta\theta$'s of up to 17 deg because of inaccuracies in the predictions. Given this ground rule, one needs to determine what magnitude of prediction error would cause a combined $\Delta\theta$ of 17 deg, and, if one could expect prediction errors for the Viking orbital phase to be bounded by this (to-be-determined) prediction error. For a $\Delta\theta = 17$ deg, one has from Ref. 3, the following received doppler frequency rate: $\approx \pm 20$ Hz/s. Differencing this value with the ramp scheme goal of ± 15 Hz/s for the (relative) received frequency rate, one wishes to determine what size prediction error would thus cause a two-way X-band doppler frequency rate error of $\approx \pm 5$ Hz/s.

For both the 500-km N-type and 500-km P-type orbits, the maximum rate of change of frequency rate is

$$\left\{ \frac{d}{dt}(\text{frequency rate}) \right\}_{\max} \approx (10 \text{ Hz/s})/\text{min}$$

such that a frequency rate error would translate into an equivalent (prediction) time error of

$$\Delta t = \frac{5 \text{ Hz/s}}{(10 \text{ Hz/s})/\text{min}} \approx 30 \text{ s}$$

If recent past experience with respect to prediction accuracy at planetary encounters, etc., proves to be a reliable guide, one can indeed expect that, in general, trajectory errors during the Viking Orbital Phase will be less than 30 s (Δt), and hence expected errors in the prediction data from which ramp rates will be generated should add less than 4 deg of $\Delta\theta$.

VI. Operational Considerations

Let one consider the simplest case of just one receiver—a Block IV X-band receiver in the two-way mode with a 10-Hz tracking loop filter setting. If one considers a 500-km P-type orbit, and using the criterion previously established in Section IV, 11 separate ramps will have to be programmed into the receiver DCO per periapsis pass. At the DSS the operation will be complicated because the DCO holds only 4 ramps at any given time, and, as the initial ramps are executed, subsequent ramps will have to be manually entered into the DCO in near real time. Additionally complicating the receiver operator's job is the fact that the ramps are exhausted in as little as three minutes, thus allowing little time for the operator to enter and verify new ramps.

Generation of the ramp instructions in the Network Operations Control Area (NOCA) should also prove to be difficult, and in particular, time-consuming. Receiver frequency predictions are not generated in the prediction system, and the only method by which they can be generated (now) is manual, with the aid of Hewlett-Packard Programmable Electronic Calculators. Also, the Block IV DCO receiver frequency level is quite unfamiliar to most of the Network Operations Control Team (NOCT). Finally, assuming the ramp instructions are generated by the NOCT, they will have to be transmitted manually (via teletype) to the DSS, with a greatly increased risk of transmission errors, etc.

The above considers only the difficulties in ramping one receiver. If the Block IV S-band receiver is also in a 10-Hz tracking loop filter configuration, it too will require ramping, under some circumstances. Consider a 500-km P-type orbit. The maximum frequency rate at X-band (two-way) is ≈ 160 Hz/s. Thus at S-band it would be $\approx (3/11) (160 \text{ Hz/s}) \approx 44$ Hz/s. From Ref. 2, the Block IV S-band receiver carrier margin equals 21.3 dB, so that (from Ref. 3), a phase error equal to 13 deg results from a receiver frequency rate of $\approx \pm 30$ Hz/s. Thus, to avoid excessive phase error, the Block IV S-band receiver will also require some ramping.

Finally, if three-way X-band doppler is ever desired from another 64-m DSS during a periapsis pass, the extremely laborious and time-consuming tasks described above will be doubled.

To summarize the above, receiver ramping during Viking Orbiter periapsis passes can be accomplished; however, it will:

- (1) Place additional burdens on the DSS receiver operator
- (2) Consume large amounts of manpower from the NOCT, because of the semimanual mode of receiver level ramp generation
- (3) Entail considerably more risk of error because of the manual mode (teletype) of transmission

VII. Use of Uplink Ramping

The idea of utilizing the DCO capability to ramp the uplink and thus reduce the total downlink frequency rate is obvious and certainly merits being investigated. For instance, considering the 500-km P-type orbit, the total periapsis 2-way doppler rate excursion is ≈ 170 Hz/s (-10 to $+160$). If one chooses and appropriately locates five uplink ramps at the following equivalent X-band frequency rates of $+10$, $+40$, $+70$, $+40$, and $+10$ Hz/s, then one will have modified the uplink such that the spacecraft will see a maximum frequency rate (at equivalent X-band level) of ± 15 Hz/s. More importantly one would reduce the total 2-way X-band downlink frequency rate excursion to ≈ 110 Hz/s (-20 to $+90$).

Instead of 11 DCO ramps in the receiver, one would now require only 7. However, 5 ramps are now required in the exciter, making a total of 12 ramps altogether. Considering the added complications of ramping the exciter and the receiver, it does not seem that ramping the uplink in the above described fashion will buy anything substantial.

A more interesting (although perhaps seemingly bizarre!) approach might be to consider over-ramping the uplink by a factor of 2. This poses no particular difficulty for the S-band spacecraft receiver, and, in any case, produces the same frequency rate at the spacecraft as if the uplink was not ramped at all. But more importantly, it should theoretically drive the downlink doppler frequency rate to some small limit such that the X-band receiver would not have to be ramped at all. As a matter of fact, this is exactly what happens. Quite simply, let one define at some time:

F_{22} = two-way X-band downlink frequency

TSF = track synthesizer frequency (transmitted uplink frequency at DCO level, ≈ 44 MHz)

\dot{r}_{up} = uplink range rate

\dot{r}_{dn} = downlink range rate

c = speed of light

Then one has

$$\begin{aligned} F_{2x} \text{ rate} &= \frac{d}{dt} [F_{2x}] \\ &= \frac{d}{dt} \left\{ 48 \frac{880}{221} TSF \left[1 - \frac{(\dot{r}_{up} + \dot{r}_{dn})}{c} \right] \right\} \\ &= -48 \frac{880}{221} TSF \left\{ \frac{d}{dt} \left[\frac{(\dot{r}_{up} + \dot{r}_{dn})}{c} \right] \right\} \end{aligned}$$

Now if one assumes a ramped TSF , say TSF_R , and a corresponding F_{2x} , say $(F_{2x})_R$, one would have

$$\begin{aligned} (F_{2x})_R \text{ rate} &= \frac{d}{dt} [(F_{2x})_R] \\ &= \frac{d}{dt} \left\{ 48 \frac{880}{221} TSF_R \left[1 - \frac{(\dot{r}_{up} + \dot{r}_{dn})}{c} \right] \right\} \\ &= 48 \frac{880}{221} \left\{ \left[1 - \frac{(\dot{r}_{up} + \dot{r}_{dn})}{c} \right] \frac{d}{dt} (TSF_R) \right. \\ &\quad \left. - TSF_R \frac{d}{dt} \left[\frac{(\dot{r}_{up} + \dot{r}_{dn})}{c} \right] \right\} \end{aligned}$$

To drive the downlink doppler frequency rate to zero, one requires

$$\frac{d}{dt} [(F_{2x})_R] = 0$$

or

$$\frac{d}{dt} (TSF_R) = \frac{TSF_R \left\{ \frac{d}{dt} \left[\frac{(\dot{r}_{up} + \dot{r}_{dn})}{c} \right] \right\}}{\left[1 - \frac{(\dot{r}_{up} + \dot{r}_{dn})}{c} \right]}$$

$$\text{since } 1 \gg \frac{(\dot{r}_{up} + \dot{r}_{dn})}{c}$$

$$\frac{d}{dt} (TSF_R) \cong TSF_R \left\{ \frac{d}{dt} \left[\frac{(\dot{r}_{up} + \dot{r}_{dn})}{c} \right] \right\}$$

and since $TSF_R \approx TSF$

$$\frac{d}{dt} (TSF_R) \cong TSF \left\{ \frac{d}{dt} \left[\frac{(\dot{r}_{up} + \dot{r}_{dn})}{c} \right] \right\}$$

Finally, from the previous definition of F_{2x} rate, one has

$$\begin{aligned} \frac{d}{dt} (TSF_R) &\cong - \frac{221}{48(880)} \frac{d}{dt} [F_{2x}] \\ &\cong - \frac{221}{48(880)} (F_{2x} \text{ rate}) \end{aligned}$$

Following the above logic, uplink ramps corresponding to those in Fig. 1 (approximately twice the uplink frequency rate and, of course, moved backward (earlier) from the times in Fig. 1 by one round-trip light time (RTLT)) were input into the 500-km P-type orbit predictions. The results in the downlink doppler frequency rate are just as expected—the X-band downlink frequency rate is constrained to ± 15 Hz/s. These results can be seen in Fig. 4. For this case no ramping of the receiver would be required. At first glance, it would not seem that anything of particular value has been achieved, since one now has 11 exciter ramps instead of 11 receiver ramps. However, on closer inspection, a number of operational benefits would appear to accrue, i.e.,

- (1) The uplink frequency level is far more familiar to the NOCT.
- (2) The necessary uplink ramp parameters can be obtained from prediction output quantities (XA and DD2) with far less effort than producing receiver level predictions and receiver level ramp parameters.
- (3) Uplink ramping requires no individual receiver frequencies, whereas receiver predictions require fairly current individual receiver parameters (the 21-MHz free-running oscillator) measured at the DSS.
- (4) Uplink ramps would routinely be transmitted within normal predictions (via high-speed data (HSD)) and would thus be virtually guaranteed free of transmission errors, in contrast to sending large amounts of receiver ramp data manually (via teletype).
- (5) When one considers the possibility of Block IV S-band tracking with a 10-Hz tracking loop filter, or, far more important, the addition of X-band 3-way tracking at a separate 64 m DSS, no additional receiver ramping is required, in marked contrast to the receiver ramping case, where the number of total required ramps increases by 100% or more—one ramped uplink covers all receivers!

In consideration of the above, the possibility of using overcompensated uplink ramping might merit further investigation.

References

1. Chaney, W., *High X-Band Doppler Offsets and Rates During Viking Orbital Phase*, IOM NSE-74-155, July 8, 1974 (JPL internal document).
2. Koerner, M., *Viking RF Receiver Phase-Locked Loop Phase Errors Produced by Spacecraft Motion*, IOM 3395-74-055, June 6, 1974 (JPL internal document).
3. *Deep Space Network/Flight Project Interface Design Handbook*, Document 810-5, Revision D, Feb. 15, 1975 (JPL internal document).

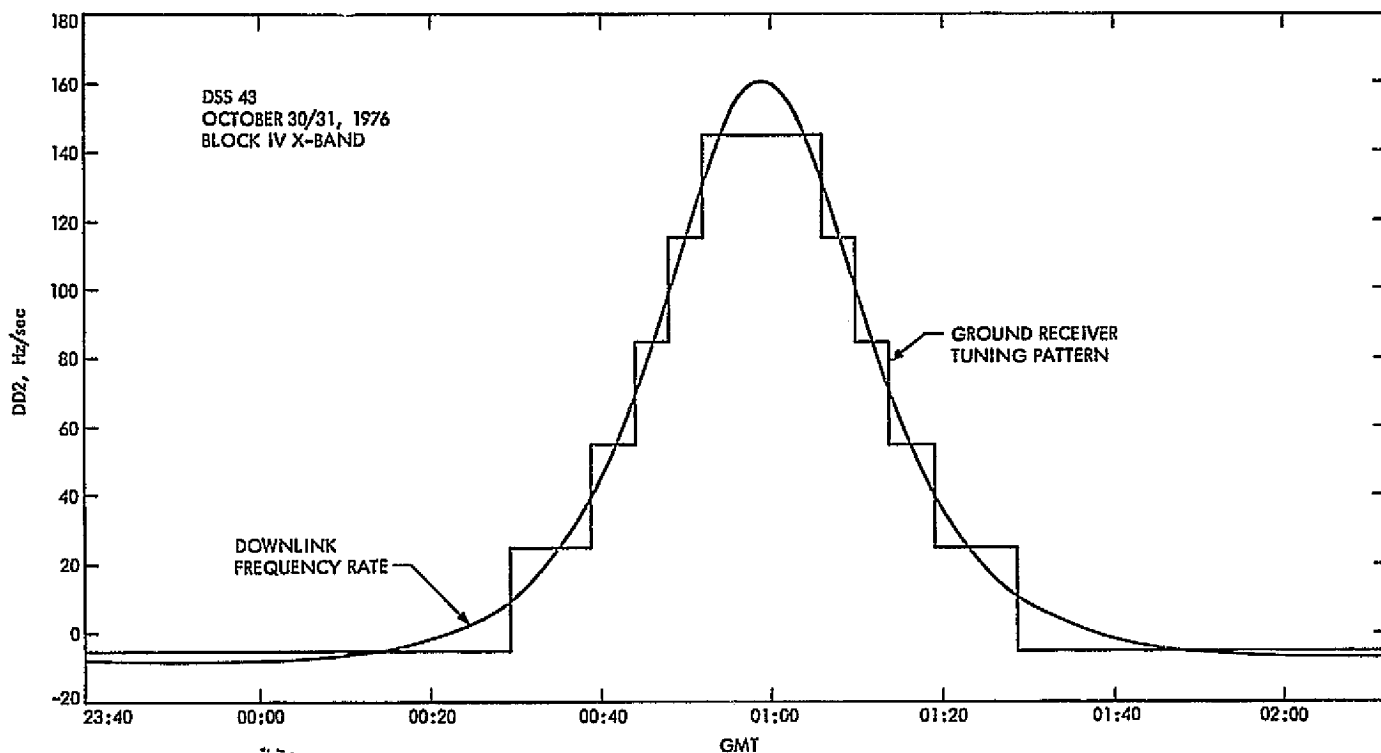


Fig. 1. Viking Orbiter 500-km/P-type orbit 2-way doppler rate versus GMT

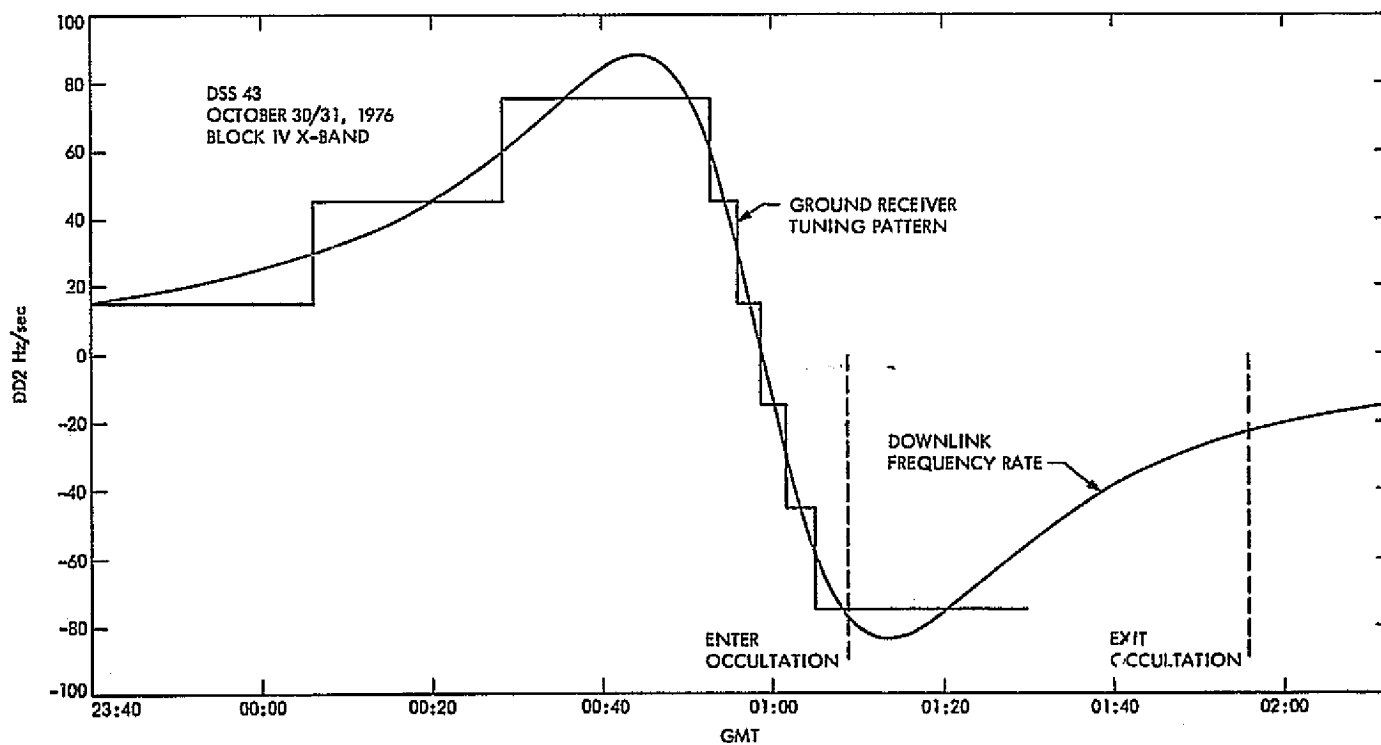


Fig. 2. Viking Orbiter 500-km/N-type orbit 2-way doppler rate versus GMT

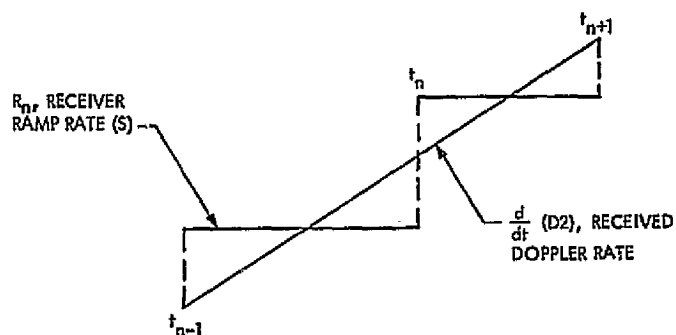


Fig. 3. Receiver ramp rates vs received doppler rate

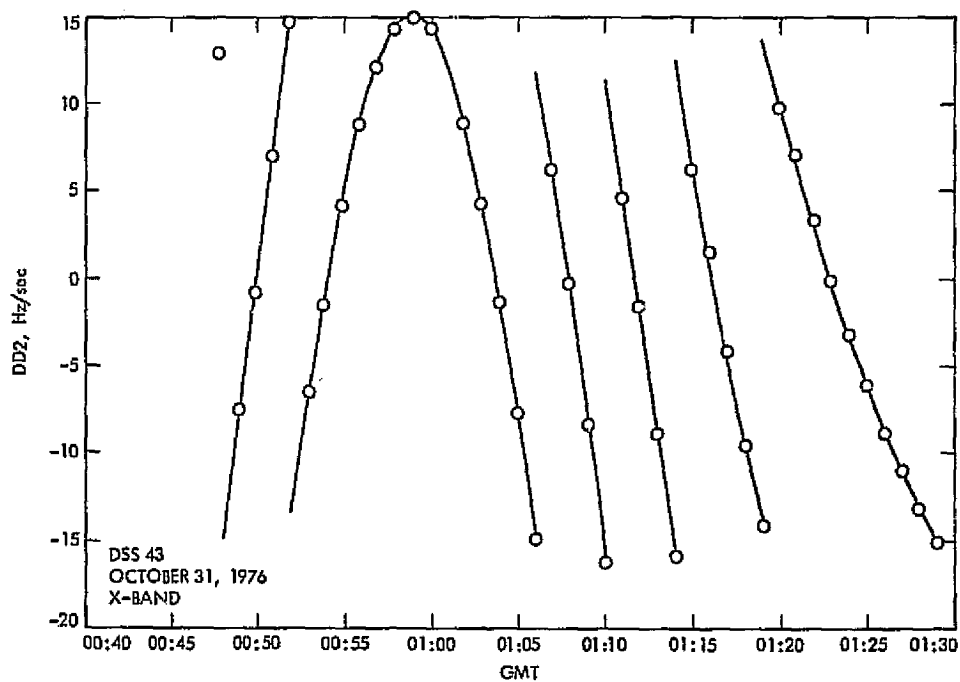


Fig. 4. D2 frequency rate with over-ramped uplink for Viking Orbiter 500-km/P-type orbit

Tracking Operations During the Pioneer 11 Jupiter Encounter

A. L. Berman and R. S. Schlaifer
Network Operations Section

Tracking operations during the Pioneer 11 Jupiter encounter proceeded quite smoothly and resulted in a highly successful encounter. Major features that distinguished this encounter from the previous Pioneer 10 Jupiter encounter were the much closer spacecraft approach to Jupiter, which induced far more dynamic excursions in the near encounter tracking parameters, and the Mars Deep Space Station two-way entry into occultation. This report details the preencounter planning and subsequent analysis of tracking operations during the Pioneer 11 Jupiter encounter phase.

I. Introduction

On December 3, 1974, at 05:21:38.9 GMT (spacecraft time), the Pioneer 11 spacecraft reached closest approach to the planet Jupiter. This encounter was simultaneously visible to both the Goldstone and the Australian Deep Space Complexes, thus allowing prime participation by two 64-m antenna Deep Space Stations—DSSs 14 and 43. Figure 1 presents an overview timeline of the near-encounter period and shows the significant tracking events in ground transmit time, spacecraft time, and ground receive time (all in GMT).

Almost exactly one year earlier, the Pioneer 10 spacecraft encountered the planet Jupiter on a similar mission and provided man with his first close-up examination of this massive planet. At that time, efforts to ensure the success of tracking operations were concentrated in the following three areas:

- (1) The occultation of the spacecraft by the Jovian satellite Io shortly before occultation of the spacecraft by Jupiter itself.
- (2) The operation of the then only recently implemented digital controlled oscillators (DCOs).

- (3) The complications in occultation strategy caused by the (then novel) very long round-trip light time (RTLT) of approximately 90 min.

The Pioneer 11 encounter, however, was significantly different from the Pioneer 10 encounter in several areas. Foremost among these were the following:

- (1) The absence of any Jovian satellite occultations of the Pioneer 11 spacecraft.
- (2) The considerably closer approach of the Pioneer 11 spacecraft to Jupiter (as compared to Pioneer 10), resulting in far more dynamic excursions in near-encounter tracking parameters. For instance, one can compare the radius of closest approach (RCA) in kilometers, the near-encounter frequency excursion at DSS 14 (ΔXA , in hertz at voltage-controlled oscillator (VCO) level) and the maximum frequency rate at DSS 14 ($d(XA)/dt$, in hertz/minute, at VCO level) as follows:

	Pioneer 10	Pioneer 11
RCA, km	203,260	113,694
ΔXA , Hz at VCO	1500	3200
$d(XA)/dt$, Hz/min	-10.3	-31.2

Figure 2 similarly illustrates the correspondingly large doppler shift (for the expected doppler modes) at enter occultation.

- (3) The decision to enter Jupiter occultation in the two-way (coherent) tracking mode for the Pioneer 11 occultation, in contrast to the Pioneer 10 enter occultation, which was performed in the one-way (noncoherent) tracking mode.

In consideration of the above, the preplanning of Pioneer 11 near Jupiter encounter tracking operations was most intensively focused on properly accounting for the very large tracking parameter excursions and the special problems of entering Jupiter occultation in the two-way tracking mode.

In the following sections the near-encounter tracking operations planning to account for the large tracking parameter excursions and the two-way enter occultation will be detailed and analyzed as to degree of success achieved. Additionally, other areas of critical tracking operations, particularly rapid reacquisition of the uplink and downlink at exit occultation and quality of near real-time tracking predictions, will be analyzed.

II. Uplink Tuning Strategy

A. Maintenance of Two-Way Lock at DSS 14 During the Enter Occultation Period

As was previously mentioned, one of the prime differences with the Pioneer 10 Jupiter encounter was the decision to have the Pioneer 11 spacecraft enter Jupiter occultation in the two-way mode. This entails a far greater risk than entering occultation in the one-way mode in that if the spacecraft receiver loses lock shortly before enter occultation, the downlink will shift from two-way to one-way (a shift on the order of several thousand hertz at S-band), and precious radio metric data would be lost while the ground receivers attempted to reestablish lock. Even if the ground receivers were able to rapidly reestablish lock, the resultant one-way doppler data would be nearly useless (for radio science purposes) because 10 or more minutes of one-way doppler data are needed to establish the drift pattern of the spacecraft beacon frequency. Finally, a switch from two-way to one-way might very possibly drive the signal out of the open-loop receiver bandwidth, thus losing this radio metric data source also. This problem was particularly appropriate to the period immediately prior to enter occultation, since it was expected that as the signal began passing through the Jovian atmosphere, there would be momentary periods of signal attenuation which could cause the spacecraft to drop lock. To mitigate this possibility to the greatest extent possible, it was proposed by Dr. A. Kliore, the occultation experimenter, that during the period of ionospheric/atmospheric traversal by the signal, the DCO at DSS 14 be used to ramp the uplink so as to approximate XA (the spacecraft best lock with doppler accounted for). The general strategy would consist of approximating the ionospheric/atmospheric period of signal traversal by a single ramp. Further, it was decided that the scheme would be defined by the following specific conditions.

Let

$TSF_{11}(t)$ = track synthesizer frequency—
transmitted uplink frequency,
at VCO level

$XA_{11}(t)$ = spacecraft best-lock uplink frequency (corrected for doppler)

Then it would be required that

$$TSF_{11}(t_0) = XA_{11}(t_0)$$

$$\left\{ \frac{d}{dt} [TSF_{11}] \right\}_{t_0} = \left\{ \frac{d}{dt} [XA_{11}] \right\}_{t_0}$$

t_0 = top of Jovian atmosphere

The rationale for the above ramping strategy would be that if there occurred momentary signal attenuation and subsequent loss of spacecraft receiver lock, the ground transmitted frequency would be at almost exactly best lock (and would continue at best lock, timewise), and hence the spacecraft receiver would be in a position to relock the uplink almost immediately.

Finally, the uplink strategy at DSS 14 was impacted by the extremely large change in the near-encounter doppler frequency, in particular, during the pre-occultation period of the pass. For instance, the total excursion of XA during this period was about 780 Hz at VCO level (75,000 Hz at S-band).

Since it was a Pioneer Project goal to keep the frequency stress at the spacecraft below approximately 250 Hz, considerable additional tuning somewhere in the pass would be required. It was proposed by the Network Operations Analysis Group (NOAG) that the same ramp necessary during the ionospheric/atmospheric traversal period be utilized by starting it at an earlier time so that the maximum stress at the spacecraft would be constrained to approximately 250 Hz, or, by starting the ramp approximately 9 min earlier. This suggestion would have the effect of simplifying overall tracking operations during the pre-occultation period since a single ramp would be easier to implement, and less risky. The suggestion was accepted by the Pioneer 11 Occultation Planning Group, and, the total uplink strategy at DSS 14 is shown in Figs. 3 and 4.

The final parameter values selected for use at DSS 14 were as follows:

Ramp start time	04:01:53	GMT
Ramp stop time	04:26:53	GMT
Starting frequency	21.988600	MHz (VCO)
Frequency rate	-0.5200	Hz/s (VCO)

B. Acquisition of the Uplink by DSS 43 After Exit Occultation

Although the spacecraft would (nominally) be commanded noncoherent for the first 10 to 15 min following exit occultation, it was concluded by the Pioneer Project that it would be expedient to acquire the uplink as soon as possible after exit occultation so as to gain command capability, if desired. To facilitate this decision, the following strategy was implemented:

- (1) DSS 43 transmitter on before exit

- (2) Uplink sweep to begin approximately 3 min following exit occultation
- (3) Sweep parameters to be chosen to yield a total sweep of approximately $XA + 60$ Hz to $XA - 100$ Hz and a sweep rate relative to the spacecraft of approximately -30 Hz/min at VCO level

The acquisition parameters finally selected in accordance with the above guidelines are as follows:

Ramp start time	05:06:00	GMT
Ramp stop time	05:11:00	GMT
Starting frequency	21.986360	MHz (VCO)
Frequency rate	-1.0000	Hz/s (VCO)

This scheme contained three crossings of XA by the transmitter frequency, and hence three separate chances of uplink acquisition, the first to occur within a minute of exit. The above uplink strategy is shown in Fig. 5.

III. Ground Receiver Strategy

A. Maintenance of Ground Receiver Lock at DSSs 14 and 43 During the Enter Occultation Period

For the enter occultation period, it was concluded that ramping the ground receivers according to the same logic as the exciter (except, of course, increasing the times by one RTLT and adjusting the frequencies and frequency rates to account for the differences between the transmitter and receiver frequency levels) would accomplish the identical goal of having the ground receivers at their best-lock frequencies in case of momentary losses of lock.

The ground receiver ramp parameters selected were:

Ramp start time	05:23:16	GMT
Ramp stop time	05:48:16	GMT
DSS 14 starting frequency	49.052579	MHz (DCO)
DSS 43 starting frequency	49.053106	MHz (DCO)
Frequency (DSSs 14 and 43) Rate	+1.6941	Hz/s (DCO)

It was subsequently assessed in near real time that the relative rate between the ground receivers and the downlink frequency at the start of the above ramp would result in an uncomfortably large dynamic phase error ($\Delta\theta$)

of approximately 20 deg plus a static phase error (SPE) of approximately 4 deg, in the desired configuration of narrow (12 Hz) tracking loop filter. To correct this possible problem area, a second receiver ramp was added which partially replaced the original ramp (above), so that the final ground receiver ramp strategy was as follows:

First ramp start time	05:05:00	GMT
DSS 14 starting frequency	49.051763	MHz (DCO)
DSS 43 starting frequency	49.052290	MHz (DCO)
Frequency (DSSs 14 and 43) rate	+1.0000	Hz/sec (DCO)
Second ramp start time	05:30:00	GMT
Frequency (DSSs 14 and 43) rate	+1.6941	Hz/sec (DCO)
Ramp stop time	05:48:16	GMT

Figure 6 shows the predicted DSS 14 ground receiver best-lock frequency versus the above ramp strategy, while Fig. 7 shows the DSS 14 downlink frequency rate versus the above ramp (rate) strategy.

B. Acquisition of the Downlink at Exit Occultation

Over the past year, and in particular during several planetary exit occultations, the DCOs have proved themselves with increasingly excellent results as a new advance in the rapid acquisition of a signal whose frequency and time of appearance are both subject to large uncertainties. The applicable mode of operation for this type of acquisition is the acquisition mode (ACQ MODE), in which a triangular frequency sweep is initiated at a fixed sweep rate and between prestored upper and lower frequency limits. After testing to determine a reasonable sweep rate (i.e., the highest sweep rate possessing an extremely high probability of acquisition), and consideration of (Pioneer Project Navigation supplied) orbital uncertainties, the following DCO acquisition mode parameters for DSSs 14 and 43 ground receivers were selected:

DCO sweep rate	± 1000 Hz/s (S-band)
DCO sweep excursion about the exit occultation point	± 5000 Hz (S-band)

These sweep patterns can be seen in Figs. 8 and 9 for DSSs 14 and 43, respectively.

IV. Postencounter Analysis

The previous sections of this report dealt with the Jovian encounter planning as it pertained to tracking operations. Procedures such as uplink tuning for the minimization of spacecraft phase error, ground receiver tuning for minimization of ground station phase error, and DCO ACQ MODE usage for downlink acquisition(s) at exit occultation were discussed and the final plans for the various phases of the operations were outlined.

In the following sections, the degree of success of the various operations will be ascertained from the vantage point of postencounter analysis of the returned radio metric data.

A. Maintenance of the Uplink From DSS 14 During the Enter Occultation Period

As was previously mentioned, an uplink ramp of 25-min duration and at a rate of approximately 50 Hz/s at S-band was executed by DSS 14 so as to maintain the maximum spacecraft receiver static phase error below 25,000 Hz at S-band and to substantially eliminate both the dynamic and the static phase error at the time of traversal of the top of the Jovian atmosphere. The success of this effort can be judged only indirectly, as there is no way of knowing what might have occurred had not the uplink tuning been performed. However, considering that the uplink was maintained throughout the time up until the loss of lock by the closed-loop ground receivers, and in fact up until the time of loss of lock by the open-loop ground receivers, the uplink tuning must be gauged as a complete success.

B. Maintenance of the Downlink by the (Closed Loop) Receivers at DSS 14 and DSS 43 During the Enter Occultation Period

As previously described, both DSSs 14 and 43 executed two receiver ramps during the enter-occultation period with a similar purpose to the uplink ramp performed by DSS 14—to substantially eliminate the static and dynamic phase error for the ground receivers at the time of traversal of the top of the Jovian atmosphere. The closed-loop receivers at DSSs 14 and 43 dropped lock at the following times:

DSS 14	05:41:48 GMT
DSS 43	05:41:49 GMT

Both of the above times can be considered favorably when compared to the loss of lock by the DSS 43 open-loop receiver at 05:42:05 GMT (as supplied by Dr. Kliore),

or only 16 to 17 seconds later. Figure 10 shows the closed-loop doppler data for both DSSs 14 and 43 immediately prior to and subsequent to the loss of lock. Although receiver ramps cannot be seen in the doppler data, the following observations, which tend to support both the accuracy of and the rationale for the ground receiver ramps, can be made:

- (1) The closed-loop receivers maintained continuous lock throughout the high-frequency rate portion of the enter-occultation period, and the dropped lock times of 05:41:48 and 05:41:49 would indicate a substantial signal entry into the atmosphere before loss of lock.
- (2) The large fluctuations seen in the closed-loop doppler data (Fig. 10) in the 30 s before loss of lock would seem to indicate that had the ground receivers not been close to the best-lock frequency and best-lock frequency rate, they might easily have been knocked out of lock.
- (3) After loss of lock, the receiver frequency (which is then directly reflected in the doppler data) can be seen in Fig. 10 to agree very closely with the predicted receiver frequency—thus indicating the ramp was correctly computed and implemented by the DSS.

Finally, it should be noted that the various tuning schemes did not take into account refraction by the Jovian atmosphere, and had it been possible to accurately predict and factor into the tuning schemes the Jovian atmosphere refraction, even better results might possibly have been obtained.

C. Downlink Acquisition by DSSs 14 and 43 at Exit Occultation

As was earlier mentioned, the use of the DCOs in the acquisition mode has produced excellent results in recent planetary occultations; the Pioneer 11 exit occultation has proved to be no exception to these results. Figures 8 and 9 show the actual receiver sweep patterns executed by DSSs 14 and 43, respectively. Using the open-loop receiver lockup times (indicated in Figs. 8 and 9) as the time of signal appearance, it can be seen from Fig. 9 that DSS 43 locked to the emergent signal on the first crossing through the received frequency (at 06:24:21 GMT), while in Fig. 8 it can be seen that DSS 14 locked to the emergent signal on the second crossing through the received frequency (at 06:24:41 GMT).

D. Acquisition of the Uplink at DSS 43 After Exit Occultation

Since the uplink acquisition sweep was performed by DSS 43 at a time when the spacecraft had been previously commanded noncoherent, it was not possible to pinpoint the exact time of uplink acquisition by extrapolating backward from the time of downlink mode change (from one-way to two- or three-way) by one RTLT, as might normally be done. All that can be said is that the uplink acquisition was routinely successful, as evidenced by the fact that the subsequent command to the spacecraft to return to coherent operations some minutes later was successfully received and executed.

E. Acquisition of the Post Occultation Two-Way Downlink by DSSs 14 and 43

In response to the postoccultation command to the spacecraft to return to the coherent mode, both DSSs 43 and 14 dropped lock at 06:41:02 GMT, at which time the downlink had shifted from one-way to two-way and three-way, respectively. Within about two minutes DSS 43 reacquired the downlink and confirmed two-way. However, DSS 14 required several additional minutes to reacquire. A study of the DSS 14 doppler data, as seen in Fig. 11, discloses that the station was searching for a two-way downlink instead of the actual three-way downlink (with DSS 43). This error at the station might have been triggered by a request from the Network Operations Control Team (NOCT) for the stations to flag their data as two-way when the proper request should have been for the stations to flag their data as either two-way or three-way, as appropriate. This slight delay in downlink acquisition by DSS 14 did not impact either the return of scientific (telemetered) data or radio metric data, due to the rapid reacquisition by DSS 43.

V. Prediction Accuracy

In virtually all recent planetary encounters, the various navigation teams have indicated that their orbital solutions will continue to improve right up until the time of encounter. Actual recent experience with both small and large planet encounters, however, suggests that clear-cut orbital accuracy improvement ends somewhere in the time period from encounter minus two days to encounter minus one week. Table 1 presents a list of various tracking parameters of interest during the Pioneer 11 encounter, as a function of the various probe ephemeris tapes (PETs) supplied by the navigation team. Once again a small but steady improvement is noted up until

the encounter-minus-two-day PET (Q635) but that the next and final preoccultation PET at E - 6 hours (Q639) represents a small net loss in prediction accuracy.

VI. Summary of Tracking Operations During the Pioneer 11 Jupiter Encounter

Tracking operations during the near-encounter period proceeded exactly as planned and resulted in a highly successful encounter. The most significant features of this

encounter, which distinguished it from the previous Jupiter encounter, were:

- (1) The very dynamic excursions in near encounter tracking parameters
- (2) The two-way entry into enter occultation

The pre-occultation planning described at length in this report would appear to have very successfully incorporated and accounted for the above features.

Table 1. Values for DSS 14

PET	Date received	Enter Occultation			Exit Occultation	
		XA at 04:20	D2 at 05:40	Time	D1 at 06:30	Time
6544	N/A	8057.7	1567912	05:40:33	1377121	06:25:14
6548	11/13/74	8030.4	1562418	N/A	1369007	N/A
6549	N/A	8028.0	1561945	05:39:35	1368785	06:24:09
6550	11/28/74	8030.5	1562432	05:39:40	1369145	06:24:14
Q631	11/29/74	8033.7	1563055	05:39:46	1369638	06:24:22
Q634	11/30/74	8034.8	1563275	05:39:49	1369820	06:24:24
Q635	12/01/74	8035.2	1563350	05:39:50	1369882	06:24:25
Q639	12/03/74 ^a	8033.8	1563072	05:39:47	1369647	06:24:22
From actual data		8036.4	1563590		1370590	
^a E - 6 h PET						

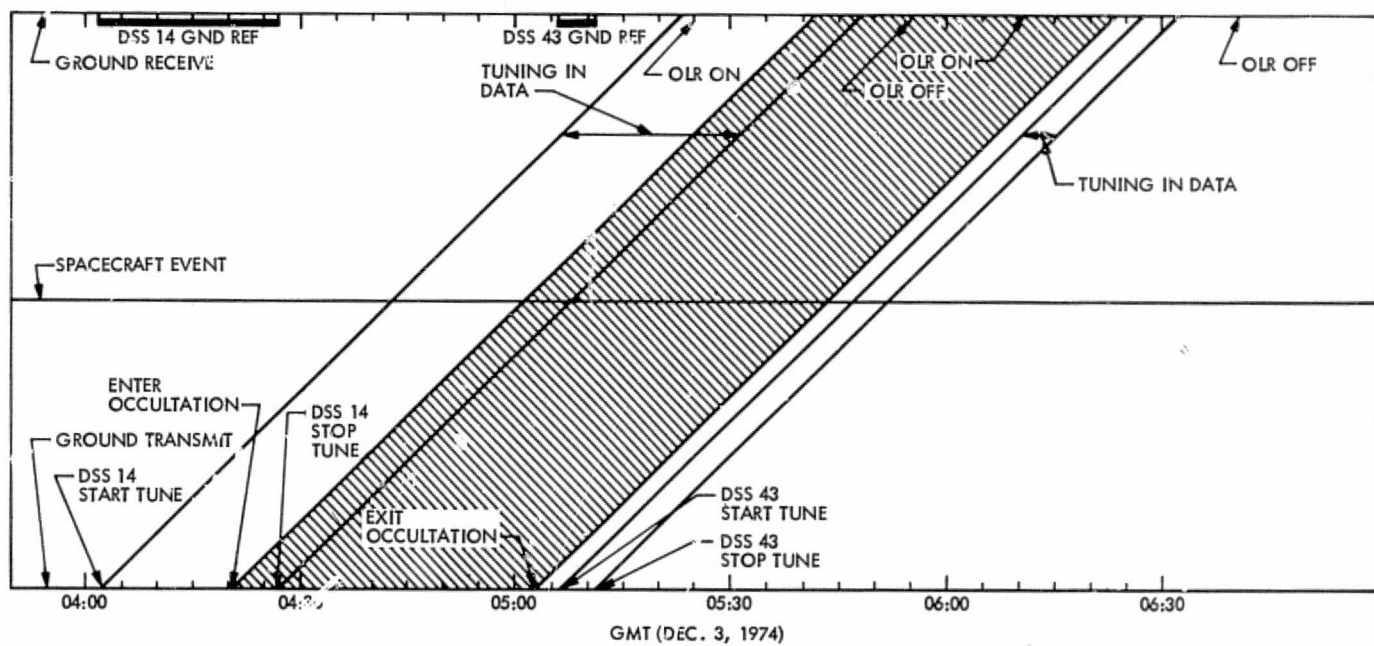


Fig. 1. Pioneer 11 Jupiter encounter

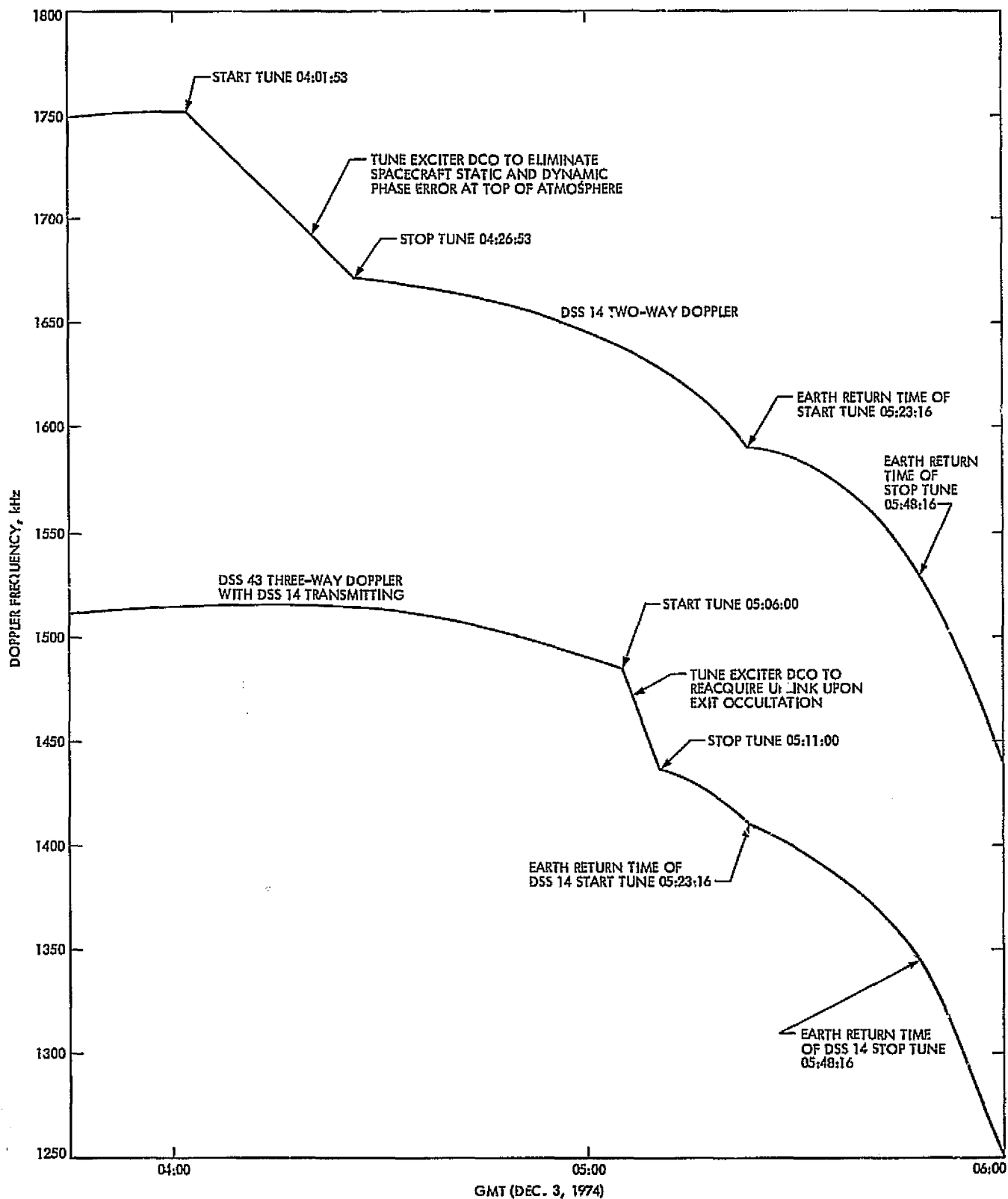


Fig. 2. DSS 14/DSS 43 doppler at enter Jupiter occultation

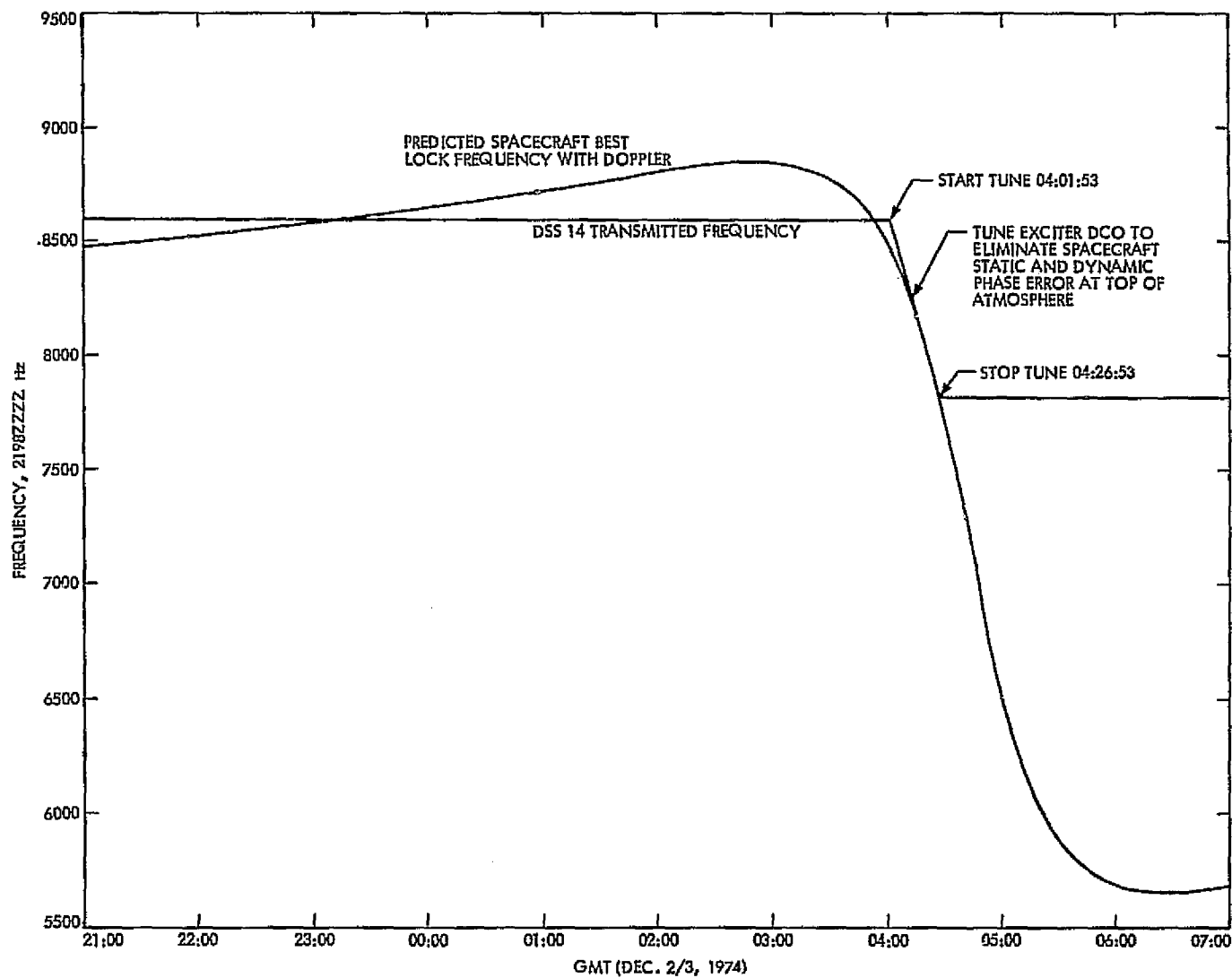


Fig. 3. DSS 14 transmitted frequency pattern

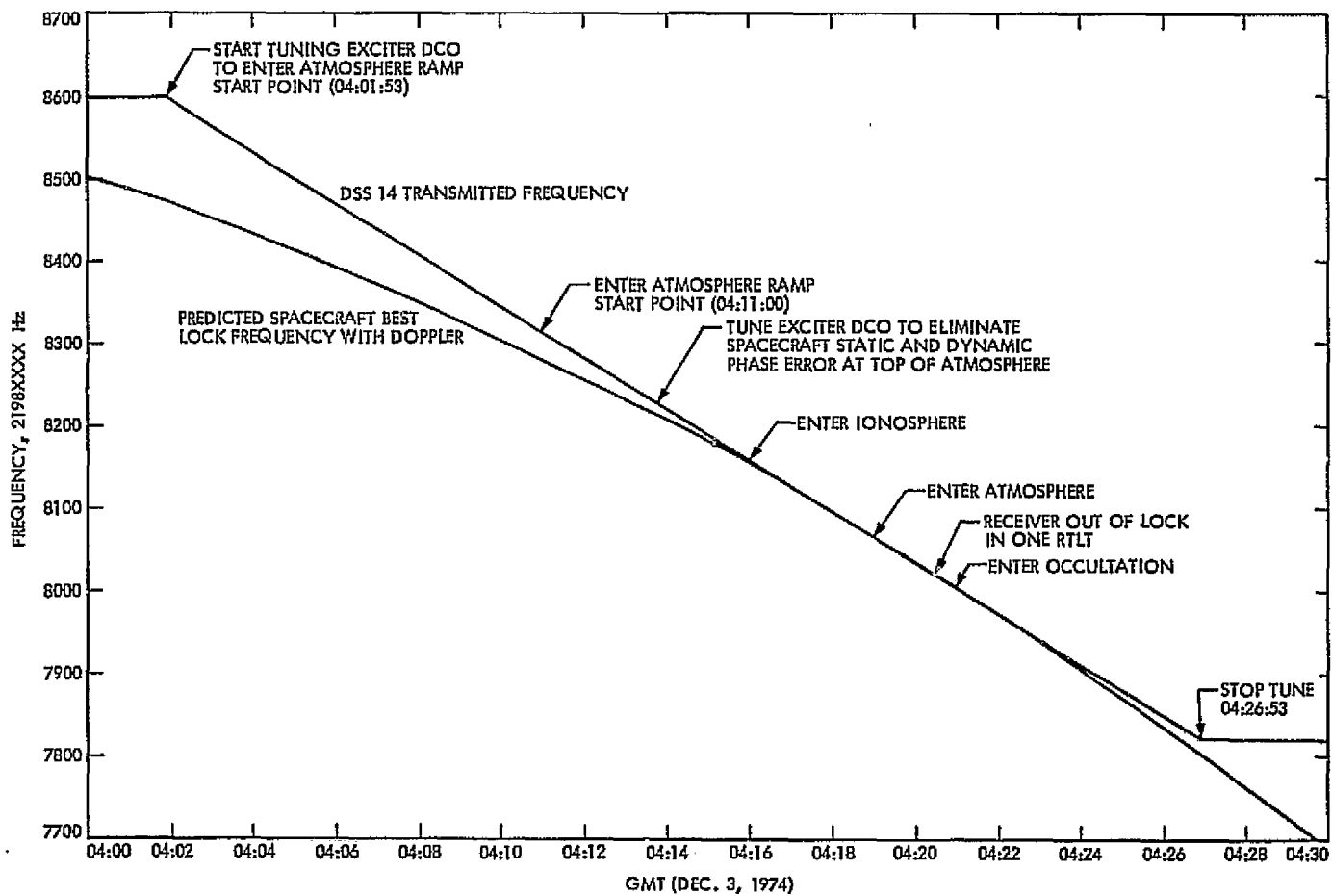


Fig. 4. DSS 14 transmitted frequency pattern at enter Jupiter occultation

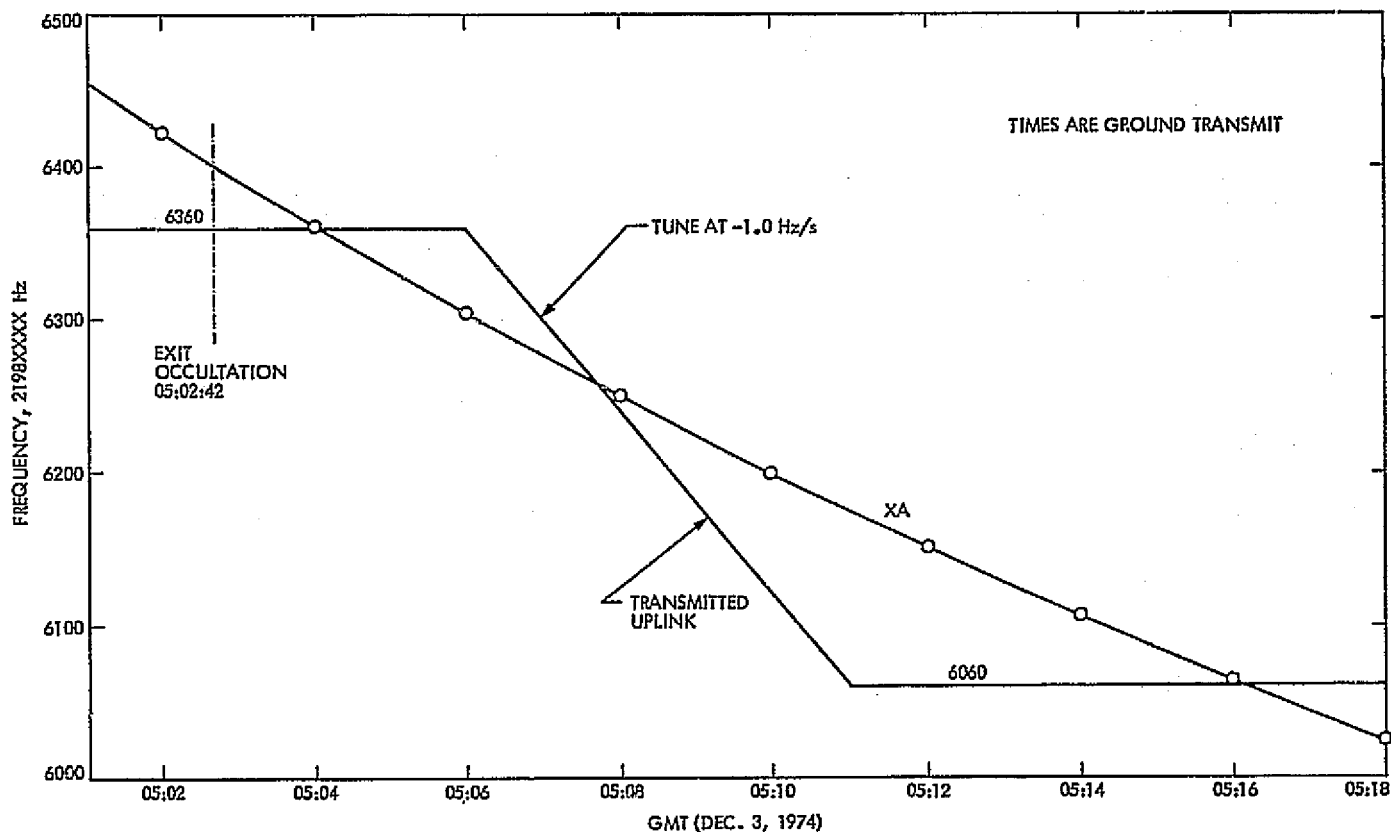


Fig. 5. Sweep pattern to acquire uplink after exit occultation at DSS 43

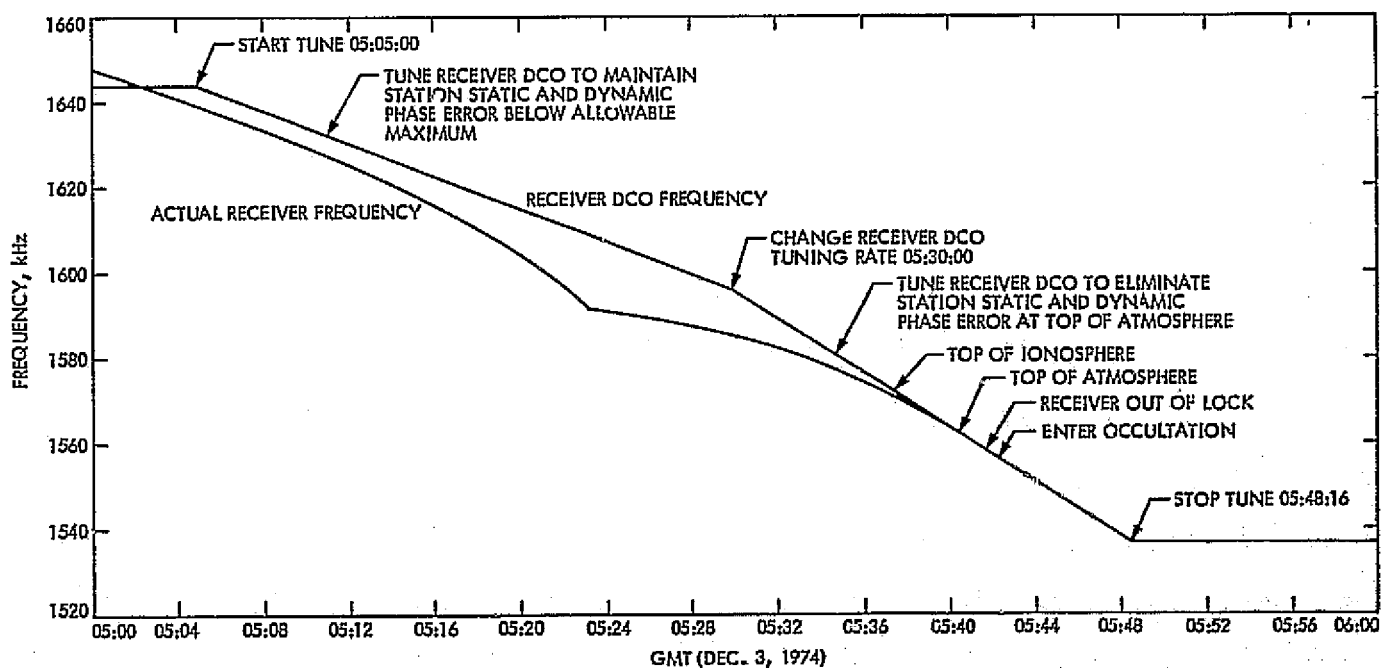


Fig. 6. DSS 14 two-way doppler at enter Jupiter occultation

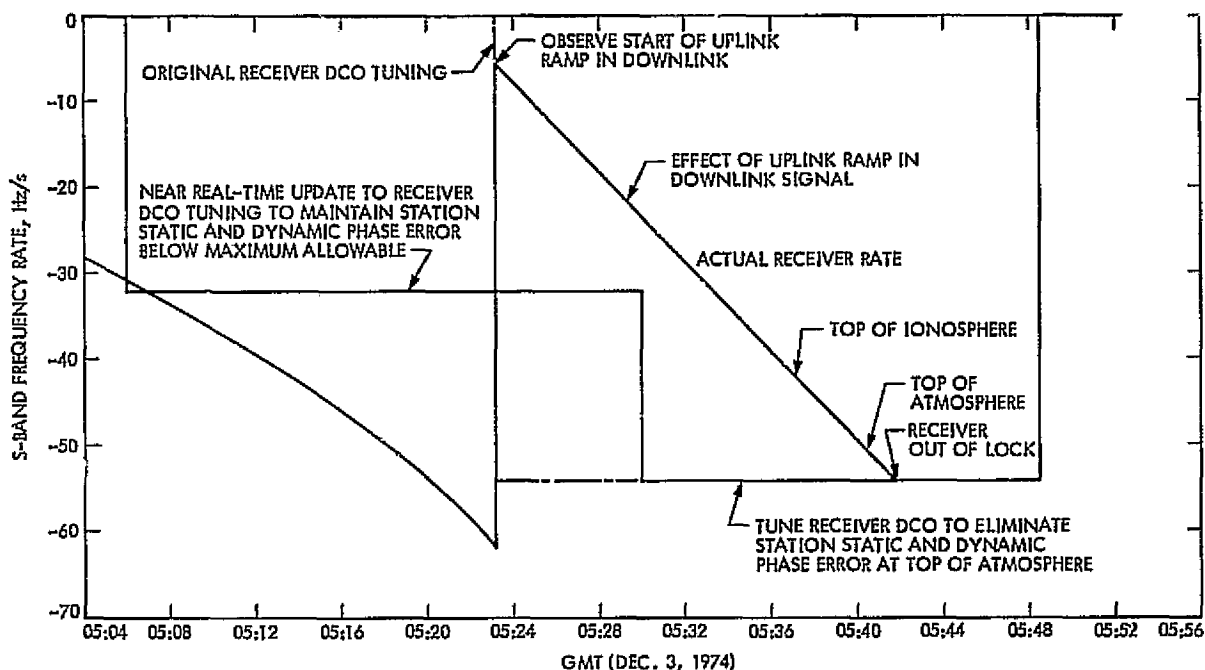


Fig. 7. DSS 14 receiver rate at enter Jupiter occultation

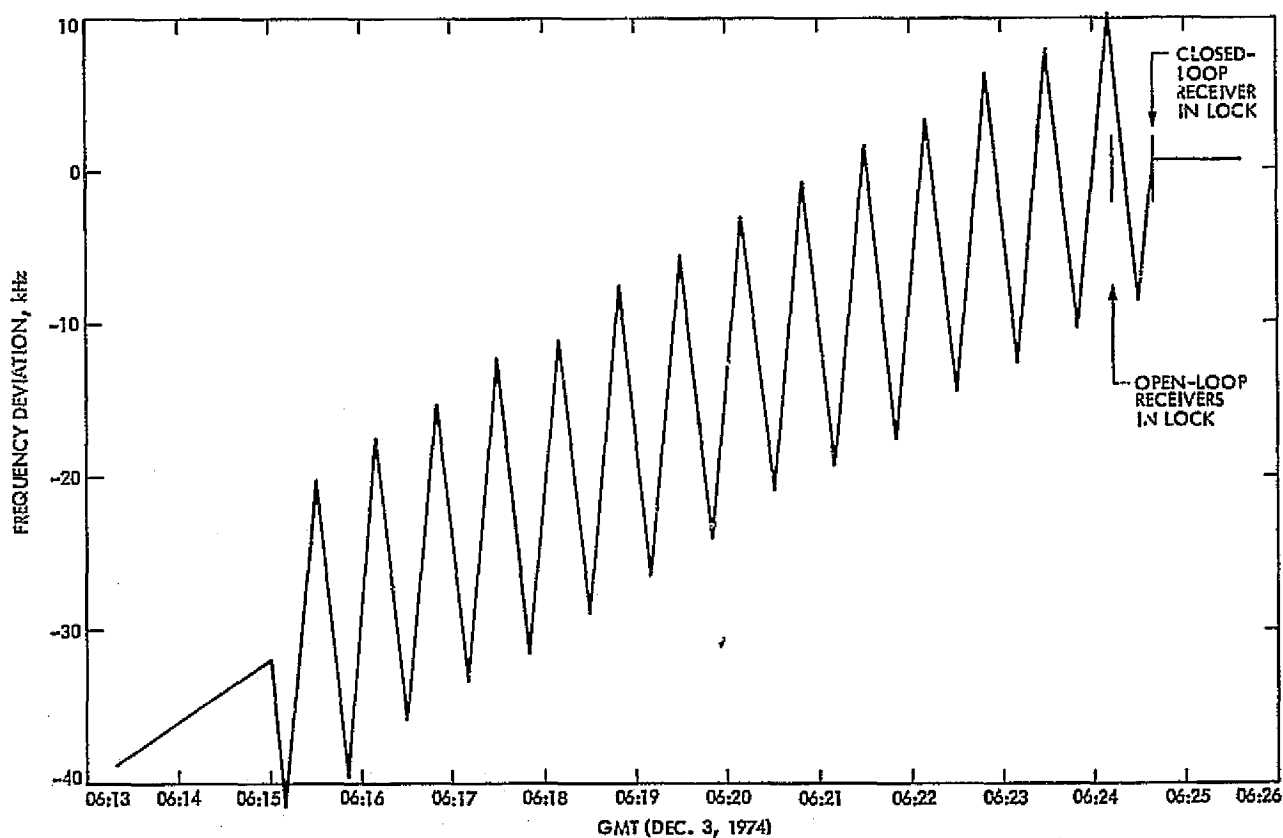


Fig. 8. DSS 14 actual minus predicted one-way doppler at exit Jupiter occultation

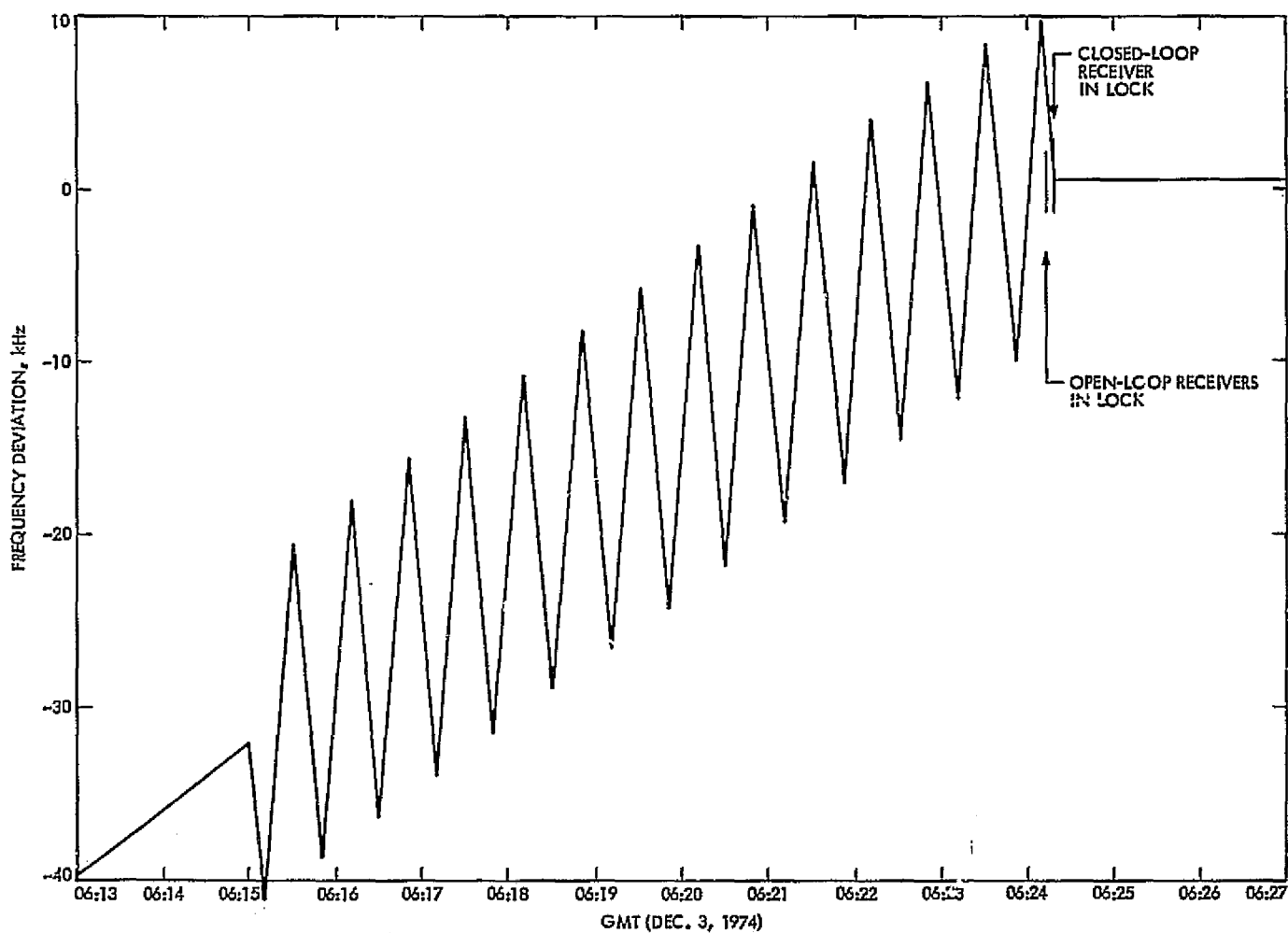


Fig. 9. DSS 43 actual minus predicted one-way doppler at exit Jupiter occultation

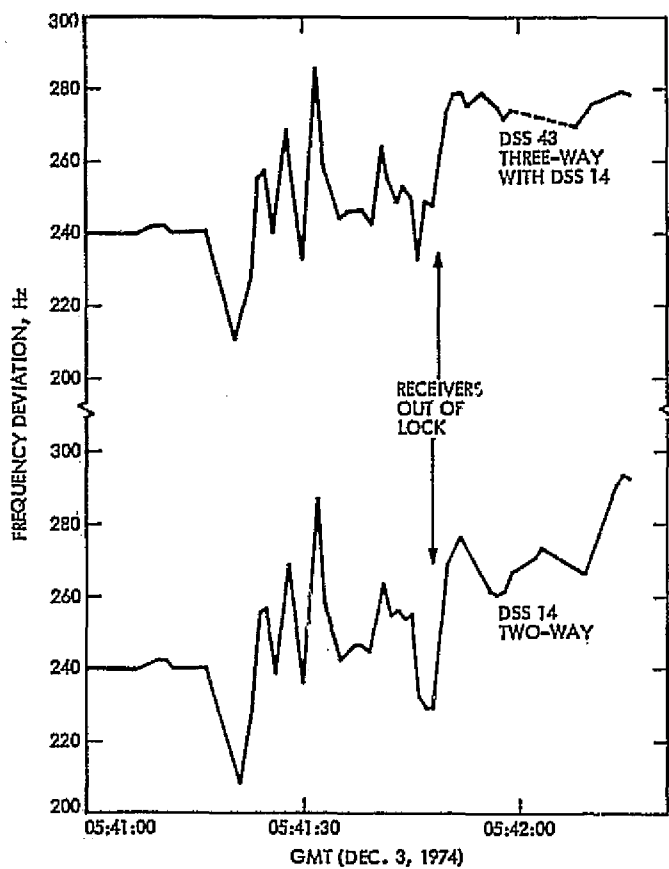


Fig. 10. DSSs 14 and 43 actual doppler minus predicted doppler at enter Jupiter occultation

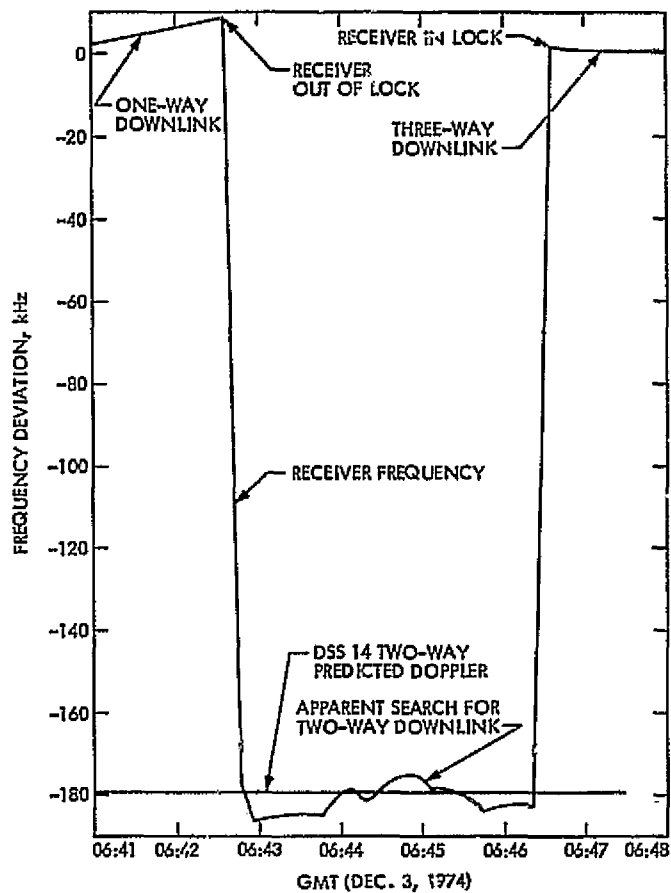


Fig. 11. DSS 14 actual minus predicted three-way doppler with DSS 43 at acquisition of coherent downlink

TDA Data Management Planning: Construction of Maximal Daily Tracking Schedules

C. A. Greenhall
Consultant to the TDA Planning Office

An algorithm is described that computes time-per-day available to each of several spacecraft that are tracked simultaneously by a DSN subnet.

I. Introduction

The algorithm described herein was written as a tool for use by the DSN in making long-range load forecasts. The input data are a set of view periods of several spacecraft as seen by each of the three stations of a subnet during a particular 24-hour period. These view periods can overlap in complicated ways; thus it is a substantial problem to compute how much time can be given to each spacecraft (S/C), given that all the S/C must be equally well covered. More precisely, let us number the S/C from 1 to n . If S/C number s is tracked for $c(s)$ hours by the subnet, then the figure of merit used in this article for the tracking schedule is

$$m = \min_s c(s)$$

We seek a tracking schedule that makes m as large as possible.

A variant of this problem requires that one of the missions, say $s = s_f$, be given 24-hour coverage. In this case, the minimum is taken over all $s \neq s_f$.

The problem is solved by converting it to a linear program. Unfortunately, the linear program is not quite a correct model of the problem, for in some cases the linear program is not feasible. If certain constraints of the problem are then relaxed, the linear program usually becomes feasible and provides useful estimates. In addition, there is a separate computation, valid for all cases, that quickly gives an upper bound on S/C coverage time.

The algorithm has been imbedded in a conversational, structured MBASIC program, called DATRAMAX (Daily TRacking MAXimizer). This form is convenient for evaluating the usefulness of the algorithm.

II. Problem Statement

A subnet of Deep Space Stations at Goldstone, Australia, and Spain is to track n spacecraft where $2 \leq n \leq 6$. The view period of each S/C at each station is given and is assumed to be constant from day to day in this model. Also given are the following nonnegative parameters: ϵ , the minimum elevation for tracking; τ , the minimum time

for a station to transfer its attention from one S/C to another; and δ , the minimum duration of a tracking period. One of the S/C may be *avored*, that is, it may be required that it be tracked by one station whenever *some* station sees it above elevation ϵ .

It is assumed that the time for a S/C to go from the horizon to elevation ϵ is approximately independent of the station and S/C locations; thus, ϵ will be given in units of time and assumed to be constant. In fact, it is sufficient simply to shorten the ends of each view period by ϵ ; we will speak then of *shortened* view periods.

A *feasible tracking schedule* is defined as follows. For each station and S/C, the station either does not track the S/C at all, or tracks it during a single subinterval of the shortened view period. The schedule is periodic with period 24 hours. At any time, no two stations track the same S/C and, of course, a station cannot track more than one S/C. The tracking periods satisfy the constraints implied by the numbers τ and δ . One of the S/C may be *avored* as mentioned above.

For any such schedule, set $c(s)$, $s = 1$ to n , equal to the total time devoted to S/C s by all three stations. The problem is to find the greatest minimum coverage

$$\max (\min_{s \neq s_f} c(s))$$

where the maximum is taken over the collection of feasible tracking schedules, and s_f is the index of the *avored* S/C. (If none are *avored*, then s_f is set equal to 0.)

III. Solution Technique

Let us label the Stations 1, 2, 3 (Goldstone, Australia, Spain) and the S/C from 1 to n .

This algorithm solves the problem for most practical cases. The exceptions occur because of additional restrictions that are placed on the class of feasible schedules. First, we assume that each shortened view period contains a nonempty tracking period (even if that tracking period reduces to a single point!) For example, if $\delta = 3$, then every view period must contain a tracking period of at least 3 hours—no tracking period can be omitted. For certain combinations of view periods, ϵ , τ , δ , and s_f , this assumption forces the constraints to become incompatible. For example, suppose that there are two S/C at the same place in the sky, and that their view periods are 2000–0900 at Goldstone, 0400–1300 at Australia, and

1200–0100 at Spain (Fig. 1). (This is an approximation of a set of real view periods.) Assume for this demonstration that $\epsilon = 0$, $\tau = 0$, $\delta = 3$, and that S/C 1 is *avored*. Then S/C 1 *must* be tracked by Goldstone at least between 0100 and 0400, by Australia at least between 0900 and 1200, and by Spain at least between 1300 and 2000, and during these periods, S/C 2 cannot be tracked. Therefore, S/C 2 can be tracked only during the periods 0400–0900, 1200–1300, and 2000–0100. But it is impossible to encase three disjoint tracking intervals of at least 3 hours each within the union of these three periods.

For most view period data, the constraints are compatible if τ and δ are set to 0.

The second restriction is less serious. For each station, the n tracking periods are disjoint subintervals of the cyclic 24-hour day; we assume that they occur in the same cyclic order as the midpoints of the Goldstone view periods. Also, the three tracking periods of each S/C are assumed to follow each other in the east-west cyclic order 1, 2, 3, 1. We feel that these assumptions are not unduly restrictive, for the configuration of view periods does not change much from station to station, and this choice seems to allow the most room for placing the tracking periods.

These additional restrictions allow the problem to be reduced to a linear program whose variables give the left and right end points of the tracking periods. Let the shortened view period of station a and S/C s have rise and set times $\rho(a, s)$ and $\sigma(a, s)$. These times can be shifted by multiples of 24 so that $0 \leq \rho(a, s) < 24$, $\rho(a, s) < \sigma(a, s) < \rho(a, s) + 24$. Let the tracking period for the combination (a, s) be

$$(\rho(a, s) + z(a, s), \sigma(a, s) - w(a, s))$$

where $z(a, s)$ and $w(a, s)$ are the nonnegative linear program variables.

Following are the linear constraints and object function:

- (1) *View constraints*: these state that the tracking periods have length $\geq \delta$:

$$z(a, s) + w(a, s) \leq \sigma(a, s) - \rho(a, s) - \delta$$

for all a, s .

- (2) *Possibility constraints*: these state that the tracking periods for a station follow each other in the cyclic midpoint order mentioned above. Let $m(s)$, $s = 1$

to n , be the midpoint of the Goldstone view period $(\rho(1, s), \sigma(1, s))$. Let s_1, \dots, s_n be a permutation of $1, 2, \dots, n$ such that $m(s_1) \leq m(s_2) \leq \dots \leq m(s_n)$. Let $s_{n+1} = s_1$,

$$\begin{aligned}\rho'(1, s_{j+1}) &= \rho(1, s_{j+1}), & \text{if } j < n \\ &= \rho(1, s_1) + 24, & \text{if } j = n\end{aligned}$$

For $a = 2$ and 3 , determine $\rho'(a, s_{j+1})$ such that

$$\begin{aligned}\rho'(a, s_{j+1}) &\equiv \rho(a, s_{j+1}) \pmod{24}, \\ -12 &< \sigma(a, s_j) - \rho'(a, s_{j+1}) - \sigma(1, s_j) + \rho'(1, s_{j+1}) < 12\end{aligned}$$

This ties the view period configurations of stations 2 and 3 to that of station 1 . The constraints are

$$w(a, s_j) + z(a, s_{j+1}) \geq \sigma(a, s_j) - \rho'(a, s_{j+1}) + \tau$$

for $a = 1$ to 3 , $j = 1$ to n . If the right-hand side is not positive, that constraint is omitted.

- (3) *Redundancy constraints*: these express the east-west order of the tracking periods of each S/C. Let \oplus be defined by

$$\begin{aligned}a \oplus 1 &= a + 1, & \text{if } a = 1 \text{ or } 2 \\ 3 \oplus 1 &= 1\end{aligned}$$

For $a = 1$ to 3 , $s = 1$ to n , determine $\rho''(a \oplus 1, s)$ such that

$$\begin{aligned}\rho''(a \oplus 1, s) &\equiv \rho(a \oplus 1, s) \pmod{24}, \\ 0 &< \rho''(a \oplus 1, s) - \rho(a, s) < 24\end{aligned}$$

The constraints are

$$w(a, s) + z(a \oplus 1, s) \geq \sigma(a, s) - \rho''(a \oplus 1, s)$$

for $a = 1$ to 3 , $s \neq s_f$. (Omit any constraint with nonpositive right-hand side.) If $s_f \neq 0$, then the constraints for $s = s_f$ are

$$\begin{aligned}w(a, s_f) + z(a \oplus 1, s_f) \\ = \max(0, \sigma(a, s_f) - \rho''(a \oplus 1, s_f))\end{aligned}$$

for $a = 1$ to 3 . (If the right-hand side is zero, we could eliminate $w(a, s_f)$ and $z(a \oplus 1, s_f)$ from the linear program, but the computer program would become more complex.)

- (4) *Object constraints and object function*: The object function to be maximized is an auxiliary variable μ , which satisfies the constraints

$$c(s) \geq \mu, \quad s \neq s_f$$

where

$$c(s) = \sum_{a=1}^3 (\sigma(a, s) - \rho(a, s) - z(a, s) - w(a, s))$$

the tracking time devoted to s by all three stations.

This linear program is solved by a general simplex routine, which, of course, reports the infeasibility of the constraints, if such is the case. Once the linear program is solved, it is easy to make a further improvement not called for by the problem statement. Let $m = \max \mu$, obtained by the previous linear program. Consider another linear program with the same variables, the same constraints (1) through (3), but with (4) replaced by

(4)* *Object constraints*:

$$c(s) \geq m + \mu, \quad s \neq s_f$$

Object function:

$$\sum_{s \neq s_f} c(s)$$

The final solution of the first program, with μ set to 0 , is given to the second program, which maximizes total tracking time while keeping each $c(s)$ not less than the best minimum coverage per S/C. The initial tableau of the second program differs very little from the final tableau of the first program, and the optimization of the second program requires few simplex iterations.

Because the algorithm sometimes causes incompatible constraints, a backup computation is provided for all cases. This gives (1) an upper bound on total tracking time, (2) time available to the favored S/C if $s_f \neq 0$, and (3) an upper bound on tracking time per unfavored S/C. The set of endpoints of the shortened view periods divides the cyclic 24-hour day into subintervals called *atoms*. For the k th atom, there is an incidence table $E_k(a, s)$, where $E_k(a, s) = 1$ if atom k is contained in the shortened view period of station a and S/C s , and $E_k(a, s) = 0$ otherwise. A *diagonal* of a 0-1 matrix (such as E_k) is defined as a subset D of the set of "1's" of the matrix such that D has no two 1's in the same row or column. (This generalizes the ordinary notion of the diagonals of a square matrix.) Let a feasible tracking schedule be constructed upon the given view periods. At any instant of time t during the k th atom, the set of index pairs (a, s) such that

station a is tracking S/C s must be a diagonal of E_k . Hence, the number of S/C being tracked at time t is bounded above by the size d_k of a *largest* diagonal of E_k . Therefore, if l_k is the length of atom k , the total tracking time of any feasible schedule cannot exceed $B = \sum d_k l_k$.

Since E_k is a 3 by n matrix, the number d_k can equal only 0, 1, 2, or 3, and a simple search suffices to discover its value. If there is a favored S/C $s_f \neq 0$, and if E_k has a 1 in column s_f , then only those diagonals of E_k that have a 1 in this column can be considered. It can be proved, however, that the maximum size of the diagonals in this restricted set again equals d_k .

The time T_f available to S/C s_f is simply $\sum l_k$, where the sum is over all k such that E_k has a 1 in column s_f . Then $B - T_f$ divided by the number of unfavored S/C is a bound on the tracking time for each of these S/C.

IV. Sample Inputs and Outputs

Suppose that there are 2 S/C with the following view periods:

	Goldstone		Australia		Spain	
	Rise	Set	Rise	Set	Rise	Set
S/C 1	0430	1748	1340	2136	2050	1033
S/C 2	2225	1046	0615	1540	1450	0327

Let $\epsilon = 0.5$ h, $\tau = 1$ h, $\delta = 3$ h, $s_f = 0$.

The "atoms" calculation yields a bound 46.02 h on total tracking and hence, a bound 23.01 h on tracking time per S/C. The linear programs compute the following tracking schedule and coverages:

	Goldstone	Australia	Spain
S/C 1	1003-1610	1610-2106	2235-1003
S/C 2	2255-0903	0903-1510	1520-2135
S/C 1:	22.51 h		
S/C 2:	22.51 h		
Total	45.02 h		

Now let $s_f = 1$. The "atoms" calculation shows 23.77 h available to the favored S/C 1, and hence, a bound of 22.25 h on tracking time for S/C 2. The tracking schedule and coverages are now

	Goldstone	Australia	Spain
S/C 1	1003-1620	1610-2106	2120-1003
S/C 2	2255-0903	0903-1510	1520-2020
S/C 1:	23.77 h		
S/C 2:	21.25 h		
Total	45.02 h		

V. Conclusions

This algorithm has two main defects caused by forcing the problem into the framework of one or two fixed linear programs. First, the linear program can be infeasible. Second, the schedules produced cannot be described as "optimal." More criteria are needed. For example, having maximized the smallest $c(s)$ (coverage of S/C s), one could then maximize the next smallest $c(s)$, and so on. Remedy of these defects may require programming with mixed real and integer variables.

In spite of these defects, the algorithm will still yield realistic estimates of time available to future missions.

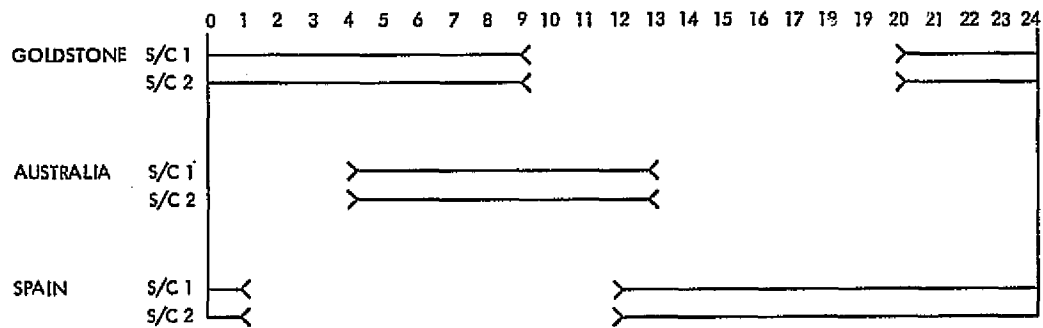


Fig. 1. An example of incompatible constraints

Quality Assurance Training and Certification Program

R. L. Sirpilla and L. H. Fisler
Quality Assurance DSN and Mechanical Hardware Section

The JPL Quality Assurance Training and Certification Program provides courses by qualified and certified instructors in the proper techniques of hand soldering, cabling and harnessing, wire wrap, cable repair, and printed conductor module repair.

I. Introduction

The JPL Quality Assurance Training and Certification Center specializes in technical training courses related to the fabrication of electronic equipment (see Table 1). These courses conform to released standards and specifications.

Good workmanship and quality are the key to dependability. The best of standards and specifications must be supplemented with personnel trained in the proper techniques of good workmanship. This quality assurance program provides the mechanics for improving personnel capabilities, and thus ensures a higher level of quality and reliability.

II. NASA Audit

During September of 1974 NASA auditors conducted a survey and audit of the JPL Quality Assurance DSN and Mechanical Hardware Section and issued a commendation

for operating a training school that services JPL on-sites, the global DSN, contractors, suppliers and Government agencies. They requested that JPL video tapes and other training materials be provided to other NASA centers upon request.

III. Scheduling of Classes

An advance schedule of training courses and events is published each month. Due to heavy work load, advance notification for registration is required. New courses are added to the training program as required to fulfill the needs of new technology.

IV. Training Equipment

The Quality Assurance Training and Certification Center provides the latest state of the art in work stations and electronic assembly equipment as shown in Figs. 1 through 7, and 9 and 10.

V. Certification

A certificate of completion is issued to each successful student and is valid for one year, at which time the student must requalify for proficiency in the specific techniques.

VI. DSS Stations, Overseas Training Program

JPL Quality Assurance provides assistance to Training Instructors at the Deep Space Stations located in Spain and Australia. These instructors are trained and certified by JPL Quality Assurance and are qualified to teach the same courses that are taught at the JPL facilities. The training programs at the overseas stations have been highly successful and this arrangement provides a continuity of consistent workmanship to established standards throughout the Network.

VII. Support to Technical Personnel

Quality Assurance personnel provide assistance to technical personnel when design problems exist. This includes areas where wire wrapping of component leads is necessary in congested areas of integrated circuit chassis, splicing techniques in restricted areas, pull tests for various types of crimping assemblies, and, in some cases, the restoration of damaged circuit boards to operational status. Technical bulletins provide other informational support on various types of coaxial assemblies now in use throughout the Deep Space Network.

VIII. Benefits to NASA/JPL

Since the inception of the Training and Certification Program in 1964, the JPL Training and Certification

Center has trained and certified in excess of 2000 students in technical courses (see Fig. 8). Results of this effort have proven conclusively that properly trained personnel have a large influence in the reduction of costs by the prevention of discrepant material.

For example, previously, in the area of cable repair, multiconductor cables were manufactured, tested, inspected, and shipped to our overseas stations. If one became damaged, it had to be replaced with a spare, returned to JPL for repair or replacement, and again shipped to the overseas station at additional cost. Since the advent of the cable repair course, a cable can now be repaired on site by qualified JPL-trained station personnel with the JPL-furnished cable repair kit for an average cost of four manhours and \$20.00 worth of material. A set of video training cassettes for cable repair is presently at each Deep Space Station for station use. Similar examples exist in the areas of wire wrapping, soldering, harnessing, and cabling.

IX. Summary

The Quality Assurance Training and Certification Program is utilized by NASA and the Department of Defense (DOD). The training is available to JPL personnel, contractor personnel who have current contracts with NASA/JPL, and Government personnel. Many NASA and DOD personnel have attended and were certified at JPL. Consistent good workmanship programs result from established standards that effectively reduce rework through proper training. Training is provided by qualified instructors with lesson plans and audio and video aids such as TV cameras, monitors, and cassettes for concurrent classroom presentations.

**Table 1. Training Courses offered by JPL Quality Assurance
Training and Certification Center**

Course	Course code	Hours
Group I: DSN/OSE^a Type		
a. Hand Soldering	A	40
b. Cabling and Harnessing	B	40
c. DSS Electronics and Fabrication (DSS Stations)	C	40
d. Wire Wrap	D	16
e. Cable Repair (DSS Stations)	E	16
f. Printed Conductor Module Repair	I	24
Group II: Flight Type		
a. Flight Cable Fabrication	G	40
Group III: Packaging, Packing/Shipping, Receiving		
a. Preservation and Packaging	H	40
Group IV: Quality Assurance		
a. Quality Assurance Inspection Techniques		40
Group V: Familiarization and Indoctrination (Supervisor Application)		
a. Wire Wrap	D	4
b. Hand Soldering	A	16
c. Cabling/Harnessing	B	16
d. Cable Repair	E	4
e. True Positioning Tolerancing	J	4
f. Printed Conductor Module Repair	I	8
^a Operational support equipment.		

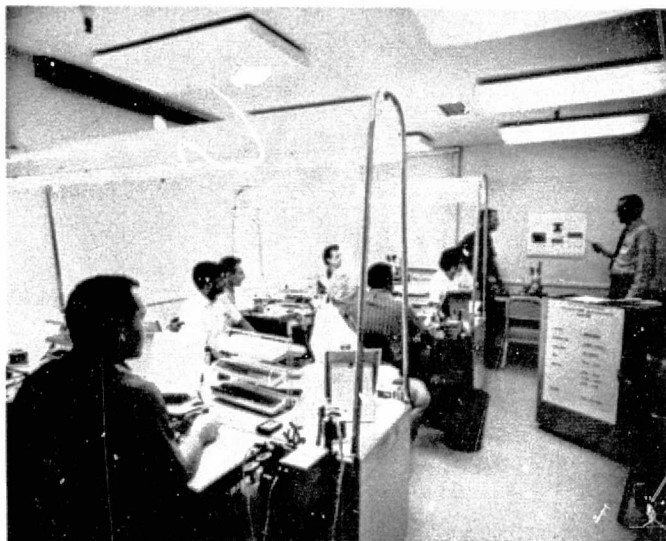


Fig. 1. Instructions are given to the students by qualified and certified instructors

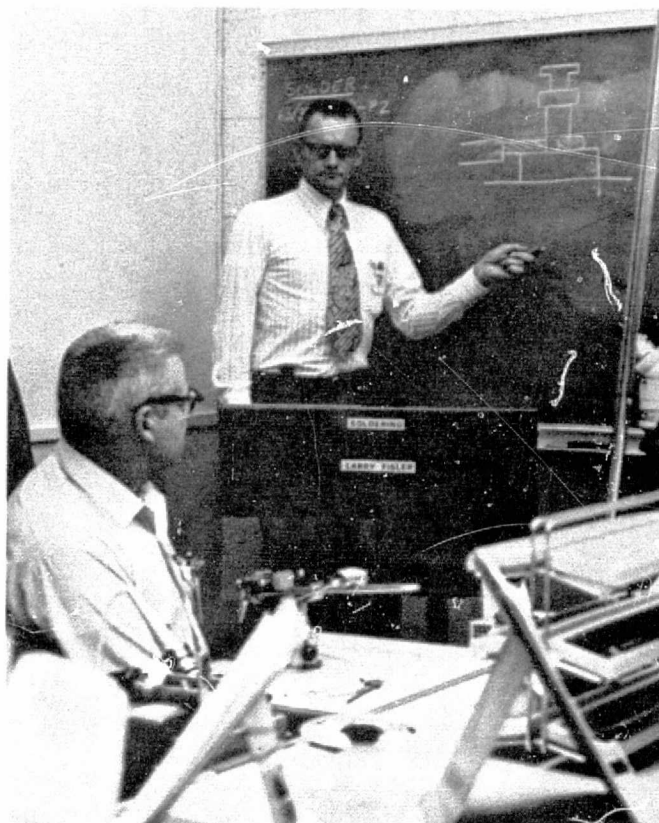


Fig. 3. Instructors provide illustrations for training technique



Fig. 2. Demonstrations are important as a follow-up to the material previously presented



Fig. 4. Work accomplished by the student is inspected by the instructor and observed by the student using the dual microscopic inspection setup

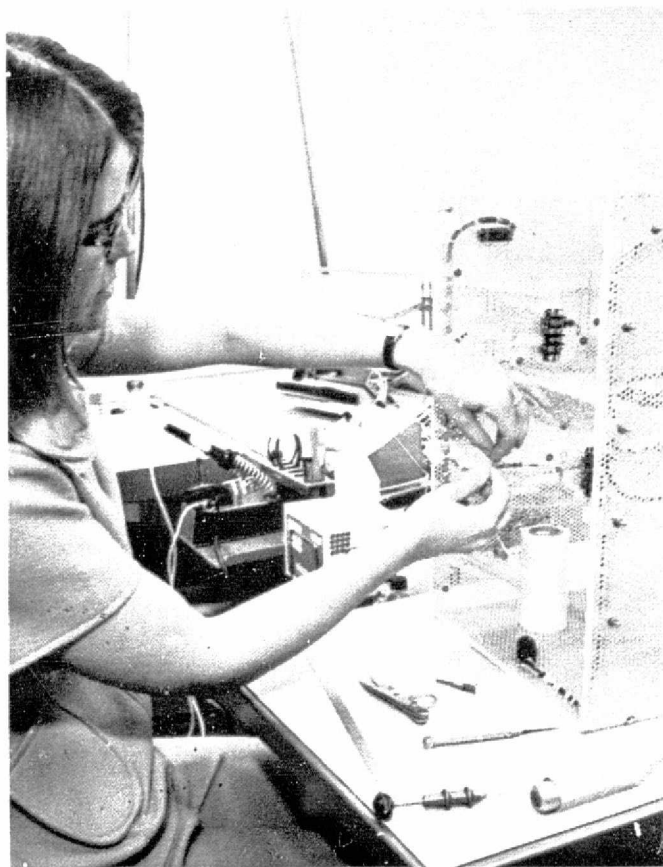


Fig. 5. Chassis cabling/wiring assembly



Fig. 6. Wire wrap assembly

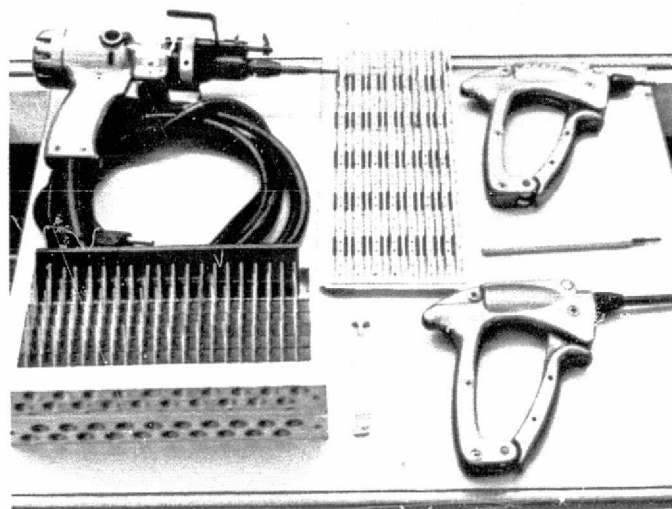
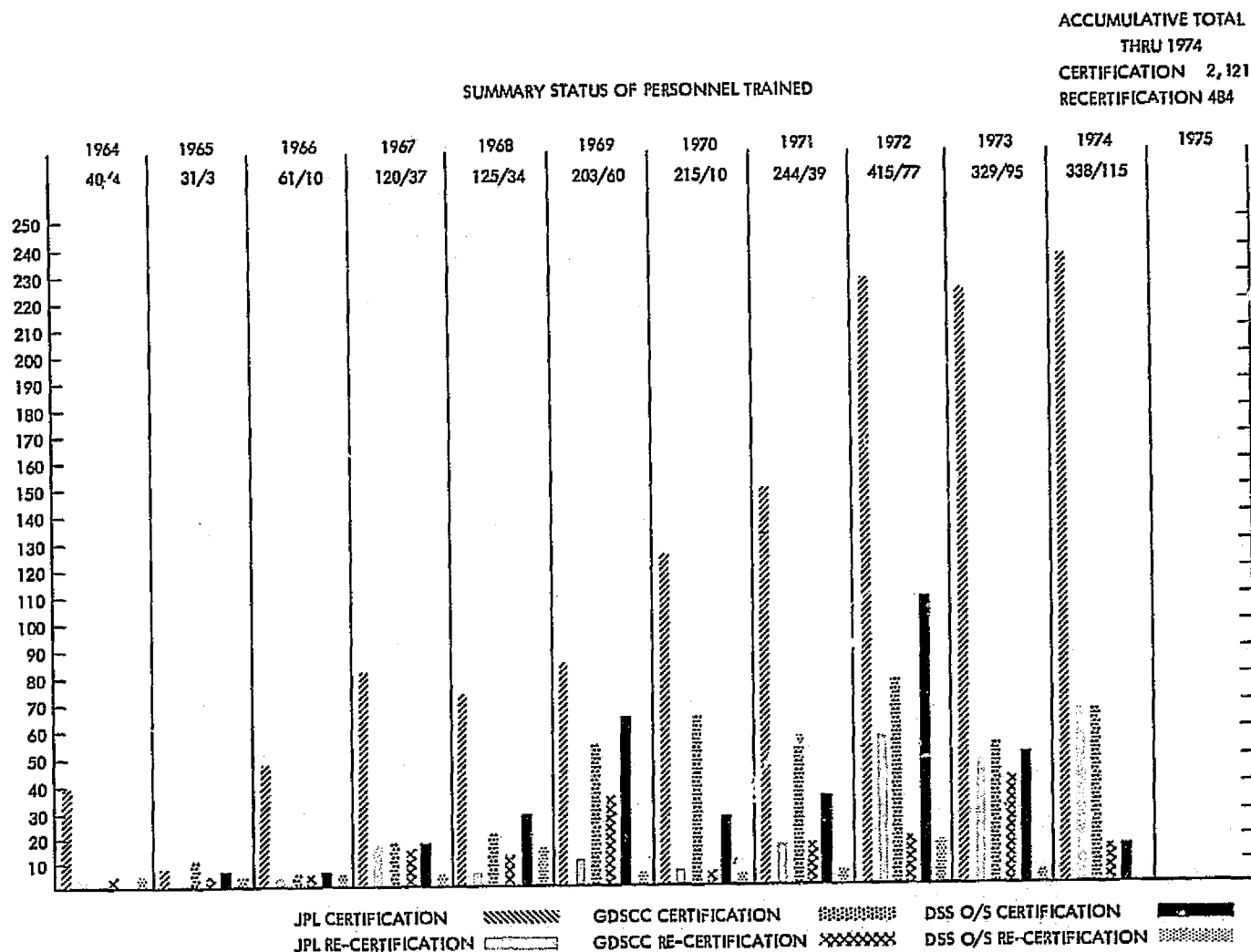


Fig. 7. Solderless (wire wrap) equipment



R. SIRPILLA TRAIN SUPV

Fig. 8. Summary status of personnel trained

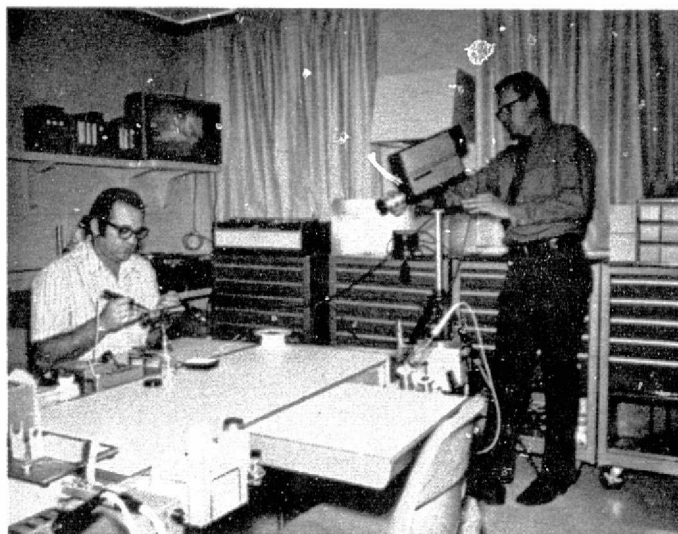


Fig. 9. TV recording for production of video training cassettes

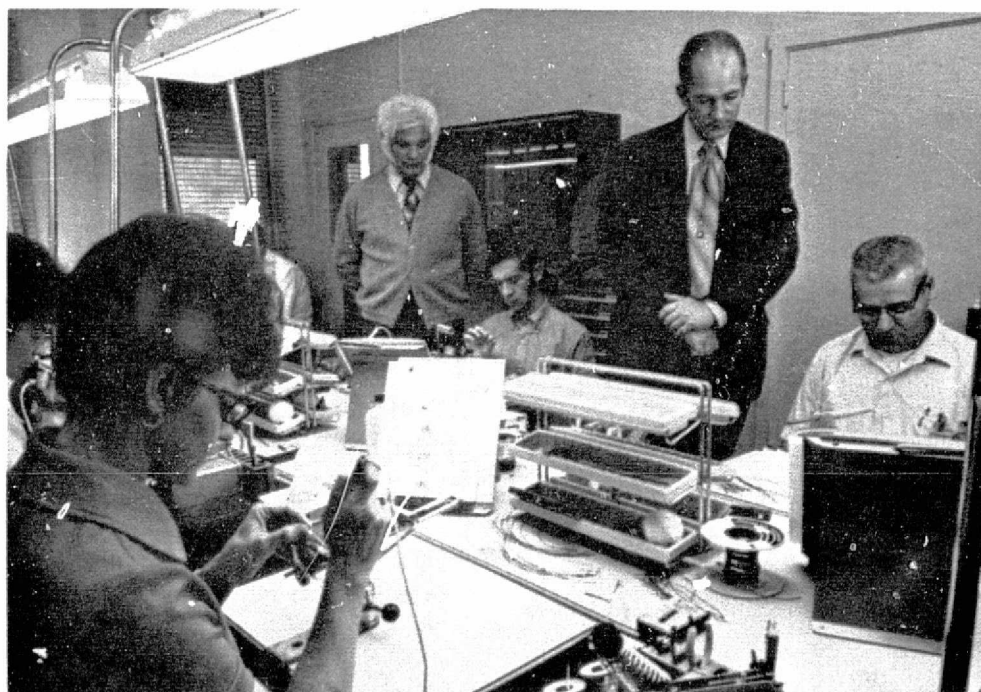


Fig. 10. Training school is periodically audited for conformance to establish criteria

Hydrogen Gas-Fueled Diesel Engine Feasibility Demonstration

R. Reynolds
DSN Engineering Section

The feasibility of a hydrogen gas-fueled diesel engine was demonstrated in a test program at Cornell University. The test engine was operated over a range of conditions to represent operation of a large diesel engine in the Goldstone Energy Program. The results of the test program supplied insight into the design requirements for a large-scale performance test program.

I. Introduction

A test program was undertaken at Cornell University under JPL contract to provide a feasibility demonstration of a hydrogen-fueled diesel engine. This fueling system is proposed as a means of operating the diesel engine power plants at Goldstone on a fuel derived from solar energy.

II. Prologue

Cornell University has a contract from the Department of Transportation for the investigation of emissions from a hydrogen-fueled, spark ignition engine. The investigation is being performed by Howard S. Homan, under the direction of Professor P. C. T. de Boer.

The test facility is a 606-cm³ (37-in.³) displacement, Waukesha Cetane Cooperative Fuel Research (CFR) engine, equipped with a hydrogen-fuel injection valve that is unique to Cornell. The valve was designed to allow

adjustment of injection duration and timing and to investigate emissions with respect to the independent variables of compression ratio, fuel/air ratio, and injection schedule parameters. The design of the valve is such that injection can be achieved during a combustion event, so that diesel operation can be simulated. Ignition was by a spark plug, energized by a conventional ignition system. The facility is equipped with instrumentation to allow measurement of efficiency, power output, engine operating pressures, fuel flows, and exhaust emissions. Additional equipment is used to safely supply, monitor, and control high-pressure hydrogen.

III. Test Description

The test program was devised to explore compression ignition over a range of compression ratios, equivalence ratios ϕ ($\phi = (\text{fuel/air ratio actual})/(\text{fuel/air ratio stoichiometric})$), and injection timing to represent pro-

jected operation of a hydrogen-fueled Caterpillar model D399 diesel engine. Table 1 is a list of these parameters.

The following parameters were measured to derive engine performance data:

- (1) Engine rpm.
- (2) Fuel flow rate.
- (3) Intake air flow rate.
- (4) Torque.
- (5) Intake air pressure.
- (6) Injection duration timing.
- (7) Cylinder pressure vs time.
- (8) Nitric oxide (NO_x) emissions.
- (9) Cylinder water jacket temperature.
- (10) Exhaust oxygen content.

In addition, any pertinent conditions or events associated with a test were noted, including ignition parameters, and subjective engine operation "quality."

Alternate ignition aids, a continuous spark system, a timed spark system, and a glow plug were supplied to aid operation where compression ignition was unsuccessful.

IV. Test Results

Included are three figures from the Cornell test report: Fig. 1, exhaust oxygen content; Fig. 2, indicated efficiency, and Fig. 3, total nitric oxides.

The data for Fig. 1 were sampled from the exhaust of the engine with an oxygen meter. The ordinate and abscissa on the graph are mole fraction of oxygen and equivalence ratio, respectively. The dashed lines are indicative of zero and complete combustion, as noted. As indicated, the combustion efficiency of the engine, as represented by these data, is poor; this is probably due to configurational effects of prechamber shape, injector location, and prechamber orifice size and location. Figure 2 is a plot of indicated thermal efficiencies as a function of equivalence ratio. Baseline data were taken on the engine with diesel oil fueling, as a comparison to the hydrogen fueling. Although there is significant scatter in the data, due to the limited number of data points, there is a trend that indicates higher efficiency on hydrogen at low equivalence ratios (this is the region of normal operation of the Caterpillar engines). This is very encouraging, and provides a potential performance advantage in reducing hydrogen generation and storage requirements.

Figure 3 provides the emissions as a function of equivalence ratio. There are not enough data points to make specific conclusions, although there seems to be little difference between diesel oil and hydrogen.

Ignition by compression was unsuccessful on the range of compression ratios and equivalence ratios. We were successful in both glow plug and spark ignition. Figures 4 and 5 show a cylinder pressure trace versus crankshaft position. Figure 5 is with spark ignition, and Fig. 4 is with glow plug. Engine operating parameters are similar. The glow plug ignition is far more satisfactory as indicated by pressure rise and peak amplitudes.

Table 1. Test parameters

Compression ratio	15.5:1 to 30.25:1
Equivalence ratio	0.1 to 0.8
Engine configuration	Prechamber (divided combustion chamber)
Engine speed	1200 rpm (nominal)
Injection timing	TDC \pm 5° (best torque)
Intake air pressure	101325 N/m ² (1 atm) (absolute)
Intake air temperature	22 \pm 6°C (72 \pm 10°F)
Ignition aid	As required

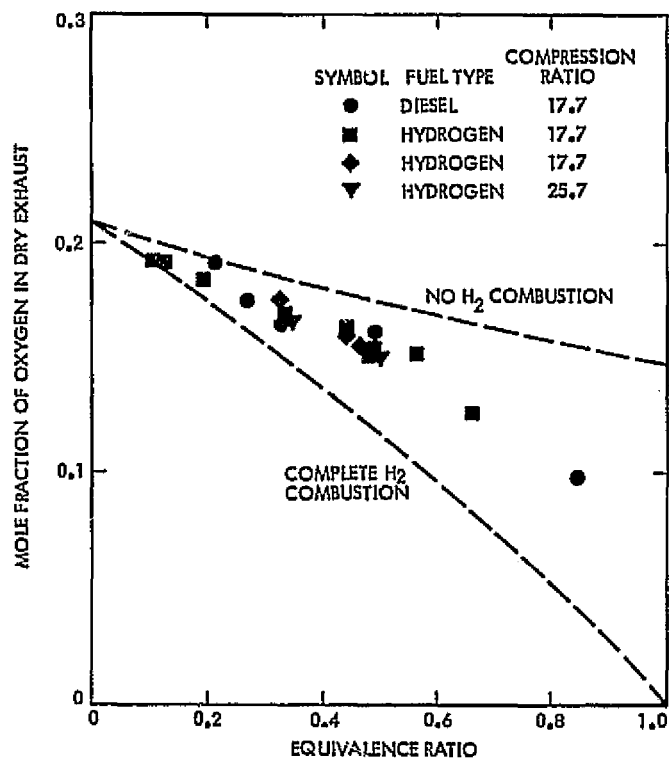


Fig. 1. Oxygen content of exhaust

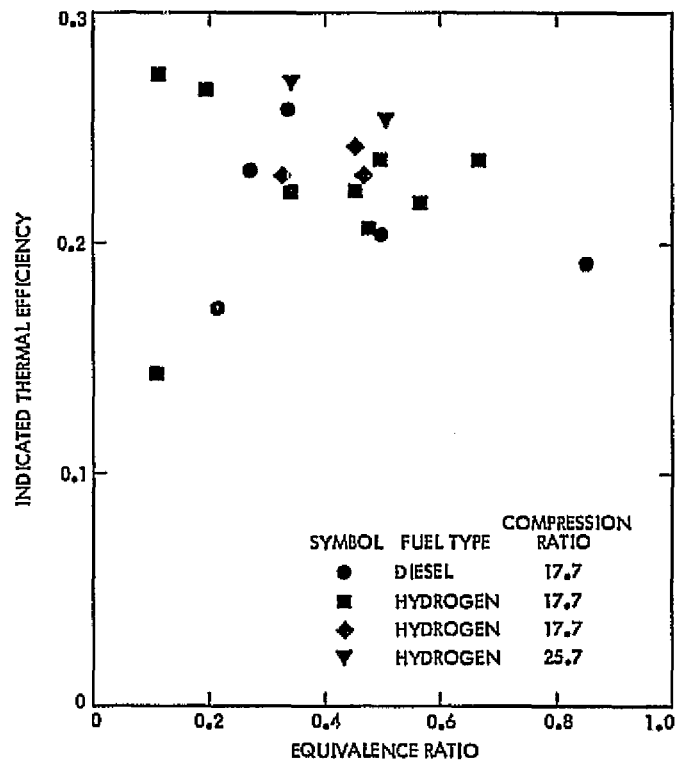


Fig. 2. Indicated efficiency

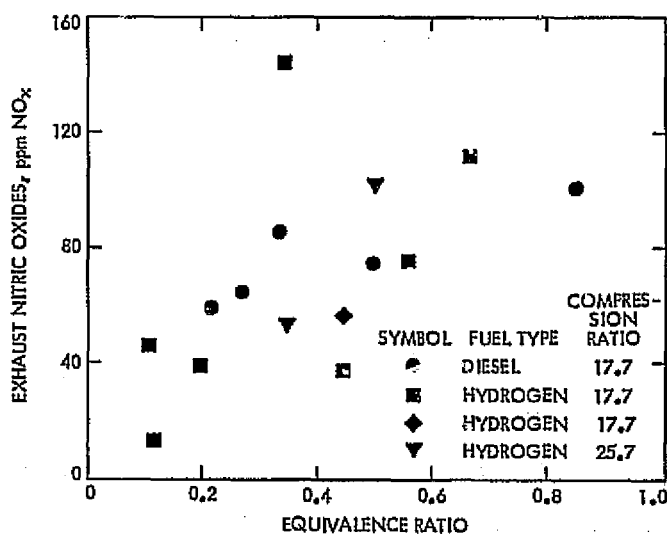


Fig. 3. Total nitric oxides

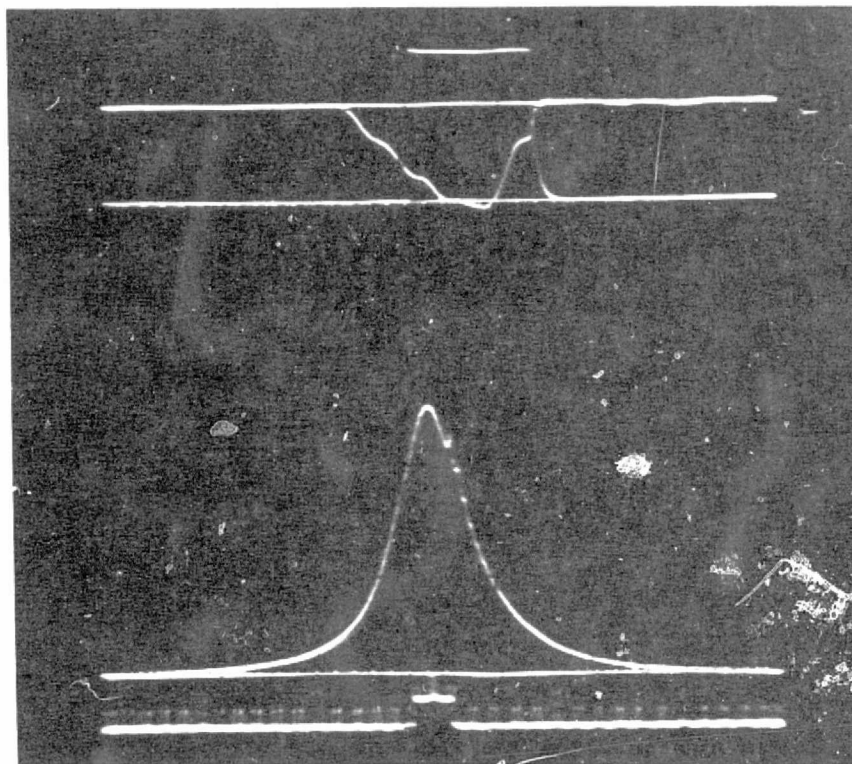


Fig. 4. Data display of engine operating on hydrogen glow plug ignition
(compression ratio = 17.6:1)

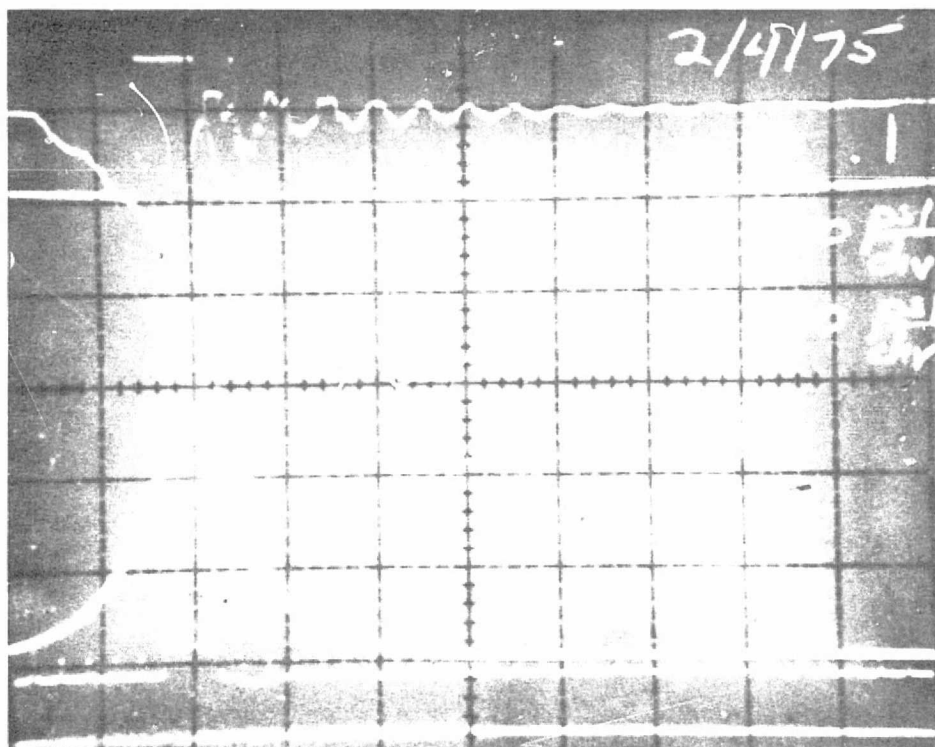


Fig. 5. Data display of engine operation on hydrogen (continuous spark ignition;
compression ratio = 17.5:1)